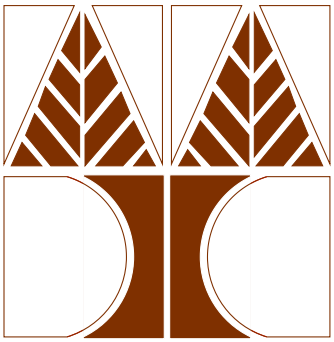

UNIVERSITY OF CYPRUS

PHYSICS DEPARTMENT

Hadron Form Factors and Hadron Deformation from Lattice QCD

PhD DISSERTATION

Giannis Koutsou

JULY 2008

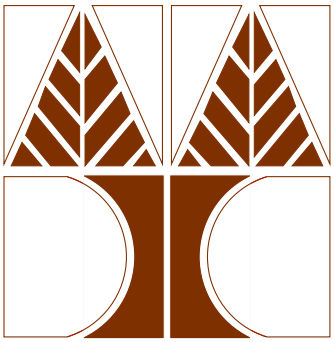

UNIVERSITY OF CYPRUS

PHYSICS DEPARTMENT

PhD Dissertation

of

Giannis Koutsou

Adviser

Constantia Alexandrou

Submitted in partial fulfillment of the requirements for the
degree of Doctor of Philosophy
in the Physics Department at the University of Cyprus

July 2008

PhD Candidate: Giannis Koutsou

Title of Dissertation: Hadron Form Factors and Hadron Deformation in Lattice QCD

Dissertation Committee:

Prof. Constantia Alexandrou, Research Supervisor

Prof. Haralambos Panagopoulos

Assist. Prof. Nicolaos Toumbas, Committee Chairman

Prof. Chris Michael

Prof. Karl Jansen

Defended on July 22, 2008

Acknowledgments

The work in this thesis could not have been possible if it where not for the constant support, knowledge and input of my supervisor Dina Alexandrou. I shall be forever grateful for the patience and trust she showed in me. As in most such theses, the results presented here are a collaborative effort of several researchers who I would like to take this opportunity to thank.

I would first of all like to thank Antonis Tsapalis who was always willing to help out and support me in the early stages of my PhD studies and with who conversations where always interesting as well as fruitful. This goes equally for Petros Dimopoulos who I would like to also thank for being a good friend. Special thanks to Theodoros Leontiou with whom our collaboration was most enjoyable. I would also like to acknowledge the indispensable input and support from Thomas Korzec.

This brings me to my fellow PhD students. Many special thanks to my dear friend Andreas Athenodorou for all those late night discussions. Thanks also to Martha Constantinou, Savvas Polydorides and Apostolos Skouroupathis for a very fun working environment.

I would also like express my gratitude to my family and especially my parents for their understanding and totally unselfish support.

And last but definitely not least I would like to thank Chrysanthi for always being there, even when sometimes she had every right not to.

This work was supported by the Cyprus Research Promotion Foundation.

Abstract

We present a lattice study of hadron form factors and hadron deformation. Hadron form factors encode information on the composite nature of hadrons, their size and shape. The calculation of these fundamental quantities from first principles provides a valuable input to ongoing and planned experiments and theoretical models. In this thesis we develop techniques for the evaluation of the nucleon electromagnetic, axial and pseudo-scalar form factors, the nucleon to Δ electromagnetic, axial and pseudo-scalar transition form factors and the Δ electromagnetic form factors. In particular, we develop methods to extract accurately both the dominant as well as the sub-dominant form factors. The latter are of particular importance since they probe hadron deformation. Our methods include smearing techniques to ensure early ground state dominance and gauge noise suppression, construction of optimized sinks to isolate the sub-dominant form factors and to obtain the largest set of momentum vectors that contribute to a given momentum transfer thereby increasing statistics and a suitable over constrained analysis that takes all statistically independent lattice measurements into account when extracting the form factors. These techniques are tested in the quenched approximation and then applied to two dynamical flavors of Wilson fermions and to domain wall valence quarks on staggered sea quarks. We show that the electric and Coulomb quadrupole nucleon to Δ transition form factors are non-zero. We also show, for the first time in lattice QCD, that the Δ electric quadrupole form factor is non-zero pointing to a deformation of the Δ. Furthermore hadron deformation is studied directly by computing density-density correlators. This is done for the pion, the ρ-meson, the nucleon and the Δ. The evaluation of the four-point function requires the computation of all-to-all propagators. We develop techniques to reliably compute all-to-all propagators using stochastic noise and dilution. In the case of the mesons we apply the one-end trick method to obtain very accurate results for the density-density correlators and show that the ρ-meson is clearly deformed. Finally we show how to extract the pion form factor using density-density correlators.

Περίληψη

Σε αυτή την εργασία μελετάμε παράγοντες μορφής (Form Factors) αδρονίων και την παραμόρφωση αδρονίων. Οι παράγοντες μορφής των αδρονίων περιέχουν πληροφορίες για την σύστασή τους, το μέγεθός τους και το σχήμα τους. Ο υπολογισμός αυτών των στοιχειωδών ποσοτήτων από πρώτες αρχές παρέχει πολύτιμες πληροφορίες τόσο σε τρέχων όσο και σε προγραμματισμένα πειράματα ως επίσης και σε θεωρητικά μοντέλα. Σε αυτή τη διπλωματική εργασία αναπτύσσουμε τις τεχνικές για τον υπολογισμό των Ηλεκτρομαγνητικών και Ασθενών παραγόντων μορφής του νουκλεονίου και της μετάβασης του νουκλεονίου σε Δέλτα ως επίσης και τους Ηλεκτρομαγνητικούς παράγοντες μορφής του Δέλτα. Ποιο συγκεκριμένα, αναπτύσσουμε τις τεχνικές για την ακριβείς εξαγωγή τόσο των πρωτεύων όσο και των δευτερευόντων παραγόντων μορφής. Οι τελευταίοι είναι ιδιαίτερης σημασίας αφού ανιχνεύουν πιθανή παραμόρφωση των υπό μελέτη αδρονίων. Οι μέθοδοί μας συμπεριλαμβάνουν τεχνικές εξομάλυνσης (smearing) για την κυριαρχία της θεμελιώδους κατάστασης όσο το δυνατό ποιο ενωρίς και την καταστολή του θορύβου βαθμίδας (gauge noise), κατασκευή βελτιστοποιημένων πηγών για την απομόνωση των δευτερευόντων παραγόντων μορφής και για να πάρουμε το μεγαλύτερο σύνολο από ανύσματα ορμής που συνεισφέρουν σε δεδομένη μεταφορά ορμής αυξάνοντας έτσι το στατιστικό δείγμα και μια κατάλληλη υπερ-περιορισμένη ανάλυση (over constrained analysis) η οποία λαμβάνει υπόψιν όλες τις στατιστικά ανεξάρτητες πλεγματικές μετρήσεις στην εξαγωγή των παραγόντων μορφής. Αυτές οι τεχνικές δοκιμάζονται αρχικά στην προσέγγιση απόσβεσης (quenched approximation) και έπειτα εφαρμόζονται σε δυο γεύσεις δυναμικών κουάρκς του Wilson ως επίσης και σε domain wall κουάρκς σθένους με staggered κουάρκς υποβάθρου. Στην εργασία δείχνουμε πως ο ηλεκτρικός και Coulomb τετραπολικός παράγοντας μορφής της Ηλεκτρομαγνητικής μετάβασης νουκλεονίου σε Δέλτα είναι μη μηδενικοί. Επίσης δείχνουμε, για πρώτη φορά στην Κβαντική Χρωμοδυναμική Πλέγματος, πως ο παράγοντας μορφής ηλεκτρικού τετραπόλου του Δέλτα είναι μη μηδενικός υποδεικνύοντας παραμόρφωση στο σωματίδιο αυτό. Πέραν αυτού, μελετάμε άμεσα το θέμα της παραμόρφωσης των αδρονίων μέσω του υπολογισμού της συνάρτησης συσχέτισης δύο πυκνοτήτων. Αυτό γίνεται για το πιόνιο, το μεσόνιο ρ, το νουκλεόνιο και το σωματίδιο Δέλτα. Ο υπολογισμός αυτής της συνάρτησης συσχέτισης τεσσάρων σημείων απαιτεί τον υπολογισμό του διαδότη από όλα τα σημεία σε όλα τα σημεία του πλέγματος (all-to-all propagator). Αναπτύσσουμε τεχνικές για τον αξιόπιστο υπολογισμό του διαδότη αυτού χρησιμοποιώντας στοχαστικές μεθόδους και την μέθοδο αραίωσης (dilution). Για την περίπτωση των μεσονίων εφαρμόζουμε επιπρόσθετα το τέχνασμα της μίας πλευράς (one-end trick) για να πάρουμε αποτελέσματα πολύ υψηλής ακρίβειας για την συνάρτηση συσχέτισης που δείχνουν πως το ρ - μεσόνιο είναι καθαρά μη σφαιρικό. Τέλος δείχνουμε πως εξάγεται ο παράγοντας μορφής του πιονίου από συναρτήσεις συσχέτισης δύο πυκνοτήτων.

Contents

List of Figures

List of Tables

Chapter 1

Introduction

Quantum Chromodynamics (QCD) is the theory that describes the nuclear strong force, the force that holds quarks to form bound states - the hadrons. Its two main characteristics that distinguish it from all other forces are *confinement* and *asymptotic freedom*. Confinement means that an infinite amount of energy is needed to free quarks from each other while asymptotic freedom means that at large energy scales (or equivalently, short distances), quarks react weakly and thus QCD can be studied perturbatively.

At nuclear scales, where many hadronic properties are measured experimentally, the QCD coupling constant is of the order of one, meaning that a perturbative expansion cannot be carried out. Thus non-perturbative methods are needed for the calculation of hadronic observables from first principles. The only available method that we have up to now is Lattice QCD. Within this approach, the theory is defined on a discreet, finite space-time box allowing, by virtue of the path integral formulation of quantum mechanics and Wick rotation to imaginary time, the numerical simulation of the theory using methods of statistical physics.

1.1 Quantum Chromodynamics

Quarks, the constituents of hadrons, interact with each other via the strong force, the mediator bosons of which are the gluons. This force is felt by particles carrying color charge which is a quantum number taking three values contrary to electric charge, which is described by just one. QCD is a gauge theory of the SU(3) gauge group. The Lagrangian of QCD is given by:

$$\mathcal{L} = \bar{\psi}(i\not{D} - m)\psi - \frac{1}{4}F^a_{\mu\nu}F^{\mu\nu}_a, \tag{1.1}$$

where $\psi(x)$ is the quark field in the fundamental representation of SU(3), i.e. a Dirac spinor which additionally carries three color indices. The operator $\not{D}$ is given by:

$$\not{D} = \gamma^\mu D_\mu = \gamma^\mu \partial_\mu + igG^a_\mu \gamma^\mu T^a, \tag{1.2}$$

where γ^μ are the Dirac matrices (a definition of the representation used throughout this thesis can be found in Appendix A), T^a the generators of SU(3), g the bare coupling constant of QCD and $G^a_\mu(x)$ a gluon field in the adjoint representation of SU(3) with

a =1,2,...,8 color components. $F^a_{\mu\nu}$ is the field tensor operator given by:

$$F^a_{\mu\nu} = \partial_\mu G^a_\nu - \partial_\nu G^a_\mu - g f_{abc} G^b_\mu G^c_\nu \tag{1.3}$$

where f_{abc} are the structure constants of the SU(3) group. Note that unlike QED where photons do not interact with each other, the term $g f_{abc} G^b_\mu G^c_\nu$, which is a consequence of the fact that SU(3) is a non-abelian unitary group, allows three and four gluon interactions. This interaction term makes QCD very different from QED. It exhibits two unique characteristics:

i) Asymptotic Freedom: At high energy scales, or equivalently short distances, QCD is asymptotically free, meaning quarks interact weakly, thus allowing a perturbative expansion of the theory. Asymptotic freedom was predicted by Frank Wilczek and David Gross [1] and David Politzer [2] in the 1970s earning them the 2004 Nobel Prize in Physics.

ii) Confinement: The amount of energy needed to free a quark from a hadron is infinite, hence there are no free quarks. Although there is no analytic proof for confinement, it is widely accepted to hold. This is mainly due to empirical evidence such as the absence of free color charges in nature, the failure of experiment to detect free quarks, and most importantly that confinement has been confirmed via numerical simulations on the lattice.

The coupling constant of QCD is of the order of one at scales already around the size of the nucleon. Thus the theory is confined at energy scales where hadronic observables are relevant, creating the need for a non-perturbative approach for the solution of QCD.

1.2 Lattice QCD

Lattice QCD is the only method for solving QCD non-perturbatively. Within this method, a discretized version of the action is defined on a finite space-time lattice, and the theory is simulated numerically using Monte Carlo methods to produce representative gluon configurations of the QCD vacuum. Observables are obtained via Feynman path integrals, i.e. averaging appropriately defined correlation functions of fermion and gluon fields over these representative configurations. Thus, through lattice QCD one obtains a first principles calculation of observables, since the QCD Lagrangian is the only input to the Feynman path integral. On the other hand, there is a freedom in the choice of the discretization of the action which, however, observables should be independent of when taking the continuum limit. The choice of the discretization is often governed by the amount of computational resources available.

1.2.1 Discretization

One cannot discretize the action in such a way as to preserve the symmetries that the continuum action exhibits. A trivial example is that of rotational invariance; on the

lattice, only discrete angles can be defined, a fact which has several implications such as what values of the orbital angular momenta are allowed. Defining QCD on a lattice has implications on deeper symmetries of elementary particle physics such as chirality. The exact SU(3) local gauge symmetry, which is a direct consequence of color charge, must be preserved in a discretized version of the QCD action. Thus, K. Wilson [3] proposed a discretization scheme where appropriate link variables where defined to connect nearest neighboring lattice sites. Such a link variable, which is defined as an SU(3) matrix, is given by the path ordered integral:

$$U(x+a\hat{\mu};x) = U_\mu(x) = \mathcal{P}e^{-ig\int_x^{x+a\hat{\mu}} dx G_\mu^b(x)T_b} \simeq e^{-igaG_\mu^b(x)T_b}, \tag{1.4}$$

where $\hat{\mu}$ is a unit vector in the μ direction and a is the lattice spacing. The gluonic part of the action ($F^a_{\mu\nu}F_a^{\mu\nu}$) is given in terms of the closed 1×1 product of links, the plaquette $P_{\mu\nu}(x)$, namely:

$$S_G = \beta\sum_x\sum_{\mu>\nu}[1-\frac{1}{3}\Re\{\mathrm{Tr}P_{\mu\nu}(x)\}], \tag{1.5}$$

where $\beta = \frac{2N_c}{g^2}$, N_c being the number of colors and $\Re$ means the real part. S_G gives the correct continuum gluonic action when $a\to 0$. To show this we shall first give the plaquette in terms of links:

$$\begin{aligned} P_{\mu\nu}(x) =& U_\mu(x)U_\nu(x+a\hat{\mu})U_\mu^\dagger(x+a\hat{\nu})U_\nu^\dagger(x) \\ =& \exp\left[-igaG_\mu^b(x)T_b\right]\exp\left[-igaG_\nu^c(x+a\hat{\mu})T_c\right]\times \\ & \exp\left[igaG_\mu^d(x+a\hat{\nu})T_d\right]\exp\left[igaG_\nu^e(x)T_e\right] \\ =& \exp\left\{-iga^2T_b\frac{G_\nu^b(x+a\hat{\mu})-G_\nu^b(x)}{a} + iga^2T_b\frac{G_\mu^b(x+a\hat{\nu})-G_\mu^b(x)}{a}\right. \\ & \left. - g^2a^2G_\mu^c(x)G_\nu^d(x)[T_c,T_d]+\mathcal{O}(a^4)\right\} \\ \xrightarrow{a\to 0}& \exp\left\{-iga^2T_b\left[\partial_\mu G_\nu^b(x)-\partial_\nu G_\mu^b(x)-gf^{bcd}G_\mu^c(x)G_\nu^d(x)\right]+\mathcal{O}(a^4)\right\} \end{aligned} \tag{1.6}$$

where in the last step we have replaced the discreet derivative with the continuum derivative:

$$\frac{G_\nu^b(x+a\hat{\mu})-G_\nu^b(x)}{a} \xrightarrow{a\to 0} \partial_\mu G_\nu^b(x). \tag{1.7}$$

Substituting the expression for the plaquette into Eq. (1.5) we obtain:

$$\begin{aligned} P_{\mu\nu}(x) &= e^{-iga^2T_bF^b_{\mu\nu}(x)+\mathcal{O}(a^4)} \\ &= 1 - iga^2T_bF^b_{\mu\nu}(x) + \frac{1}{2}g^2a^4T_bF^b_{\mu\nu}(x)T^cF^{\mu\nu}_c(x) + \mathcal{O}(a^6) \\ \Rightarrow S_G &= \frac{\beta g^2a^4}{6}\sum_x\sum_{\mu>\nu}\mathrm{Tr}[T_bF^b_{\mu\nu}(x)T^cF^{\mu\nu}_c(x)] \\ &= \frac{\beta g^2a^4}{6}\sum_x\sum_{\mu>\nu}F^b_{\mu\nu}(x)F^{\mu\nu}_c(x)\frac{\delta_{bc}}{2}. \end{aligned} \tag{1.8}$$

Since the field tensor is antisymmetric ($F^b_{\mu\nu}(x) = -F^b_{\nu\mu}(x)$) the sum over μ and ν can be written as:

$$\sum_{\mu>\nu}F^b_{\mu\nu}(x)F^{\mu\nu}_b(x) = \frac{1}{2}\sum_{\mu,\nu}F^b_{\mu\nu}(x)F^{\mu\nu}_b(x). \tag{1.9}$$

Hence the plaquette action is equivalent to the gluonic part of the continuum action when $a \to 0$:

$$\begin{aligned} S_G =& \frac{\beta g^2a^4}{6}\sum_x\frac{1}{4}F^b_{\mu\nu}F^{\mu\nu}_b \xrightarrow{a\to 0} \frac{\beta g^2a^4}{6}\frac{1}{a^4}\int d^4x\frac{1}{4}F^b_{\mu\nu}F^{\mu\nu}_b \\ =& \int d^4x\frac{1}{4}F^b_{\mu\nu}F^{\mu\nu}_b. \end{aligned} \tag{1.10}$$

This discretized version of the action is indeed invariant under a local gauge transformation:

$$\begin{aligned} \psi(x) \to \tilde{\psi}(x) &= e^{-ig\alpha^c(x)T_c}\psi(x) = \mathcal{U}(x)\psi(x), \\ G^c_\mu(x) \to \tilde{G}^c_\mu(x) &= G^c_\mu(x) + \partial_\mu\alpha^c(x) \Rightarrow \\ U(x+a_\mu;x) \to \tilde{U}(x+a_\mu;x) &= \mathcal{U}(x+a_\mu)U(x+a_\mu;x)\mathcal{U}^\dagger(x), \end{aligned} \tag{1.11}$$

where $a_\mu = a\hat{\mu}$, since the plaquette, in terms of a path ordered product of links, transforms as:

$$\begin{aligned} P_{\mu\nu}(x) =& \mathcal{P}U(x;x+a_\nu)U(x+a_\nu;x+a_\nu+a_\mu)\times \\ & U(x+a_\nu+a_\mu;x+a_\mu)U(x+a_\mu;x) \\ \to \tilde{P}_{\mu\nu}(x) =& \mathcal{U}(x)P_{\mu\nu}\mathcal{U}^\dagger(x), \end{aligned} \tag{1.12}$$

thus leaving the trace invariant. For the fermion action, the discretization is not as straight forward. Let us consider a naive discretization of the Dirac operator. The QCD action for fermions would then read:

$$S_F = a^4\sum_x\frac{1}{2a}\gamma^\mu[\bar{\psi}(x)U_\mu(x)\psi(x+a\hat{\mu}) - \bar{\psi}(x)U^\dagger_\mu(x-a\hat{\mu})\psi(x-a\hat{\mu})] + m\bar{\psi}(x)\psi(x). \tag{1.13}$$

Now let us consider the propagator of a fermion in a free field i.e. $U_\mu(x) = \mathbb{1}$. The Fourier transform of the Dirac operator gives:

$$G(p) = [\frac{i}{a}\gamma^\mu \sin(ap_\mu) + m]^{-1}, \tag{1.14}$$

which, at $m = 0$ has extra poles at finite a compared to a single pole at the origin when $a \to 0$. This means that on the lattice the naively discretized Dirac operator describes more than one particle, since $\sin(ap_\mu)$ becomes zero at every corner of the momentum-space lattice. The action proposed by Wilson solves this so called fermion doubling problem by adding an extra double derivative term:

$$\begin{aligned} S_F = \quad & a^4 \sum_{x,\mu} \bar{\psi}(x)\gamma^\mu D_\mu \psi(x) - a\frac{r}{2}\bar{\psi}(x) D_\mu D^\mu \psi(x) + m\bar{\psi}(x)\psi(x) \\ = & -a^4 \sum_{x,\mu} \frac{1}{2a}[\bar{\psi}(x)(r-\gamma_\mu)U_\mu(x)\psi(x+a\hat{\mu}) \\ & \qquad + \bar{\psi}(x)(r+\gamma_\mu)U_\mu^\dagger(x-a\hat{\mu})\psi(x-a\hat{\mu})] \\ & + a^4 \sum_x (m + \frac{4}{a}r)\bar{\psi}(x)\psi(x), \end{aligned} \tag{1.15}$$

where the Wilson parameter $r \in (0, 1]$ with $r = 0$ corresponding to the naive discretization. The double derivative term added gives the extra fermions a different dependence on the lattice spacing a, namely it gives them a mass that goes to infinity as $a \to 0$. Thus at sufficiently small lattice spacings a the doublers are suppressed. The Wilson hopping parameter: $\kappa = \frac{1}{2am+8r}$ is a more convenient parameter than the bare mass since by rescaling the fermion fields $\psi(x) \to \frac{\sqrt{2\kappa}}{a^{3/2}}\psi(x)$, the action assumes the simpler form:

$$\begin{aligned} S_F = & -\kappa \sum_{x,\mu} [\bar{\psi}(x)(r-\gamma_\mu)U_\mu(x)\psi(x+a\hat{\mu}) \\ & \qquad + \bar{\psi}(x)(r+\gamma_\mu)U_\mu^\dagger(x-a\hat{\mu})\psi(x-a\hat{\mu})] \\ & + \sum_x \bar{\psi}(x)\psi(x). \end{aligned} \tag{1.16}$$

The value of κ at which the mass of the pseudo-scalar meson, the pion, becomes zero is referred to as κ critical (κ_c). The action can be conveniently rewritten in the form:

$$\begin{aligned} S_F = & \sum_{x,y} \bar{\psi}(x) D_W(x;y)\psi(y), \\ D_W(x;y) = & -\kappa \sum_\mu [(r-\gamma_\mu)U_\mu(x)\delta_{x+a\hat{\mu},y} + (r+\gamma_\mu)U_\mu^\dagger(y)\delta_{x-a\hat{\mu},y}] + \delta_{x,y}, \end{aligned} \tag{1.17}$$

with the Wilson Dirac operator, $D_W(x;y)$, being the discretized version of the massive Dirac operator $i\not{D} - m$. It is quite trivial to see that a local gauge transformation as in Eq. (1.11) leaves the total discretized QCD action ($S_F + S_G$) invariant.

Wilson fermions explicitly break chiral symmetry at finite lattice spacing even for

$m = 0$, due to the terms proportional to r. In other words, the cost of removing the doublers, which appeared in the naive discretization, is the explicit breaking of chiral symmetry, since the massless Wilson-Dirac operator no longer anticommutes with γ_5 at finite a:

$$\gamma_5 D_W + D_W \gamma_5 \sim ar\gamma_5 D^\mu D_\mu. \tag{1.18}$$

A no-go theorem has been proved by Nielsen and Ninomiya [4] stating that any discretized, local version of the Dirac operator cannot preserve chiral symmetry at finite lattice spacing while simultaneously avoiding doublers. Ginsparg and Wilson [5] propose a way around the no-go theorem by allowing the anticommutator of the discretized Dirac matrix and γ_5 to be non-zero at finite lattice spacing. The so called Ginsparg-Wilson relation reads:

$$\gamma_5 D + D\gamma_5 = aD\gamma_5 D. \tag{1.19}$$

Such a discretized Dirac operator is invariant under the chiral-like transformation:

$$\psi \to \tilde{\psi} = e^{-i\gamma_5(1-\frac{1}{2}aD)\theta}\psi \tag{1.20}$$

which is the continuum chiral transformation when $a \to 0$. Two formulations that satisfy Eq. (1.19) are Domain Wall fermions [6] and Overlap fermions [7]. Briefly, in the Overlap formulation, the Dirac operator is discretized as $D_{\text{Over}} = m[1 + \gamma_5 \text{sgn}(\gamma_5 D_W)]$ where sgn denotes the sign function. Apart from the complications that arise in Monte Carlo simulations due to the sign function, redefining operators within this formulation can often be tedious. Within the domain wall fermion formulation, on the other hand, a five dimensional Wilson Dirac operator is defined. Fermions of opposite handedness are located on the boundaries of the fifth dimension and thus chiral symmetry is preserved for a large enough extent of this fifth dimension. Until recently, simulating QCD with these actions was impractical due to the great amount of computational resources needed compared to Wilson fermions.

1.2.2 Path Integral Formulation

Observables in lattice QCD are measured via the path integral formulation of quantum mechanics. Within this picture, the vacuum expectation value of an operator $\mathcal{O}$ is given by:

$$\langle\Omega|\mathcal{O}|\Omega\rangle = \frac{1}{Z}\int \mathcal{D}\psi(x)\mathcal{D}\bar{\psi}(x)\mathcal{D}U(x)\mathcal{O}[\bar{\psi},\psi,U]e^{-\frac{i}{\hbar}S[\bar{\psi},\psi,U]} \tag{1.21}$$

where $\mathcal{D}\psi(x)$, $\mathcal{D}\bar{\psi}(x)$ and $\mathcal{D}U(x)$ denote integration over all possible fermion and gluon configurations (over all paths), while the partition function Z is given by:

$$Z = \int \mathcal{D}\psi(x)\mathcal{D}\bar{\psi}(x)\mathcal{D}U(x)e^{-\frac{i}{\hbar}S[\bar{\psi},\psi,U]}. \tag{1.22}$$

Wick rotating to a Euclidean space-time $t \to it$ we have:

$$\langle\Omega|\mathcal{O}|\Omega\rangle = \frac{1}{Z}\int \mathcal{D}\psi(x)\mathcal{D}\bar{\psi}(x)\mathcal{D}U(x)\mathcal{O}e^{-S[\bar{\psi},\psi,U]\frac{1}{\hbar}}, \tag{1.23}$$

which thus allows a statistical treatment of quantum field theory. Numerically, one would define a lattice with the gluons connecting neighboring sites and the fermions living on the sites as we have seen previously in this section. We would then generate representative gluon and quark configurations via Monte Carlo methods, with probability of $e^{-\frac{S}{\hbar}}/Z$. The vacuum expectation value of an arbitrary observable would then be its average over these quark and gluon configurations.

In practice however, the numerical estimation of the path integral has an intrinsic problem: the fermion fields integrated over in the path integral must be represented by anticommuting numbers. Thus $\bar{\psi}(x)$ and $\psi(x)$ are Grassmann numbers, obeying Grassmann algebra. It is impossible to represent such numbers on a computer, at least at a level low enough for such an integration to be practical. The way around this is to integrate over the fermionic degrees of freedom analytically. The consequence of this integration as we shall see below, is that the problem becomes much more computationally involved. We shall first show that the integration of the fermion variables in the partition function gives rise to the determinant of the Dirac operator $M = \not{D} + m$:

$$Z_F[U] = \int \mathcal{D}\psi(x)\mathcal{D}\bar{\psi}(x)e^{-S_F[\bar{\psi},\psi,U]} = \int \mathcal{D}\psi\mathcal{D}\bar{\psi}e^{-\bar{\psi}M[U]\psi} = \det M[U]. \tag{1.24}$$

This can be shown by going to diagonal basis for $M = \mathcal{U}^{-1}M_d\mathcal{U}$, and then transforming the integration variables according to $\xi = \mathcal{U}\psi$ and $\bar{\xi} = \bar{\psi}\mathcal{U}^{-1}$. Since $\det\mathcal{U} = 1$, the Jacobian of the change of variables is one. Hence the fermionic integral can be written as:

$$\int \prod_i d\xi_i \prod_j d\bar{\xi}_j \prod_k (1 + \bar{\xi}_k\xi_k\lambda_k) \tag{1.25}$$

where $\lambda_k = (M_d)_{k,k}$ are the eigenvalues of M, and we have merged all indices of the fermion fields (spatial, color and Dirac) to a single index. According to Grassmann algebra, $\int d\xi = 0$ and $\int d\xi\, \xi = 1$, ξ being a Grassmann variable. Hence the only term of the product $\prod_k(1 + \bar{\xi}_k\xi_k\lambda_k)$ that has a non-zero integral is $\prod_k \bar{\xi}_k\xi_k\lambda_k$ which gives:

$$\int \prod_i d\xi_i \prod_j d\bar{\xi}_j \prod_k \bar{\xi}_k\xi_k\lambda_k = \prod_k \lambda_k = \det M[U]. \tag{1.26}$$

To summarize:

$$Z = \int \mathcal{D}\psi\mathcal{D}\bar{\psi}\mathcal{D}U e^{\bar{\psi}M[U]\psi + S_G[U]} = \int \mathcal{D}U \det M[U] e^{-S_G[U]}. \tag{1.27}$$

We can also quite generally carry out this integration for an arbitrary observable. In terms of fermion fields, any measurable quantity is expressed as a vacuum expectation value of

time-ordered correlation functions. Since fermion fields cannot appear squared, we can quite generally write:

$$\langle \mathcal{O}(x_1,...,x_n,y_1,...,y_n)\rangle = \langle \Omega|\psi(x_n),...,\psi(x_1)\bar{\psi}(y_n),...,\bar{\psi}(y_1)|\Omega\rangle = \frac{1}{Z}\int \mathcal{D}\psi(x)\mathcal{D}\bar{\psi}(x)\mathcal{D}U(x)\psi(x_n),...,\psi(x_1)\bar{\psi}(y_n),...,\bar{\psi}(y_1)e^{-\bar{\psi}M[U]\psi+S_G[U]}. \tag{1.28}$$

The integration over fermion fields can be computed through repeated differentiation of auxiliary fermion fields θ and $\bar{\theta}$ which are set to zero at the end:

$$\begin{aligned}\langle\mathcal{O}\rangle =& \frac{1}{Z}\partial_{\bar{\theta}(x_n)},...,\partial_{\bar{\theta}(x_1)}\partial_{\theta(y_n)},...,\partial_{\theta(y_1)}\ Z_{\theta,\bar{\theta}}\big|_{\theta=\bar{\theta}=0} \\ =& \frac{1}{Z}\partial_{\bar{\theta}(x_n)},...,\partial_{\bar{\theta}(x_1)}\partial_{\theta(y_n)},...,\partial_{\theta(y_1)}\int \mathcal{D}\psi\mathcal{D}\bar{\psi}\mathcal{D}U e^{\bar{\psi}M[U]\psi+\bar{\psi}\theta+\bar{\theta}\psi+S_G[U]}\Big|_{\theta=\bar{\theta}=0}\end{aligned} \tag{1.29}$$

We can evaluate this integral by completing the square in the exponent via a change of variables: $\bar{\xi}=\bar{\psi}+\bar{\theta}M^{-1}[U]$ and $\xi=\psi+M^{-1}[U]\theta$:

$$Z_{\theta,\bar{\theta}} = \int \mathcal{D}U \det D[U] e^{\bar{\theta}M^{-1}[U]\theta+S_G[U]}. \tag{1.30}$$

According to Wick's theorem, the repeated differentiation of the remaining exponent $e^{\bar{\theta}M^{-1}\theta}$ gives all possible permutations of the inverse Dirac matrix M between the arguments of the fermions ψ and antifermions $\bar{\psi}$ (x_i and y_i), i.e.:

$$\begin{aligned}&\partial_{\bar{\theta}(x_n)},...,\partial_{\bar{\theta}(x_1)}\partial_{\theta(y_n)},...,\partial_{\theta(y_1)}\ e^{\bar{\theta}M^{-1}\theta}\Big|_{\theta=\bar{\theta}=0} = \\ &\sum_{q,p}(-1)^{P_{q,p}}M^{-1}(x_{q_n},y_{p_n})...M^{-1}(x_{q_1},y_{p_1}),\end{aligned} \tag{1.31}$$

where the sum is along all possible q,p combinations and the number of permutations $P_{q,p}$ comes from the anticommutation relation of fermion fields, i.e. when permuting two derivatives a minus sign appears $\partial_{\theta(x)}\partial_{\theta(y)}=-\partial_{\theta(y)}\partial_{\theta(x)}$.

Having integrated analytically over the fermion fields we rewrite the path integral for an arbitrary $2n$-point function:

$$\langle \mathcal{O}(x_1,...,x_n,y_1,...,y_n)\rangle = \frac{1}{Z}\int \mathcal{D}U\sum_{q,p}(-1)^{P_{q,p}}M^{-1}(x_{q_n},y_{p_n},U)...M^{-1}(x_{q_1},y_{p_1},U)e^{\ln(\det M[U])-S_G[U]}, \tag{1.32}$$

with:

$$Z=\int \mathcal{D}U e^{\ln[\det M[U]]-S_G[U]}. \tag{1.33}$$

Thus we can now simulate the theory to obtain any correlation function since only an integral over all possible gluon configurations is left. Representative gluon configurations

can be generated via Monte Carlo methods with a probability $e^{\ln[\det M]-S_G}/Z$. For a given correlation function we use the Wick theorem to reach to an expression between quark propagators ($M^{-1}(x;y;U)$) and average this expression over all gluon configurations.

The modified probability means a computation of $\det M$ is needed for every update of the gluon field in the Monte Carlo simulation. Additionally, the evaluation of correlation functions requires the calculation of the inverse of the Dirac operator M for every gluon configuration generated. These two steps, which are direct consequences of the fact that we had to integrate the fermion fields out analytically, are the most computationally intensive parts of any simulation in lattice QCD. In fact, early calculations where carried out ignoring the determinant in the Monte Carlo simulation, an approximation known as quenching. The quenched approximation is still used in modern measurements since it is fast to simulate and thus provides a test of methods to be applied to dynamical actions, which are more expensive to simulate.

Chapter 2

Lattice Methods

In this chapter we shall discuss the main methods used for the study of hadronic observables within lattice QCD. Having already elaborated on the basic principles of lattice QCD, we go on to show how one computes vacuum expectation values and, furthermore, how these are associated with physical quantities. We shall begin by showing how the mass of a hadron can be extracted from its propagator and how this can be computed on the lattice. This shall be followed by an introduction to stochastic techniques used for the estimation of all-to-all propagators. We also describe the techniques used to improve the signal of observables on the lattice such as smearing techniques. Finally we shall introduce three-point functions and explain their importance in association with hadron structure.

2.1 Two-point functions

The aim here is to show that the mass of hadrons can be extracted from the two-point correlator, and to demonstrate this with an example computation on the lattice. We start off by writing the two-point correlator at the hadron level:

$$C(t) = \sum_{\vec{x}} \langle \Omega | \chi(\vec{x}, t) \bar{\chi}(\vec{0}, 0) | \Omega \rangle, \tag{2.1}$$

where $\chi(\vec{x}, t)$ is an interpolating operator that acts on the vacuum creating a hadron with the same quantum numbers as those of the hadron under study. In the Heisenberg picture, we can always shift the operators to the origin by multiplying on both sides with appropriate unitary operators:

$$C(t) = \sum_{\vec{x}} \langle \Omega | e^{-i\hat{\vec{p}}\cdot\vec{x}} e^{\hat{H}t} \chi(\vec{0}, 0) e^{-\hat{H}t} e^{i\hat{\vec{p}}\cdot\vec{x}} \bar{\chi}(\vec{0}, 0) | \Omega \rangle, \tag{2.2}$$

where $\hat{\vec{p}}$ is the momentum operator and $\hat{H}$ the QCD Hamiltonian. Note that we have already performed a Wick rotation to Euclidean time, i.e. $t \to it$. We now insert a complete set of momentum and energy states:

$$\mathbb{1} = \sum_{\vec{k}, n} |n, \vec{k}\rangle \langle n, \vec{k}|, \tag{2.3}$$

where n counts all the QCD Hamiltonian many-body eigenstates. Inserting Eq. (2.3) between χ and $\bar{\chi}$ of Eq. (2.2) we have:

$$C(t) = \sum_{\vec{x},n,\vec{k}} |\langle\Omega|\chi(\vec{0},0)|n,\vec{k}\rangle|^2 e^{-E_n(\vec{k})t} e^{i\vec{k}\cdot\vec{x}} = \sum_n |\langle\Omega|\chi(\vec{0},0)|n,\vec{0}\rangle|^2 e^{-m_n t}, \tag{2.4}$$

where $E_n(\vec{k})$ is the energy eigenvalue of the n^{th} state and the sum over $\vec{x}$, the sink coordinate, projects the two-point function to zero momentum. We have introduced the mass m_n of the n'th state as the energy of the state at zero momentum ($m_n = E_n(\vec{0})$). Now, the only terms that survive the sum over n are those states which have the same quantum numbers as those of the trial state, due to the overlap term $\langle\Omega|\chi|n,\vec{0}\rangle$. At this point we shall be more specific and consider the pion, since it is the simplest hadron. The states that would give non-zero overlap with the interpolating operator of the pion would be the pion and all excitations of the pion as well as multi-pion states. Thus:

$$C(t) = \sum_{n'} |\langle\Omega|\chi_\pi(\vec{0},0)|\pi(n',\vec{0})\rangle|^2 e^{-m_{n'}t}. \tag{2.5}$$

If the time t is large enough, then excited state contributions to the correlator are suppressed, since the correlator decays exponentially with the energy of the state in the exponent. Thus the ground state mass (the pion mass in this case) can be extracted:

$$C_\pi(t) \xrightarrow{t\gg 1} |Z_\pi(\vec{0})|^2 e^{-m_\pi t} \tag{2.6}$$

where $Z_\pi(\vec{p})\sqrt{m_\pi/E_\pi(\vec{p})} = \langle\Omega|\chi_\pi(\vec{0},0)|\pi(\vec{p})\rangle$. The kinematic term is a normalization convention which preserves covariance of the correlator under Lorenz transformations. At this point, we need to express the pion two-point correlation function in terms of quark propagators. We begin by defining the interpolating operator in terms of quark field operators. For instance, the +1 charged pion interpolating operator would be $\chi_{\pi^+}(x) = \bar{d}(x)\gamma_5 u(x)$ where u and d are quark field operators and a trace over color indices is implied. To be a little more general, for the following example we shall assume an interpolating field of the form: $\chi_\Gamma(x) = \bar{d}(x)\Gamma u(x)$, where Γ is an arbitrary gamma structure, i.e. the trial state is some +1 charged meson. The two-point function in terms of the quark field operators is written as:

$$\begin{aligned} C_\pi(\vec{x},t) = \langle\Omega|\chi_\Gamma(\vec{x},t)\bar{\chi}_\Gamma(\vec{0},0)|\Omega\rangle = \\ \langle\Omega|\bar{d}^a_\mu(\vec{x},t)\Gamma_{\mu\nu}u^a_\nu(\vec{x},t)\bar{u}^b_{\mu'}(\vec{0},0)\bar{\Gamma}_{\mu'\nu'}d^b_{\nu'}(\vec{0},0)|\Omega\rangle, \end{aligned} \tag{2.7}$$

where we imply summation over repeated indices. Integration of this expression over the fermion fields u and d gives rise to quark propagators, as we have seen in Chapter 1. There

is only one way to contract the quark with the antiquark fields, shown by the lines:

$$\langle\Omega|\overbrace{\bar{d}^a_\mu(x)\Gamma_{\mu\nu}\overbrace{u^a_\nu(x)\bar{u}^b_{\mu'}(0)}\bar{\Gamma}_{\mu'\nu'}d^b_{\nu'}(0)}|\Omega\rangle = \langle\Gamma_{\mu\nu}G^{ab}_{\nu\mu'}(x;0)\bar{\Gamma}_{\mu'\nu'}G^{ba}_{\nu'\mu}(0;x)\rangle \tag{2.8}$$

where $x = (t, \vec{x})$ and G is the quark propagator i.e. the inverse of the Dirac matrix: $G(x;x_0) = (\not{D} + m)^{-1} = M^{-1}(x;x_0)$. Here we assume degeneracy between up and down quark hence we do not discriminate between the propagator of the up quark and that of the down quark. The antihermiticity of the Dirac matrix implies the forward going propagator is associated with the backwards going through the relation:

$$G(x;x_0) = \gamma_5 G^\dagger(x_0;x)\gamma_5. \tag{2.9}$$

Hence Eq. (2.8) can be rewritten as:

$$\langle \mathrm{Tr}[\Gamma' G(x;0)\bar{\Gamma}' G^\dagger(x;0)]\rangle, \tag{2.10}$$

where $\Gamma' \equiv \Gamma\gamma_5$. For the case of the π^+, $\Gamma = \gamma_5$ and the two-point correlator is simply a trace over the square of the propagator:

$$C(\vec{x},t) = \langle \mathrm{Tr}\left[|G(x;0)|^2\right]\rangle. \tag{2.11}$$

The computation of the mass of a hadron thus involves, numerically, the inversion of the Dirac matrix for each gauge configurations. We summarize the result:

$$\sum_{\vec{x}}\langle \mathrm{Tr}\left[|G(\vec{x},t;0)|^2\right]\rangle \xrightarrow{t\gg 1} |Z_\pi(\vec{0})|^2 e^{-m_\pi t} \tag{2.12}$$

Note that not all components of the inverse need to be computed. Only the propagator from the origin to all lattice sites is required in order to carry out the sum over $\vec{x}$ in Eq. (2.12). A somewhat more involved example is that of the nucleon two-point function. An interpolating field with the quantum numbers of the proton is:

$$\chi^N_\sigma(x) = \varepsilon^{abc}[u^a_\mu(x)(C\gamma_5)_{\mu\nu}d^b_\nu(x)]u^c_\sigma(x) \tag{2.13}$$

where C is the charge conjugation operator $C = \gamma_0\gamma_2$. Note that the interpolating operator has been defined to carry a free spinor index σ since the proton is a spin $\frac{1}{2}$ particle. There are now two ways to contract the up quark fields, hence the proton propagator is a sum

of two terms:

$$\langle\Omega|\chi^N_\sigma(x)\bar{\chi}^N_{\sigma'}(0)|\Omega\rangle = \tag{2.14}$$
$$\langle\Omega|\varepsilon^{abc}\overbrace{u^a_\mu(x)(C\gamma_5)_{\mu\nu}d^b_\nu(x)\underbrace{u^c_\sigma(x)\varepsilon^{a'b'c'}}\bar{u}^{c'}_{\sigma'}(0)}\bar{d}^{b'}_{\nu'}(0)\overbrace{(\overline{C\gamma_5})_{\nu'\mu'}\bar{u}^{a'}_{\mu'}(0)}|\Omega\rangle$$
$$= \varepsilon^{abc}\varepsilon^{a'b'c'}[C\gamma_5 G(x;0)\overline{C\gamma_5}]^{bb'}_{\nu\nu'}$$
$$[G^{cc'}_{\sigma\sigma'}(x;0)G^{aa'}_{\mu\mu'}(x;0) - G^{ac'}_{\mu\sigma'}(x;0)G^{ca'}_{\sigma\mu'}(x;0)].$$

The lines connecting the quark fields above the expression show one possible contraction while the lines below show the other. There is only one way to contract the down quarks, hence we do not show this contraction.

Non-perturbative diagrams are regularly used to depict correlation functions. In Fig 2.1 we show the diagrams corresponding to the two-point function of a meson and a baryon. Time direction is from right to left. The lines denote quark propagators, with the arrows denoting the direction in which the quark propagates:

$$(\vec{y},t_y)\bullet\longleftarrow\bullet(\vec{x},t_x) = G(\vec{y},t_y;\vec{x},t_x). \tag{2.15}$$

Quarks propagate forwards in time while antiquarks propagate backwards in time. These are non-perturbative Feynman diagrams, in the sense that all orders of gluon exchange as well as quark loops are possible and thus omitted in the diagrams.

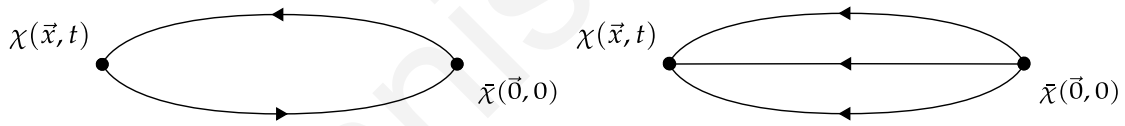

Figure 2.1: Diagrams of two-point functions. Left for mesons and right for baryons.

We return to the case of mesons, to note that for a lattice simulated with periodic or antiperiodic boundary conditions in time, the correlation function of a meson is periodic over the time extent of the lattice (L_t). For instance, Eq. (2.12) becomes:

$$\sum_{\vec{x}}\langle\mathrm{Tr}\left[|G(\vec{x},t;0)|^2\right]\rangle \xrightarrow{t\gg1} |Z_\pi(\vec{0})|^2(e^{-m_\pi t}+e^{-m_\pi(L_t-t)})$$
$$= |Z_\pi(\vec{0})|^2 e^{-m_\pi\frac{L_t}{2}}\cosh\left[m_\pi(t-\frac{L_t}{2})\right]. \tag{2.16}$$

As an example, we shall demonstrate the methods described above for the two lightest mesons: the pseudo-scalar and the vector meson. We consider the ρ meson of spin 1. The interpolating operator used is of the general form $\bar{d}\Gamma u$ where $\Gamma = \frac{\gamma_1-i\gamma_2}{2}, \gamma_3, \frac{\gamma_1+i\gamma_2}{2}$ for the

+1,0 and -1 spin projections respectively. The *effective mass* is typically constructed as:

$$m^H_{\text{eff}}(t) = \log \frac{C_H(t)}{C_H(t+1)} \xrightarrow{t \gg 1} M^H, \tag{2.17}$$

which in the large time limit where excited state contributions are damped is equal to the mass of the hadron. For mesons where the correlator is periodic as in Eq. (2.16), we can make use of the whole of the time extent of the lattice. Namely, we define the effective mass as the solution of:

$$\frac{C_H(t)}{C_H(t+1)} = \frac{\cosh\left[m^H_{\text{eff}}(t)(t - \frac{L_t}{2})\right]}{\cosh\left[m^H_{\text{eff}}(t)(t+1 - \frac{L_t}{2})\right]}, \quad m^H_{\text{eff}}(t) \xrightarrow{1 \ll t \ll Lt} M^H \tag{2.18}$$

For the case of baryons the backwards propagating baryon corresponds to that of opposite parity, which is not degenerate with the forwards propagating. For instance, the nucleon two-point correlator on a lattice with periodic or antiperiodic boundary conditions in time is given by:

$$C_N(t) = |Z_N(\vec{0})| e^{-m_N t} - |Z_{N^-}(\vec{0})| e^{m_{N^-}(t - L_t)} \tag{2.19}$$

where N^- denotes the negative parity nucleon.

In Fig. 2.2 we show such plots of the pion and the ρ meson effective masses as a function of time.

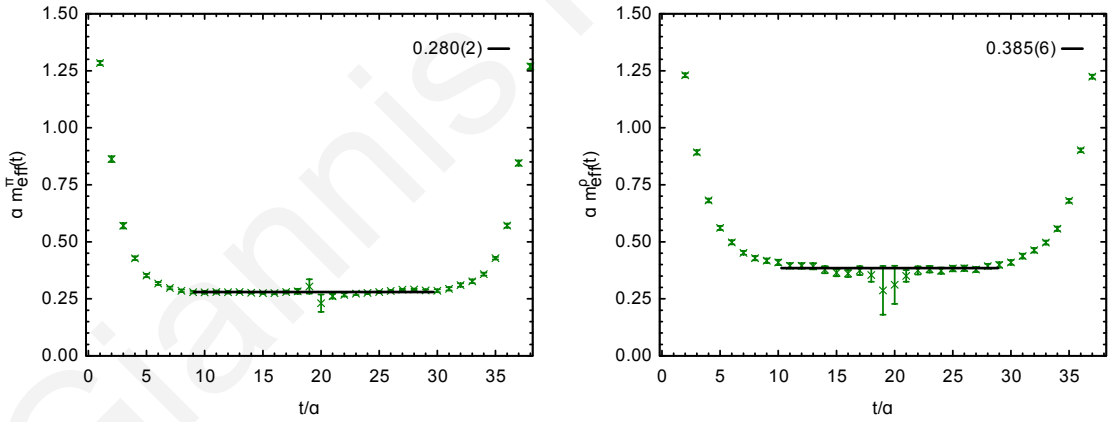

Figure 2.2: Effective mass plots of the pseudo-scalar meson (left) and the vector meson (right) as a function of the time separation from the source. The straight lines show fits to a constant.

For this simple example, the simulation was carried out over an ensemble of 60 dynamical Wilson $N_F = 2$ configurations with the Wilson hopping parameter set to $\kappa = 0.1575$ and $\beta = 5.6$, while the dimensions of the lattice are $24^3 \times 40$ [8]. We shall omit further details of the simulation carried out for these plots at the moment, since at this point we simply would like to demonstrate how the analysis is carried out. As can be seen, at small time separations from the source the correlation function is contaminated by contributions from excited states. At larger time separations we see that the effective mass converges

to a constant, evidence that the correlation function is dominated by the ground state and that excited state contributions can be neglected. We thus extract the ground state energy by fitting to a constant the plateau region of the effective mass plot. For this specific simulation we have $am_\pi = 0.280(2)$ and $am_\rho = 0.385(6)$. The lattice spacing for this specific lattice is $a \simeq 0.077$ fm, or equivalently $a^{-1} \simeq 2.56$ GeV. The spacing was set in Ref. [8] using the nucleon mass at the chiral limit. Hence the values of the masses in physical units are: $m_\pi = 0.716(5)$ GeV and $m_\rho = 0.986(15)$ GeV.

2.2 Signal Improvement Techniques

To obtain the correlation functions presented in the previous section, an inversion of the Dirac matrix was performed. As already mentioned, the inversion need not be carried out for all spatial color and Dirac indices of the matrix. Indeed, for the previous computation, we needed the propagator from all spinor and color indices of the source coordinates (the origin) to all spinor and color indices of all lattice sites. The inversion is carried out by solving the linear system:

$$\eta^c_\kappa(z) = \sum_x M^{ca}_{\kappa\mu}(z;x)\psi^a_\mu(x), \tag{2.20}$$

where $M = \not{D} - m$. Numerically this is achieved via conjugate-gradient methods. $\eta(z)$ is set to a delta function, i.e. $\eta^c_\kappa(z) = \delta(y-z)\delta_{\nu\kappa}\delta_{bc}$. Thus solving for $\psi(x)$ we obtain the inverse of the Dirac matrix from coordinate y, color index b and Dirac index ν to all lattice sites and all color and Dirac components:

$$\psi^a_\mu(x) = \sum_z G^{ac}_{\mu\kappa}(x;z)\eta^c_\kappa(z) = G^{ab}_{\mu\nu}(x;y) \tag{2.21}$$

For the previous computation twelve such inversions where carried out, one for each color and Dirac component of the source vector η at the origin, in order to carry out the trace in Eq. (2.10).

Using delta functions as the source vector for the inversion is the simplest choice one can make, however this is not the optimum choice. Indeed, this is equivalent to creating the meson localized at the origin and fixing the constituent quarks to a specific color and spin state. Although in the large time limit the initial state of the meson should be irrelevant, it is crucial to arrange so that the initial state has as much overlap with the ground state as possible since the correlator, as Eq. (2.12) dictates, is an exponentially decaying function over time, while statistical errors remain approximately constant. An exception is the pion correlator, where statistical errors drop with the rate of the correlator itself, thus the relative error remains constant. An argument explaining this behavior can be found in Ref. [9]. In general though, the later in time the excited states are damped the larger the relative statistical errors of the correlator will be.

A well known method for increasing the overlap of the ground state with that of the initial state, and consequently suppressing the initial state overlap with excited states, is

the so called *gauge invariant Gaussian smearing* of the sources, also known as Wuppertal smearing [10, 11]. The smeared source is obtained from the point source (or local source) via:

$$\eta^{sm}(\vec{x},t) = \sum_{\vec{y}} F(\vec{x},\vec{y};U(t))\,\eta(\vec{y},t), \tag{2.22}$$

where:

$$F(\vec{x},\vec{y};U(t)) = [1+\alpha H(\vec{x},\vec{y};U(t))]^n$$

and

$$H(\vec{x},\vec{y};U(t)) = \sum_{k=1}^{3}\left[U_k(\vec{x},t)\delta_{\vec{x},\vec{y}-a\hat{k}} + U_k^{\dagger}(\vec{x}-a\hat{k},t)\delta_{\vec{x},\vec{y}+a\hat{k}}\right]. \tag{2.23}$$

The hopping parameter α and smearing iterations n are tuned according to the problem at hand. In Fig. 2.3 we show a contour plot of the r.m.s radius defined by:

$$\langle r^2\rangle = \frac{\sum_{\vec{r}} r^2\eta^{\dagger}(\vec{r})\eta(\vec{r})}{\sum_{\vec{r}}\eta^{\dagger}(\vec{r})\eta(\vec{r})}, \tag{2.24}$$

as a function of the two parameters α and n. As can be seen, for a value of α greater than around 1.5, for a given number of smearing iterations, the radius of the Gaussian source is only slightly affected by α. Depending on the correlator needed, one can select the values of α and n for the r.m.s desired.

Since the initial state smearing is dependent on the gauge configuration U, further improvement can be achieved by *link smearing* i.e. smearing the links that enter the Gaussian smearing hopping matrix (H). In short, this involves replacing each gauge link of the configuration with a product of gauge links that follow a path with the same end points, in a gauge invariant manner. The resulting link, often referred to as a fat link, is thus an average of the original link plus equivalent gauge paths constructed by neighboring links. There are several link smearing schemes in the literature such as stout [12], APE smearing [13] and Hypercubic blocking (or HYP smearing) [14]. APE smearing is relatively simpler than HYP smearing. With APE smearing, one replaces the original thin link with the sum of 1×1 nearest neighboring *staples*, a staple being the product of three links: $S_{\mu\nu}(x) = U_\nu(x)U_\mu(x+\hat{\nu})U_\nu^{\dagger}(x+\hat{\mu})$. Thus APE smearing is defined as:

$$U_\mu^{APE}(x) = \mathrm{Proj}_{SU(3)}[U_\mu(x) + \frac{\omega}{6}\sum_{\nu\neq\mu} S_{\mu\nu}(x)] \tag{2.25}$$

where $\mathrm{Proj}_{SU(3)}$ means to project the resulting matrix to $SU(3)$ to preserve gauge invariance and ω is a tunable parameter. HYP smearing is somewhat more complicated since it involves three "APE" steps. Briefly, in the last step, the original thin link is replaced,

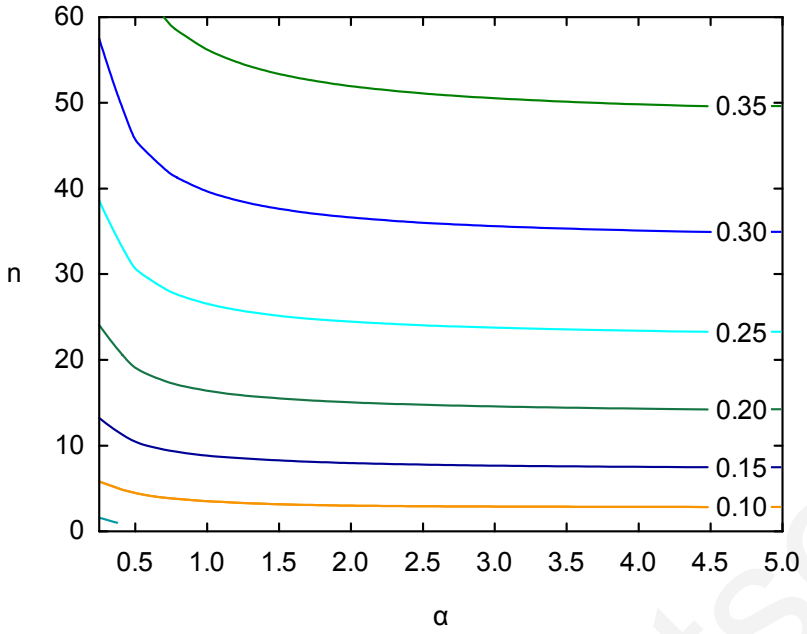

Figure 2.3: Contours of the r.m.s. radius of the smeared source vector plotted against the Wuppertal smearing parameters α and n. The contour labels are in fm.

as in APE smearing by itself plus staples:

$$U_\mu^{HYP}(x) = \tag{2.26}$$
$$\mathrm{Proj}_{SU(3)}[(1-\omega_1)U_\mu(x) + \frac{\omega_1}{6}\sum_{\pm\nu\neq\mu}\tilde{S}_{\nu;\mu}(x)\tilde{S}_{\mu;\nu}(x+\hat{\nu})\tilde{S}^\dagger_{\nu;\mu}(x+\hat{\mu})],$$

only now the links $\tilde{S}$ that make up the staples are fat links themselves, constructed via:

$$\tilde{S}(x)_{\mu;\nu} = \tag{2.27}$$
$$\mathrm{Proj}_{SU(3)}[(1-\omega_2)U_\mu(x) + \frac{\omega_2}{4}\sum_{\pm\rho\neq\nu,\mu}\bar{S}_{\rho;\nu\mu}(x)\bar{S}_{\mu;\rho\nu}(x+\hat{\rho})\bar{S}^\dagger_{\rho;\nu\mu}(x+\hat{\mu})].$$

Finally, in the first step, the fat links $\bar{S}$ are constructed entirely by thin links:

$$\bar{S}_{\mu;\nu,\rho}(x) = \tag{2.28}$$
$$\mathrm{Proj}_{SU(3)}[(1-\omega_3)U_\mu(x) + \frac{\omega_3}{2}\sum_{\pm\eta\neq\rho,\nu,\mu}U_\eta(x)U_\mu(x+\hat{\eta})U^\dagger_\eta(x+\hat{\mu})].$$

Note that the fat links are projected to $SU(3)$ in each step separately. The parameters ω_1, ω_2 and ω_3 are tuned in Ref. [14]. Namely, the authors minimize the largest plaquette fluctuations on a test ensemble of Wilson quenched configurations. The parameters obtained are $\omega_1 = 0.75$, $\omega_2 = 0.6$ and $\omega_3 = 0.3$.

In Fig. 2.4 we test the effects of Wuppertal smearing and gauge link smearing us-

ing the effective mass of the nucleon. This test was carried out on a small ($16^3 \times 32$) quenched lattice using Dirichlet boundary conditions in time. This choice of boundary conditions means the correlator shows no periodicity thus the effective mass is computed via: $M_{\rm eff}(t) = \log[R(t)]$. Comparison of the local-local (no Wuppertal smearing on either side) correlator with the local-smeared (Wuppertal smearing on either source or sink) correlator shows that Wuppertal smearing damps excited states considerably, with a plateau showing as early as 6 time slices from the source. If additionally we use APE or HYP smearing for the links that enter the Gaussian smearing hopping matrix, we see an additional reduction in excited state contamination. The Wuppertal smearing parameters (α and n) are taken as in Ref. [15]. Namely these are $\alpha = 4.0$ and $n = 50$ which correspond to an r.m.s of around 0.35 fm as we can see from Fig. 2.3. As for the link smearing, we see the two methods have the same effect on the effective mass. We choose to use HYP smearing in all computations carried out hereon.

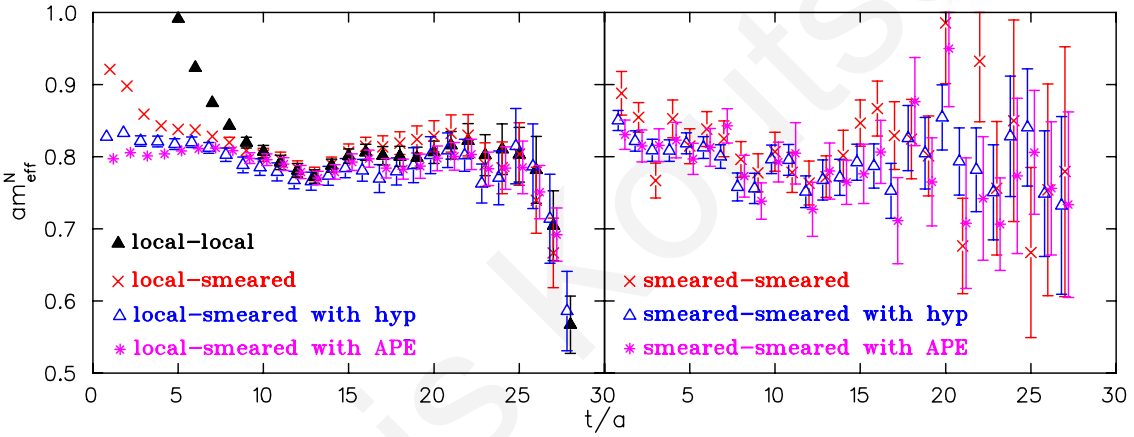

Figure 2.4: Nucleon effective mass versus time using local-local (filled triangles) correlators, Wuppertal smearing with no link smearing (crosses), Wuppertal smearing with HYP gauge link smearing (open triangles) and Wuppertal smearing with APE smearing on the links (asterisks). The left graph shows the result of smearing on one side only, while the right graph shows results from smearing on both ends.

In Figs. 2.5 and 2.6 we show effective mass plots for the pseudo-scalar and vector meson respectively using no Gaussian smearing (local-local), smearing on the source only (local-smeared) and smearing on both source and sink states (smeared-smeared) for the same Wilson N_F=2 ensemble used to produce Fig. 2.2, using antiperiodic conditions in time. The Wuppertal smearing parameters are the same as those mentioned previously. HYP smearing is used for the links that enter the Wuppertal smearing hopping matrix. As for the case of the nucleon effective mass, this test shows that gauge invariant Gaussian smearing of the initial and final states indeed increases their overlap with the ground state considerably. Apart from the fact that a more accurate plateau can be identified in the effective mass due to the early damping of excited states, this has further implications in the case where currents are inserted between source and sink (three-point and four-point

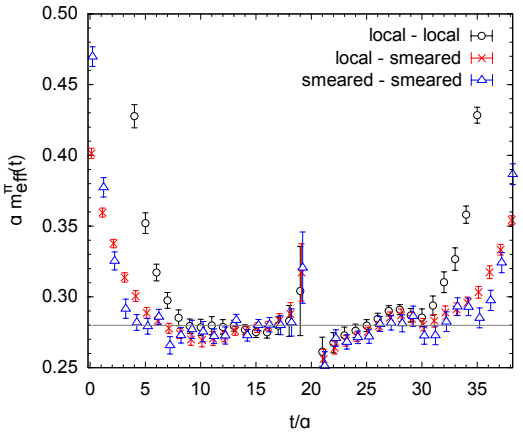

Figure 2.5: Pseudo-scalar meson effective mass versus time using local-local (open circles), local-smeared (crosses) and smeared-smeared (open triangles) correlators.

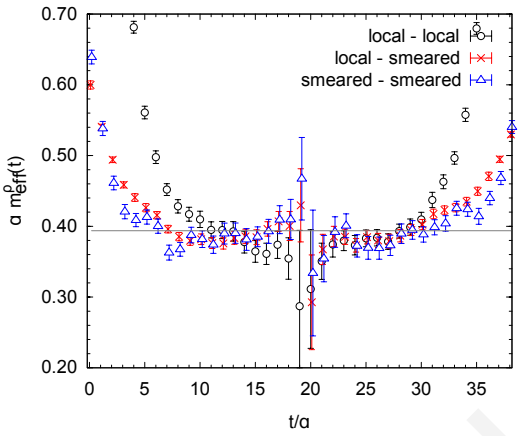

Figure 2.6: Vector meson effective mass versus time. The notation is the as Fig. 2.5.

functions). We shall discuss three-point functions in this chapter. Four-point functions shall be introduced in Chapter 7.

2.3 Dispersion Relation

So far, we have shown how to extract the mass of a hadron from the two-point correlator. It is straight forward to generalize the methods and compute the two-point correlator at finite momentum, thus obtaining the energy of the hadron at arbitrary momenta. Namely, this is achieved if one sums over the sink coordinate using a phase i.e. by Fourier transforming the two-point correlator:

$$C(\vec{p},t) = \sum_{\vec{x}} e^{-i\vec{p}\cdot\vec{x}} C(\vec{x},t) = |\langle\Omega|\chi_{\mathcal{H}}(0)|\mathcal{H}(\vec{p})\rangle| e^{-E(\vec{p})t}, \tag{2.29}$$

where $\mathcal{H}$ denotes any hadronic state and $\chi_{\mathcal{H}}$ denotes the interpolating operator for this state. In Fig. 2.7 we show the energy of the pion as a function of the momentum squared. For this plot we have averaged over all lattice momentum vectors that contribute to the same $\vec{p}^2$ i.e. for $\vec{p} = \frac{2\pi}{L}(n_x, n_y, n_z)$ where L is the spatial extent of the lattice, we average over all vectors $\vec{n}$ with the same $\vec{p}^2$. The dashed line shows the continuum dispersion relation $E(\vec{p}^2) = \sqrt{m^2 + p^2}$. As we can see, at the relatively low momenta this plot shows, the energy of the pion calculated on the lattice is well described by the continuum dispersion relation.

2.4 Stochastic Techniques

In this section we shall elaborate on techniques used to obtain an estimate for the all-to-all propagator using stochastic techniques. As mentioned in the previous sections, one need not compute the inverse of the Dirac matrix from all lattice sites to all lattice

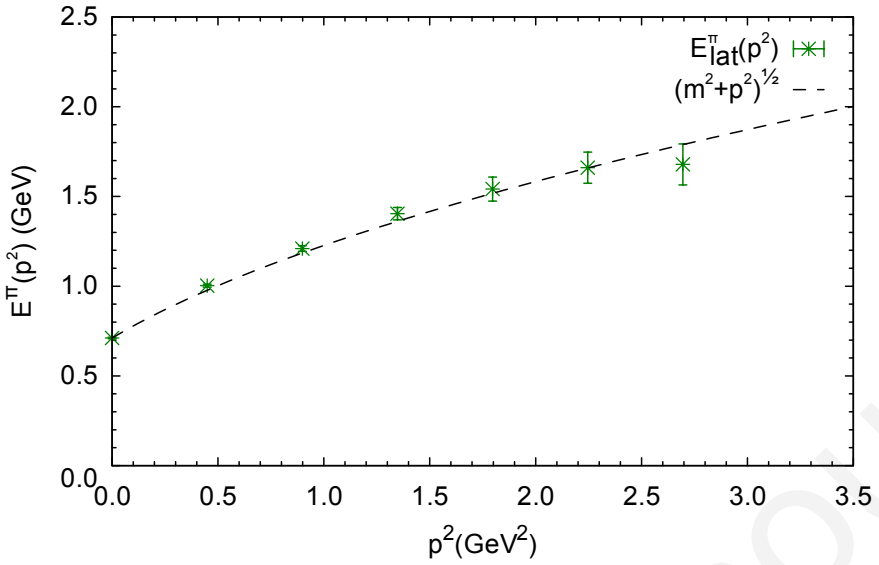

Figure 2.7: Pion energy as a function of the momentum squared. The dashed line shows the continuum dispersion relation.

sites (the all-to-all propagator) in order to compute, for instance, two-point correlation functions. In fact, calculating the all-to-all propagator explicitly is far too computationally demanding to be practical in the first place, since one would need to invert, i.e. solve the linear equation in Eq. (2.21), twelve times for all lattice sites. Even for a relatively small lattice, say $16^3 \times 32$, one would need of the order of a million inversions for every gauge configuration in the ensemble (compared to twelve inversions used to obtain the effective mass of the particles in the previous sections).

It is thus apparent that it is impractical to compute the all-to-all propagator explicitly. However, having the all-to-all propagator would allow averaging over volume correlation functions thus utilizing entirely all the information contained in a single gauge configuration. For instance, for the pion:

$$\sum_{\vec{x}\vec{x}_0} \langle \mathrm{Tr}\left[|G(\vec{x},t;\vec{x}_0,t_0)|^2\right]\rangle \xrightarrow{t\gg 1} V_3 |\langle\Omega|\chi_\pi(\vec{0},0)|\pi(\vec{0})\rangle|^2 e^{-m_\pi t}, \tag{2.30}$$

where V_3 is the spatial volume of the lattice.

A well known method of estimating all-to-all propagators is by using stochastic techniques [16]. In this approach, a set of orthogonal, random sources are used to invert the Dirac matrix. The resulting solution vectors are then combined with the random sources to gain an estimate of the all-to-all propagator. Formally, one defines an ensemble of *noise*

sources such that:

$$\frac{1}{N_r}\sum_{r=1}^{N_r}\xi_\mu^a(x)_r = \langle\xi_\mu^a(x)\rangle_r = 0$$

$$\text{and} \tag{2.31}$$

$$\frac{1}{N_r}\sum_{r=1}^{N_r}\xi_\mu^a(x)_r\xi_{\mu'}^{*a'}(x')_r = \langle\xi_\mu^a(x)\xi_{\mu'}^{*a'}(x')\rangle_r = \delta(x-x')\delta_{\mu\mu'}\delta_{aa'}$$

where $\langle\rangle_r$ denotes an average over the stochastic ensemble and N_r is the size of the ensemble. Inverting using these ξ's as sources one obtains a set of *solution* vectors:

$$\phi_\mu^a(x)_r = \sum_y G_{\mu\nu}^{ab}(x,y)\xi_\nu^b(y)_r, \tag{2.32}$$

which can the be combined to gain an estimate for the all-to-all propagator:

$$\begin{aligned}\langle\phi_\mu^a(x)\xi_\nu^{*b}(y)\rangle_r &= \sum_{y'} G_{\mu\nu'}^{ab'}(x;y')\langle\xi_{\nu'}^{b'}(y')\xi_\nu^{*b}(y)\rangle_r \\ &= \sum_{y'} G_{\mu\nu'}^{ab'}(x;y')\delta(y-y')\delta_{\nu\nu'}\delta_{bb'} \\ &= G_{\mu\nu}^{ab}(x;y).\end{aligned} \tag{2.33}$$

The above equations are exact i.e. for a set of sources obeying Eq. (2.31) one obtains the exact all-to-all propagator through Eq. (2.33). In practice however, the noise vector completeness relations are approximated, since obeying them exactly would be equivalent to computing the all-to-all propagator explicitly i.e. an inversion from every lattice site.

A common choice for the noise vectors is Z(2) noise where every component of the noise vectors ξ is set, with equal probability, to one of the four fourth-roots of 1: $\xi_\mu^a(x) = \{1, i, -1, -i\}$. This choice guarantees:

$$\langle\xi_\mu^a(x)\xi_\mu^{*a}(x)\rangle_r = 1 \quad \text{(no sum on repeated indices)}. \tag{2.34}$$

However, the off diagonal elements of the average cross product are only approximately zero since this relies on the cancellation between equally probable 1,-1 pairs and i, $-i$ pairs. Hence the delta functions in Eq. (2.31) are only approximately satisfied introducing *stochastic noise* in the estimation of the all-to-all propagator. Whether one gains from this method or not relies on whether for a reasonable size of the stochastic ensemble (N_r), the increase in statistics from the double sum on both source and sink coordinates outweighs the stochastic noise introduced in the propagator estimation, thus leading to a more accurate two-point function than using point-to-all propagators.

2.4.1 Dilution

A well known technique used to suppress stochastic noise is dilution [17]. With dilution one distributes the elements of a noise source over certain color, spin and volume components of multiple new noise sources setting the remaining components to zero. For instance, spin dilution would be achieved via:

$$\xi^a_\mu(x)_{(r,\sigma)} = \xi^a_\mu(x)_r \delta_{\mu\sigma}, \tag{2.35}$$

where $\xi^a_\mu(x)_r$ is a noise vector in the original undiluted set and $\xi^a_\mu(x)_{(r,\sigma)}$ is a noise vector in the diluted ensemble. Spin dilution is four-fold dilution i.e. the total number of noise vectors N_r (and thus inversions) quadruples.

Dilution suppresses stochastic noise since most of the elements of each noise vectors are set exactly to zero. Thus the off diagonal elements in the orthogonality relation in Eq. (2.31) are more consistent with zero the more one dilutes. In Ref. [17] the authors demonstrate that one sees a reduction of stochastic noise even when keeping the number of inversions, and hence computational cost, constant, i.e. diluting a noise vector to n new vectors reduces stochastic noise compared to inverting for n undiluted noise vectors.

2.4.2 One-end trick

Having described stochastic methods for the estimation of all-to-all propagators, one can use them to calculate two-point correlators, summed on both source and sink coordinates. We rewrite the general meson two-point function at the quark propagator level (Eq. (2.10)) summing on both sides:

$$\sum_{\vec{x}_0,\vec{x}} \mathrm{Tr}[\Gamma' G(x;x_0)\bar{\Gamma}' G^\dagger(x;x_0)] = \tag{2.36}$$
$$\sum_{\vec{x}_0,\vec{x}} \mathrm{Tr}[\Gamma' \sum_r \frac{1}{N_r}\phi(x)_r \otimes \xi^\dagger(x_0)_r \bar{\Gamma}' \sum_{r'} \frac{1}{N_r}[\phi(x)_{r'} \otimes \xi^\dagger(x_0)_{r'}]^\dagger],$$

where $\otimes$ denotes an outer product. A double volume sum is needed over source and sink coordinate as well as a double sum over the stochastic ensemble. The double volume sum can be quite computationally demanding in practice, especially for large lattices, say $32^3 \times 64$.

The so called Liverpool one-end trick [18] relies on the realization that one can combine appropriately solution vectors to yield two-point meson correlators, summed over source and sink coordinates, without the need to carry out the sum on one end explicitly. We shall demonstrate this for the pion, to start with, which is the simplest case. We consider the combination:

$$\frac{1}{N_r}\sum_{r,\vec{x}} \phi^\dagger(\vec{x},t;t_0)_r \phi(\vec{x},t;t_0)_r \tag{2.37}$$

where we have added an argument to the solution vectors to denote that the noise vectors

used in the inversion are localized on a specific time-slice, i.e. $\xi^a_\mu(x)_r = \xi^a_\mu(\vec{x})_r\delta(t-t_0)$ and thus the solution vectors ϕ are now written as:

$$\phi^a_\mu(\vec{x},t;t_0)_r = \sum_{\vec{x}_0} G^{ab}_{\mu\nu}(\vec{x},t;\vec{x}_0,t_0)\xi^b_\nu(\vec{x}_0)_r. \tag{2.38}$$

This combination gives:

$$\begin{aligned}
&\frac{1}{N_r}\sum_{\vec{x},r}\phi^\dagger(\vec{x},t;t_0)_r\phi(\vec{x},t;t_0)_r = \\
&\sum_{\vec{x},\vec{x}'_0,\vec{x}''_0} G^{*ab}_{\mu\nu}(x;x'_0)G^{ac}_{\mu\kappa}(x;x''_0)\frac{1}{N_r}\sum_r \xi^{*b}_\nu(x'_0)_r\xi^c_\kappa(x''_0)_r = \\
&\sum_{\vec{x},\vec{x}'_0,\vec{x}''_0} G^{*ab}_{\mu\nu}(x;x'_0)G^{ac}_{\mu\kappa}(x;x''_0)\delta_{bc}\delta_{\nu\kappa}\delta(\vec{x}'_0-\vec{x}''_0) = \\
&\sum_{\vec{x},\vec{x}'_0}\mathrm{Tr}\left[|G(x;x_0)|^2\right]
\end{aligned} \tag{2.39}$$

where $x'_0 = (t_0,\vec{x}'_0)$ and $x''_0 = (t_0,\vec{x}''_0)$. Thus this combination gives the pion two-point function, with the sum over the source coordinate ($\vec{x}_0$) automatically carried out. Although this is straight forward for the case of the pion, it may not be apparent how it generalizes to other mesons. For a general meson we must use a specific sort of spin dilution: $\xi^a_\mu(x)_{(r,\sigma)} = \xi^a(x)_r\delta_{\mu\sigma}$ where r counts sets of four stochastic vectors and σ labels the vectors in the set, hence the total number of vectors quadruples. Note that this sort of dilution is different than that described earlier on. In this case, the random entries are the same within the diluted set only shifted by the spinor index. With this condition for the noise sources, one can generalize the one-end trick to arbitrary mesons with interpolating operators of the form $\chi_\Gamma = \bar{d}\Gamma u$:

$$\begin{aligned}
&\frac{1}{N_r}\sum_{\vec{x},r}\phi^a_\mu(\vec{x},t;t_0)_{(r,\nu)}\Gamma'_{\nu\sigma}\phi^{*a}_\kappa(\vec{x},t;t_0)_{(r,\sigma)}\bar{\Gamma}'_{\kappa\mu} = \\
&\sum_{\vec{x},\vec{x}'_0,\vec{x}''_0} G^{ab}_{\mu\nu}(x;x'_0)\Gamma'_{\nu\sigma}G^{*ab'}_{\kappa\sigma}(x;x''_0)\bar{\Gamma}'_{\kappa\mu}\delta(\vec{x}'_0-\vec{x}''_0)\delta_{bb'} = \\
&\sum_{\vec{x},\vec{x}'_0}\mathrm{Tr}\left[G(x;x_0)\Gamma G^\dagger(x_0;x)\bar{\Gamma}\right],
\end{aligned} \tag{2.40}$$

where $\Gamma' = \Gamma\gamma_5$ and $\bar{\Gamma} = \gamma_0\Gamma^\dagger\gamma_0$.

In Fig. 2.8 we compare the effective mass plots derived on one hand using the one-end trick and on the other using the usual method with point-to-all propagators, for the pseudoscalar meson. No smearing is done on neither source nor sink for this calculation. The stochastic inversions were carried out using one spin diluted noise vector per configuration hence 4 inversions in total. The obvious conclusion is that the correlators computed using the one-end trick carry smaller errors. On average, the relative error is reduced by approximately 2.7, equivalent to around $\sim$7 increase in statistics. This comes at a lower

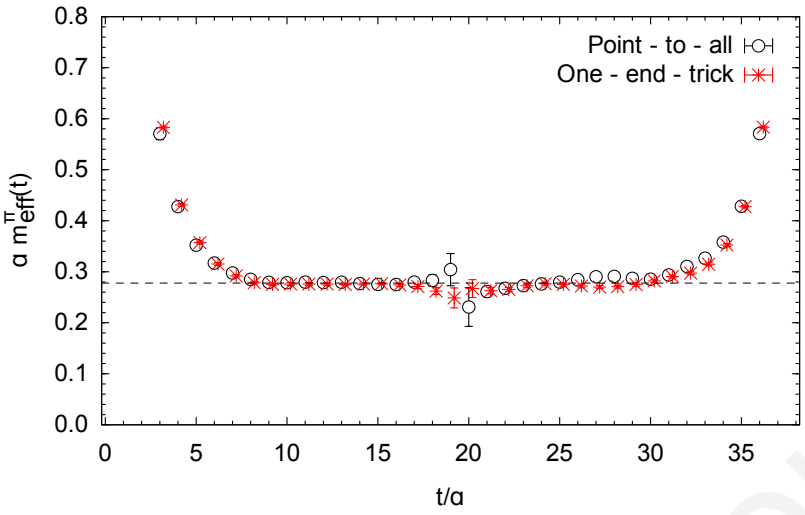

Figure 2.8: Comparison between the effective mass derived using the one-end trick (asterisks) and using the standard method with point-to-all propagators (open circles) for the case of the pion when no smearing is applied.

computational cost since point-to-all propagators need twelve inversions per configuration, three more than the stochastic inversions. This shows that indeed the sum over volume outweighs the stochastic noise introduced in the propagator, leading to a more accurate determination of the two-point correlator over the same ensemble.

It should be noted here that this way of computing two-point functions fixes the momentum of the hadron via the automatic summation of the source coordinate $\vec{x}_0$. To obtain the two-point function at arbitrary momenta, one would need to explicitly carry out the double sum thus Fourier transforming over source and sink coordinates. Alternatively, one can select the momentum prior to the inversion, multiplying the stochastic source with an appropriate momentum phase. Then the one-end trick could be carried out to obtain the two-point correlator at finite momentum, though a new inversion would be needed for every momentum vector.

2.5 Three-Point Functions

As already mentioned, hadronic observables on the lattice are computed via measuring the vacuum expectation value of appropriately defined correlation functions. We have so far presented the simple case of the two-point correlation function from which, as we have seen, we can directly extract the mass of hadrons. More complex correlation functions, on the other hand, give insight to more detailed information on hadron structure such as hadron charge radii, hadron decay amplitudes, coupling constants, form factors etc.

Using three-point correlation functions, one can study hadron form factors, from which information on the shape of hadrons can be extracted as well as hadron couplings and Generalized Parton Distributions. The general form of such a three-point function is

given by:

$$G^{\mathcal{H}'\mathcal{J}^\mu\mathcal{H}}(x;x_1) = \langle\Omega|\chi_{\mathcal{H}'}(x)\mathcal{J}^\mu(x_1)\bar{\chi}_{\mathcal{H}}|\Omega\rangle, \tag{2.41}$$

where $\chi_{\mathcal{H}}$ and $\chi_{\mathcal{H}'}$ are interpolating operators of hadrons $\mathcal{H}$ and $\mathcal{H}'$ respectively while $\mathcal{J}$ is some insertion operator, typically a current insertion which may carry a Dirac index μ, such as an electromagnetic current, a pseudo-scalar current, an axial vector current and so on. In Fig. 2.9 we show a generic diagram of the three-point function for the case of baryons. Note that if the initial and final states are the same ($\mathcal{H}' = \mathcal{H}$) then in principle, the three-point correlator additionally takes a contribution from a disconnected diagram (right diagram).

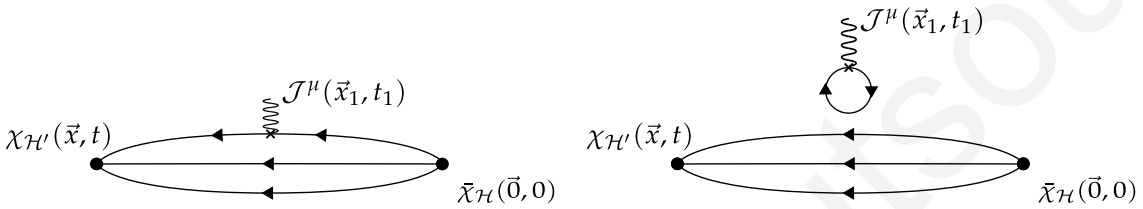

Figure 2.9: The diagram of an arbitrary baryon three-point function.

It is more convenient to carry out this evaluation in momentum space. Since we have already fixed the initial state to the origin, we shall Fourier transform over $\vec{x}_1$ and $\vec{x}$ and thus the momentum of the initial state shall be fixed accordingly due to momentum conservation. Inserting two sets of complete eigenstates, the three-point correlation function thus gives:

$$\begin{aligned}
&\sum_{\vec{x},\vec{x}_1} e^{-i\vec{x}\cdot\vec{p}'} G^{\mathcal{H}'\mathcal{J}^\mu\mathcal{H}}(\vec{x},t;\vec{x}_1,t_1) e^{-i\vec{x}_1\cdot\vec{p}_1} = \\
&\sum_{\vec{x},\vec{x}_1} e^{-i\vec{x}\cdot\vec{p}'} \langle\Omega|\chi_{\mathcal{H}'} e^{-\hat{H}t} e^{i\vec{x}\cdot\hat{\vec{p}}'} e^{-i\vec{x}_1\cdot\hat{\vec{p}}'} e^{\hat{H}t_1} \mathcal{J}^\mu e^{-\hat{H}t_1} e^{i\vec{x}_1\cdot\hat{\vec{p}}'} \bar{\chi}_{\mathcal{H}}|\Omega\rangle e^{-i\vec{x}_1\cdot\vec{p}_1} = \\
&\sum_{\substack{\vec{x},\vec{x}_1 \\ \vec{k},\vec{k}',n,n'}} \langle\Omega|\chi_{\mathcal{H}'}|n',\vec{k}'\rangle\langle\vec{k},n|\bar{\chi}_{\mathcal{H}}|\Omega\rangle \times \\
&\qquad e^{-E_{n'}(\vec{k}')(t-t_1)} e^{-i\vec{x}\cdot(\vec{p}'-\vec{k}')} \langle n',\vec{k}'|\mathcal{J}^\mu|n,\vec{k}\rangle e^{-E_n(\vec{k})t_1} e^{-i\vec{x}_1\cdot(\vec{k}'-\vec{k}+\vec{p}_1)}.
\end{aligned} \tag{2.42}$$

The volume sums fix the momentum of the final state ($\mathcal{H}'$) to $\vec{p}'$ and of the initial state ($\mathcal{H}$) to $\vec{p} \equiv \vec{p}' - \vec{p}_1$. Furthermore, in the large time limit $t - t_1 \gg 1$ and $t_1 \gg 1$, the ground state contribution will dominate over excited states in the sums over n and n'. Thus:

$$\begin{aligned}
&G^{\mathcal{H}'\mathcal{J}^\mu\mathcal{H}}(\vec{p},\vec{p}';t,t_1) \equiv \sum_{\vec{x},\vec{x}_1} e^{-i\vec{x}\cdot\vec{p}'} G^{\mathcal{H}'\mathcal{J}^\mu\mathcal{H}}(\vec{x},t;\vec{x}_1,t_1) e^{-i\vec{x}_1\cdot(\vec{p}'-\vec{p})} = \\
&\langle\Omega|\chi_{\mathcal{H}'}|\mathcal{H}'(\vec{p}')\rangle\langle\mathcal{H}(\vec{p})|\bar{\chi}_{\mathcal{H}}|\Omega\rangle\langle\mathcal{H}'(\vec{p}')|\mathcal{J}^\mu|\mathcal{H}(\vec{p})\rangle e^{-E_{\mathcal{H}'}(\vec{p}')(t-t_1)} e^{-E_{\mathcal{H}}(\vec{p})t_1}.
\end{aligned} \tag{2.43}$$

and by defining $Z_{\mathcal{H}}(\vec{q}) \equiv \sqrt{\frac{M_{\mathcal{H}}}{E_{\mathcal{H}}(\vec{q})}}\langle\Omega|\chi_{\mathcal{H}}|\mathcal{H}(\vec{q})\rangle$:

$$G^{\mathcal{H}'\mathcal{J}^\mu\mathcal{H}}(\vec{p},\vec{p}';t,t_1) = Z_{\mathcal{H}'}(\vec{p}')Z^*_{\mathcal{H}}(\vec{p})\sqrt{\frac{M_{\mathcal{H}}M'_{\mathcal{H}}}{E_{\mathcal{H}}(\vec{p})E_{\mathcal{H}'}(\vec{p'})}}\langle\mathcal{H}'(\vec{p}')|\mathcal{J}^\mu|\mathcal{H}(\vec{p})\rangle \times e^{-E_{\mathcal{H}'}(\vec{p}')(t-t_1)}e^{-E_{\mathcal{H}}(\vec{p})t_1}. \tag{2.44}$$

The expectation value $\langle\mathcal{H}'(\vec{p}')|\mathcal{J}^\mu|\mathcal{H}(\vec{p})\rangle$ is what we want to extract from the three-point function. For $\mathcal{H} = \mathcal{H}'$, at zero momentum, this gives the coupling of the hadron with the current $\mathcal{J}^\mu$. At finite momentum, one derives hadron form factors associated with this current, which in turn provide a comparison with experiment. For off diagonal elements $\mathcal{H} \neq \mathcal{H}'$, this is the *transition amplitude* which can be parametrized in terms of transition form factors.

A standard way of isolating the expectation value from the three-point correlator, is to divide with an appropriate combination of two-point correlators. This combination should cancel the unknown overlaps $Z_{\mathcal{H}}$ and $Z_{\mathcal{H}'}$ as well as the exponential terms $e^{-E(\vec{p}')(t-t_1)}$ and $e^{-E(\vec{p})t_1}$. There are many ways to construct such ratios, however since the two-point function is an exponentially decaying function, the time extent of the two-point correlators should be kept as short as possible. One such optimal ratio is given via:

$$R(\vec{p},\vec{p}';t,t_1;\mu) = \frac{G^{\mathcal{H}'\mathcal{J}^\mu\mathcal{H}}(\vec{p},\vec{p}';t,t_1)}{G^{\mathcal{H}'\mathcal{H}'}(t,\vec{p}')} \times \sqrt{\frac{G^{\mathcal{H}\mathcal{H}}(t-t_1,\vec{p})G^{\mathcal{H}'\mathcal{H}'}(t_1,\vec{p}')G^{\mathcal{H}'\mathcal{H}'}(t,\vec{p}')}{G^{\mathcal{H}'\mathcal{H}'}(t-t_1,\vec{p}')G^{\mathcal{H}\mathcal{H}}(t_1,\vec{p})G^{\mathcal{H}\mathcal{H}}(t,\vec{p})}}. \tag{2.45}$$

This ratio is optimal since the largest time extent the two-point functions it involves go up to is t; the time separation between source and sink. This is important since we do not want the ratio to introduce more statistical noise than the three-point function already carries. Similarly to two-point functions, this ratio is then plotted against time (t_1 or t according to the problem) in search for a plateau which is then fitted to a constant. In Fig. 2.10 we show an example of such an analysis. We show this for the dominant form factor of the Nucleon to Δ electromagnetic transition [19]. The calculation is performed in the reference frame where the final state is at rest i.e. $\vec{p}' = 0$, $\vec{p} = -\vec{p}_1 = -\vec{q}$. The plot shows the first four non-zero momenta $\vec{q} = \frac{2\pi}{L}(n_x, n_y, n_z)$, $n^2 = 1, 2, 3$ and 4. The computation was carried out on two ensembles of Asqtad improved staggered configurations by MILC [20] using Domain Wall Fermions [6,21,22] in the valence sector. The lattice spacing is approximately $a \simeq 0.124$ fm$= 0.65$ GeV^{-1}. In this calculation, the sink time slice is held fixed at $t/a = 8$ while the insertion time slice t_1 is varied in search for a plateau. We shall elaborate on the specifics of this calculation further on. At this point we show this plot to demonstrate that a plateau is reached in the ratio with the insertion time slice as close as two time slices from the source or sink. This is possible because we have used Wuppertal smearing on both initial and final states to effectively damp excited state contributions. This evaluation

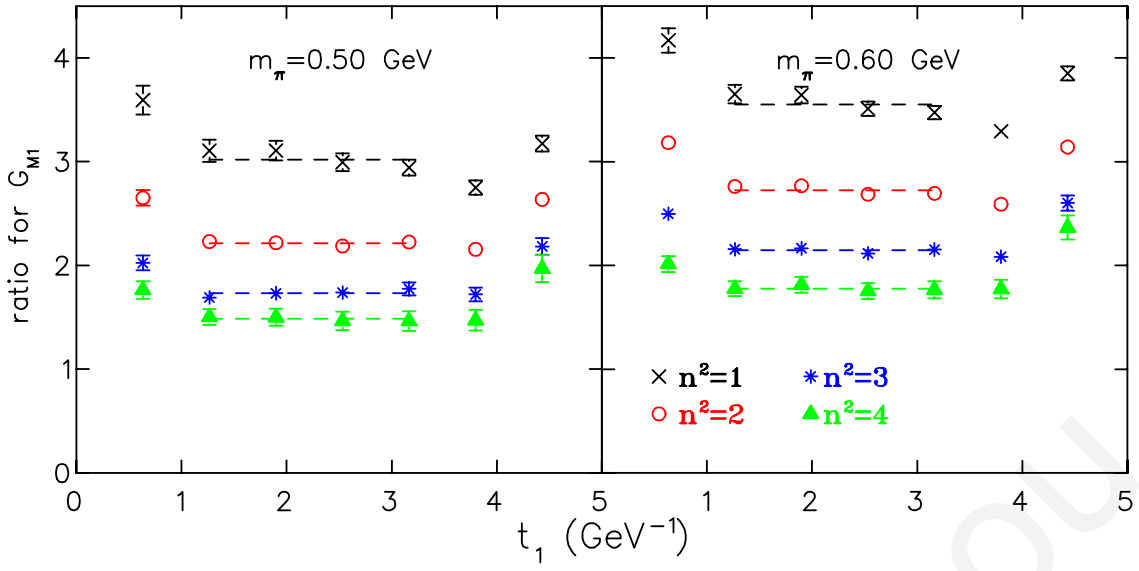

Figure 2.10: Ratios, versus the insertion time, for the $\mathcal{G}_{M1}$ nucleon to Δ electromagnetic form factor at two pion masses.

would not be possible to such a high accuracy without these excited state suppression methods, since the large time extents involved would introduce a significant increase in statistical errors.

So far we have not commented on the propagation of the statistical error of the quantities studied. In all quantities shown the error propagation was achieved through jackknife analysis. Thus possible correlations between the statistical measurements have been taken into account in the error of the ratios. Unless specifically stated, it is implied that all errors presented here on are jackknife errors.

2.5.1 Sequential Inversion

So far, we have shown the general idea of how one extracts from the lattice transition amplitudes given the three-point correlation function. We now proceed to give the details of the calculation. At the quark propagator level, the Fourier transform over the two spatial coordinates $\vec{x}$ and $\vec{x}_1$ requires the knowledge of the all-to-all propagator, just as in the case where one wants the two-point function summed over both ends. To see this, we shall return to the simple case of an arbitrary meson with an interpolating operator of the form: $\chi_\Gamma = \bar{d}\Gamma u$. For simplicity we shall assume a local current of the form $\mathcal{J}^\mu = Q_d \bar{d}\gamma^\mu d$

as the insertion operator. Performing the contractions for this simple case we have:

$$\begin{aligned}
&\langle\Omega|\chi_\Gamma(x)\mathcal{J}^\mu(x_1)\bar{\chi}_\Gamma(0)|\Omega\rangle \\
&\qquad = Q_d\langle\Omega|\bar{d}(x)\Gamma u(x)\bar{d}(x_1)\gamma^\mu d(x_1)\bar{u}(0)\bar{\Gamma}d(0)|\Omega\rangle \\
&= -Q_d\mathrm{Tr}[\Gamma G(x;0)\bar{\Gamma}G(0;x_1)\gamma^\mu G(x_1;x)] \\
&\qquad + Q_d\mathrm{Tr}[G(x_1;x_1)\gamma^\mu]\mathrm{Tr}[\Gamma G(x;0)\bar{\Gamma}G(0;x)],
\end{aligned} \tag{2.46}$$

where Q_d is the charge of the down quark. The second term corresponds to a disconnected diagram, similar to the right diagram of Fig. 2.9. The Fourier transform over the coordinates $\vec{x}$ and $\vec{x}_1$ requires the knowledge of the all-to-all propagator $G(x_1;x)$ for the case of the connected contribution, first term given in Eq. (2.46), and $G(x_1;x_1)$ for the disconnected contribution (second term). Up to recently, the evaluation of the all-to-all propagator via stochastic techniques was too computationally intensive for these kind of calculations. Hence, in most cases, the disconnected contribution is neglected. For the case of the connected diagram the sequential inversion technique is employed to automatically sum over the relevant coordinate in the three-point function.

With the sequential inversion technique, one defines an appropriate source vector so that one of the sums over $\vec{x}$ or $\vec{x}_1$, for the case of the connected diagram, is carried out through an inversion of the Dirac matrix. One chooses which of the two sums to carry out through the sequential inversion depending on the problem at hand. If the method is applied to carry out the sum over $\vec{x}$, then this is called the *fixed sink* sequential method since this fixes the momentum of the final state. Alternatively, one can compute the three-point function via the *fixed current* method, which means the sequential inversion performs the sum over the insertion coordinate $\vec{x}_1$. With this method, the insertion momentum is fixed as well as the insertion operator.

To return to our example of an arbitrary meson, the three-point correlation function in terms of quark propagators is given by:

$$\begin{aligned}
&G^{\chi_\Gamma\gamma^\mu\chi_\Gamma}(\vec{p},\vec{p}';t,t_1) = \\
&\qquad -\sum_{\vec{x},\vec{x}_1} Q_d e^{-i\vec{p}'\cdot\vec{x}}\mathrm{Tr}[\Gamma G(x;0)\bar{\Gamma}G(0;x_1)\gamma^\mu G(x_1;x)]e^{-i\vec{x}_1\cdot(\vec{p}'-\vec{p})}.
\end{aligned} \tag{2.47}$$

The first step to evaluating $G^{\chi_\Gamma\gamma^\mu\chi_\Gamma}$ is to obtain the point-to-all propagator from the source to all lattice sites, $G(x;0)$. For the fixed current approach the appropriate *sequential source* is given by:

$$K^{ab}_{\rho\sigma}(\vec{x},t_x;\vec{q};\mu) = (\gamma_5\gamma^\mu\gamma_5)_{\rho\rho'}G^{ab}_{\rho'\sigma'}(\vec{x},t_x;\vec{0},0)(\gamma_5)_{\sigma'\sigma}\delta(t_x-t_1)e^{i\vec{x}\cdot\vec{q}}, \tag{2.48}$$

which through inversion gives the sequential propagator:

$$S(\vec{y},t_y;t_1;\vec{q};\mu)=\sum_{\vec{x}}G(\vec{y},t_y;\vec{x},t_1)\gamma_5\gamma^\mu\gamma_5 G(\vec{x},t_1;\vec{0},0)\gamma_5 e^{i\vec{x}\cdot\vec{q}}\Rightarrow \tag{2.49}$$
$$S^\dagger(\vec{y},t_y;t_1;\vec{q};\mu)\gamma_5=\sum_{\vec{x}}G(\vec{0},0;\vec{x},t_1)\gamma^\mu G(\vec{x},t_1;\vec{y},t_y)e^{-i\vec{x}\cdot\vec{q}}.$$

The three-point function can now be constructed in terms of this sequential propagator:

$$G^{\chi_\Gamma\gamma^\mu\chi_\Gamma}(\vec{p},\vec{p}';t,t_1)= \tag{2.50}$$
$$-\sum_{\vec{x}}Q_d e^{-i\vec{p}'\cdot\vec{x}}\mathrm{Tr}[\Gamma G(x;0)\bar{\Gamma}S^\dagger(x;t_1;\vec{p}'-\vec{p};\mu)\gamma_5].$$

Notice that the momentum of the current $\vec{p}'-\vec{p}$, the operator inserted γ^μ as well as the insertion time t_1 are set when constructing the sequential source. Thus a new inversion is needed for each of these parameters one would like to vary. On the other hand, one can change arbitrarily the state at the sink (Γ) and can obtain the correlator for any sink momentum ($\vec{p}'$) and for any sink time t.

Alternatively, for the fixed sink approach, the sequential source is constructed via:

$$K^{ab}_{\rho\sigma}(\vec{x},t_x;\vec{q};\Gamma)=\Gamma_{\rho\sigma'}G^{ab}_{\sigma'\sigma}(\vec{x},t_x;\vec{0},0)\delta(t_x-t)e^{-i\vec{x}\cdot\vec{q}}, \tag{2.51}$$

which when inverted gives the sequential propagator:

$$S(\vec{y},t_y;t;\vec{q};\Gamma)=\sum_{\vec{x}}G(\vec{y},t_y;\vec{x},t)\Gamma G(\vec{x},t;\vec{0},0). \tag{2.52}$$

Thus the three-point function can be constructed by:

$$G^{\chi_\Gamma\gamma^\mu\chi_\Gamma}(\vec{p},\vec{p}';t,t_1)= \tag{2.53}$$
$$-\sum_{\vec{x_1}}Q_d\mathrm{Tr}[S(x_1;t;\vec{p}';\Gamma)\bar{\Gamma}G(0;x_1)\gamma^\mu]e^{-i\vec{x}_1\cdot(\vec{p}'-\vec{p})}.$$

Here, the final state (Γ), the final state momentum $\vec{p}'$ as well as the sink time slice t are fixed when constructing the sequential source. The advantage of this method is that the insertion operator can change arbitrarily as well as the insertion momentum $\vec{p}'-\vec{p}$ and the insertion time slice t without the need for a new inversion. This gives the matrix element for arbitrary momentum transfer, compared to the fixed insertion method where the momentum transfer is fixed prior to the sequential inversion.

After contracting the sequential propagator with the forward propagator, one obtains a function of the insertion coordinate which by Fourier transform gives the three-point function at arbitrary momentum. We would like to note here that in practice one does not have access to any, arbitrarily large momentum transfer of the matrix element though. As shall be seen in the measurements that follow in the next Chapters, one can extract reliable results up to momentum transfers of around 2 GeV^2. The reason is that the

three-point function, as well as the two-point functions that are used in the ratio, are exponentially decaying functions with time with the energy of the hadron for the given momentum appearing in the exponent. The larger the momentum transfer, the faster the three-point function falls with time, and since statistical errors are constant this means that the signal is lost earlier. The advantage of being able to probe any momentum lies in the fact that the interesting quantities we want to extract from the three-point function are usually functions of the momentum transfer squared. Hence by having access to all the lattice momentum vectors we can average over all momenta that give the same momentum transfer squared thus improving statistics.

The sequential source method can be generalized to more complicated three-point function calculations such as baryon three-point functions which we shall see in the next chapters. Here we have presented the method for the simple case of mesons in order to demonstrate the basic concepts of the sequential inversion and to explain the two approaches; the fixed sink and the fixed current approach.

In the chapters that follow, we shall present results for the nucleon electromagnetic form factors as well as the nucleon to Δ electromagnetic transition form factors computed via the sequential inversion technique. For these two calculations the fixed sink approach was used, choosing the sink momentum as zero. As shall be seen, this approach was chosen so that several operators can be inserted, which in turn allows the construction of combinations of correlators which isolate specific form factors. More importantly, this method allows the computation of the three-point function at arbitrary insertion momentum without additional computational cost.

Chapter 3

Nucleon Electromagnetic Form Factors

The structure of hadrons is a topic still being investigated experimentally as well as theoretically. The ingredients of the nuclei, the nucleons, are the building blocks of visible matter and thus understanding their characteristics and structure within QCD is one of the main goals of the theory. Experimentally, basic features of the nucleons such as their size, charge distribution and magnetization are probed via the scattering of electrons on nucleons. This electromagnetic interaction is parametrized in terms of two form factors, the nucleon electromagnetic form factors.

The nucleon electromagnetic matrix element is given by:

$$\langle N(p',s')|j_\mu|N(p,s)\rangle = \sqrt{\frac{M_N^2}{E_N(\vec{p}')E_N(\vec{p})}}\bar{u}(p',s')\mathcal{O}_\mu u(p,s), \tag{3.1}$$

where

$$\mathcal{O}_\mu = \gamma_\mu F_1(q^2) + \frac{i\sigma_{\mu\nu}q^\nu}{2M_N}F_2(q^2). \tag{3.2}$$

p (s) and p' (s') are the initial and final momenta (spins) of the nucleon while $q^\mu = p'^\mu - p^\mu$ is the momentum transfer. $F_1(q^2)$ is the Dirac form factor, with $F_1(0) = \mathcal{Q}_N$ is the charge of the nucleon while $F_2(q^2)$ is the Pauli form factor with $F_2(0) = \kappa_N$ is its anomalous magnetic momentum. The earliest measurement of these form factors was in the 1950's [23] where the two proton form factors were found to have the same dependence on the momentum transfer squared up to $\sim$0.5 GeV^2. More specifically, this measurement established that the form factors have a dipole dependence on $Q^2 = -q^2$:

$$G_d(Q^2) = (1 + \frac{Q^2}{0.71})^{-2}. \tag{3.3}$$

Using Rosenbluth separation [24], the electric (G_E) and magnetic (G_M) nucleon form factors, known as Sachs form factors, are extracted:

$$\begin{aligned} G_E(q^2) =& F_1(q^2) + \frac{q^2}{(2M_N)^2}F_2(q^2), \\ G_M(q^2) =& F_1(q^2) + F_2(q^2). \end{aligned} \tag{3.4}$$

Measurements of these two form factors showed that at low momentum transfers their

ratios with the dipole form factor $G_d(Q^2)$ of Eq. (3.3) were approximately consistent. Next generation experiments [25] that measure the ratio $\mu G_E/G_M$ directly through polarization experiments, have indicated that this ratio falls off approximately linearly indicating that the electric form factor falls faster than the magnetic form factor. One can find reviews of experimental measurements in Refs. [26, 27].

Given the experimental situation, it is thus of interest to calculate these form factors from first principles. Accurate measurement on the lattice can provide a comparison with experiment as well as a better determination of phenomenologically interesting quantities such as the electric and magnetic r.m.s. radii. In this chapter we shall present a lattice computation of the nucleon electromagnetic form factors [15]. We improve on a previous quenched calculation [28] by going to lighter pion masses as well as using unquenched gauge configurations. Additionally the accuracy of this measurement is improved by employing techniques such as including all lattice momentum vectors that contribute to the same momentum transfer squared and constructing an optimized sink for a specific form factor.

3.1 Lattice Formulation

As explained more generally in Chapter 2, the calculation of the matrix element of Eq. (3.1) on the lattice requires the calculation of a three-point function:

$$G^{Nj^\mu N}(t_2, t_1; \vec{p}', \vec{p}; \Gamma) = \sum_{\vec{x}_2, \vec{x}_1} e^{-i\vec{x}_2\cdot\vec{p}'} \langle\Omega|\Gamma^{\beta\alpha}\chi^N_\alpha(\vec{x}_2, t_2) j_\mu(\vec{x}_1, t_1)\bar{\chi}^N_\beta(\vec{0}, 0)|\Omega\rangle e^{-i\vec{x}_1\cdot(\vec{p}'-\vec{p})}, \tag{3.5}$$

where Γ are projection matrices, which in the basis given in Appendix A are given by:

$$\Gamma_i = \frac{1}{2}\begin{pmatrix} \sigma_i & 0 \\ 0 & 0 \end{pmatrix} \; i = 1, 2, 3 \quad \text{and} \quad \Gamma_4 = \frac{1}{2}\begin{pmatrix} \mathbb{1} & 0 \\ 0 & 0 \end{pmatrix}, \tag{3.6}$$

while $\chi^N(x)$ is a nucleon interpolating operator and $j_\mu(x)$ is an electromagnetic current given by:

$$\begin{aligned} \chi^N_\alpha(x) =& \varepsilon^{abc} u^{a\top}_\mu(x)(C\gamma_5)_{\mu\nu} d^b_\nu(x) u^c_\alpha(x) \\ j_\mu(x) =& \mathcal{Q}_u \bar{u}(x)\gamma_\mu u(x) + \mathcal{Q}_d \bar{d}(x)\gamma_\mu d(x). \end{aligned} \tag{3.7}$$

$\mathcal{Q}_u$ and $\mathcal{Q}_d$ are the electric charge of the up and down quarks respectively. As given above, j_μ is not a conserved current, i.e. it is not a Noether current of the lattice action. For the calculation we additionally use the lattice conserved electromagnetic current:

$$j_\mu(x) = \sum_f \mathcal{Q}_f \kappa[\bar{\psi}_f(x+\hat{\mu})(1+\gamma_\mu)U^\dagger_\mu(x)\psi_f(x) - \bar{\psi}_f(x)(1-\gamma_\mu)U_\mu(x)\psi_f(x+\hat{\mu})], \tag{3.8}$$

where $f = u, d$ and κ is the Wilson hopping parameter. We take a symmetric combination of the conserved current:

$$j_\mu(x) \to [j_\mu(x) + j_\mu(x - \hat{\mu})]/2. \tag{3.9}$$

As in the simple case of the pion presented in Chapter 2, this three-point function has a disconnected contribution. On the lattice this requires the computation of an all-to-all propagator which is generally more difficult to calculate due to the large number of inversions one needs if one is to employ stochastic techniques. In this work we avoid the need to compute the disconnected contribution by computing the isovector proton form factors given by:

$$\begin{aligned} G_E(q^2) =& G_E^p(q^2) - G_E^n(q^2) \\ G_M(q^2) =& G_M^p(q^2) - G_M^n(q^2), \end{aligned} \tag{3.10}$$

where G_E^p (G_M^p) and G_E^n (G_M^n) are the electric (magnetic) form factors of the proton and neutron respectively. In the computation of these isovector form factors, the quark loops cancel if we assume degeneracy between up and down quarks. To be more specific, assuming isospin SU(2) flavor symmetry, the current from which the isovector form factors are computed is given by:

$$\langle p|\frac{2}{3}\bar{u}\gamma_\mu u - \frac{1}{3}\bar{d}\gamma_\mu d|p\rangle - \langle n|\frac{2}{3}\bar{u}\gamma_\mu u - \frac{1}{3}\bar{d}\gamma_\mu d|\rangle = \langle p|\bar{u}\gamma_\mu u - \bar{d}\gamma_\mu d|p\rangle. \tag{3.11}$$

Thus the propagator corresponding to the up quark loop cancels with that corresponding to the down quark loop.

As shown in Chapter 2, the matrix element is extracted from the three-point function by dividing it with an appropriate ratio of two-point functions. The two-point function in the large time limit is given by:

$$G^{NN}(t, \vec{p}; \Gamma_4) = \Gamma_4^{\beta\alpha} \sum_s \langle \Omega|\chi_\alpha^N|N(\vec{p}, s)\rangle\langle N(\vec{p}, s)|\bar{\chi}_\beta^N|\Omega\rangle e^{-E_N(\vec{p})t}. \tag{3.12}$$

where we trace the Dirac indices of the nucleon interpolating operator with Γ_4. The above expression is reached to by inserting a complete set of states to the nucleon two-point function:

$$\sum_{s,n,\vec{p}} |n, \vec{p}, s\rangle\langle n, \vec{p}, s| = \mathbb{1}, \tag{3.13}$$

where s is the spin quantum number. Adopting a basis of the states as given in Chapter 2, the overlap of a nucleon state with the interpolating operator is defined by:

$$\langle \Omega|\chi_\alpha^N|N(\vec{p}, s)\rangle = Z^N(\vec{p})\sqrt{\frac{M_N}{E_N(\vec{p})}}u_\alpha(\vec{p}, s), \tag{3.14}$$

where u is a Dirac spinor. Using the spin sum rule for Euclidean space-time:

$$\sum_s u(p,s)\bar{u}(p,s) = \frac{-i\not{p} + M_N}{2M_N} \tag{3.15}$$

the two-point function, traced with the projection matrix Γ_4, gives:

$$G^{NN}(t,\vec{p},\Gamma_4) = \frac{E_N(\vec{p}) + M_N}{E_N(\vec{p})}|Z_N(\vec{p})|^2 e^{-E_N(\vec{p})t}. \tag{3.16}$$

On the other hand, the three-point function, after inserting two sets of complete states gives, in the large time limit $t_2 - t_1 \gg 1$ and $t_1 \gg 1$:

$$G^{Nj^\mu N}(t_2,t_1;\vec{p}',\vec{p};\Gamma) = \tag{3.17}$$

$$\sum_{s,s'}\Gamma^{\beta\alpha}Z_N(\vec{p}')\sqrt{\frac{M_N}{E_N(\vec{p}')}}u_\alpha(\vec{p}',s')\bar{u}_{\alpha'}(\vec{p}',s')\sqrt{\frac{M_N^2}{E_N(\vec{p})E_N(\vec{p}')}}\mathcal{O}^\mu_{\alpha'\beta'}\times$$

$$u_{\beta'}(\vec{p},s)\bar{u}_\beta(\vec{p},s)\bar{Z}_N(\vec{p})\sqrt{\frac{M_N}{E_N(\vec{p})}}e^{-E_N(\vec{p}')(t_2-t_1)}e^{-E_N(\vec{p})t_1}$$

$$= \frac{Z_N(\vec{p}')\bar{Z}_N(\vec{p})}{4E_N(\vec{p}')E_N(\vec{p})}\mathrm{Tr}\left[\Gamma\left(-i\not{p}' + M_N\right)\mathcal{O}^\mu\left(-i\not{p} + M_N\right)\right]. \tag{3.18}$$

The ratio is thus constructed and the matrix element is extracted by identifying a plateau in the large time limit. The ratio is given by:

$$\begin{aligned} R(t_2,t_1,\vec{p}',\vec{p};\Gamma;\mu) =& \frac{G^{Nj^\mu N}(t_2,t_1;\vec{p}',\vec{p};\Gamma)}{G^{NN}(t_2,\vec{p}';\Gamma_4)} \\ &\times\left[\frac{G^{NN}(t_2-t_1,\vec{p};\Gamma_4)G^{NN}(t_1,\vec{p}';\Gamma_4)G^{NN}(t_2,\vec{p}';\Gamma_4)}{G^{NN}(t_2-t_1,\vec{p}';\Gamma_4)G^{NN}(t_1,\vec{p};\Gamma_4)G^{NN}(t_2,\vec{p};\Gamma_4)}\right]^{1/2} \\ &\xrightarrow[t_1\gg 1]{t_2-t_1\gg 1}\Pi(\vec{p}',\vec{p},\Gamma,\mu). \end{aligned} \tag{3.19}$$

In this specific measurement we have chosen to use the fixed sink sequential inversion method. As demonstrated in Chapter 2 this means that the sum over the sink coordinate is carried out by the inversion of an appropriately constructed source. This allows for any momentum transfer, as well as any direction of the electromagnetic current (μ) to be selected without further inversions. On the other hand, we must fix the final state and its momentum before the sequential inversion. We choose to set the momentum of the sink, $\vec{p}'$ to zero. The momentum transfer, defined by $q^\mu = p^{\mu'} - p^\mu$ is thus given by $\vec{q} = -\vec{p}$ in this frame.

The projection matrix Γ which is used in the three-point function allows to select combinations with the current direction μ so that a specific form factor is isolated. Although μ can be arbitrarily varied after the sequential inversion, the matrix Γ is traced over the final and initial states and thus appears in the sequential source. Thus it must be selected

before the sequential inversion. We find two combinations that isolate the electric form factor and one that isolates the magnetic:

$$\Pi(\vec{0}, -\vec{q}; \Gamma_k; \mu = i) = \mathcal{K}(\vec{q}) \frac{1}{2M_N} \varepsilon_{ijk} q_j G_M(Q^2) \tag{3.20}$$

$$\Pi(\vec{0}, -\vec{q}; \Gamma_4; \mu = i) = \mathcal{K}(\vec{q}) \frac{q_i}{2M_N} G_E(Q^2) \tag{3.21}$$

$$\Pi(\vec{0}, -\vec{q}; \Gamma_4; \mu = 4) = \mathcal{K}(\vec{q}) \frac{E(\vec{q}) + M_N}{2M_N} G_E(Q^2) \tag{3.22}$$

with $\mathcal{K}(\vec{q}) = \frac{2M_N^2}{E_N(\vec{q})(E_N(\vec{q})+M_N)}$. For the two combinations that give the Electric form factor (Eqs. (3.21) and (3.22)) we need only perform the sequential inversion using the sequential source with Γ_4. Eq. (3.20) on the other hand, is in fact a set of three equations. Thus we reduce the number of sequential inversions needed for $G_M(Q^2)$ to one, by constructing a linear combination of these sinks. In this way, we obtain the largest set of lattice measurements that give G_M with only one sequential inversion:

$$\begin{aligned} S_m(\vec{q}, i) =& \sum_{k=1}^{3} \Pi(\vec{0}, -\vec{q}; \Gamma_k; \mu = i) \\ =& \frac{\mathcal{K}(\vec{q})}{2M_N} [(p_2 - p_3)\delta_{1,i} + (p_3 - p_1)\delta_{2,i} + (p_1 - p_2)\delta_{3,i}] G_M(Q^2). \end{aligned} \tag{3.23}$$

In Appendix B we perform the contractions of the quarks in the nucleon three-point function, expressing them in terms of quark propagators. We carry on to show how one constructs the sequential source, which for this case is rather non trivial as compared to the pion three-point function, shown in Chapter 2.

3.2 Interpolation of Experimental Results

As mentioned previously, one of the goals of this calculation is to directly compare the nucleon electromagnetic form factors with experiment. The experimental data for the neutron and proton form factors are available separately albeit at non coincident momentum transfers. In order to subtract one from the other and yield the isovector form factors we must interpolate the experimental results to the same Q^2 values.

In Fig. 3.1 we show experimental results for the electric and magnetic form factors of the proton and neutron. These results are obtained in a wide range of experiments [29–43]. For the Electric form factor, we need to extrapolate the data of the proton to values of Q^2 between 0.25 and 1.0 GeV^2 while for the neutron we need to extrapolate to low momentum transfer. For the neutron electric form factor we use the Galster parametrization [44]:

$$G_E^n(Q^2) = \frac{-\mu_n \tau}{1 + 5.6\tau} G_d(Q^2) \tag{3.24}$$

where $\tau = Q^2/4M_N^2$, $\mu_n = -1.91315$ and G_d is the dipole given in Eq. (3.3). This provides a good description of the experimental data. We compute the derivative of Eq. (3.24) at

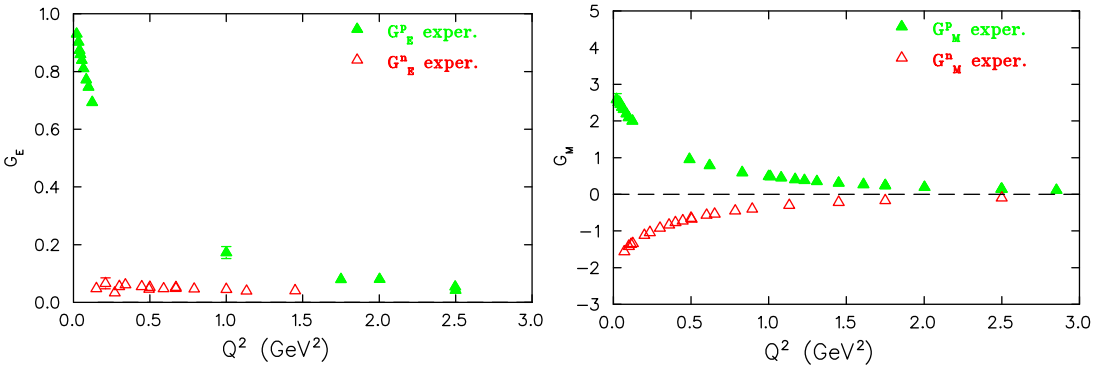

Figure 3.1: Experimental results for the electric (left) and magnetic (right) Sachs form factors for the proton (filled triangles) and the neutron (open triangles).

the Q^2 needed and interpolate the data accordingly. In the case of the proton Electric form factor, we **fit** to a dipole form and carry out the same procedure. This is also done for the magnetic form factors, although in cases where two measurements are close enough to the intermediate Q^2 desired, we favor a finite difference approximation.

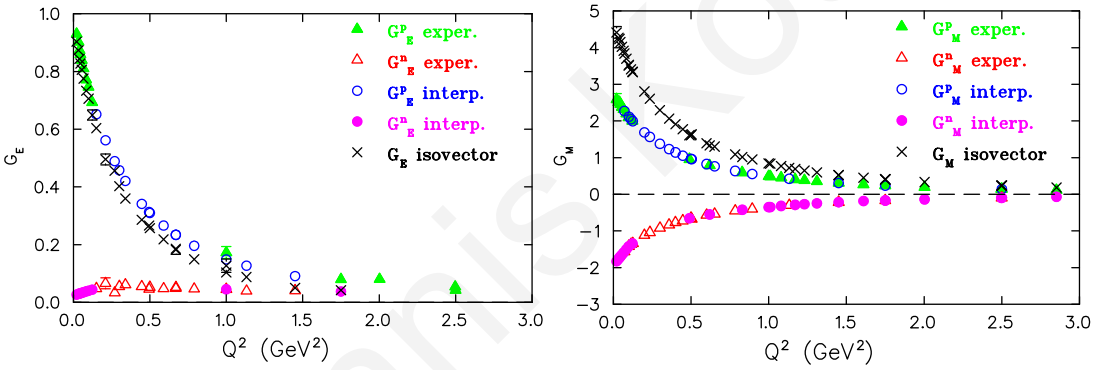

Figure 3.2: Interpolated results (open circles for proton, filled circles for neutron) compared to raw experimental results (filled triangles for proton, open triangles for neutron). Left for the electric and right for the magnetic form factors. The crosses show the isovector form factor; the difference between the proton and neutron form factors.

In Fig. 3.2 we show the result of interpolating the experimental data and the resulting isovector form factor computed by the difference of the proton minus the neutron form factor. The electric isovector form factor is only slightly lower than the proton electric form factor due to the small neutron electric form factor. In Fig. 3.3 we show the ratio $\mu G_E/G_M$ for both the proton and the isovector form factors extracted by interpolating the experimental data. As can be seen the ratio of isovector form factors is steeper at low momentum transfers compared to the ratio of the proton form factors. At higher Q^2 however, the isovector remains approximately the same. Investigating this behavior with precise measurements from lattice QCD is one of the goals.

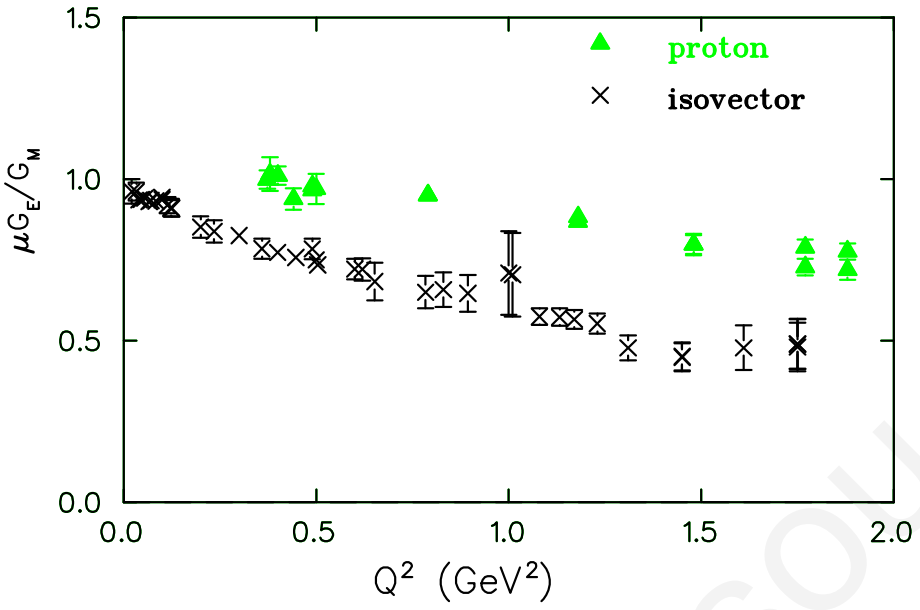

Figure 3.3: Ratio of G_E/G_M of the isovector (crosses) obtained by interpolating the experimental data and the proton (triangles).

3.3 Lattice Parameters and Optimization

For the results that follow, one ensemble of quenched Wilson configurations is used as well as three ensembles of Wilson $N_F = 2$ dynamical configurations. The quenched configurations are used since the low computational cost provides access to larger lattices which in turn allow for finer lattice momenta. A $32^3 \times 64$ lattice at $\beta = 6.0$ using three pion masses is thus used, allowing a smallest momentum transfer of 0.15 GeV^2. The unquenched calculation is carried out on two ensembles of gauge configurations provided by the SESAM Collaboration [8] and one ensemble from the DESY-Zeuthen group [45]. All three of these ensembles are simulated using $\beta = 5.6$ meaning a lattice spacing of approximately ~ 0.08 fm, which is comparable with that of the quenched calculation ~ 0.09 fm. Thus, discrepancies between the results using the dynamical configurations with those using the quenched lattices will be a measure of unquenching effects since the two calculations exhibit similar finite a effects. Details of the lattices used in this calculation can be found in Table 3.1. The lattice spacing for these configurations was set by requiring the nucleon mass at the chiral limit to be equal to the physical nucleon mass. The chiral extrapolation was carried out using two forms:

$$\begin{aligned} aM_N(m_\pi^2) &= aM_N(0) + c_0 m_\pi^2, \\ aM_N(m_\pi^2) &= aM_N(0) + c_1 m_\pi^2 + c_2 m_\pi^3. \end{aligned} \tag{3.25}$$

The discrepancy between the value of a obtained by using these two Ansätze gives the systematic error, which we found larger than the statistical error. Thus we quote the

Table 3.1: Details of the gauge configuration ensembles used in this calculation. The Wilson dynamical configurations at $\kappa = 0.1575$ and $\kappa = 0.1580$ are taken from [8] while the ensemble at $\kappa = 0.15825$ was taken from [45].

number of confs	κ	am_π	aM_N
Quenched $32^3 \times 64$	$a^{-1} = 2.14(6)$ GeV		
200	0.1554	0.263(2)	0.592(5)
200	0.1558	0.229(2)	0.556(6)
200	0.1562	0.192(2)	0.518(6)
	κ_c =0.1571	0.	0.439(4)
Unquenched $24^3 \times 40$	$a^{-1} = 2.56(10)$ GeV		
185	0.1575	0.270(3)	0.580(7)
157	0.1580	0.199(3)	0.500(10)
Unquenched $24^3 \times 32$	$a^{-1} = 2.56(10)$ GeV		
200	0.15825	0.150(3)	0.423(7)
	$\kappa_c = 0.1585$	0.	0.366(13)

systematic error in Table 3.1.

As we have seen in Chapter 2 smearing of the initial and final states improves ground state dominance considerably, so that a plateau is identified at earlier time slices. Fig. 2.4 shows that excited state contamination is suppressed as early as three time slices from the source when employing both Wuppertal smearing on the initial state and HYP smearing in the links that enter the source smearing. This allows us to set the sink time-slice close enough to the source so that statistical noise is under control, while simultaneously leaving enough time slices in between to vary the insertion time in search for a plateau. For both quenched and unquenched cases we use the same set of parameters for the smearing, namely $n = 50$ iterations and $\alpha = 4.0$, i.e. the same parameters used for the example plots of the previous chapter.

The nucleon two-point function is shown in Fig. 3.4 where we plot the nucleon energy for the smallest lattice momentum available $|\vec{p}| = \frac{2\pi}{L}$. This is done for the quenched lattice using the lightest pion mass. The effective energy plotted is constructed from the ratio of correlators: $E^N_{\text{eff}}(\vec{p}, t) = -\log\left[C(\vec{p}, t+1)/C(\vec{p}, t)\right]$. In the large time limit, the ratio gives a plateau at the value of the energy. The dashed line shows a fit to a constant. The solid line shows a fit to a form which takes into account the first excited state, i.e. to the form:

$$C(\vec{p}, t) = |\langle\Omega|\chi^N_\alpha|N(\vec{p}, s)\rangle|^2 e^{-E_N(\vec{p})t} + |\langle\Omega\chi^N_\alpha|N'(\vec{p}, s)\rangle|^2 e^{-E_{N'}(\vec{p})t}, \tag{3.26}$$

where N' is the first excitation of the nucleon and $E_{N'}$ its energy. The ratio $f_N(\vec{p}, t) = -\log[C(\vec{p}, t+1)/C(\vec{p}, t)]$, keeping the term associated with the first excitation, now gives:

$$f_N(\vec{p}, t) = E_N(\vec{p}) - \log\left(\frac{1 + r_N(\vec{p})\exp[-\delta_N(\vec{p})(t+1)]}{1 + r_N(\vec{p})\exp(-\delta_N(\vec{p})t)}\right) \tag{3.27}$$

where r_N is the ratio between the overlaps and δ_N the energy splitting:

$$\begin{aligned} r_N(\vec{p}) =& \frac{|\langle\Omega|\chi_\alpha^N|N(\vec{p},s)\rangle|^2}{|\langle\Omega|\chi_\alpha^N|N'(\vec{p},s)\rangle|^2} \\ \delta_N(\vec{p}) =& E_{N'}(\vec{p}) - E_N(\vec{p}). \end{aligned} \tag{3.28}$$

The solid line in Fig. 3.4 shows a three parameter fit to Eq. (3.27) determining $E_N(\vec{p})$, $r_N(\vec{p})$ and $\delta_N(\vec{p})$. Consistency with the dashed line shows that whether we fit the whole correlator considering a first excited state or fit from $t/a = 4$ to a constant we find the same value for the energy. Hence excited state contamination can be neglected for $t/a \geq 4$ for this lattice spacing. A source-sink separation of $t/a = 11$ or 5 GeV^{-1} which is what we take for the quenched case is thus a reasonable choice. For the unquenched Wilson configurations which are simulated on slightly finer lattices we take $t/a = 12$ which gives a source-sink separation of approximately 4.9 GeV^{-1}.

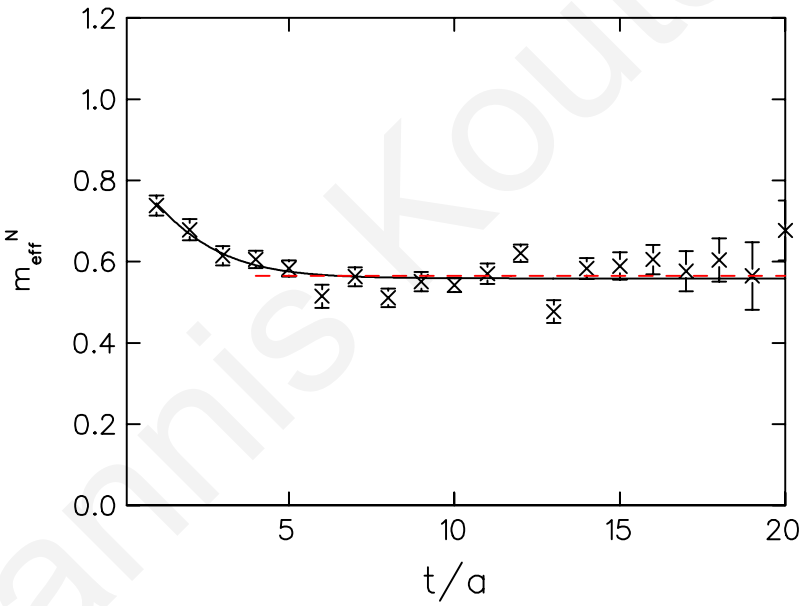

Figure 3.4: Nucleon energy plot for $|\vec{p}| = \frac{2\pi}{L}$ versus time. The dashed line is a fit to a constant while the solid line shows a fit to Eq. (3.27).

It is evident from Eqs. (3.20–3.22) that more than one lattice measurement yields the form factors at a given Q^2. To extract the form factors using all lattice measurements available we solve the over-complete set of equations:

$$P(\vec{q};\mu) = D(\vec{q};\mu)F(Q^2), \tag{3.29}$$

where $P(\vec{q};\mu)$ is a vector of the lattice measurements, i.e. of the different $\Pi(0;-\vec{q};\Gamma;\mu)$

combinations at a given Q^2. F is the vector of form factors we want to extract:

$$F(Q^2) = \begin{pmatrix} G_E(Q^2) \\ G_M(Q^2) \end{pmatrix} \tag{3.30}$$

and $D(\vec{q};\mu)$ is a matrix of kinematic terms which can be read off from Eqs. (3.20–3.22). $F(Q^2)$ is extracted by minimizing:

$$\chi^2 = \sum_{k=1}^{N} \left(\frac{D_{ki}F_i(Q^2) - P_k}{w_k} \right)^2 \tag{3.31}$$

where the index k counts all the μ and $\vec{q}$ combinations that contribute to a given Q^2 and w_k is the statistical error the lattice measurement P_k carries. Minimizing with respect to F_i gives $(DF - P) \cdot D^\top = 0$. The inversion is achieved through the singular value decomposition of $D_{k,i}$, i.e. we numerically compute the decomposition of $\tilde{D}_{ki} = D_{ki}/w_k$ into:

$$\tilde{D} = U\Sigma V^\dagger \tag{3.32}$$

where, assuming $\tilde{D}$ is an $M \times 2$ matrix, U is an $M \times M$ unitary matrix, Σ an $M \times 2$ diagonal matrix and V a 2×2 unitary matrix. We thus extract the form factors by:

$$F = V\Sigma^{-1}U^\dagger\tilde{P} \tag{3.33}$$

where $\tilde{P}_k = P_k/w_k$.

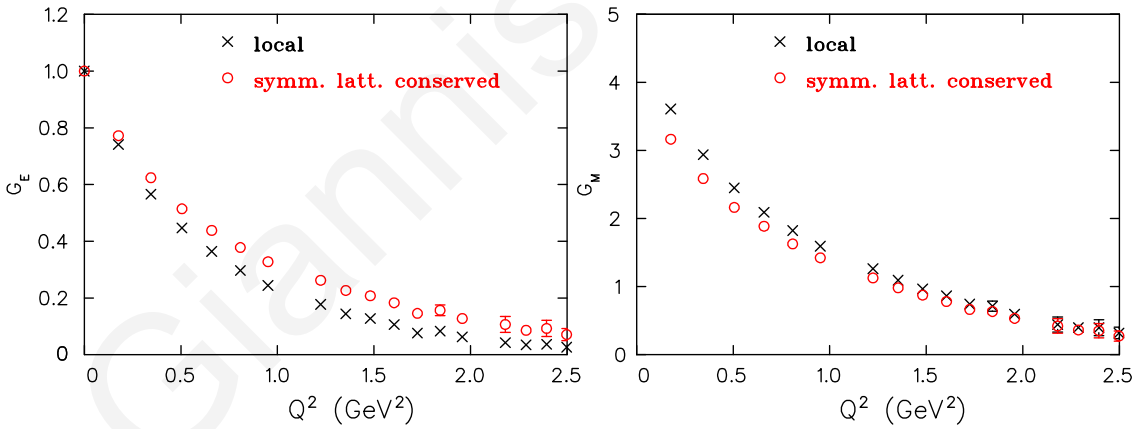

Figure 3.5: The electric isovector form factor (left) and the isovector magnetic form factor (right) computed using a local current (crosses) and the symmetrized lattice conserved current as in Eq. (3.9) (open circles).

Before going on to the main results, we shall give details on two tests carried out to check lattice techniques. In Fig. 3.5 we show a comparison between the electric isovector form factor computed using the lattice conserved current given in Eqs. (3.8) and (3.9) and the local current given in Eq. (3.7). The form factor computed with the local current has been normalized requiring charge conservation, i.e. requiring $G_E(0) = 1$. This gives a

renormalization constant $Z_V = G_E^{-1}(0) = 0.67$ for the electromagnetic current. The test was carried out for the quenched case with $\kappa = 0.1554$. As can be seen, results for both the electric and magnetic form factor show deviations when using the local or the lattice conserved current. Furthermore, the discrepancy found in the two form factors is not in the same direction. This means the ratio of G_E/G_M will show an even larger discrepancy between the two choices for the current. This discrepancy shows that lattice artifacts are not completely negligible for these values of the lattice spacing.

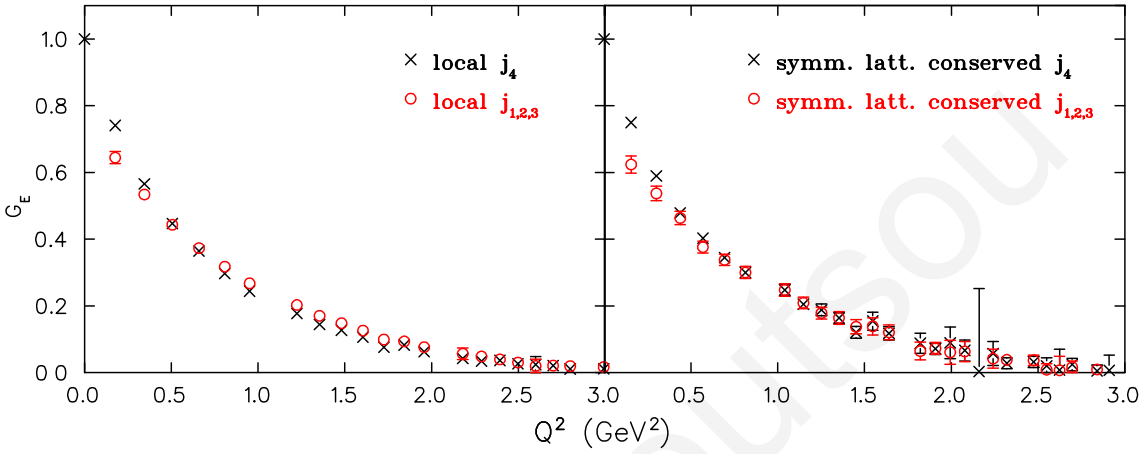

Figure 3.6: The electric isovector form factor computed using the combination in Eq. (3.21) (circles) and the combination given in Eq. (3.22) (crosses). We show this using both the local current (left) and the conserved current (right).

A second test was carried out where we computed G_E on one hand using Eq. (3.21) and on the other hand using Eq. (3.22). The result of this test is shown in Fig. 3.6. The discrepancy between the two combinations at low Q^2 for both lattice currents can be understood by noticing that G_E is multiplied by q_i in Eq. (3.21). As $\vec{q} \to 0$ the inverse of the momentum vector $\vec{q}_i$ becomes inaccurate leading to an erroneous value for G_E. However, at momentum transfers larger than $\sim$0.5 GeV^2 we see that there are slight discrepancies for the case of the local current while the results using the conserved current are in better agreement. We therefore choose to use the lattice conserved current for the calculations that follow. Furthermore, we only use Eq. (3.22) to extract G_E for momentum transfers lower than $Q^2 < 0.5$ GeV^2.

3.4 Results

In Fig. 3.7 we show the electric isovector form factor computed on the lattice using both quenched and unquenched ensembles of Table 3.1 at all three pion masses each. The results are compared to the interpolated experimental data. As can be seen, the value of the form factor decreases slightly with decreasing pion mass bringing the lattice data closer to experiment as we approach the chiral limit. In Fig. 3.8 we plot the ratio of the electric form factor over the dipole form factor G_d. This is done so we can better detect discrepancies with experiment. We see that the unquenched results show a stronger quark

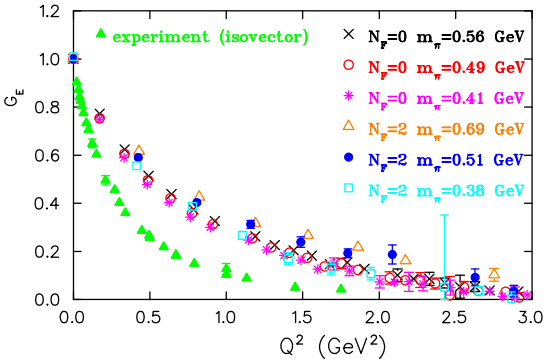

Figure 3.7: The electric isovector form factor. Lattice results are compared to experiment (filled triangles). Wilson quenched are denoted by the crosses, open circles and asterisks for $\kappa = 0.1554$, $\kappa = 0.1558$ and $\kappa = 0.1562$ respectively while dynamical Wilson $N_F = 2$ are denoted by the open triangles, filled circles and open squares for $\kappa = 0.1575$, $\kappa = 0.1580$ and $\kappa = 0.15825$ respectively.

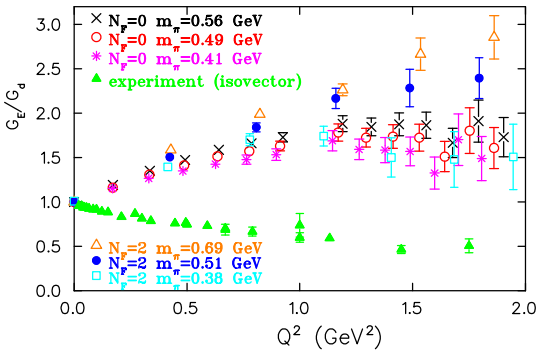

Figure 3.8: The electric isovector form factor divided by the dipole form factor. The notation is the same as that of Fig. 3.7.

mass dependence than the quenched results, pointing to a smaller value in the chiral limit. However, the slope of the lattice data at small momentum transfers has the opposite sign than that of the experiment. This discrepancy could be attributed either to possible discretization effects, or that we are too far away from the chiral limit for a meaningful comparison with experiment. As for the first possibility, assessing finite a effects requires the computation of the form factors at different lattice spacings. The lattices available to us at the time of this analysis were restricted to a single lattice spacing, hence such an investigation was not possible within the amount of resources available. As for the second possible source of discrepancy – that we are too far away from the chiral limit – we are once again limited by resources as to how light a pion mass we can reach. Nevertheless, we will present a chiral extrapolation in the next section.

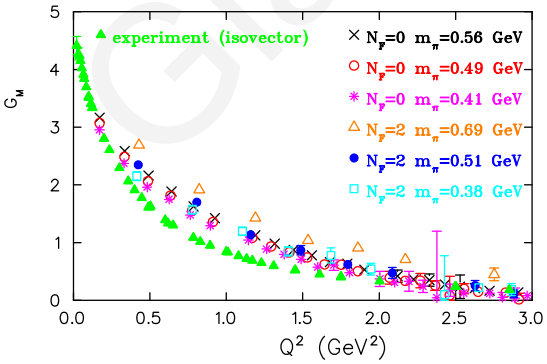

Figure 3.9: The magnetic isovector form factor. The notation is the same as that of Fig. 3.7.

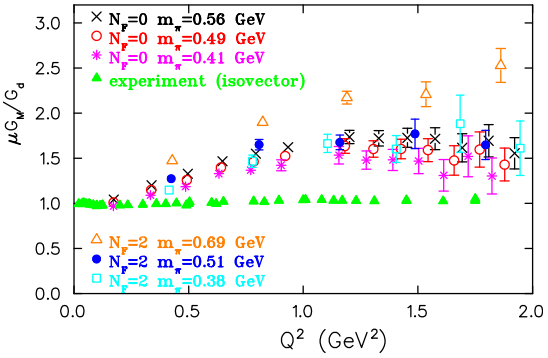

Figure 3.10: The magnetic isovector form factor divided by the dipole form factor. The notation is the same as that of Fig. 3.7.

In Fig. 3.9 we show the magnetic form factor, computed using the optimal source given in Eq. (3.23). The conclusion is the same as for G_E; that the lattice data decrease with decreasing pion mass thus approaching the experimental results. We show the ratio G_M/G_d in Fig. 3.10, where we notice the stronger dependence of the unquenched results with the quark mass, as already noted in the case of G_E/G_d. We note that the experimental data for the magnetic form factor are well described by the dipole form G_d which is why they show an approximately zero slope in Fig. 3.10. At least for the pion masses available for this work, this seems not to be the case for the lattice data where we note a positive slope, as in the case of G_E/G_d (Fig. 3.8).

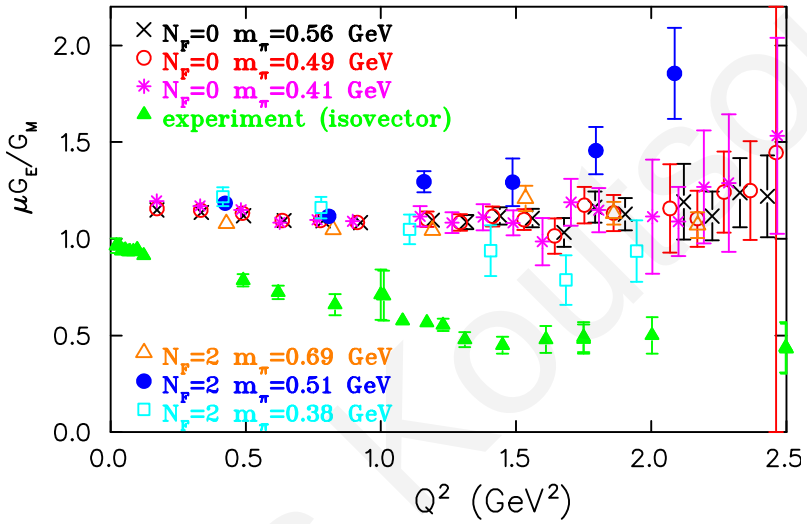

Figure 3.11: The ratio of the electric over the magnetic form factors compared to experiment. The notation is the same as that of Fig. 3.7.

We show the experimentally interesting ratio $\mu G_E/G_M$ in Fig. 3.11. As can be seen, the ratio is quite insensitive to the pion mass as well as unquenching effects contrary to G_E and G_M plotted separately. We once again see a discrepancy with experimental data, namely the lattice data show a smaller if not zero slope than that of the experimental data which is clearly negative.

The Dirac (F_1) and Pauli (F_2) form factors are plotted in Fig. 3.12. These are linear combinations of the Sachs form factors (Eq. (3.4)). They are phenomenologically interesting since in the non-relativistic limit, the slope of F_1 is associated with the transverse size of the nucleon [46]. We see a discrepancy of the lattice data for F_1 as compared to experiment, as well as a weak quark mass dependence. The apparent insensitivity to the quark mass means that a chiral extrapolation would need to be non-trivial in order for lattice and experiment to yield consistent results in the chiral limit. F_2 on the other hand has a stronger quark mass dependence and is expected to come closer to experiment after extrapolating to zero pion mass.

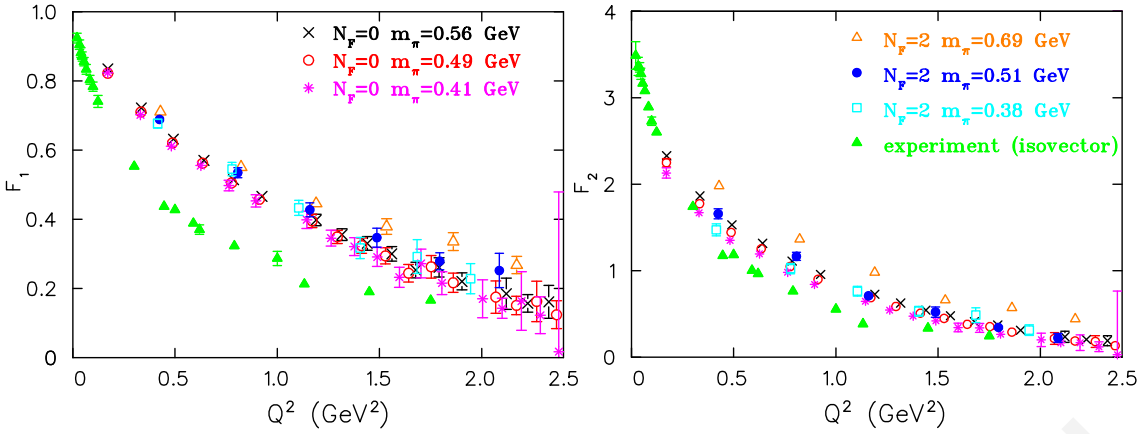

Figure 3.12: The Dirac (left) and Pauli (right) form factors compared with experiment. The notation is the same as that of Fig. 3.7.

3.5 Chiral Extrapolation

As noted above, one of the sources of discrepancy between the lattice results and the experiment may be the fact that we are too far away from the chiral limit. The form factors were calculated at pion masses in the range between 0.41 and 0.56 GeV for the quenched case and in the range between 0.38 and 0.69 GeV using Wilson dynamical configurations. The statistical accuracy of the measurement allows momentum transfers (squared) up to around 2 GeV^2. The only recent work in which a chiral expansion for these form factors is presented [47] is limited to small momentum transfers. For high enough momentum transfers though (Q^2 >0.5 GeV^2), we expect that non-linear terms in the extrapolation are suppressed.

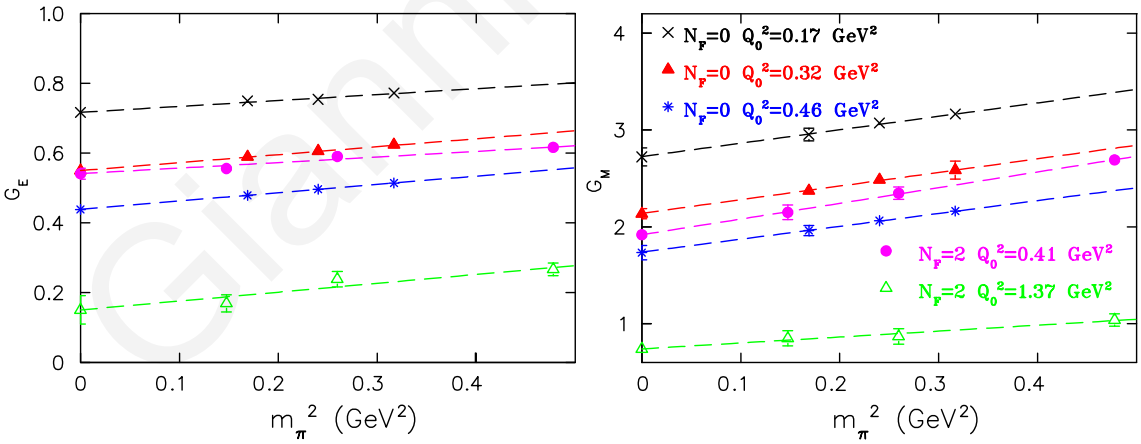

Figure 3.13: The electric (left) and magnetic (right) form factors as a function of the pion mass squared for several momentum transfers. For the quenched case we take the three lowest Q^2 (crosses, filled triangles and asterisks with increasing Q^2) while for the unquenched case we take the lowest (filled circles) and 1.37 GeV^2 (open triangles). Q_0^2 denotes the momentum transfer at the chiral limit.

We investigate this in Fig. 3.13 where we plot $G_E(Q^2)$ and $G_M(Q^2)$ as a function of

the pion mass squared at several momentum transfers. For the quenched calculation we do this for the three lowest momentum transfers while for the calculation using dynamical Wilson fermions we do this for the the lowest momentum transfer and for $Q^2 = 1.37$ GeV^2. In the reference frame where the final state is stationary, the momentum transfer squared is given by $Q^2 = 2M_N(E_N(\vec{q}) - M_N)$. Since the nucleon mass M_N is a function of the pion mass itself, the form factors computed at different pion masses are not available at equal momentum transfer Q^2. For the purpose of illustrating the linear dependence in Fig. 3.13, we use the physical nucleon mass for M_N and denote the momentum transfer using this mass as Q_0^2. As we can see all data are well described by a straight line meaning that for these relatively high pion masses terms non-linear to m_π^2 are suppressed. We therefore consider a linear extrapolation to the chiral limit. There is a freedom as to how we choose this extrapolation from the fact that the Q^2 values are different at different pion masses due to the dependence of the nucleon mass to the pion mass. To first order this dependence is linear to the pion mass squared and hence we can write:

$$f(Q^2, m_\pi) = f(Q_0^2, 0) + Am_\pi^2, \tag{3.34}$$

where Q^2 is the momentum transfer at the given pion mass and Q_0^2 is that at zero pion mass. Indeed, this is a good approximation since even at relatively large momentum transfer of 1.37 GeV^2 as shown in Fig. 3.13, the value of the form factor is linear to m_π^2. Alternatively, we can interpolate the data so that at each pion mass we have the form factors at the same Q^2 values. This approach should give the same chiral limit for the form factors something we have indeed verified. We hereon carry out the extrapolation using the first method described.

In Fig. 3.14 we show the result of this linear extrapolation for the case of the electric to dipole form factor ratio and for the case of the magnetic to dipole form factor ratio. As can be seen, the electric form factor still shows a large discrepancy with experiment for both the unquenched and the quenched case which is a result of the weak quark mass dependence already noted in the previous section. The discrepancy however is smaller in the case of the magnetic form factor where, as can be seen, the extrapolated results are closer to experiment. We have additionally carried out extrapolations for the Dirac and Pauli form factors. In Fig. 3.15 we show the linearly extrapolated form factors compared to the interpolated experimental data. As can be seen the extrapolated results indicate that unquenching effects are small. Furthermore, the Pauli form factor (F_2) is in agreement with experimental data for momentum transfers larger than 0.5 GeV^2. As expected from the results shown in the previous section, this is not the case for the Dirac (F_1) form factor where we see that the experimental data fall more rapidly than the lattice results.

It is meaningful to attempt an extraction of the magnetic moment $G_M(0)$ from the lattice data. As can be seen by Eq. (3.20), there is no combination of the direction of the current and the direction of the momentum transfers that gives $G_M(0)$ directly. This means we must fit the data to an Ansatz in order to extrapolate to $Q^2 = 0$. We consider

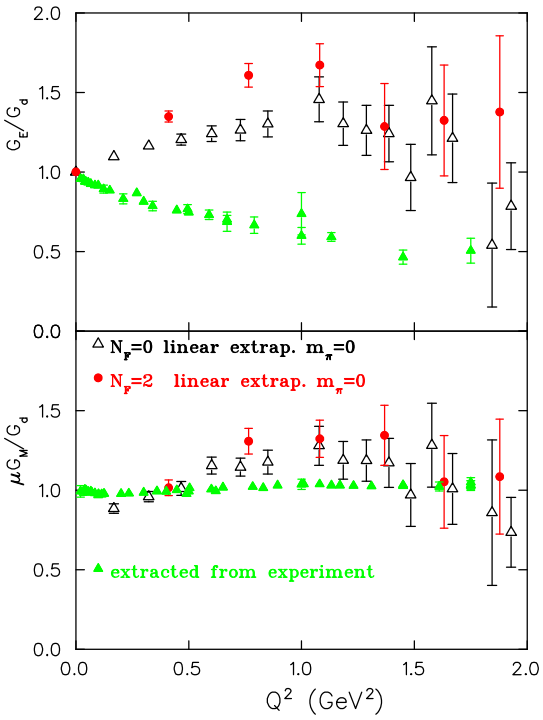

Figure 3.14: The ratio of the electric to dipole form factor G_E/G_d (upper) and magnetic to dipole $\mu G_M/G_d$ (lower) as a function of Q^2 after a linear extrapolation to the chiral limit. We denote results for the quenched case with open triangles and results for the unquenched case with filled circles. The results for the experimental isovector ratios (filled triangles) where extracted by interpolating the experimental data.

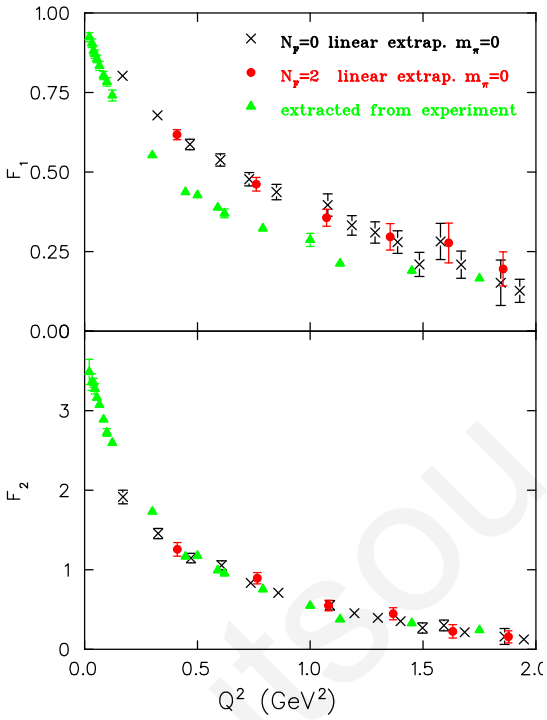

Figure 3.15: The form factors F_1 (upper) and F_2 (lower) as a function of Q^2. Crosses show quenched results at the chiral limit, and filled circles unquenched results. The results for the experimental isovector ratios (filled triangles) where extracted by interpolating the experimental data.

a dipole form for both electric and magnetic form factors:

$$G_M(Q^2) = \frac{G_M(Q^2)}{(1+Q^2/M_m)^2} \qquad (3.35)$$
$$G_E(Q^2) = \frac{G_E(Q^2)}{(1+Q^2/M_e)^2}.$$

In Fig. 3.16 we show fits for the intermediate pion masses of the quenched and unquenched calculation. Using the data up to $Q^2 \simeq 2.5$ GeV^2 we obtain good fits ($\chi^2 < 1$). For comparison we include fits to an exponential which the magnetic form factor seems to be equally well described by. We however choose to use the dipole forms since this better describes both electric and magnetic form factors.

In Table 3.2 we summarize the values of the magnetic moments as well as the dipole masses extracted by fitting. The values quoted at the chiral limit are from fitting to the extrapolated data. As can be seen, the values of the dipole masses and the magnetic moment decrease with decreasing pion mass which is what is expected by the plots shown

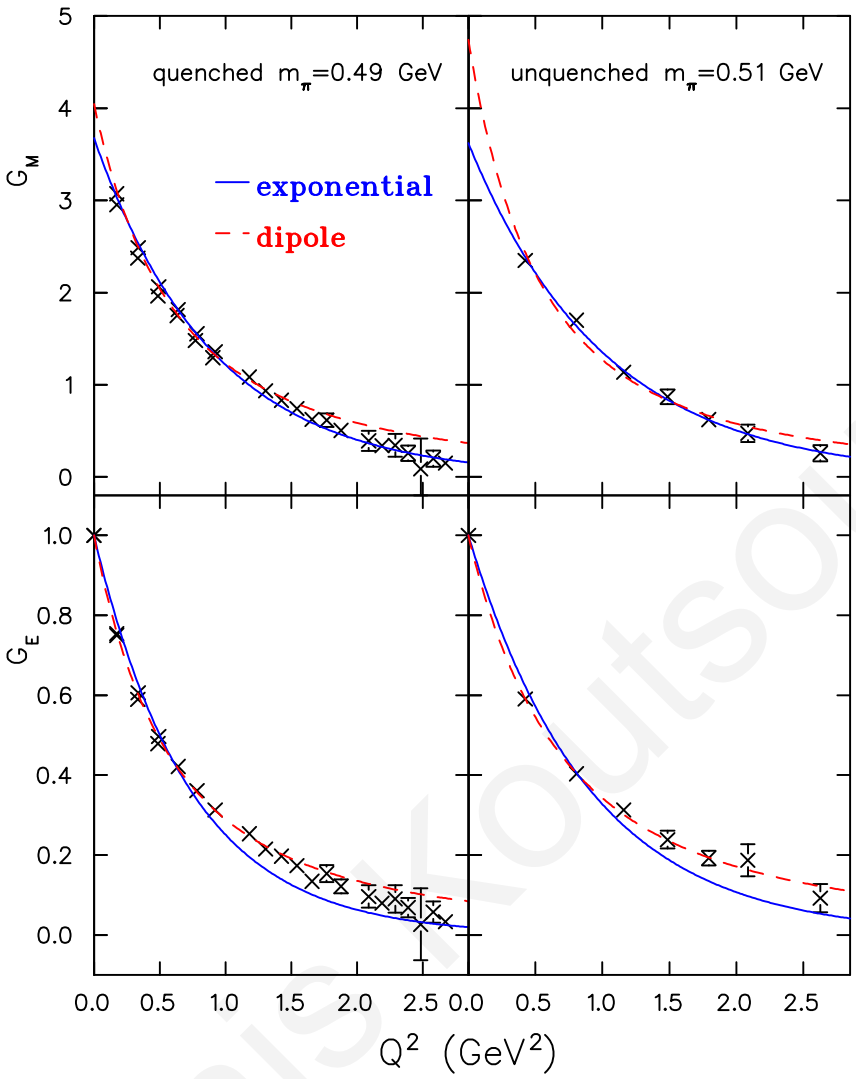

Figure 3.16: The magnetic (upper) and electric (lower) form factors for the quenched (left) and the unquenched (right) cases. Fits to dipole form are shown by the dashed lines while fits to an exponential by the solid lines.

so far. For the unquenched case we notice that the dipole masses at the chiral limit are rather close to the proton dipole mass of $M_d = 0.71$ GeV^2.

We plot the values quoted in Table. 3.2 against the pion mass squared in Fig. 3.17. We additionally include in this plot lattice results from Ref. [28] at a lattice spacing of $a^{-1} = 1.83$ GeV which is close enough to our quenched calculation for comparison. The calculation of the form factors in Ref. [28] was carried out using perturbatively improved Wilson fermions. In order to compare with this measurement we rescale the magnetic moment by the ratio of the physical nucleon mass to that measured on the lattice. As can be seen, there is an agreement between the two lattice computations. A linear extrapolation of the quenched results yields $G_M(0) = 3.67(3)$ which is consistent with the value obtained when fitting to the extrapolated form factors, given in Table. 3.2. Linearly

Table 3.2: The magnetic moments $G_M(0)$ as well as the electric and magnetic dipole masses M_e and M_m extracted by fitting G_E and G_M to dipole forms. The values given at the chiral limit where compute by fitting to the extrapolated form factors.

κ	$G_M(0)$	$M_m(\mathrm{GeV}^2)$	$M_e(\mathrm{GeV}^2)$	$\langle r_1^2\rangle^{\frac{1}{2}}$(fm)	$\langle r_2^2\rangle^{\frac{1}{2}}$(fm)
Quenched $32^3\times 64$			$a^{-1}=2.14(6)$ GeV		
0.1554	4.11(7)	1.29(4)	1.24(1)	0.520(5)	0.64(1)
0.1558	4.02(8)	1.28(4)	1.15(1)	0.538(6)	0.64(1)
0.1562	3.90(9)	1.19(4)	1.08(1)	0.550(8)	0.66(1)
κ_c =0.1571	3.73(13)	1.03(5)	0.90(2)	0.585(13)	0.72(2)
Unquenched $24^3\times 40$			$a^{-1}=2.56(10)$ GeV		
0.1575	4.45(14)	1.53(7)	1.55(1)	0.467(7)	0.58(2)
0.1580	4.34(43)	1.23(16)	1.41(2)	0.462(23)	0.67(5)
Unquenched $24^3\times 32$			$a^{-1}=2.56(10)$ GeV		
0.15825	4.10(46)	1.17(17)	1.19(4)	0.500(29)	0.68(6)
κ_c =0.1585	3.25(48)	0.792(17)	0.66(4)	0.756(36)	0.79(13)

extrapolating the magnetic and electric dipole masses also gives values consistent with those obtained when fitted to the extrapolated data. Namely we get $M_m = 1.09(10)$ GeV^2 and $M_m = 0.89(4)$ GeV^2.

In Table. 3.2 we have included the Dirac and Pauli radii ($\langle r_1^2\rangle^{1/2}$ and $\langle r_2^2\rangle^{1/2}$) which are associated with the slope of the Dirac and Pauli form factors at $Q^2 = 0$:

$$\langle r_k^2\rangle = -\frac{6}{F_k(Q^2)}\frac{dF_k(Q^2)}{dQ^2}\bigg|_{Q^2=0} = \frac{12}{M_k}, \tag{3.36}$$

where M_1 and M_2 are the Dirac and Pauli dipole masses. Since the F_1 and F_2 are linear combinations of G_E and G_M, we can express the Dirac and Pauli radii in terms of the electric and magnetic dipole masses:

$$\langle r_1^2\rangle = \frac{12}{M_e} - \frac{3F_2(0)}{2M_N^2} \quad \text{and} \quad \langle r_2^2\rangle = \frac{12[1+F_2(0)]}{F_2(0)M_m} - \frac{\langle r_1^2\rangle}{F_2(0)}, \tag{3.37}$$

where $F_2(0)$ is obtained by $F_2(0) = G_M(0) - 1$.

The linear fits we have attempted so far do not take into account pion cloud effects, which are expected to be large at small pion masses. As we approach the chiral limit, we expect non-linear m_π^2 terms to dominate in the extrapolation. For the case of the isovector magnetic moment and isovector radii a calculation has been carried out within a chiral effective theory determining their quark mass dependence [48]. For the case of the

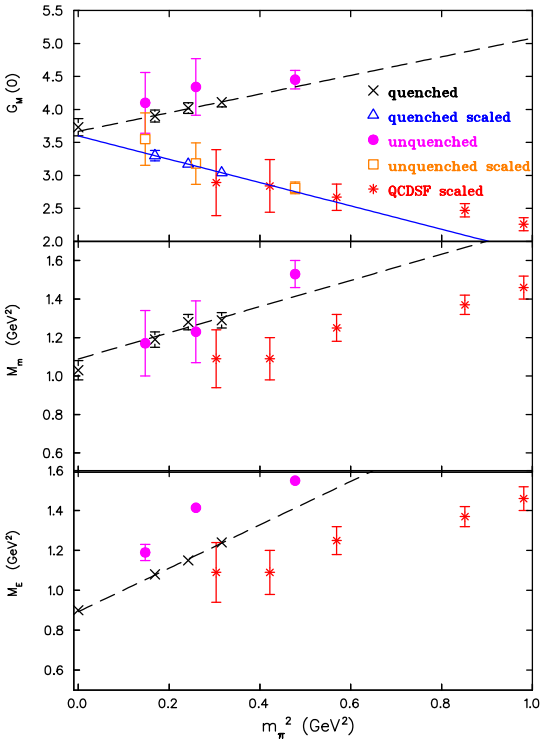

Figure 3.17: The magnetic moment (top), magnetic dipole mass (center) and electric dipole mass (bottom) as a function of the pion mass squared. The values where extracted by fitting to dipole forms. Quenched results are denoted by the crosses, unquenched by the filled circles and the asterisks denote lattice results from Ref. [28]. The points at $m_\pi^2 = 0$ where obtained by fitting the dipole forms to the extrapolated lattice results.

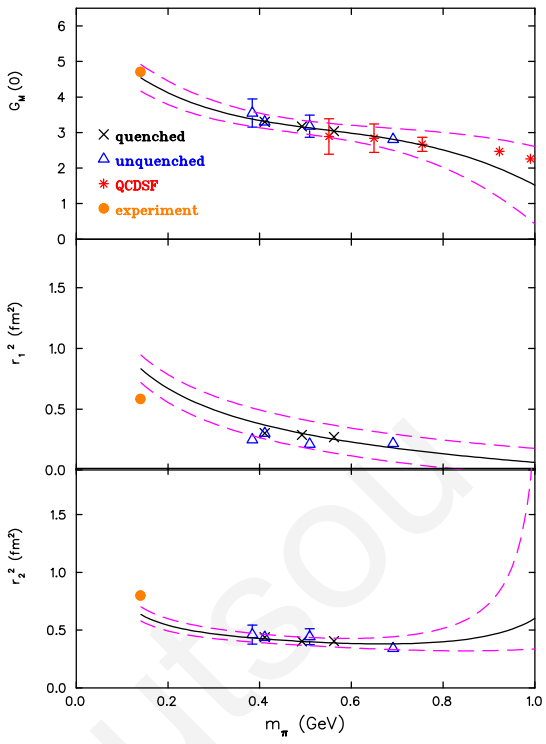

Figure 3.18: The magnetic moment (top), Dirac radius (center) and Pauli radius (bottom) as a function of the pion mass squared. Quenched results are denoted by the crosses, unquenched by the open triangles and the asterisks denote lattice results from Ref. [28]. The circles denote the experimental values.

isovector anomalous magnetic moment, this chiral effective theory gives us:

$$\begin{aligned}\kappa_{\mathrm{v}}(m_\pi) =& \kappa_{\mathrm{v}}(0) - \frac{g_A^2 m_\pi M_N}{4\pi F_\pi^2} + \frac{2c_A^2 \Delta M_N}{9\pi^2 F_\pi^2}\left[R_1(m_\pi) + \log\left(\frac{m_\pi}{2\Delta}\right)\right] \\ &- 8E_1 M_N m_\pi^2 + \frac{4c_A c_V g_A M_N m_\pi^2}{9\pi^2 F_\pi^2}\log\left(\frac{2\Delta}{\lambda}\right) + \frac{4c_A c_V g_A M_N m_\pi^3}{27\pi F_\pi^2 \Delta} \\ &- \frac{8c_A c_V g_A \Delta^2 M_N}{27\pi^2 F_\pi^2}\left[\left(1 - \frac{m_\pi^2}{\Delta^2}\right) R_1(m_\pi) + \left(1 - \frac{3m_\pi^2}{2\Delta^2}\right)\log\left(\frac{m_\pi}{2\Delta}\right)\right],\end{aligned} \tag{3.38}$$

where

$$R_1(m) = \frac{\sqrt{\Delta^2 - m^2 + i\epsilon}}{2\Delta}\log\left(\frac{\Delta + \sqrt{\Delta^2 - m^2 + i\epsilon}}{\Delta - \sqrt{\Delta^2 - m^2 + i\epsilon}}\right). \tag{3.39}$$

Δ denotes the mass splitting between the nucleon and the Δ-baryon, i.e. $\Delta = M_\Delta - M_N$. As in Ref. [48], we fix g_a, c_A, F_π, M_N and Δ to their physical values. We quote these values in Table 3.3. We then fit to the magnetic moment to obtain $\kappa_v(0)$, c_v and E_1.

We set the regularization scale to $\lambda = 0.6$ GeV, once again following Ref. [48]. For the fit we use both quenched and unquenched lattice data. The curve obtained is shown in Fig. 3.18 with the dashed line showing the error. We see that the value of the magnetic moment measured experimentally is within the error band of the fit. This reflects the fact that the linear extrapolation of G_M/G_d gave results which we saw were relatively close to the experimental data (Fig. 3.14). The values of $\kappa_v(0)$, c_v and E_1 obtained by the fit are included in Table 3.3.

Table 3.3: The first column lists the fixed parameters and the second their values at the physical pion mass. The third column gives the fitted parameters and the fourth their fitted values.

Fixed parameter	Empirical value	Fitted parameter	Fitted value
g_A	1.267	$\kappa_{\rm v}(0)$	6.08(11)
c_A	1.125	c_V	-2.75(50) GeV^{-1}
F_π	0.0924 GeV	E_1	-5.60 (5) GeV^{-3}
M_N	0.9389 GeV	B_{10}	-0.3(3) GeV^{-3}
Δ	0.2711 GeV	B_{c2}	0.61(4)

We also extrapolate the Dirac and Pauli radii. The one-loop results given in Ref. [28] read:

$$r_1^2 = -\frac{1}{(4\pi F_\pi)^2}\left[1 + 7g_A^2 + \left(10g_A^2 + 2\right)\log\left(\frac{m_\pi}{\lambda}\right)\right] - \frac{12B_{10}}{(4\pi F_\pi)^2} + \frac{c_A^2}{54\pi^2 F_\pi^2}\left[26 + 30\log\left(\frac{m_\pi}{\lambda}\right) + 30R_2(m_\pi)\right] \tag{3.40}$$

and

$$r_2^2 = \frac{1}{\kappa_{\rm v}(m_\pi)}\left[\frac{g_A^2 M_N}{8F_\pi^2\pi m_\pi} + \frac{c_A^2 M_N}{9F_\pi^2\pi^2\Delta}R_2(m_\pi) + 24M_N B_{c2}\right] \tag{3.41}$$

where

$$R_2(m) = \frac{\Delta}{2\sqrt{\Delta^2 - m^2 + i\epsilon}}\log\left(\frac{\Delta + \sqrt{\Delta^2 - m^2 + i\epsilon}}{\Delta - \sqrt{\Delta^2 - m^2 + i\epsilon}}\right). \tag{3.42}$$

For the Dirac radius we need only determine B_{10} by the fit. For r_2, we fit varying B_{c2} using $\kappa_v(m_\pi)$ with the parameters reached to in the fit of the magnetic moment. The values obtained for B_{10} and B_{c2} are included in Table 3.3. In Fig. 3.18 we show the curves obtained by these fits. We see that the fit does not follow the pion mass dependence of the lattice results for the Dirac radius, leading to an extrapolation which is outside error band compared to experiment. This is not surprising, given the insensitivity F_1 exhibited with respect to the pion mass in Fig. 3.12.

3.6 Summary of Results

In this chapter we have presented a study of the nucleon electromagnetic form factors in quenched and $N_F = 2$ Wilson lattice QCD. We have improved on a previous lattice calculation [28] by going to lighter quark masses (down to 380 MeV for unquenched) and to larger lattices ($32^3 \times 64$ with $a \simeq 0.9$ fm for the quenched case) thus allowing access to finer lattice momenta. We avoid having to compute the disconnected contribution by computing the isovector form factors. In order to make contact with experiment, we interpolate experimental results for the proton and neutron form factors at Q^2 not available in order to compute the isovector form factors at these momentum transfers. Comparing lattice data at different pion masses, we reach the conclusion that the form factors decrease with decreasing pion mass which is in the direction of the experimental data. Unquenching effects are consistently found to be small, at least at the pion masses available. We observe a linear dependence of the form factors to the pion mass squared, hence we attempt a linear extrapolation. This linear extrapolation however, does not settle discrepancies with experiment. We have also presented our results in terms of the Dirac and Pauli form factors. The linearly extrapolated Pauli form factors show good agreement with experiment which is not the case for the Dirac form factor.

A calculation is available in chiral effective theory to one-loop, which has derived the dependence of the isovector anomalous magnetic moment and of the Dirac and Pauli radii. We attempt an extrapolation to the chiral limit using this result with both quenched and unquenched data entering the fit. For the case of the anomalous magnetic moment, consistency is observed with the experimental value. This is not the case for the Dirac radius which shows little dependence on the pion mass, at least for the values considered here. Since the lattices available to us are of approximately the same lattice spacing, to assess whether finite lattice spacing effects are responsible for these discrepancies is not possible. On the other hand, the quenched lattices are large enough to exclude finite volume effects as a possible source of this discrepancy. As we go to lighter pion masses, pion cloud contributions are expected to be more important, giving rise to terms non-linear to m_π^2 in the extrapolation. A future analysis of these observables, when more resources will be available and thus allow lighter pion masses, would be able to probe this expected non-linear dependence.

Chapter 4

Nucleon to Δ Electromagnetic Transition Form Factors

In the previous chapter we presented a lattice study of the nucleon electromagnetic form factors which provide insight to phenomenologically interesting quantities such as the nucleon charge radius and its magnetic moment. In this chapter we shall investigate the shape of the nucleon which is still an open issue despite various efforts of at least two decades [49, 50]. Experimentally, one investigates the question of whether a nucleus or molecule is deformed by probing for its quadrupole moment, which indicates a non spherical charge distribution if non zero. However, the nucleon spectroscopic quadrupole moment is zero since it is a spin-1/2 state. This does not mean that the nucleon charge distribution is spherical, since it may still have an intrinsic deformation. The quadrupole moment Q of a given state measured in the laboratory frame is associated with its intrinsic quadrupole moment Q_0 (that measured in the rest frame of this state) by:

$$Q = \frac{3K^2 - J(J+1)}{(J+1)(2J+3)} Q_0, \tag{4.1}$$

where J is the spin of the state and K is its projection on the z axis in the rest frame of the state. For a nucleon ($J = 1/2$) this equation always yields $Q = 0$ irrespective of whether its intrinsic quadrupole moment (Q_0) is non zero. The Δ-baryon on the other hand, being a spin-3/2 state, can have a non zero spectroscopic quadrupole moment. Indeed, preliminary lattice results corroborate this [51] as we shall see in Chapter 6. To probe a possible deformation in the nucleon experimentally, one looks at the sub-dominant form factors of the nucleon to Δ electromagnetic transition. Namely, if these two form factors are found to be non zero, this indicates that either the nucleon or the Δ or both are deformed. In this chapter we shall present a lattice study of the nucleon to Δ electromagnetic transition form factors in unquenched lattice QCD [19].

The motivation for this measurement comes from several recent experiments where the sub-dominant form factors where measured to high accuracy particularly at low momentum transfers [52–58]. Since these electric and coulomb ($E2$ and $C2$) amplitudes are sub-dominant, high accuracy is required if we are to exclude zero. A calculation from first principles indicating non-zero values for these form factors is particularly important since experimental results require modeling. The first lattice calculation of this quantity was carried out in the quenched approximation with limited statistics [59]. Although with

errors large enough that zero could not be excluded, the form factors where found consistently negative. In Ref. [60] the calculation of the three-point function was carried out with two major improvements which we have already seen in Chapter 3. Carrying out the sequential inversion through the sink allowed the insertion of any electromagnetic current which maximized the number of statistically independent lattice measurements for a given configuration. On the other hand, an optimization of the sequential source was performed so that a given three-point function isolated a specific form factor. These improvements led to results accurate enough for a zero value to be excluded in the quenched case.

In this chapter we present a calculation of the nucleon to Δ electromagnetic transition form factors using the techniques developed using dynamical quarks. We use the same quenched and $N_F = 2$ dynamical fermions, with the parameters given in Table 3.1, as we used for the computation of the nucleon electromagnetic form factors. Additionally, we will use a Hybrid scheme where the sea quark discretization, i.e. the discretization used for the Dirac operator that enters the determinant in the Monte Carlo update, is different from the valence quark discretization, which is the discretization of the Dirac operator used for the quark propagators. In recent years, the use of such Hybrid actions has grown, since simulations of chiral fermions such as Overlap or Domain Wall are still impractically expensive, at least for large enough lattices. On the other hand, using these actions to invert the Dirac equation and compute the quark propagator is now feasible by currently available computational resources. Therefore these chiral actions are being used in the valence sector, over ensembles of already available gluon configurations generated with a different lattice discretization. For this work we use configurations generated by the MILC collaboration in the sea sector [20] and Domain Wall fermions [6, 21, 22] in the valence sector. The MILC configurations are simulated with an Asqtad improved Staggered action [61]. Staggered, or Kogut-Susskind fermions [62], address the problem of the appearance of doublers in the naive discretization of the Dirac operator by reducing them by a factor of four through a unitary transformation of the fermion fields. A remnant chiral symmetry is thus preserved in the discretized action as well as a reduced number of doublers. An advantage is that the Staggered fermions are $\mathcal{O}(a)$ improved, meaning lattice artifacts appear to $\mathcal{O}(a^2)$. The Asqtad improvement used in the MILC lattices additionally removes artifacts of order $\mathcal{O}(a^2)$. These MILC configurations are simulated using 2+1 flavors of quarks, i.e. two degenerate (up and down) quarks and a heavier strange quark.

Therefore, in this calculation, we use two discretization schemes to evaluate the transition form factors in unquenched QCD: We use dynamical Wilson fermions both in the valence and sea sector which preserves unitarity. These carry lattice artifacts linear to the lattice spacing. We also use a Hybrid scheme which is $\mathcal{O}(a)$ improved, preserves chiral symmetry on the lattice and for which we have configurations for pion masses as low as 350 MeV. The cost is that the theory is only unitary at zero lattice spacing. In Ref. [63] it is shown that the physical parameters in the mixed (or hybrid) action Lagrangian are the same up to perturbative a dependent constants. Furthermore, we shall compare results

between this Hybrid approach and results obtained using Wilson fermions and consistency between these two schemes will provide a non-trivial check of lattice artifacts.

4.1 Lattice Formulation

The nucleon to Δ electromagnetic transition matrix element is given by:

$$\langle \Delta(p',s')|j_\mu|N(p,s)\rangle = \left(-\frac{2}{3}\frac{M_N M_\Delta}{E_\Delta(p)E_N(p)}\right)^{1/2} \bar{u}_\sigma(\vec{p}',s')\mathcal{O}_{\sigma\mu}u(\vec{p},s) \tag{4.2}$$

where u_σ is a spin-3/2 spinor in the Rarita-Schwinger formalism and u a Dirac spinor. The matrix element, in terms of Sachs form factors gives [64]:

$$\mathcal{O}_{\sigma\mu} = \mathcal{G}_{M1}(q^2)\mathcal{K}^{M1}_{\sigma\mu} + \mathcal{G}_{E2}(q^2)\mathcal{K}^{E2}_{\sigma\mu} + \mathcal{G}_{C2}(q^2)\mathcal{K}^{C2}_{\sigma\mu}, \tag{4.3}$$

where the kinematic factors are given by:

$$\begin{aligned}
\mathcal{K}^{M1}_{\sigma\mu} =& -\frac{3}{(M_N+M_\Delta)^2+Q^2}\frac{M_\Delta+M_N}{2M_N} i\varepsilon_{\sigma\mu\alpha\beta}p^\alpha p'^\beta \\
\mathcal{K}^{E2}_{\sigma\mu} =& -\mathcal{K}^{M1}_{\sigma\mu} + 6\Omega^{-1}(Q^2)\frac{M_\Delta+M_N}{2M_N} 2i\gamma_5\varepsilon_{\sigma\lambda\alpha\beta}p^\alpha p'^\beta \varepsilon_\mu^{\lambda\gamma\delta}p_\gamma p'_\delta \\
\mathcal{K}^{M1}_{\sigma\mu} =& -6\Omega^{-1}(q^2)\frac{M_\Delta+M_N}{2M_N} i\gamma_5 q_\sigma[q^2(p+p')_\mu - q\cdot(p+p')q_\mu]
\end{aligned} \tag{4.4}$$

where

$$\begin{gathered}
\Omega(Q^2) = [(M_\Delta+M_N)+Q^2][(M_\Delta-M_N)^2+Q^2], \\
q^\mu = p'^\mu - p^\mu \quad \text{and} \quad Q = (iq^0,\vec{q}).
\end{gathered} \tag{4.5}$$

The Rarita-Schwinger spin sum is given by:

$$\begin{aligned}
&\sum_s u_\sigma(p,s)\bar{u}_\tau(p,s) = \\
&\qquad \frac{-i\not{p}+M_\Delta}{2M_\Delta}[\delta_{\sigma\tau} + 2p_\sigma p_\tau 2M_\Delta^2 - i\frac{p_\sigma\gamma_\tau - p_\tau\gamma_\sigma}{3M_\Delta} - \frac{1}{3}\gamma_\sigma\gamma_\tau].
\end{aligned} \tag{4.6}$$

The electric $\mathcal{G}_{E2}$ and Coulomb $\mathcal{G}_{C2}$ quadrupole form factors are sub-dominant to the magnetic dipole form factor $\mathcal{G}_{M1}$. It is customary to quote the ratios of the two sub-dominant form factors to the magnetic dipole form factor:

$$R_{EM} = -\frac{\mathcal{G}_{E2}}{\mathcal{G}_{M1}} \quad \text{and} \quad R_{SM} = -\frac{|\vec{q}|}{2M_\Delta}\frac{\mathcal{G}_{C2}}{\mathcal{G}_{M1}}, \tag{4.7}$$

also quoted as EMR and CMR respectively.

The method and techniques used to compute the matrix element on the lattice are quite similar to those explained in Chapter 3. We compute the nucleon to Δ three-point

function:

$$G^{\Delta j^\mu N}(t_2,t_1;\vec{p}',\vec{p};\Gamma)_\sigma = \sum_{\vec{x}_2,\vec{x}_1} e^{-i\vec{x}_2\cdot\vec{p}'}\langle\Omega|\Gamma^{\beta\alpha}\chi^{\Delta_\sigma}_\alpha(\vec{x}_2,t_2)j_\mu(\vec{x}_1,t_1)\bar{\chi}^N_\beta(\vec{0},0)|\Omega\rangle e^{-i\vec{x}_1\cdot(\vec{p}'-\vec{p})}, \tag{4.8}$$

where the interpolating operator for the nucleon is the same as in the previous chapter (Eq. (3.7)) as well as the projection matrices (Eq. (3.6)). The interpolating operator for the Δ is given by:

$$\chi^{\Delta_\sigma}_\alpha(x) = \frac{1}{\sqrt{3}}\varepsilon^{abc}\left\{2[u^a_\mu(x)(C\gamma_\sigma)_{\mu\nu}d^b_\nu(x)]u^c_\alpha(x) + [u^a_\mu(x)(C\gamma_\sigma)_{\mu\nu}u^b_\nu(x)]d^c_\alpha(x)\right\}. \tag{4.9}$$

We consider the conserved current for the case of Wilson fermions (Eq. (3.8)) and the local current for the case of Domain Wall fermions. The renormalization factor Z_V for the electromagnetic current in this case is known at each pion mass considered. We use the fixed-sink method, i.e. like in the case of the nucleon form factors we carry out the sequential inversion through the sink, setting the final state, the Δ in this case, to zero momentum. We construct a ratio between two-point functions and the three-point function such that unknown overlaps and exponentials cancel and look for a plateau varying the insertion time-slice. The ratio is given by:

$$\begin{aligned} R_\sigma(t_2,t_1,\vec{p}',\vec{p};\Gamma;\mu) =& \frac{G^{\Delta j^\mu N}_\sigma(t_2,t_1;\vec{p}',\vec{p};\Gamma)}{G^{\Delta\Delta}_{ii}(t_2,\vec{p}';\Gamma_4)} \\ &\times\left[\frac{G^{NN}(t_2-t_1,\vec{p};\Gamma_4)G^{\Delta\Delta}_{ii}(t_1,\vec{p}';\Gamma_4)G^{\Delta\Delta}_{ii}(t_2,\vec{p}';\Gamma_4)}{G^{\Delta\Delta}_{ii}(t_2-t_1,\vec{p}';\Gamma_4)G^{NN}(t_1,\vec{p};\Gamma_4)G^{NN}(t_2,\vec{p};\Gamma_4)}\right]^{1/2} \\ &\xrightarrow[t_1\gg 1]{t_2-t_1\gg 1}\Pi_\sigma(\vec{p}',\vec{p},\Gamma,\mu), \end{aligned} \tag{4.10}$$

where the two-point function for the Δ is given by:

$$\begin{aligned} G^{\Delta\Delta}_{\sigma\sigma}(t,\vec{p},\Gamma) =& \sum_{\vec{x}} e^{-i\vec{p}\cdot\vec{x}}\Gamma^{\beta\alpha}\langle\Omega|\chi^{\Delta_\sigma}_\alpha(\vec{x},t)\bar{\chi}^{\Delta_\sigma}_\beta(\vec{0},0)|\Omega\rangle \\ &\xrightarrow{t\gg 1}|Z_\Delta(\vec{p})|^2\frac{M_\Delta}{E_\Delta}e^{-E_\Delta(\vec{p})t}\mathrm{Tr}\left[\Gamma\left(\frac{-i\not{p}+M_\Delta}{2M_\Delta}\right)\right]\frac{2}{3}(1+\frac{p^2_\sigma}{M^2_\Delta}). \end{aligned} \tag{4.11}$$

which for the case where the final state is at rest ($\vec{p}'=0$) then the two-point function for the Δ entering the ratio is given by:

$$G^{\Delta\Delta}_{ii}(t,\vec{0},\Gamma_4)\xrightarrow{t\gg 1}|Z_\Delta(\vec{p})|^2\frac{2}{3}e^{-E_\Delta(\vec{p})t},\quad i=1,2,3. \tag{4.12}$$

There are three combinations of the current direction and projection matrix Γ that isolate

the three form factors:

$$\Pi_\sigma(\vec{0},-\vec{q};\Gamma_4;\mu) = i\mathcal{A}\varepsilon^{\sigma 4\mu j}p^j\mathcal{G}_{M1}(Q^2), \tag{4.13}$$

$$\begin{aligned}\Pi_\sigma(\vec{0},-\vec{q};\Gamma_k;\mu=j) =& \mathcal{A}\Big\{\frac{1}{2}(p_\sigma\delta_{kj}-p_k\delta_{\sigma j})\mathcal{G}_{M1}(Q^2)\\ &-\Big[\frac{3}{2}(p_\sigma\delta_{kj}+p_k\delta_{\sigma j}-\frac{3p_\sigma p_k p_j}{\vec{p}^2}\Big]\mathcal{G}_{E2}(Q^2)\\ &-\frac{E_N-M_\Delta}{2M_\Delta}p_j\left(\delta_{\sigma k}-\frac{3p_\sigma p_k}{\vec{p}^2}\right)\mathcal{G}_{C2}(Q^2)\Big\},\end{aligned} \tag{4.14}$$

$$\Pi_\sigma(\vec{0},-\vec{q};\Gamma_k;\mu=4) = i\mathcal{B}\left(\delta_{\sigma k}-\frac{3p_\sigma p_k}{\vec{p}^2}\right)\mathcal{G}_{C2}, \tag{4.15}$$

where $k,j=1,2,3$ and:

$$\begin{aligned}\mathcal{A} =& \sqrt{\frac{2}{3}}\frac{M_\Delta+M_N}{4M_N E_N}\sqrt{\frac{E_N}{E_N+M_N}},\\ \mathcal{B} =& \frac{\vec{p}^2}{2M_\Delta}\mathcal{A}.\end{aligned} \tag{4.16}$$

Each time we change the sequential source we must perform a new inversion. For the fixed sink method we shall use here, the projection matrix Γ and the Δ index σ must be chosen before the sequential inversion. Naively, Eq. (4.13), for instance, gives four sequential sources, one for each value of σ. The same is true for Eqs. (4.14) and 4.15 where we could define a sequential source for every non-zero σ-k combination. This is, of course, not optimal. We thus define linear combinations of the above three-point functions to use as sequential sources and obtain the most lattice measurements of the form factors possible for a single sequential inversion. These linear combinations are given below:

$$\begin{aligned}S_1(\vec{q};\mu) =& \sum_{\sigma=1}^{3}\Pi_\sigma(\vec{0},-\vec{q};\Gamma_4;\mu)\\ =& i\mathcal{A}\left[(p_2-p_3)\delta_{1,\mu}+(p_3-p_1)\delta_{2,\mu}+(p_1-p_2)\delta_{3,\mu}\right]\mathcal{G}_{M1},\\ S_2(\vec{q};\mu=j) =& \sum_{\sigma\neq k=1}^{3}\Pi_\sigma(\vec{0},-\vec{q};\Gamma_k;j)\\ =& -3\mathcal{A}\Big\{\left[(p_2+p_3)\delta_{1,j}+(p_3+p_1)\delta_{2,j}+(p_1+p_2)\delta_{3,j}\right]\mathcal{G}_{E2}(Q^2)\\ &-2\frac{p_j}{\vec{p}^2}(p_1p_2+p_1p_3+p_3p_2)[\mathcal{G}_{E2}(Q^2)+\frac{E_N-M_\Delta}{2M_\Delta}\mathcal{G}_{C2}]\Big\},\\ S_2(\vec{q};\mu=4) =& -\frac{i6\mathcal{B}}{\vec{p}^2}(p_1p_2+p_2p_3+p_1p_3)\mathcal{G}_{C2}(Q^2).\end{aligned} \tag{4.17}$$

We remind that μ is the direction of the current insertion and thus is not fixed when constructing the sequential source. The above combinations can thus be computed with two sequential inversions, one for S_1 and one for S_2. The measurements are analyzed by solving an over-complete set of equations, as described in the previous chapter, where all lattice momenta and currents that contribute to a given form factor at a give Q^2 value are

taken into account.

Note that $\mathcal{G}_{C2}$ cannot be extracted from S_2 for the lowest lattice momentum $\vec{q} = \frac{2\pi}{L}(1,0,0)$, since this gives zero for all kinematic factors multiplying it. In order to extract the form factor at this specific momentum we use a third combination:

$$\begin{aligned} S_3(\vec{q};\mu) =& \Pi_3(\vec{0},-\vec{q};\Gamma_3;\mu) - [\Pi_1(\vec{0},-\vec{q};\Gamma_1;\mu) + \Pi_2(\vec{0},-\vec{q};\Gamma_2;\mu)]/2 \\ =& \frac{3\mathcal{A}}{2} p_\mu \left[2\left(\delta_{\mu 3} - \frac{p_3^2}{\vec{p}^2}\right)\mathcal{G}_{E2}(Q^2) + \frac{E_N - M_\Delta}{2M_\Delta}\left(1 - 3\frac{p_3^2}{\vec{p}^2}\right)\mathcal{G}_{C2}(Q^2)\right] \\ & \text{for} \quad \mu = 1,2,3 \quad \text{and} \\ =& \frac{3i\mathcal{B}}{2}\left(1 - 3\frac{p_3^2}{\vec{p}^2}\right)\mathcal{G}_{C2}(Q^2) \quad \text{for} \quad \mu = 4. \end{aligned} \tag{4.18}$$

4.2 Lattice Parameters and Optimization

The details concerning the Wilson ensembles used in this work can be found in Table 3.1 in the previous chapter. In Table 4.1 we list the details concerning the MILC lattices we used for the Domain Wall calculation. The lattice spacing for these lattices is $a = 0.1241$ fm with a 2% error determined from heavy quark spectroscopy [65]. For initial tests we analyzed the MILC configurations taking half the lattice and setting Dirichlet boundary conditions in time. This halved the computational time of the inversion. For the lightest pion mass (~ 0.36 GeV) we have analyzed lattices at two volumes to perform checks for finite volume effects. Domain Wall fermions [6, 21, 22] preserve chiral symmetry on the lattice when the fifth dimension is infinite $L_5 \to \infty$. When L_5 is finite, the chiral symmetry breaking can be parametrized to a residual mass [66]. A criterion for setting the extent of the fifth dimension is to demand the residual mass caused by the symmetry breaking be at most an order of magnitude smaller than the Domain Wall quark mass. For the masses considered here, an extent of $L_5/a = 16$ is sufficient for this. To match the parameters of the Domain Wall calculation to those of the MILC lattices a tuning was performed [67] demanding that the lightest pseudo-scalar meson obtained by using Staggered quarks matched that using Domain Wall valence quarks.

Table 4.1: Parameters and number of gauge field configurations used for the hybrid action.

#	L_S (fm)	$(am_{\mathrm{u,d/s}})^{\mathrm{Asqtad}}$	$(am_{\mathrm{u,d}})^{\mathrm{DWF}}$	m_π (GeV)	m_π/m_ρ	m_N (GeV)	m_Δ (GeV)
Volume: $20^3\times 32$, b.c: Dirichlet							
150	2.5	0.03/0.05	0.0478	0.606(2)	0.588(7)	1.329(9)	1.662(21)
150	2.5	0.02/0.05	0.0313	0.502(4)	0.530(11)	1.255(19)	1.586(36)
Volume: $28^3\times 32$, b.c: Dirichlet							
118	3.5	0.01/0.05	0.0138	0.364(1)	0.387(7)	1.196(25)	1.561(41)
Volume: $20^3\times 64$, b.c: antiperiodic							
200	2.5	0.03/0.05	0.0478	0.594(1)	0.585(7)	1.416(20)	1.683(22)
198	2.5	0.02/0.05	0.0313	0.498(3)	0.525(8)	1.261(17)	1.589(35)
100	2.5	0.01/0.05	0.0138	0.362(5)	0.401(13)	1.139(25)	1.488(71)
Volume: $28^3\times 64$, b.c: antiperiodic							
300	3.5	0.01/0.05	0.0138	0.353(2)	0.368(8)	1.191(19)	1.533(27)

Before going on to present the results for the nucleon to Δ electromagnetic transition form factors we shall show several tests we performed. Due to the fact that the sub-dominant form factors are especially noisy, these tests will reassure that the form factors where indeed extracted reliably. We start by checking ground state dominance. As in the calculation of the previous chapter, we use Gaussian smearing of the initial and final states and HYP smearing for the gauge links. In Fig. 3.4 we tested ground state dominance for the nucleon at the smallest non-zero momentum by fitting both to a constant and by considering first excited state contribution. The two fits yielded consistent results for the effective energy for as close as four time-slices from the source.

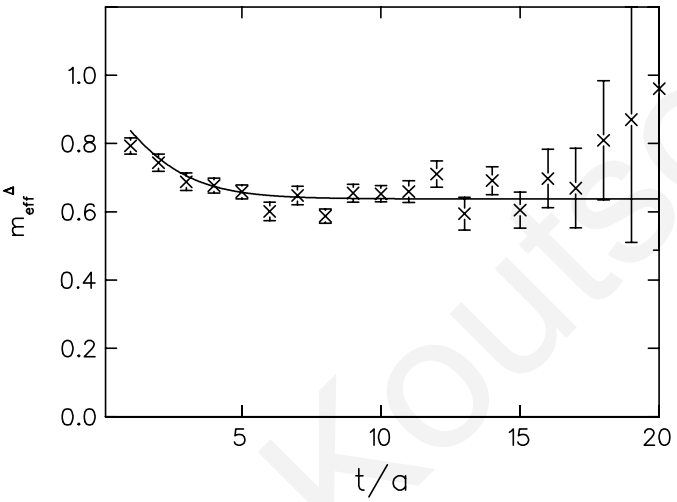

Figure 4.1: Δ-baryon effective mass plot. The dashed line is a fit to a constant while the solid line shows a fit to Eq. (3.27).

In Fig. 4.1 we show the same for the Δ-baryon. Since we set the Δ to zero momentum we only check the effective mass. The conclusion is the same, i.e. that fitting to a constant is consistent with taking into account first excited state contributions. Fitting both the nucleon and the Δ to Eq. (3.27) we can obtain r_Δ, r_N and their corresponding energy splittings δ_Δ and δ_N. We then use these values to fit to the ratio of Eq. (4.10) by using a form that includes first excited state contributions to the three-point function:

$$f(t_1) = \frac{b_0 + b_1\sqrt{r_N}\exp\left(-\delta_N t_1\right) + b_2\sqrt{r_\Delta}\exp(-\delta_\Delta(t_2-t_1))}{\sqrt{(1+r_\Delta\exp(-\delta_\Delta t_2))(1+r_N\exp(-\delta_N t_2))}}\times \sqrt{\frac{(1+r_N\exp(-\delta_N(t_2-t_1)))(1+r_\Delta\exp(-\delta_\Delta t_1))}{(1+r_\Delta\exp(-\delta_\Delta(t_2-t_1)))(1+r_N\exp(-\delta_N t_1))}}. \tag{4.19}$$

This is a three parameter fit to determine b_0, b_1 and b_2. We perform this test on the quenched lattice at two source-sink separations. This is shown in Fig. 4.2 for a single lattice momentum $\vec{q} = \frac{2\pi}{L}(0,1,0)$ for the case of $\mathcal{G}_{M1}$. As can be seen, fitting to a constant while omitting the first and last two time-slices yields a value for the ratio consistent with fitting to Eq. (4.19) where first excited state contributions are included. The left figure

corresponds to a source-sink separation of 11 time-slices compared to 13 for the right graph. The shorter source-sink separation carries smaller errors, as expected. We remind that in the actual analysis we use all lattice momenta that give the same form factor at the given Q^2 value. This is just one momentum vector of the 12 momentum vectors that, according to the source S_1 in Eq. (4.17), give $\mathcal{G}_{M1}$ at the first non-zero allowable momentum transfer.

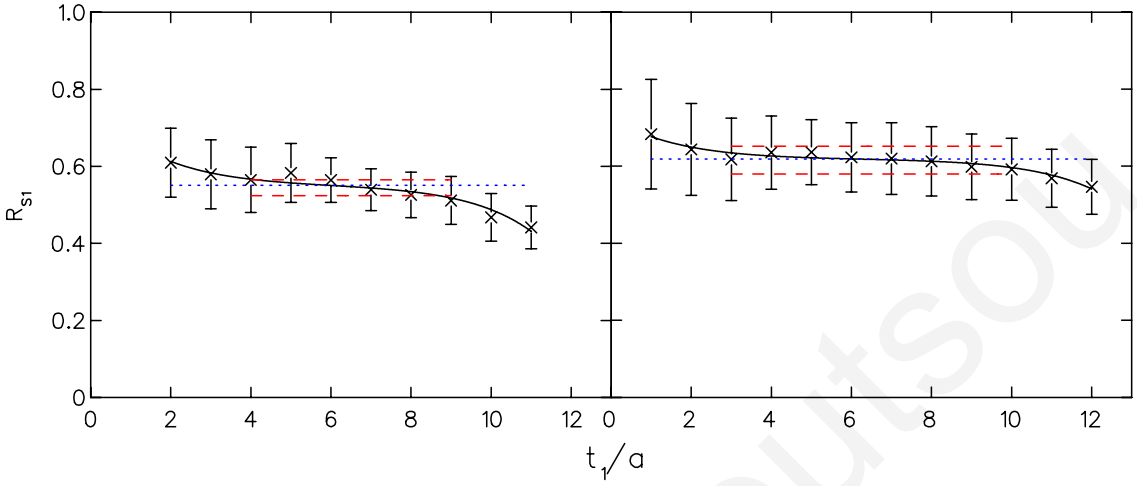

Figure 4.2: The ratio from which $\mathcal{G}_{M1}$ is extracted, for $\vec{q} = \frac{2\pi}{L}(0,1,0)$ for the quenched case. Left for sink time-slice $t_2/a = 11$ from the source and right for $t_2/a = 13$. The dotted line is a fit to a constant while the solid line shows a fit to Eq. (4.19). The dashed lines show the error band when fitting to a constant.

Since the form factors we are interested in are sub-dominant we require as accurate a determination of the three-point function as possible. Thus carefully selecting the source-sink separation is crucial for this measurement. On one hand, we need enough time between source and sink to vary the insertion time-slice and determine reliably a plateau. On the other hand, the closer the sink is to the source, the more accurate the three-point function, given the exponential decay of the signal.

In Fig. 4.3 we show the $\mathcal{G}_{M1}$ ratio for the first four lattice momenta at two different source-sink separations. For the purposes of this check we have averaged over the currents and momentum vectors that contribute to the given value of the form factor (in practice the form factor is fitted separately to each current and momentum vector in the over-constraint analysis). The conclusion is that for both these separations the form factor is consistent. Since the errors are smaller for the shorter separation, while still leaving room to vary t_1 in between, we set $t_2/a = 11$ for the quenched calculation. This corresponds to about 5.1 GeV^{-1}. Thus in the Hybrid scheme we check between a source-sink separation of 5 GeV^{-1} (or $t_2/a = 8$) and 6.3 GeV^{-1} (or $t_2/a = 10$). The comparison is shown in Fig. 4.4 for the case of the $20^3 \times 64$ lattice at $m_\pi = 0.498(2)$ GeV. As in the case of the quenched calculation, we see that the magnetic dipole form factor is consistent for both source-sink separations.

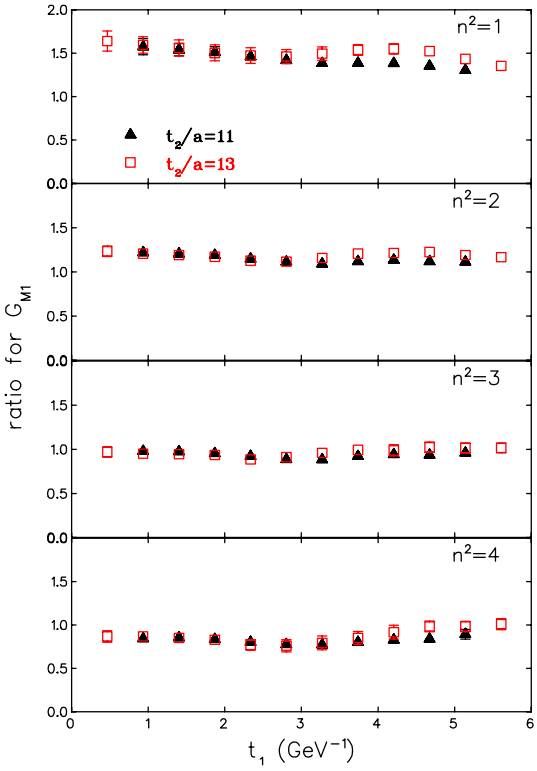

Figure 4.3: $\mathcal{G}_{M1}$ ratio in the quenched approximation for the first four lattice momenta at two different source-sink separations: $t_2/a = 11$ (triangles) and $t_2/a = 13$ (squares). The results for $t_2/a = 11$ have been shifted to the right by a time-slice so that the midpoints coincide.

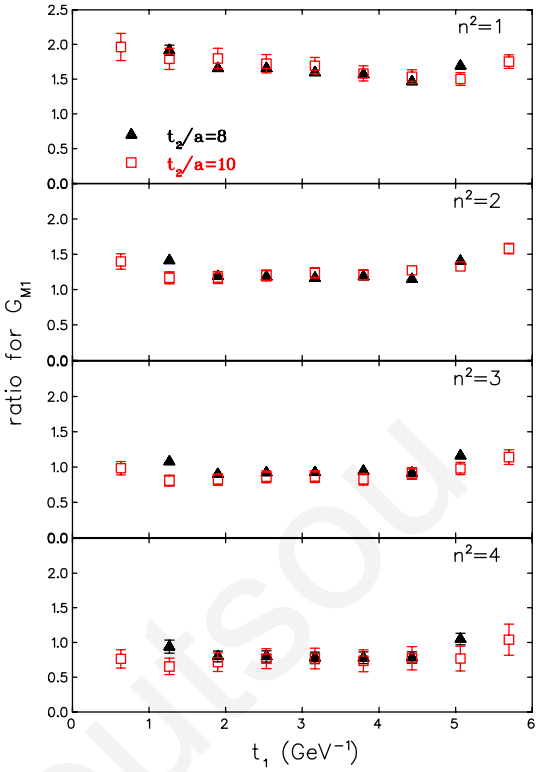

Figure 4.4: $\mathcal{G}_{M1}$ ratio computed in the Hybrid scheme for the first four lattice momenta at two different source-sink separations: $t_2/a = 0$ (triangles) and $t_2/a = 10$ (squares). The results for $t_2/a = 11$ have been shifted to the right by a time-slice so that the midpoints coincide.

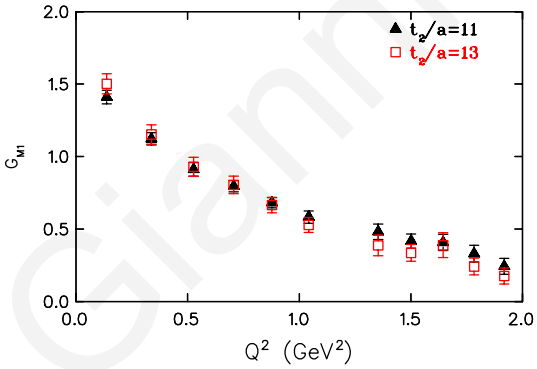

Figure 4.5: $\mathcal{G}_{M1}$ ratio in the quenched approximation at two different source-sink separations: $t_2/a = 11$ (triangles) and $t_2/a = 13$ (squares).

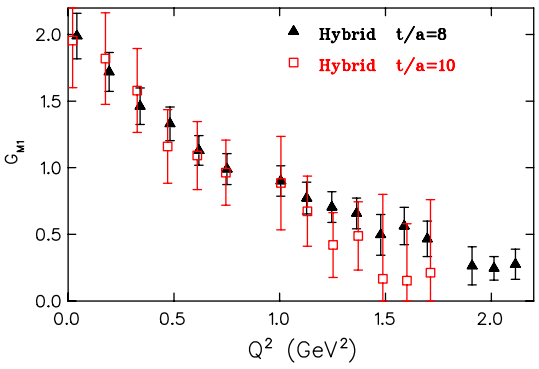

Figure 4.6: $\mathcal{G}_{M1}$ ratio computed in the Hybrid scheme at two different source-sink separations: $t_2/a = 0$ (triangles) and $t_2/a = 10$ (squares).

In Fig. 4.5 we plot the $\mathcal{G}_{M1}$ ratio after fitting to each lattice measurement separately by solving the over-complete set of equations (Eq. (3.31)) for the quenched case. This is done for both the source-sink separations as an additional consistency check. The form factor is found in agreement with both source sink separations. We do the same for the

Hybrid case in Fig. 4.6. In this case, the larger separation is much noisier compared to the shorter separation. This is on one hand due to the fact that we have used the smallest pion mass available and on the other due to the fact that the lattice spacing is larger here and thus the difference between the two source-sink separations is larger (∼0.38 fm).

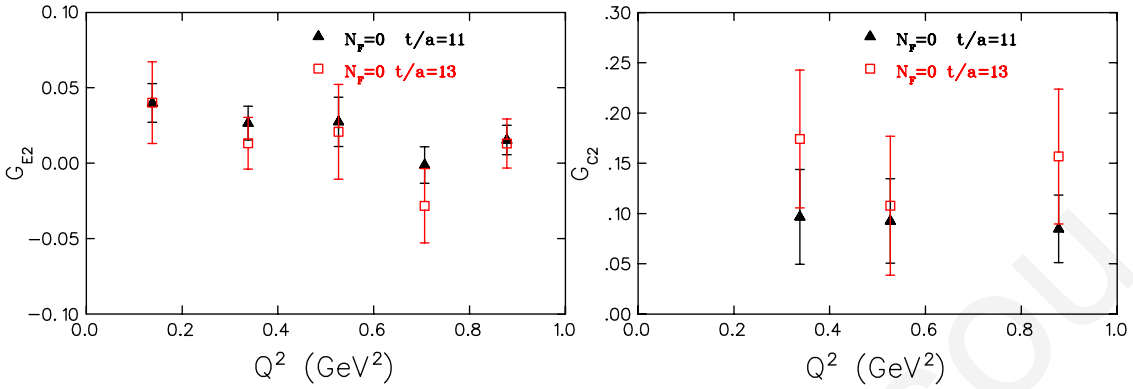

Figure 4.7: The electric quadrupole (left) and the Coulomb quadrupole (right) form factors for the quenched case at two sink-source separations: $t_2/a = 11$ (triangles) and $t_2/a = 13$ (squares).

To complement these checks we have plotted $\mathcal{G}_{E2}$ and $\mathcal{G}_{C2}$ at the two sink-source separations in Fig. 4.7. As can be seen the shorter separation yields the form factors with smaller errors and consistent with the larger separation. It is apparent from these checks that it is safe to use the shortest of the two separations in both quenched and unquenched calculations. In fact, for the lightest pion mass in the Hybrid scheme using the larger of the two separations gives results prohibitively noisy as we have seen in Fig. 4.6. Hence we fix the separation to about 5 GeV^{-1} meaning $t_2/a = 8$ for the Hybrid calculation, $t_2/a = 11$ for the quenched and $t_2/a = 12$ for the Wilson dynamical calculation.

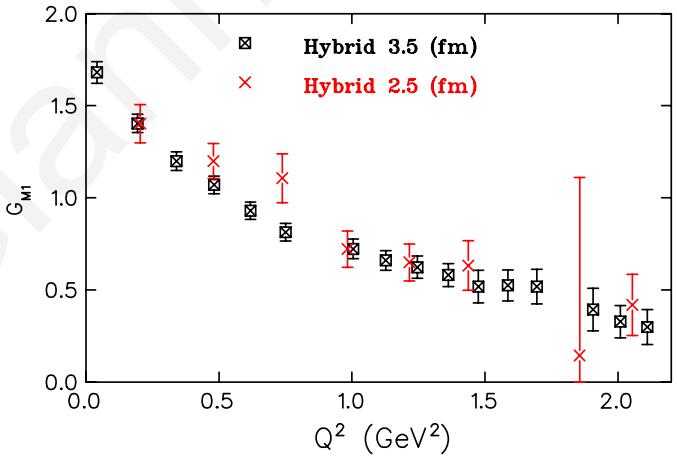

Figure 4.8: The $\mathcal{G}_{M1}$ form factor in the Hybrid scheme for a pion mass of $m_\pi \simeq 0.36$ GeV computed on a lattice of 3.5 fm spatial extent (crosses) and 2.5 fm spatial extent (crossed squares).

As a final test we use the two lattices we have that are different in size but at equal pion

mass to check for the effect the finite volume may have on the measurement. The quantity $L_s m_\pi$, L_s being the spatial extent of the lattice, is typically used to gauge finite volume effects. These two lattices, quoted in Table 4.1, are of pion mass $m_\pi \simeq 0.36$ GeV. The larger of the two has a side of 3.5 fm and thus $L_s m_\pi = 6.4$ while the other a side of 2.5 fm or $L_s m_\pi = 4.6$. For both these lattices we have computed the $\mathcal{G}_{M1}$ form factor for 100 configurations. We compare the results in Fig. 4.8. We see that the smaller lattice carries larger statistical errors but is consistent with the large lattice. Hence any volume effects affecting the measurement are within statistical errors. All the lattices we use in this work are of $L_s m_\pi \geq 4.5$ with the exception of the lightest Wilson $N_F = 2$ lattice. Hence we expect finite volume effects to be within statistical errors for these configurations. Since for the lightest mass of the Wilson $N_F = 2$ simulation there is only one lattice volume available, we cannot assess in the same way finite volume effects for this case.

4.3 Lattice Results

In Fig. 4.3 we show the results for the dominant magnetic dipole form factor at all three pion masses for each lattice action used. For the hybrid we show results using the lattices with the large time extent ($20^3 \times 64$ for the two heaviest pion masses and $28^3 \times 64$ for the lightest). We see that the value of the form factor decreases with the pion mass. For the case of the quenched calculation, the dependence on the pion mass is weaker as in the case of the nucleon form factors we have seen in the previous chapter. Both fits to an exponential form ($f_0 \exp(Q^2/M^2)$) and to a dipole form ($g_0/(1 + Q^2/M^2)$) describe the data well as can be seen by the dashed and the dotted line respectively in Fig. 4.3 where fits to the lightest of the pion masses for each simulation where performed. We find a dipole mass of $M = 1.30(3)$ GeV compared to 0.78 GeV which is found experimentally.

In Fig. 4.10 we plot the same data only grouped by similar pion mass. From this figure we see that the hybrid and Wilson dynamical results are in agreement which indicates that lattice artifacts are under control since these two actions exhibit different finite lattice spacing effects. Another conclusion is that unquenching effects are small for this quantity, at least at the pion masses considered here, since quenched and unquenched results are found consistent.

In Fig. 4.11 we plot the lightest pion mass of the hybrid scheme against experimental results. There are two models routinely used to extract the magnetic dipole form factor from experimental data; the phenomenological model MAID [76] and the pion cloud dynamical model referred to as the SL model [77]. In Fig. 4.11 the experimental results are obtained by the MAID model. As can be seen the lattice results are higher for momentum transfers larger than around 0.5 GeV. This is in fact expected since Fig. 4.3 shows that the $\mathcal{G}_{M1}$ decreases with decreasing pion mass hence we expect these points to come closer to experiment as we approach the chiral limit. On the other hand, the two points corresponding to the two smallest momentum transfers are lower than experiment. To assess the error due to the choice of the experimental model we show in Fig. 4.12 the lattice

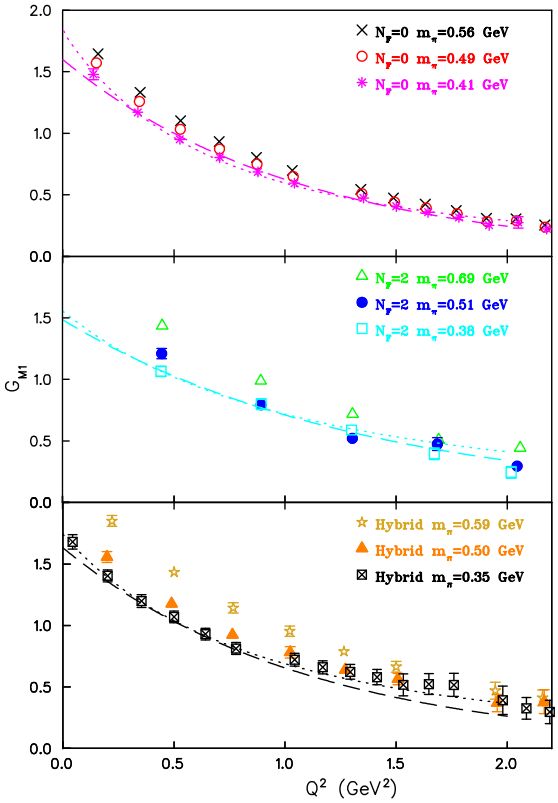

Figure 4.9: $\mathcal{G}_{M1}$ as a function of Q^2 for all m_π available grouped by discretization scheme. In the upper graph we plot the Wilson quenched results at $m_\pi = 0.56$ GeV (crosses), $m_\pi = 0.49$ GeV (open circles) and $m_\pi = 0.41$ GeV (asterisks). In the middle graph we plot the Wilson unquenched results at $m_\pi = 0.69$ GeV (open triangles), $m_\pi = 0.51$ GeV (filled circles) and $m_\pi = 0.38$ GeV (open squares). In the lower graph we plot the results from the Hybrid scheme at $m_\pi = 0.59$ GeV (open stars), $m_\pi = 0.50$ GeV (filled triangles) and $m_\pi = 0.35$ GeV (crossed boxes). The dotted lines show fits to a dipole while the dashed lines show fits to an exponential all for the lightest pion mass of each simulation.

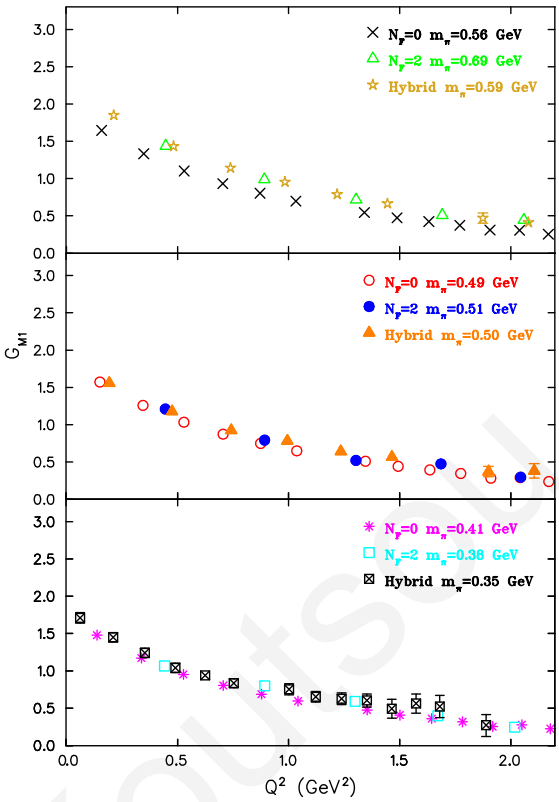

Figure 4.10: $\mathcal{G}_{M1}$ as a function of Q^2 grouped by similar pion mass for all simulations. In the upper graph we show the heaviest pion mass, in the middle the intermediate pion mass and in the lower graph the lightest pion mass of all three lattice actions used. The notation is the same as that of Fig. 4.3.

data compared to the experimental data extracted using MAID and the SL model. As can be seen the two models yield results outside statistical error bars. Given this systematic error, the lattice result for the second largest momentum transfer is consistent with experiment and hence only the smallest momentum transfer is lower. Unfortunately, at the moment, we cannot conclude whether this is expected within chiral effective theory, since such a calculation has not been carried out for these quantities. One point we can make though, according to Ref. [78], is that pion cloud contributions to the EMR and CMR ratios are expected to be larger at low momentum transfers. Whether this accounts for the discrepancy of this lowest momentum transfer or not cannot be said at this moment

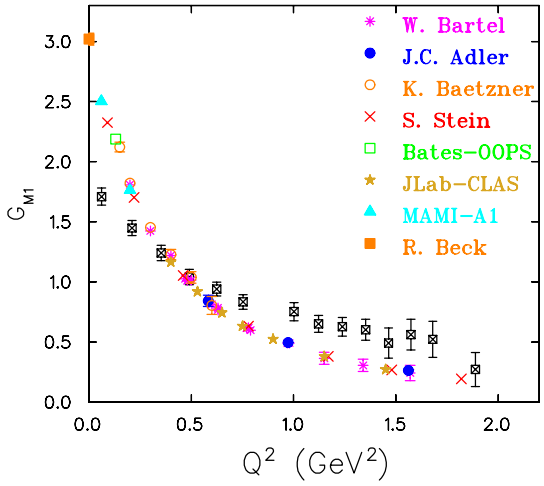

Figure 4.11: The magnetic dipole form factor as a function of the momentum transfer Q^2 at the smallest pion mass of the Hybrid calculation (crossed boxes) compared to experimental results. The asterisks are from Ref. [68], the filled circles from Ref. [69], the open circles from Ref. [70], the crosses from Ref. [71] the open squares from Ref. [53], the stars from Ref. [55, 72, 73], the filled triangles from Ref. [58, 74] and the filled square from Ref. [75].

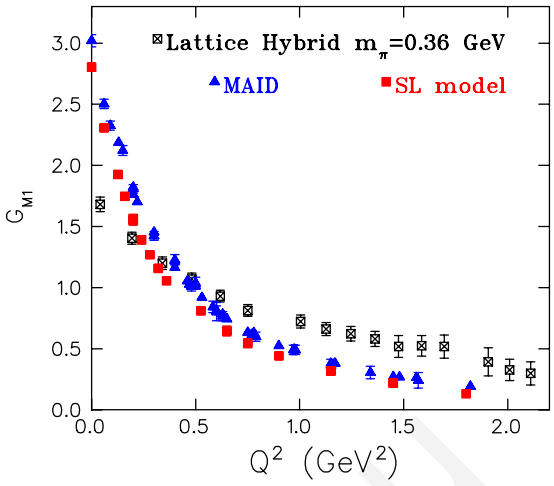

Figure 4.12: The magnetic dipole form factor as a function of the momentum transfer Q^2 at the smallest pion mass of the Hybrid calculation (crossed boxes) compared to experimental results obtained using two models: MAID (triangles) and the SL model (filled squares).

though.

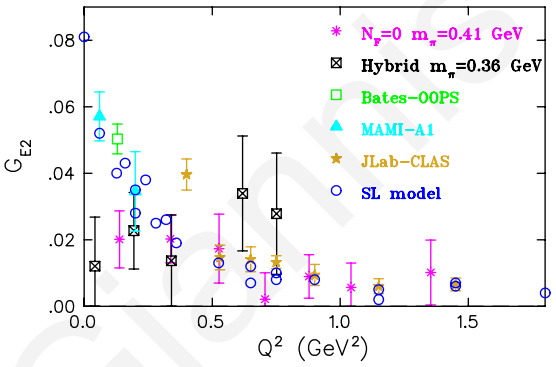

Figure 4.13: The electric quadrupole form factor for the lightest pion mass in both the quenched (filled circles) and the hybrid approach (crossed boxes). The filled triangles are from Ref. [56,57], the open squares from Ref. [79] and the stars from Ref. [55]. The open circles are results obtained using the SL model from Ref. [77] where no errors where quoted.

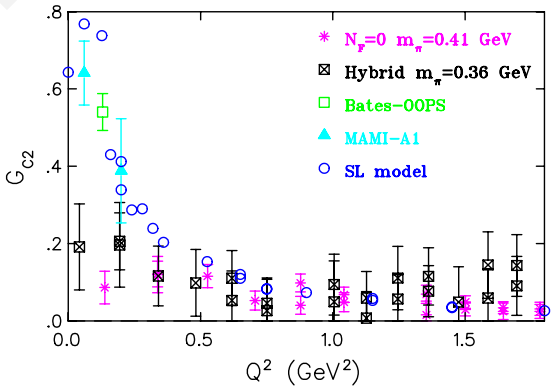

Figure 4.14: The Coulomb quadrupole form factor for the lightest pion mass in both the quenched (filled circles) and the hybrid approach (crossed boxes). The notation is the same as that of Fig. 4.13.

The sub-dominant form factors $\mathcal{G}_{E2}$ and $\mathcal{G}_{C2}$ are shown in Figs. 4.13 and 4.14 respectively. Although these form factors carry large errors, we see that the lattice results are consistent with the experimental data excluding the lowest momentum transfer available.

As in the case of the $\mathcal{G}_{M1}$, this first point is lower than experiment in both quenched and the hybrid approach. For the case of the $\mathcal{G}_{C2}$ form factor of the lightest pion mass in the hybrid scheme, we have additionally used the combination S_3 (Eq. (4.18)) for the sequential source in order to obtain this form factor at the smallest available momentum transfer and improve the signal obtained using S_2 for other momentum transfers. We note here that all numerical results used for the graphs presented in this chapter can be found tabulated in Appendix C.

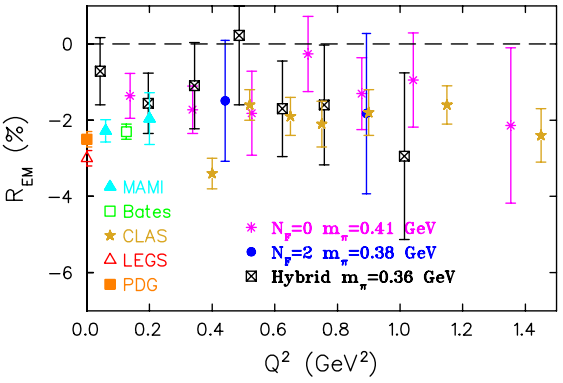

Figure 4.15: The ratio of the electric quadrupole form factor to the magnetic dipole at the lightest pion mass for the quenched (asterisks), Wilson dynamical (filled circles) and hybrid (crossed boxes) calculations compared to experiment. The filled triangles are from Ref. [56, 57], the open squares from Ref. [79], the stars from Ref. [55], the open triangles from Ref. [52] and the filled squares from Ref. [80]. The MAID model was used for the extraction of these experimental results.

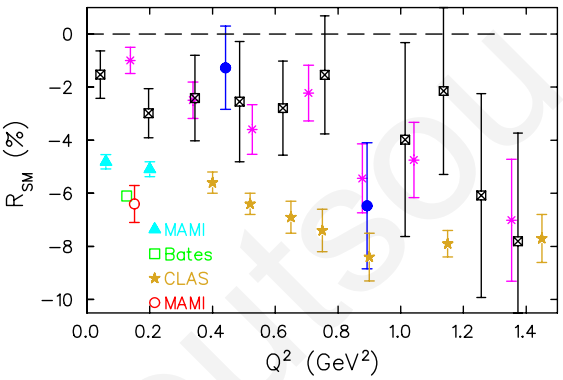

Figure 4.16: The ratio of the Coulomb quadrupole form factor to the magnetic dipole at the lightest pion mass of all three simulations compared to experiment. The notation is the same as that of Fig. 4.15.

In order to compare with experiment, in Figs. 4.15 and 4.16 we show the ratios EMR and CMR of the sub-dominant to the dominant form factor. An additional advantage of plotting ratios is that some systematic sources of error may cancel. For the case of the EMR we see agreement between quenched and the hybrid approach as well as a noisy but consistently negative signal. For the CMR the quenched results are clearly negative and non-zero but are smaller in amplitude than the experimental results. The fact that the hybrid approach at the lowest two momentum transfer yields a CMR ratio closer to the experiment is an indication that unquenching effects are more profound for this quantity. A study in chiral perturbation theory [78] has shown that for this ratio pion cloud contributions become significant as $Q^2 \to 0$. A calculation at smaller pion masses with improved statistics will enable an investigation on whether this unquenching effect is due to the pion cloud. At the moment such a computation is impractical, due to the massive computational resources chiral fermions require.

4.3.1 Summary of Results

In this chapter we have presented lattice results for the nucleon to Δ electromagnetic transition form factors. The two sub-dominant form factors of this transition, the electric and Coulomb quadrupole form factors, are experimentally interesting since they reveal information on the nucleon/Δ system deformation; if they are non-zero this means either the nucleon or the Δ-baryon or both are non-spherical. We have calculated these form factors using a hybrid action with Asqtad improved Staggered fermions in the sea sector and Domain Wall fermions in the valence sector. We have additionally performed the calculation in Wilson $N_F = 2$ and Wilson quenched lattice QCD. For the dominant form factor – the magnetic dipole $\mathcal{G}_{M1}$ – we find consistency between the three lattice discretization schemes. This means that pion cloud contributions to this particular quantity are small, since in the quenched approximation quark pair creation from the vacuum is not allowed. Furthermore, the consistency between Wilson $N_F = 2$ and the Hybrid calculation indicates that discretization errors are smaller than statistical errors since the two actions carry lattice artifacts to different order of the lattice spacing.

Despite these reassuring findings we see a discrepancy between lattice results and experimental results for the magnetic dipole form factor. The trend exhibited by the lattice data when reducing the pion mass is that the form factor decreases. This brings all but the point at the smallest momentum transfer of the large 28^3 MILC lattice closer to experiment. We have performed the calculation on lattices of a different size but same pion mass and found that results are consistent thus eliminating finite volume effects as the source of discrepancy for this lowest momentum transfer. Therefore this disagreement is most likely due to the range of pion masses we have considered, meaning an analysis at lower pion masses is needed to assess the source of this discrepancy. At the moment a chiral extrapolation of this quantity is unavailable, although a study has shown that pion cloud contributions are expected to be large.

For the case of the sub-dominant form factors the conclusions are similar. In this case, the systematic error carried by the experimental results is relatively larger due to the smallness of the amplitude of these quantities. We compare the ratios of the sub-dominant to the dominant form factors as this is the usual way these form factors are presented. Calculating ratios of these quantities may also cancel some systematics. The EMR is found consistent with experiment which is negative and non-zero. The CMR is also found negative and non zero albeit it is smaller in amplitude than what is found experimentally. This work has shown however, that the hybrid result is closer to experiment than the quenched, indicating that pion cloud contributions may be important for this specific quantity at these low momentum transfers. A future study, when more computational resources will be available, could go to pion masses as low as 300 MeV thus shedding light on the significance of the pion cloud.

Chapter 5

Axial Nucleon and Nucleon to Δ Transition Form Factors

In Chapters 3 and 4 we presented a study of the nucleon and nucleon to Δ electromagnetic matrix elements by computing the corresponding form factors. In this chapter we shall extend this study to weak matrix elements by calculating the axial nucleon form factors and the nucleon to Δ axial transition form factors. We shall additionally calculate the pion-nucleon form factor, $G_{\pi NN}$, and the pion-nucleon-Δ form factor, $G_{\pi N\Delta}$ [81].

The nucleon coupled to an axial current is parametrized in terms of two form factors: the nucleon axial form factor, G_A, and the induced pseudo-scalar form factor, G_p. Unlike the electromagnetic form factors studied so far, these quantities are less well known, mainly due to the fact that their experimental measurement is more difficult. An exception is the axial charge of the nucleon $g_A = G_A(0)$ which can be measured precisely from β-decay. Results from neutrino scattering [82] and pion electroproduction experiments [83,84] have measured its q^2 dependence. The pseudo-scalar induced form factor G_p is less well known. The main source of information concerning experimental measurements of this quantity is via muon capture and radiative muon capture, found in Ref. [85].

Even less studied are the nucleon to Δ axial transition form factors. The nucleon to Δ axial transition is parametrized in terms of four form factors [86]. The two dominant, analogous to G_A and G_p are C_5^A and C_6^A respectively, while the two sub-dominant are denoted by G_3^A and G_4^A. We shall focus on the calculation of the two dominant form factors in this chapter. Experimentally, these form factors have been evaluated via neutrino interactions in hydrogen and deutrium and can be found in Ref. [87].

These quantities are equally not well known on the lattice. As is the case with experimental measurements, there have been several lattice measurements of the axial charge g_A [88–90]. However, apart from an early lattice calculation published in 1995 [91] which used relatively large pion masses in the quenched approximation, only recently have lattice studies of the q^2 dependence of these matrix elements become available [67, 92].

In addition to the form factors noted above, we shall present a calculation of the pion-nucleon form factor, $G_{\pi NN}$, and the pion-nucleon-Δ form factor, $G_{\pi N\Delta}$. Calculation of these quantities requires knowledge of the renormalized quark mass which we shall evaluate using the axial Ward-Takahashi identity (AWI). The nucleon axial form factors and the pion-nucleon form factor are associated with each other via the diagonal Goldberger-Treiman relations. Similarly the axial nucleon to Δ transition form factors are associated

with the pion-nucleon-Δ form factor via the off diagonal Goldberger-Treiman relation. This calculation will provide a check of these relations from first principles.

As we shall show explicitly in the next section, the computational effort for extracting these quantities is minimal since we can use the same sequential propagators used in Chapters 3 and 4. This is an advantage of the fixed sink method; that we can insert any operator without any new inversions. We use the Wilson N_F=2 configurations and Wilson quenched configurations given in Table 3.1 for the calculation of the nucleon axial and pion-nucleon form factors. In addition to these configurations, we use the hybrid scheme with the configurations listed in Table 4.1 for the nucleon to Δ transition form factors.

5.1 Lattice Formulation

The axial and pseudo-scalar currents used are given by:

$$A^a_\mu(x) = \bar{\psi}(x)\gamma_\mu\gamma_5\frac{\tau^a}{2}\psi(x) \quad \text{and} \quad P^a(x) = \bar{\psi}(x)\gamma_5\frac{\tau^a}{2}\psi(x) \tag{5.1}$$

respectively. $\psi(x)$ is the isospin doublet with components the up and down quarks which we assume to be degenerate. The index a acts on flavor space and τ^a are the three Pauli matrices.

5.1.1 Matrix Elements

For the calculation carried out here, we specifically consider $a = 3$, i.e. A^3_μ as the axial current. The nucleon axial matrix element is given by:

$$\langle N(p',s')|A^3_\mu|N(p,s)\rangle = i\left(\frac{M_N^2}{E_N(p')E_N(p)}\right)^{1/2}\bar{u}(p',s')\mathcal{O}_\mu\frac{\tau^3}{2}u(p,s), \tag{5.2}$$

where:

$$\mathcal{O}_\mu = G_A(q^2)\gamma_\mu\gamma_5 + \frac{q_\mu\gamma_5}{2M_N}G_p(q^2). \tag{5.3}$$

p' (s') and p (s) are the momenta (spins) of the final and initial states respectively and $q^\mu = p'^\mu - p^\mu$ is the momentum transfer. The nucleon to Δ axial transition form factors are given by:

$$\langle \Delta(p',s')|A^3_\mu|N(p,s)\rangle = i\sqrt{\frac{2}{3}}\left(\frac{M_N M_\Delta}{E_\Delta(p')E_N(p)}\right)^{1/2}\bar{v}_\sigma(p',s')\mathcal{O}_{\sigma\mu}u(p,s), \tag{5.4}$$

where:

$$\mathcal{O}_{\sigma\mu} = \left(\frac{C_3^A(q^2)}{M_N}\gamma^\nu + \frac{C_4^A(q^2)}{M_N^2}p'^\nu\right)(g_{\sigma\mu}g_{\rho\nu} - g_{\sigma\rho}g_{\mu\nu})q^\rho + C_5^A(q^2)g_{\sigma\mu} + \frac{C_6^A(q^2)}{M_N^2}q_\sigma q_\mu. \tag{5.5}$$

u is a Dirac spinor denoting the nucleon while v denotes the Δ^+ spinor in the Rarita-Schwinger formalism.

For the pseudo-scalar form factors we need knowledge of the pion decay constant f_π and the renormalized quark mass m_q. On the lattice we can use the relation:

$$\langle \Omega | A_\mu^a(0) | \pi^b(p) \rangle = i f_\pi p_\mu \delta^{ab} \tag{5.6}$$

which couples the pion to the axial current in order calculate f_π from a two-point function. For the calculation of the renormalized quark mass we use the axial Ward-Takahashi identity which reads:

$$\partial^\mu A_\mu^a(x) = 2 m_q P^a(x). \tag{5.7}$$

By taking the expectation value of this relation between the vacuum and a zero momentum pion state we have:

$$m_q = \frac{\langle \Omega | A_0^a | \pi^a(0) \rangle}{2 \langle \Omega | P^a | \pi^a(0) \rangle}. \tag{5.8}$$

In order to define the form factors $G_{\pi NN}$ and $G_{\pi N\Delta}$ in terms of matrix elements of the pseudo-scalar current we must first relate the pseudo-scalar current to the pion field. The divergence of the axial current yields:

$$\partial^\mu A_\mu^a(x) = f_\pi m_\pi^2 \pi^a(x), \tag{5.9}$$

where π^a is a component of the isospin triplet pion field. This relation is known as the partially conserved axial current (PCAC) hypothesis. Assuming PCAC, along with Eq. (5.7), we have:

$$\pi^a(x) = \frac{2 m_q P^a(x)}{f_\pi m_\pi^2}. \tag{5.10}$$

We can now define the pion-nucleon form factor via:

$$2 m_q \langle N(p', s') | P^3 | N(p, s) \rangle = i \left(\frac{M_N^2}{E_N(p') E_N(p)} \right)^{1/2} \frac{f_\pi m_\pi^2 G_{\pi NN}(q^2)}{m_\pi^2 - q^2} \bar{u}(p', s') \gamma_5 \frac{\tau^3}{2} u(p, s) \tag{5.11}$$

and similarly the pion-nucleon-Δ form factor via:

$$2 m_q \langle \Delta(p', s') | P^3 | N(p, s) \rangle = i \sqrt{\frac{2}{3}} \left(\frac{M_N M_\Delta}{E_\Delta(p') E_N(p)} \right)^{1/2} \frac{f_\pi m_\pi^2 G_{\pi N\Delta}(q^2)}{m_\pi^2 - q^2} \bar{v}_\sigma(p', s') \frac{q_\sigma}{2 M_N} u(p, s). \tag{5.12}$$

From the definitions of these form factors, the strong couplings $g_{\pi NN}$ and $g_{\pi N\Delta}$ are given by $g_{\pi NN} = G_{\pi NN}(0)$ and $g_{\pi N\Delta} = G_{\pi N\Delta}(0)$ respectively.

5.1.2 Goldberger-Treiman Relations

The PCAC hypothesis relates the axial form factors with the pseudo-scalar form factors. These relations are known as the Goldberger-Treiman relations (GTR). The diagonal GTR associates the axial nucleon form factors with $G_{\pi NN}$:

$$G_A(q^2) + \frac{q^2}{4M_N^2} G_p(q^2) = \frac{1}{2M_N} \frac{2G_{\pi NN}(q^2) f_\pi m_\pi^2}{m_\pi^2 - q^2}, \tag{5.13}$$

while the off diagonal GTR associates the axial nucleon to Δ transition form factors with $G_{\pi N\Delta}$:

$$C_5^A(q^2) + \frac{q^2}{M_N^2} C_6^A(q^2) = \frac{1}{2M_N} \frac{G_{\pi N\Delta}(q^2) f_\pi m_\pi^2}{m_\pi^2 - q^2}. \tag{5.14}$$

Assuming pion pole dominance for the induced pseudo-scalar nucleon form factor $G_p(q^2)$ and for $C_6^A(q^2)$ we have:

$$\begin{aligned} \frac{1}{2M_N} G_p(q^2) \simeq & \frac{2G_{\pi NN}(q^2) f_\pi}{m_\pi^2 - q^2} \\ \frac{1}{M_N} C_6^A(q^2) \simeq & \frac{1}{2} \frac{G_{\pi N\Delta}(q^2) f_\pi}{m_\pi^2 - q^2} \end{aligned} \tag{5.15}$$

Using these relations and Eqs. (5.13) and (5.14) we obtain the simplified Goldberger-Treiman relations:

$$\begin{aligned} f_\pi G_{\pi NN}(q^2) = & M_N G_A(q^2) \\ f_\pi G_{\pi N\Delta}(q^2) = & 2M_N C_5^A(q^2). \end{aligned} \tag{5.16}$$

5.1.3 Three-Point Functions

The methodology used to extract the form factors from the lattice is the same as that used in Chapters 3 and 4. For the nucleon axial form factors we compute the three-point function:

$$\begin{aligned} G^{NA_\mu^3 N}(t_2, t_1; \vec{p}', \vec{p}; \Gamma) = & \\ \sum_{\vec{x}_2, \vec{x}_1} e^{-i\vec{x}_2 \cdot \vec{p}'} \langle \Omega | \Gamma^{\beta\alpha} \chi_\alpha^N(\vec{x}_2, t_2) A_\mu^3(\vec{x}_1, t_1) \bar{\chi}_\beta^N(\vec{0}, 0) | \Omega \rangle e^{-i\vec{x}_1 \cdot (\vec{p}' - \vec{p})}, & \end{aligned} \tag{5.17}$$

where the interpolating operator for the nucleon, χ^N, is given by Eq. (3.7) and the projection matrices, Γ, are given in Eq. (3.6). We divide the three-point function with a combination of two-point functions to cancel unknown overlaps and exponentials and look

for a plateau in the large time limit:

$$\begin{aligned} R^A(t_2,t_1,\vec{p}',\vec{p};\Gamma;\mu) =& \frac{G^{NA^3_\mu N}(t_2,t_1;\vec{p}',\vec{p};\Gamma)}{G^{NN}(t_2,\vec{p}';\Gamma_4)} \\ &\times \left[\frac{G^{NN}(t_2-t_1,\vec{p};\Gamma_4)G^{NN}(t_1,\vec{p}';\Gamma_4)G^{NN}(t_2,\vec{p}';\Gamma_4)}{G^{NN}(t_2-t_1,\vec{p}';\Gamma_4)G^{NN}(t_1,\vec{p};\Gamma_4)G^{NN}(t_2,\vec{p};\Gamma_4)}\right]^{1/2} \\ &\xrightarrow[t_1\gg 1]{t_2-t_1\gg 1} \Pi^A(\vec{p}',\vec{p},\Gamma,\mu). \end{aligned} \tag{5.18}$$

We use the same kinematics as in Chapters 3 and 4, namely we consider the reference frame where the final state, with momentum $\vec{p}'$, is at rest. The momentum transfer in this frame is $\vec{q} = -\vec{p}$, where $\vec{p}$ is the momentum of the initial state. We take $Q^2 = -q^2 > 0$, Q^2 being the Euclidean momentum transfer squared. Given these kinematics, the ratio in Eq. (5.18), after excited states are suppressed by the large time extents, is given by:

$$\Pi^A(\vec{0},-\vec{q},\Gamma_k;\mu) = i\frac{\mathcal{C}}{4M_N}\left[\left[(E_N(\vec{q})+M_N)\delta_{k,\mu}+q_k\delta_{\mu 4}\right]G_A(Q^2) - \frac{q_\mu q_k}{2M_N}G_p(Q^2)\right] \tag{5.19}$$

where

$$\mathcal{C} = \left(\frac{2M_N^2}{E_N(\vec{q})\left[E_N(\vec{q})+M_N\right]}\right)^{1/2}, \quad k=1,2,3$$

and $\Pi^A(\vec{0},-\vec{q},\Gamma_4;\mu) = 0$. The summation over the sink spatial index, $\vec{x}_2$, is carried out using a sequential inversion through the sink, as in the case of the electromagnetic form factors seen in Chapters 3 and 4. This requires fixing the projection matrix Γ before inverting. The index μ of the axial current and the momentum transfer $\vec{q}$ can be varied after the sequential inversion. We take a linear combination of the three-point function in Eq. (5.19) to increase statistics. This defines a sequential source which when inverted and traced with the forward propagator yields the three-point function from a maximal set of lattice measurements. The linear combination we take is given by:

$$\begin{aligned} S^A(\vec{q};j) =& \sum_{k=1}^{3}\Pi^A(\vec{0},-\vec{q},\Gamma_k,\mu=j) \\ =& i\frac{\mathcal{C}}{4M_N}\left[(E_N(\vec{q})+M_N)\,G_A(Q^2) - (q_1+q_2+q_3)\frac{q_j}{2M_N}G_p(Q^2)\right], \end{aligned} \tag{5.20}$$

where $j = 1,2,3$. Note that this is the same linear combination as in Eq. (3.23) used in the calculation of the nucleon electromagnetic form factors. Since with the fixed sink method the sequential source is independent of the operator inserted, we can use the same sequential propagators as those used for the calculation in Chapter 3. We need only recombine the sequential propagator with the forward propagator using the axial current instead of the electromagnetic current, and solve the over-complete set of equations as described in Chapter 3 in Eqs. (3.29)–(3.33) where the kinematics are now read off Eq. (5.20).

The pion-nucleon form factor $G_{\pi NN}$ is obtained in an identical manner, only the axial

current A^3_μ is now replaced with the pseudo-scalar current P^3. The ratio $R^P(t_2, t_1, \vec{p}', \vec{p}; \Gamma; \mu)$ is obtained by taking the ratio of the three-point function $G^{NP^3N}(t_2, t_1; \vec{p}', \vec{p}; \Gamma)$ with the combination of two-point functions given in Eq. (5.18). In the large $t_2 - t_1$ and t_1 limit the ratio becomes independent of time. In the reference frame where the final state is at rest we have:

$$\Pi^P(\vec{0}, -\vec{q}; \Gamma_k; \gamma_5) = \mathcal{C}\frac{q_k}{2M_N}\frac{f_\pi m_\pi^2}{2m_q(m_\pi^2 + Q^2)}G_{\pi NN}(Q^2) \tag{5.21}$$

and $\Pi^P(\vec{0}, -\vec{q}; \Gamma_4; \gamma_5) = 0$. We use the same linear combination as in the case of the axial current:

$$S^P(\vec{q}; \gamma_5) = \sum_{k=1}^{3}\Pi^P(\vec{0}, -\vec{q}; \Gamma_k; \gamma_5) = \mathcal{C}\frac{q_1 + q_2 + q_3}{2M_N}\frac{f_\pi m_\pi^2}{2m_q(m_\pi^2 + Q^2)}G_{\pi NN}(Q^2), \tag{5.22}$$

which allows us to use the same sequential propagators as those used to compute the axial form factors. We shall explain how we extract the renormalized quark mass, m_q, and the pion decay constant, f_π, in the next subsection.

To calculate the nucleon to Δ axial transition form factors we use the three-point function:

$$\begin{aligned} G_\sigma^{\Delta A^3_\mu N}(t_2, t_1; \vec{p}', \vec{p}; \Gamma) = & \\ \sum_{\vec{x}_2, \vec{x}_1} e^{-i\vec{x}_2\cdot\vec{p}'}\langle\Omega|\Gamma^{\beta\alpha}\chi_\alpha^{\Delta\sigma}(\vec{x}_2, t_2)A^3_\mu(\vec{x}_1, t_1)\bar{\chi}^N_\beta(\vec{0}, 0)|\Omega\rangle e^{-i\vec{x}_1\cdot(\vec{p}-\vec{p}')}, & \end{aligned} \tag{5.23}$$

where $\chi^{\Delta\sigma}(x)$ is the Δ interpolating operator given in Eq. (4.9). The ratio we take to cancel overlaps and exponentials is the same as that used in the electromagnetic transition:

$$\begin{aligned} R^A_\sigma(t_2, t_1, \vec{p}', \vec{p}; \Gamma; \mu) = & \frac{G_\sigma^{\Delta A^3_\mu N}(t_2, t_1; \vec{p}', \vec{p}; \Gamma)}{G^{\Delta\Delta}_{ii}(t_2, \vec{p}'; \Gamma_4)} \\ & \times\left[\frac{G^{NN}(t_2 - t_1, \vec{p}; \Gamma_4)G^{\Delta\Delta}_{ii}(t_1, \vec{p}'; \Gamma_4)G^{\Delta\Delta}_{ii}(t_2, \vec{p}'; \Gamma_4)}{G^{\Delta\Delta}_{ii}(t_2 - t_1, \vec{p}'; \Gamma_4)G^{NN}(t_1, \vec{p}; \Gamma_4)G^{NN}(t_2, \vec{p}; \Gamma_4)}\right]^{1/2} \\ & \xrightarrow[t_1 \gg 1]{t_2 - t_1 \gg 1}\Pi^A_\sigma(\vec{p}', \vec{p}, \Gamma, \mu), \end{aligned} \tag{5.24}$$

where we take the Δ two-point function traced over spatial polarizations, $i = 1, 2, 3$. We take the final state, the Δ in this case, to be at rest. The kinematics are thus the same as in the case of the nucleon axial form factors, namely the momentum transfer is $\vec{q} = -\vec{p}$. In this reference frame, the ratio in Eq. (5.24) gives:

$$\begin{aligned} \Pi^A_k(\vec{0}, -\vec{q}; \Gamma_4; \mu = j) = i\mathcal{B}\Big\{ & \\ & - \left[\frac{E_N(\vec{q}) - 2M_\Delta + M_N}{2}\delta_{kj} + \frac{p^k p^j}{2(E_N(\vec{q}) + M_N)}\right]C_3^A(Q^2) \\ & - \left[(E_N(\vec{q}) - M_\Delta)\frac{M_\Delta}{M_N}\delta_{kj}\right]C_4^A(Q^2) + M_N\delta_{kj}C_5^A(Q^2) - \frac{p^k p^j}{M_N}C_6^A(Q^2)\Big\} \end{aligned} \tag{5.25}$$

for $\mu = j = 1, 2, 3$ while for $\mu = 4$ we have:

$$\Pi_k^A(\vec{0}, -\vec{q}; \Gamma_4; \mu = 4) = \mathcal{B} p^k \left[C_3^A(Q^2) + \frac{M_\Delta}{M_N} C_4^A(Q^2) + \frac{E_N(\vec{q}) - M_\Delta}{M_N} C_6^A(Q^2) \right], \quad (5.26)$$

where

$$\mathcal{B} = \left(\frac{2}{3}\right)^{1/2} \frac{[(E_N(\vec{q}) + M_N)/E_N(\vec{q})]^{1/2}}{3M_N}. \quad (5.27)$$

We take linear combinations of the three-point function so that for a given Q^2 the maximum number of lattice measurements contribute to the form factors. We find three combinations given by:

$$\begin{aligned} S_1^A(\vec{q}; 4) =& \sum_{\sigma=1}^{3} \Pi_\sigma^A(\vec{0}, -\vec{q}; \Gamma_4; \mu = 4) \quad (5.28) \\ =& \mathcal{B} \sum_{k=1}^{3} p^k \left[C_3^A(Q^2) + \frac{M_\Delta}{M_N} C_4^A(Q^2) + \frac{E_N(\vec{q}) - M_\Delta}{M_N} C_6^A(Q^2) \right], \end{aligned}$$

$$\begin{aligned} S_1^A(\vec{q}; j) =& \sum_{\sigma=1}^{3} \Pi_\sigma^A(\vec{0}, -\vec{q}; \Gamma_4; j) \quad (5.29) \\ =& i\mathcal{B} \Big\{ - \frac{C_3^A(Q^2)}{2} \left[(E_N(\vec{q}) - 2M_\Delta + M_N) + (p_1 + p_2 + p_3) \frac{p^j}{E_N(\vec{q}) + M_N} \right] \\ & - \frac{M_\Delta}{M_N} (E_N(\vec{q}) - M_\Delta) C_4^A(Q^2) + M_N C_5^A(Q^2) - \frac{C_6^A(Q^2)}{M_N} p^j (p_1 + p_2 + p_3) \Big\}, \end{aligned}$$

$$\begin{aligned} S_2^A(\vec{q}; j) =& \sum_{\sigma \neq k=1}^{3} \Pi_\sigma^A(\vec{0}, -\vec{q}; \Gamma_k; j) \quad (5.30) \\ =& i \frac{\mathcal{A}}{2} \Big\{ (p_1 + p_2 + p_3) \left[\delta_{j1}(p_2 - p_3) + \delta_{j2}(p_3 - p_1) + \delta_{j3}(p_1 - p_2) \right] C_3^A(Q^2) \Big\}, \end{aligned}$$

$$\begin{aligned} S_3^A(\vec{q}; j) =& \Pi_3^A(\vec{0}, -\vec{q}; \Gamma_3; \mu = j) - \frac{1}{2} \Big[\Pi_1^A(\vec{0}, -\vec{q}; \Gamma_1; \mu = j) + \Pi_2^A(\vec{0}, -\vec{q}; \Gamma_2; \mu = j) \Big] \quad (5.31) \\ =& i\mathcal{A} \left[\frac{9}{4} (\delta_{j1} p_2 p_3 - \delta_{j2} p_1 p_3) C_3^A(Q^2) \right], \end{aligned}$$

where $j = 1, 2, 3$ and

$$\mathcal{A} = \frac{\mathcal{B}}{E_N(\vec{q}) + M_N}. \quad (5.32)$$

These combinations are the same as those calculated for the electromagnetic transition. Thus we can compute the axial transition nucleon to Δ form factors without any new inversions. Since in this study we are concerned with the dominant form factors C_5^A and C_6^A, we only use the sequential propagator obtained by S_1^A in Eqs. (5.28 and 5.29). We refer to Ref. [92] for a lattice study which additionally evaluated the sub-dominant form

factors.

The $G_{\pi N\Delta}$ form factor is computed in the same manner, by replacing the axial current A^3_μ by the pseudo-scalar current P^3. After taking the ratio with the combination of two-point functions, and assuming $t_2 - t_1$ and t_1 are large enough for the suppression of excited states, we have:

$$\Pi^P_\sigma(\vec{0}, -\vec{q}; \Gamma_4; \gamma_5) = \left(\frac{2}{3}\right)^{1/2} \left(\frac{E_N(\vec{q}) + M_N}{E_N(\vec{q})}\right)^{1/2} \frac{q_\sigma}{6M_N} \frac{f_\pi m_\pi^2}{2m_q(m_\pi^2 + Q^2)} G_{\pi N\Delta}(Q^2). \quad (5.33)$$

The optimal combination is given by:

$$\begin{aligned} S^P_{N\Delta}(\vec{q}; \gamma_5) &= \sum_{\sigma=1}^{3} \Pi^P_\sigma(\vec{0}, -\vec{q}; \Gamma_4; \gamma_5) \quad (5.34) \\ &= \left(\frac{2}{3}\right)^{1/2} \left(\frac{E_N(\vec{q}) + M_N}{E_N(\vec{q})}\right)^{1/2} \left[\frac{q_1 + q_2 + q_3}{6M_N} \frac{f_\pi m_\pi^2}{2m_q(m_\pi^2 + Q^2)}\right] G_{\pi N\Delta}(Q^2), \end{aligned}$$

which is the same combination as that used for the case of the axial nucleon to Δ transition, thus the same sequential propagators can be used.

5.1.4 Extraction of f_π and m_q

The evaluation of $G_{\pi NN}$ and $G_{\pi N\Delta}$ requires knowledge of the renormalized quark mass m_q. This is defined via the AWI given in Eq. (5.7). Due to the discretization of the action, the AWI on the lattice has corrections. For Wilson fermions these are of order a. For domain wall fermions, as we have described in Chapter 4, the effect of the finite fifth dimension can be thought of as a residual mass. This introduces an additional term in the divergence of the axial current which goes to zero as the fifth dimension goes to infinity [93]. Since we set the fifth dimension such that this residual mass is at most an order of magnitude smaller than the quark mass, we assume corrections to the AWI are small and compute m_q from Eq. (5.7). For this purpose we define the pion axial-vector two-point function:

$$C^A_{\mathrm{LS}}(t) = \sum_{\vec{x}} \langle \Omega | A^3_4(\vec{x}, t) \tilde{A}^3_4(\vec{0}, 0) | \Omega \rangle \quad (5.35)$$

where the axial current given in Eq. (5.1) is the interpolating operator. $\tilde{A}$ denotes a smeared interpolating operator while C^A_{LS} denotes that the two-point function is taken between a smeared initial state and a local final state. Similarly the pion pseudo-scalar two-point function is given by:

$$C^P_{\mathrm{LS}}(t) = \sum_{\vec{x}} \langle \Omega | P^3(\vec{x}, t) \tilde{P}^3(\vec{0}, 0) | \Omega \rangle. \quad (5.36)$$

We define the effective quark mass as the ratio:

$$m_{\rm eff}^{\rm AWI}(t) = \frac{m_\pi}{2}\frac{Z_A}{Z_P}\frac{C_{\rm LS}^A(t)}{C_{\rm LS}^P(t)}\left(\frac{C_{\rm SS}^P(t)}{C_{\rm SS}^A(t)}\right)^{1/2} \tag{5.37}$$

and look for a plateau in the large t limit. Z_A and Z_P are the renormalization constants of the axial and pseudo-scalar currents respectively. This specific combination of local-smeared and smeared-smeared two-point functions is chosen since this does not require knowledge of the overlap of the smeared interpolating operator with the pion state. As we shall see in the next sections, knowledge of the pseudo-scalar renormalization, Z_P, is not needed since for all physical quantities this cancels. Similarly, the pion decay constant, f_π, is extracted by looking for a plateau in the large t limit of the ratio:

$$f_\pi^{\rm eff}(t) = Z_A\left(\frac{2}{m_\pi}\right)^{1/2}\frac{C_{\rm LS}^A(t)}{\sqrt{C_{\rm SS}^A(t)}}e^{m_\pi t/2}. \tag{5.38}$$

5.2 Lattice Parameters and Optimization

As mentioned in the introduction of this chapter, for the nucleon axial form factors we use the same configurations used in the calculation of the nucleon electromagnetic form factors. Namely, we use Wilson quenched configurations at three pion masses and three ensembles of dynamical Wilson N_F=2 configurations. The parameters for these lattices are given in Table 3.1. For the case of the nucleon to Δ axial transition and pion-nucleon-Δ form factor, we additionally use the hybrid scheme which we used to calculate the nucleon to Δ electromagnetic transition form factors in Chapter 4, where domain wall fermions are used in the valence sector and staggered fermions are used in the sea sector. The details for these configurations are listed in Table 4.1. We use gauge invariant Gaussian smeared initial and final states to increase overlap with the ground state. We additionally use hyper-cubic blocking on the gauge links that enter the hopping matrix of the Gaussian smearing to reduce gauge noise. The source sink separation was taken the same as that of the previous calculations, namely we take t_2/a=11 for the quenched lattices, t_2/a=12 for the Wilson dynamical and t_2/a=8 for the hybrid scheme. Although these separations where fixed from the previous calculation since we use the same sequential propagators, We shall present checks that these source-sink separations are large enough to suppress excited state contamination for the case of the axial and pseudo-scalar form factors.

As in the previous chapters, before showing the results of this study we shall first present initial checks carried out. In Fig. 5.1 we show plots of the effective quark mass $m_{\rm eff}^{\rm AWI}(t)$ given in Eq. (5.37) as a function of time. This is done for the three discretization schemes considered here, for each pion mass. For the case of domain wall fermions, the correlator should reach a plateau at the quark mass we input in the domain wall Dirac matrix, given in Table 4.1 under $(am_{u,d})^{\rm DWF}$. Any discrepancy observed is attributed to the residual quark mass due to the finite size of the fifth dimension. For Wilson fermions

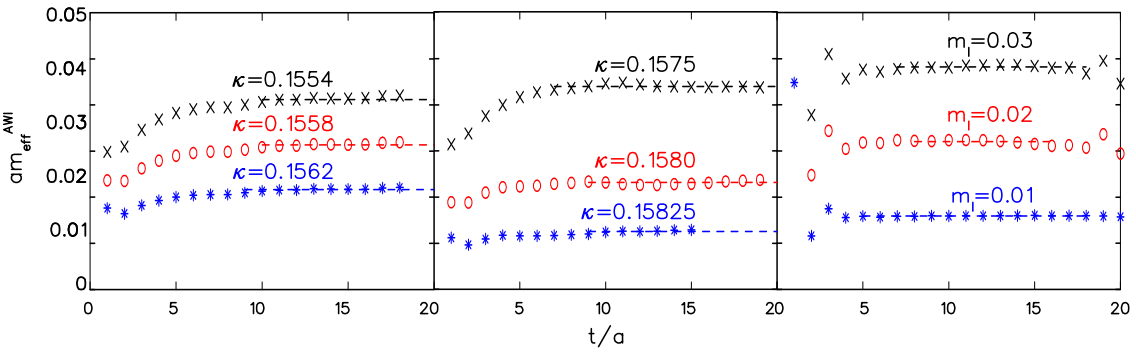

Figure 5.1: Effective quark mass in lattice units, as defined in Eq. (5.37), at the three pion masses of each discretization scheme considered: left for the quenched case, center for Wilson dynamical and right for the hybrid scheme. The dashed lines show fits to a constant over the range spanned.

the AWI has corrections of $\mathcal{O}(a)$. As we decrease the pion mass we thus expect systematic errors to grow since the right hand side of Eq. (5.7) becomes dominated by the $\mathcal{O}(a)$ term due to the correction. We shall come back to this issue when discussing results for the form factors.

In Fig. 5.2 we show the ratio used to extract the pion-nucleon form factor as a function of the insertion time-slice t_1. For the purpose of this check, we average the ratio over all lattice momenta that contribute to a given Q^2 value and multiply with $\mathcal{C}\frac{q_1+q_2+q_3}{2M_N}$. As can be seen, at intermediate values of t_1 the separation between the insertion and sink, t_2-t_1, and the insertion and source, t_1, is large enough so that excited state contamination is suppressed, thus the ratio becomes t_1 independent. According to Eq. (5.21), the value fitted in the plateau region is given by:

$$R^P(t_2,t_1,\vec{0},-\vec{q};\Gamma_k;\gamma_5)\frac{2M_N}{\mathcal{C}(q_1+q_2+q_3)} \xrightarrow[t_1\gg 1]{t_2-t_1\gg 1} \frac{f_\pi m_\pi^2 G_{\pi NN}(Q^2)}{2m_q(Q^2+m_\pi^2)Z_P} \tag{5.39}$$

in which the pseudo-scalar current renormalization Z_P cancels, as we have already mentioned. Thus this quantity, as all other physical quantities we shall see in this chapter, is independent of the value of Z_P we use. We remind that in practice this is not how we carry out the analysis. The form factors are extracted by fitting for each momentum vector independently, then taking the average. This is done when minimizing χ^2 in the over-constraint analysis described in Chapter 3. In Fig. 5.3 we show the corresponding ratio for the pion-nucleon-Δ form factor. As can be seen, for all three discretization schemes used, the ratio becomes independent of t_1 when the insertion is 2–3 time-slices from the source, allowing us to fit to a constant.

In Fig. 5.4 we show the ratio used to extract the axial nucleon form factors as a function of the insertion time t_1. Here we do not average over all momentum vectors contributing to a given Q^2 but rather plot representative lattice momentum vectors separately. As can be seen the time separations are large enough so that a plateau can be identified.

As we have already mentioned, the sequential propagators used are taken from the previous evaluations of the corresponding electromagnetic form factors, thus no extra

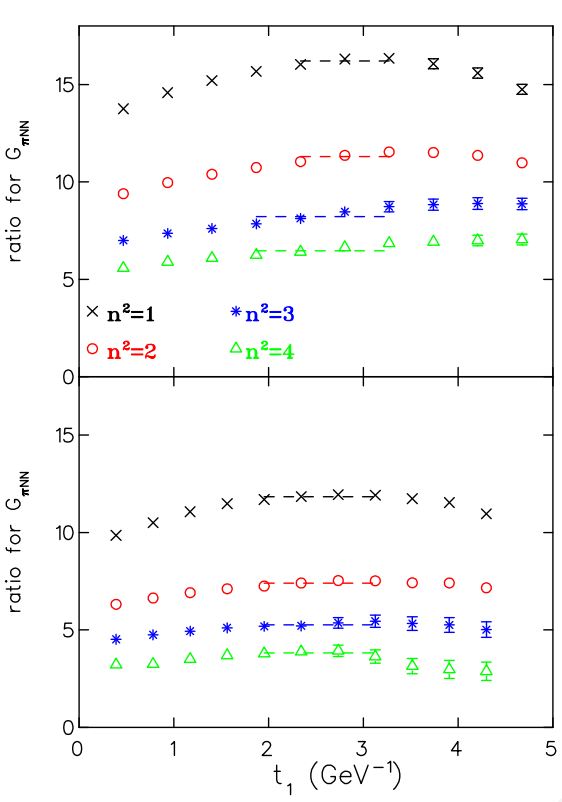

Figure 5.2: The ratio R^P used to extract the pion-nucleon form factor for the four lowest non-zero momentum transfers Q^2. Top using quenched Wilson fermions at m_π=0.49 GeV and bottom using dynamical Wilson fermions at m_π=0.69 GeV. The dashed lines are fits to the range they span.

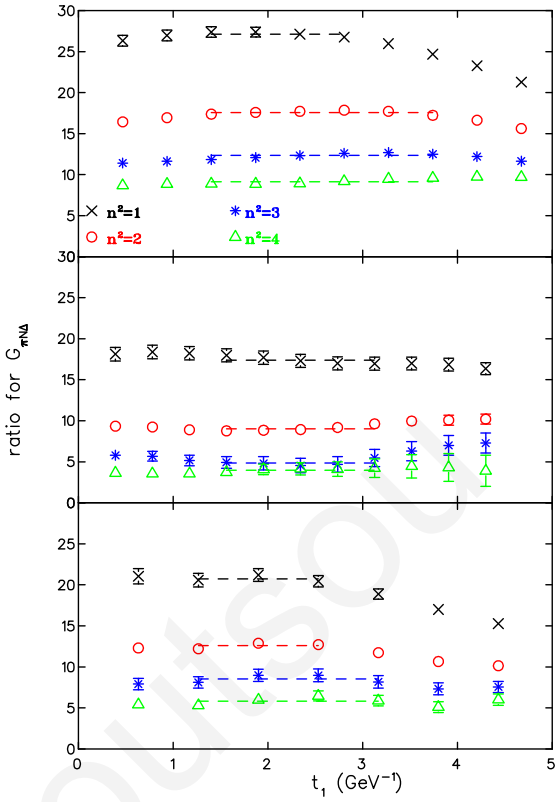

Figure 5.3: The ratio $R^P_{N\Delta}$ used to extract the pion-nucleon-Δ form factor for the four lowest non-zero momentum transfers Q^2. Top using quenched Wilson fermions, center for dynamical Wilson fermions and bottom for the hybrid scheme. We show the lattices with a pion mass of approximately 0.5 GeV for each discretization scheme.

sequential inversions are needed. Although the source-sink separation has been fixed for the calculation of the electromagnetic form factors, we have performed several checks where we increase the source-sink separation and check for consistency. In Fig. 5.5 we show the ratio from which the axial nucleon form factors are obtained and the ratio from which $G_{\pi NN}$ is obtained as a function of the insertion time-slice for two source-sink separations, namely t_2/a=11 and t_2/a=13. We carry out this check using the quenched lattice at the smallest pion mass $m_\pi = 0.41$ GeV. We see that increasing the source-sink separation by two time-slices yields consistent plateaus except for the lowest momentum transfer of the $G_{\pi NN}$ form factor where we see that the larger source-sink separation yields a larger value for the form factor. Given the consistency observed for all other momentum transfer, we can conclude that the origin of this discrepancy is most likely not due to the increase in the source-sink separation. The most probable cause is that because this form factor is obtained by dividing with $q_1 + q_2 + q_3$, the extraction becomes ill-defined as $\vec{q} \to 0$ and thus the extracted value becomes erroneous.

The effect of increasing the source-sink separation on the values extracted for the form

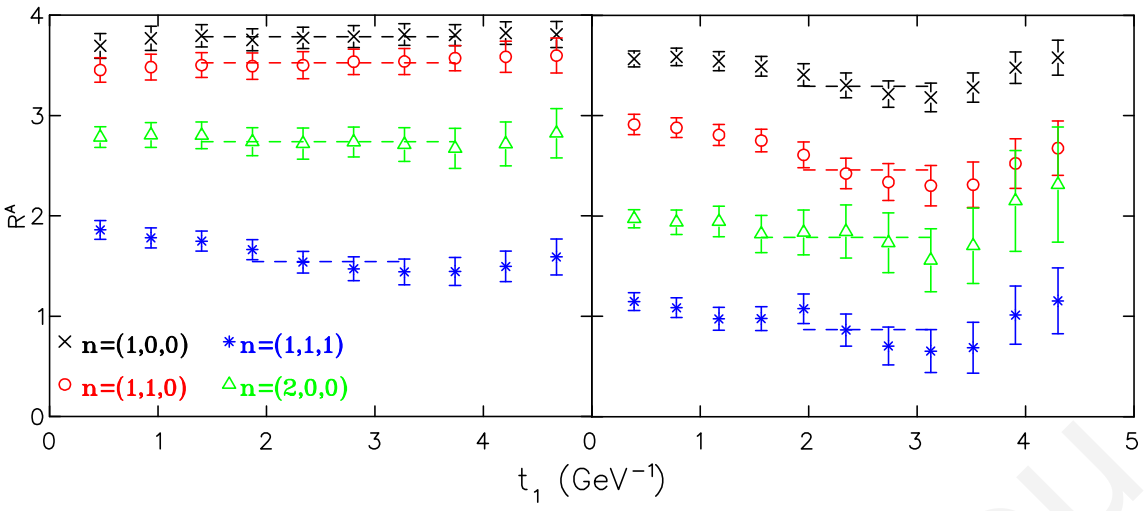

Figure 5.4: The ratio used to extract the axial nucleon form factors G_A and G_p as a function of the insertion time-slice t_1 for representative lattice momentum vectors. Left for the quenched case at $m_\pi = 0.49$ GeV and right for dynamical Wilson fermions at m_π=0.51 GeV.

factors can be seen in Fig. 5.6 where we compare the axial nucleon form factors G_A and induced pseudo-scalar G_p and the pion-nucleon form factor $f_\pi G_{\pi NN}/m_q$ for the two source-sink separations of Fig 5.5. As can be seen the form factors are consistent up to ~ 1.5 GeV. At higher momentum transfer the three-point function becomes noisy, and numerically the Fourier transform gives an underestimated error due to the small statistics. An exception is the lowest momentum transfer for the pion-nucleon form factor which appears to be underestimated for the shorter separation, which is what we have seen in Fig. 5.5. Given the consistency of all other measurements and the accuracy obtained using the shorter separation, we fix t_2/a=11 with the hindsight that $G_{\pi NN}$ may be underestimated at the smallest Q^2 value.

In Fig. 5.7 we carry out the same check for the nucleon to Δ matrix element in the hybrid scheme. Here we compute the form factors by setting the separation to t_2/a=10 time-slices and inverting using Dirichlet boundary conditions cutting the lattice at half the temporal extent. This is compared to setting t_2/a=8 on the full lattice with anti-periodic boundary conditions. As can be seen the two separations yield consistent results. The larger separation, however, is much noisier than the shorter separation, thus we fix the separation at t_2/a=8 for the hybrid scheme.

In Fig. 5.8 we check for finite volume effects by computing the three form factors on two ensembles at equal pion mass but different volume, as we have done for the electromagnetic transition in Chapter 4. The results are consistent meaning that $m_\pi L_s \geq 4.6$, which is what we obtain for the smaller lattice, is sufficient for finite size effects to be negligible. All lattices considered obey $m_\pi L_s \geq 4.6$, except for the dynamical Wilson lattice at the smallest pion mass. Since a larger lattice at this small pion mass is unavailable, we cannot assess the size of finite volume effects on the form factors computed using this lattice.

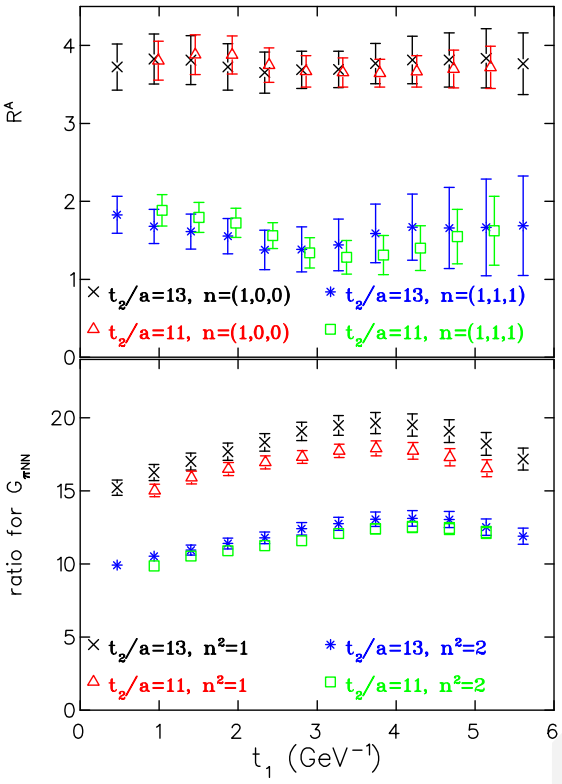

Figure 5.5: The ratio that yields G_A and G_p (top) and the ratio that yields $G_{\pi NN}$ (bottom) as a function of the insertion time-slice t_1 for two source-sink separations, t_2/a=11 and t_2/a=13. The results for t_2/a=11 have been shifted to the right by a time-slice so that its median coincides with that for $t_2/a = 13$. The results where obtained in the quenched approximation at m_π=0.41 GeV.

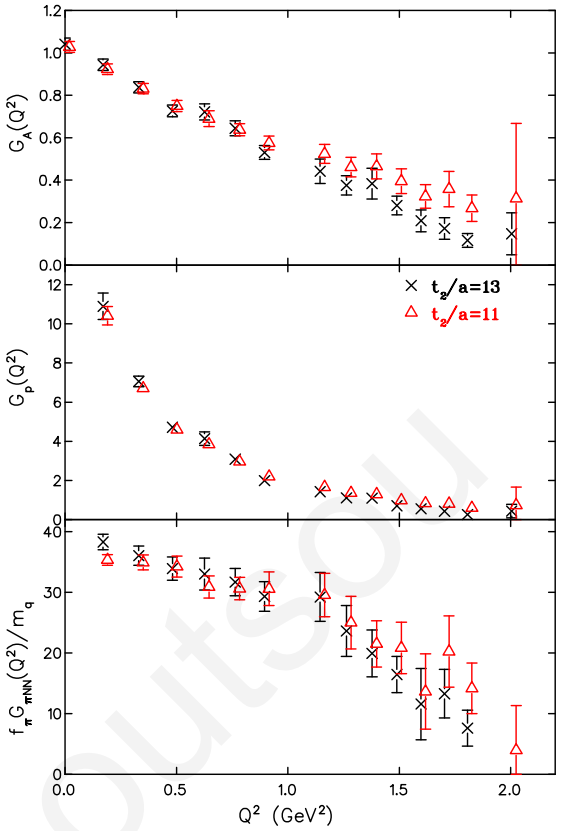

Figure 5.6: The axial nucleon form factors G_A (top) and G_p (center) as well as the pion-nucleon form factor $f_\pi G_{\pi NN}/m_q$ (bottom) as a function of Q^2 for two source-sink separations: t_2/a=11 (open triangles) and t_2/a=13 (crosses). We consider the smallest quark mass in the quenched approximation (m_π =0.41 GeV).

5.3 Lattice Results

We will first show results on ratios of form factors. In the ratios we shall show the renormalized quark mass cancels, eliminating one potential source of systematic error. Additionally, ratios show weaker dependence on the pion mass and thus are more suited for comparison with results at the physical point.

In Fig. 5.9 we show the ratio of the pion-nucleon-Δ form factor with the pion-nucleon form factor. Since the momentum transfer, Q^2, depends on the nucleon mass for the case of $G_{\pi NN}$ and on both nucleon and Δ masses for the case of $G_{\pi N\Delta}$, we must interpolate the two form factors to same Q^2 values in order to take the ratio. As can be seen this ratio, within statistical error, shows no dependence on the momentum transfer. Fitting to a constant we obtain 1.60(2). The Wilson dynamical results are consistent with the quenched results albeit with larger errors. Fitting to a constant we obtain 1.63(4).

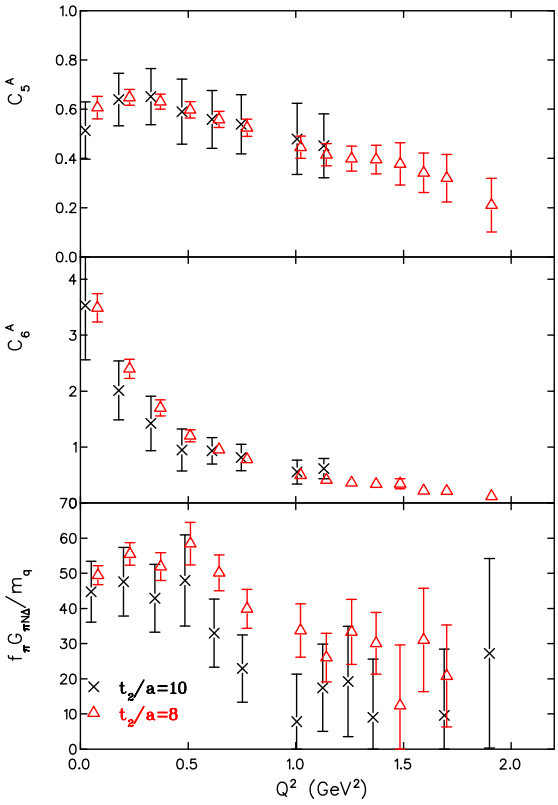

Figure 5.7: The nucleon to Δ axial transition form factors C_5^A (top) and C_6^A (center) and the pion-nucleon-Δ form factor $f_\pi G_{\pi N\Delta}/m_q$ (bottom) for the lightest pion mass in the hybrid scheme at two source sink separations: t_2/a=8 (open triangles) and t_2/a=10 (crosses).

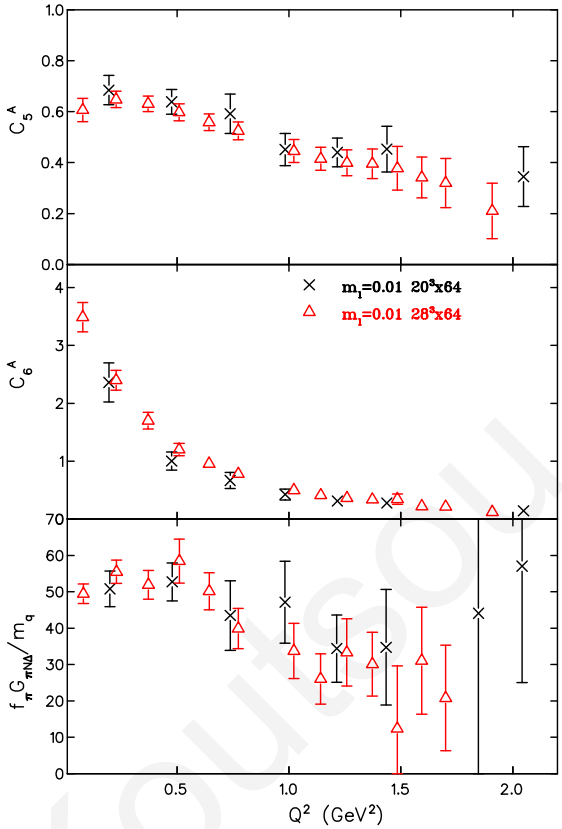

Figure 5.8: The nucleon to Δ axial transition form factors C_5^A (top) and C_6^A (center) and the pion-nucleon-Δ form factor $f_\pi G_{\pi N\Delta}/m_q$ (bottom) for the lightest pion mass in the hybrid scheme at two lattice volumes: L_s = 2.5 fm (crosses) and L_s = 3.5 fm (open triangles).

According to the simplified GTRs given in Eq. (5.16), the ratio shown in Fig. 5.9 should be equal to $2C_5^A(Q^2)/G_A(Q^2)$:

$$G_{\pi N\Delta}(Q^2)/G_{\pi NN}(Q^2) = 2C_5^A(Q^2)/G_A(Q^2). \tag{5.40}$$

We test this equality by showing this ratio in Fig. 5.10. As can be seen the ratio is independent of Q^2 within error bars as in the case of the ratio between the pion-nucleon-Δ and pion-nucleon form factors. Fitting to a constant yields 1.61(1) for the quenched results which is consistent with what we find for the ratio of the pseudo-scalar form factors. The results obtained using dynamical Wilson fermions lie slightly higher and fitting to a constant yields 1.74(4).

We can use the GTRs along with their simplified form in order to eliminate the pseudo-scalar form factors $G_{\pi NN}$ and $G_{\pi N\Delta}$. This rearrangement, which is another manifestation of the assumption that the form factors G_p and C_6^A are described by a pion pole, associates

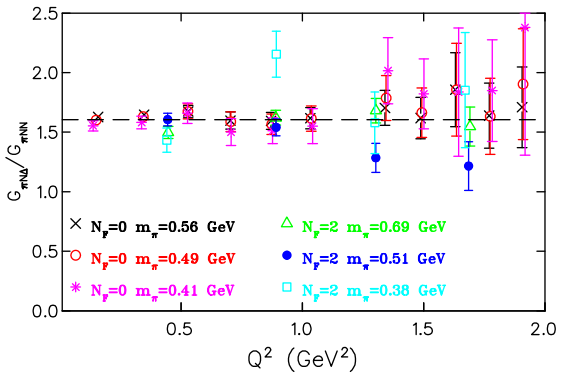

Figure 5.9: The ratio $G_{\pi N\Delta}(Q^2)/G_{\pi NN}(Q^2)$ using quenched Wilson fermions at m_π=0.56 GeV (crosses), m_π=0.49 GeV (open circles) and m_π=0.41 GeV (asterisks) and using two degenerate flavors of Wilson fermions at m_π=0.69 GeV (open triangles), m_π=0.51 GeV (filled circles) and m_π=0.38 GeV (open squares). The dashed line shows the result of fitting the quenched results to a constant which yields 1.60(2).

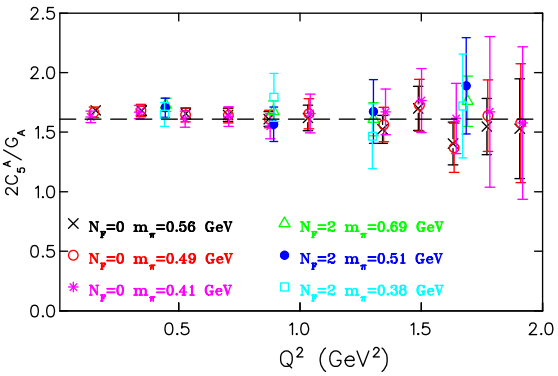

Figure 5.10: The ratio $2C_5^A(Q^2)/G_A(Q^2)$ which according to the simplified GTRs is equal to $G_{\pi N\Delta}(Q^2)/G_{\pi NN}(Q^2)$. The notation is the same as in Fig. 5.9. Fitting the quenched results to a constant yields 1.61(1).

the ratios via:

$$G_{\pi N\Delta}(Q^2)/G_{\pi NN}(Q^2) = 2C_5^A(Q^2)/G_A(Q^2) = 8C_6^A(Q^2)/G_P(Q^2). \tag{5.41}$$

In Fig. 5.11 we plot $8C_6^A(Q^2)/G_P(Q^2)$ as a function of the momentum transfer squared. The conclusion for this ratio is the same as that of the other two ratios seen so far, that within error bars we see no Q^2 dependence. Fitting the quenched and dynamical Wilson results to a constant we find 1.71(3) and 1.79(4) respectively which are approximately 7% larger than what is obtained when fitting the quenched results for $G_{\pi N\Delta}(Q^2)/G_{\pi NN}(Q^2)$. Given these comparisons we can conclude that on the few percent level the simplified GTRs are indeed satisfied.

We can additionally test the GTRs without assuming a pion pole for G_p and C_6^A. For this we take the ratio of the off-diagonal GTR given in Eq. (5.14) over the diagonal GTR given in Eq. (5.13). This ratio should be equal to unity if both these relations hold. This is indeed what we observe in Fig. 5.12 where we plot this ratio as a function of the momentum transfer squared.

Assuming pion pole dominance of the form factors G_p and C_6^A, along with the GTRs given in Eqs. (5.13) and (5.14), implies that G_p has a stronger Q^2 dependence than G_A and, similarly, that C_6^A has a stronger Q^2 dependence than C_5^A:

$$G_p(Q^2) = \frac{4M_N^2}{m_\pi^2}\frac{G_A(Q^2)}{1+Q^2/m_\pi^2} \tag{5.42}$$

$$C_6^A(Q^2) = \frac{M_N^2}{m_\pi^2}\frac{C_5^A(Q^2)}{1+Q^2/m_\pi^2}. \tag{5.43}$$

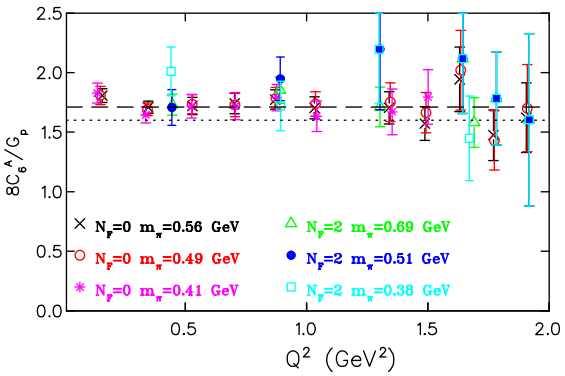

Figure 5.11: The ratio $8C_6^A(Q^2)/G_p(Q^2)$ which according to the simplified GTRs is equal to $G_{\pi N\Delta}(Q^2)/G_{\pi NN}(Q^2)$. The notation is the same as in Fig. 5.9. The dashed line is the result of fitting the quenched results to a constant which yields 1.71(3). The dotted line shows 1.6, which is what is obtained when fitting $G_{\pi N\Delta}(Q^2)/G_{\pi NN}(Q^2)$ to a constant, shown in Fig. 5.9.

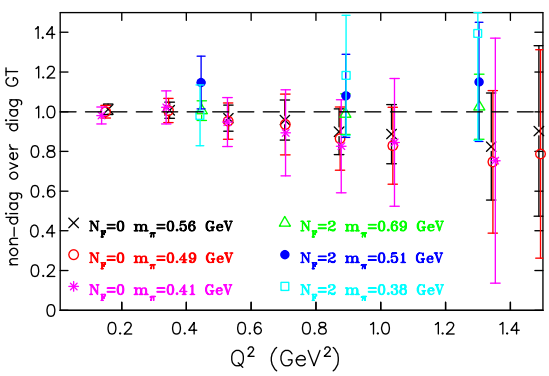

Figure 5.12: The ratio of the off-diagonal GTR over the diagonal GTR given in Eqs. (5.14) and (5.13) respectively. The notation is the same as in Fig. 5.9.

In Fig. 5.13 we plot the ratio $G_p(Q^2)/G_A(Q^2)$ as a function of Q^2. In the same plot we include results in the hybrid scheme taken from Ref. [67] which where calculated on the same lattices we consider here for the nucleon to Δ transition form factors. Eq. (5.42) predicts the form of this ratio and is shown with the dashed line in this plot for the quenched case at the lightest pion mass, m_π=0.41 GeV. We additionally fit the ratio for each pion mass to the monopole form:

$$\frac{c_0}{Q^2/m^2+1} \tag{5.44}$$

to obtain c_0 and m. The result of these fits are shown in Table 5.1.

In Fig. 5.14 we show the ratio $C_6^A(Q^2)/C_5^A(Q^2)$. Assuming pion pole dominance, the form of this ratio is given by Eq. (5.43). We show the curve obtained by this prediction for two cases: for the quenched results at the lightest pion mass, shown by the dashed line, and for the hybrid case at the lightest pion mass, shown by the dotted line. Fitting to Eq. (5.44) the quenched results at the lightest pion mass yields the solid curve. The parameters obtained by fitting each pion mass are given in Table 5.1. As can be seen, we find that the monopole mass obtained by fitting is larger than the corresponding pion mass. An additional conclusion is that at low momentum transfer, where pion cloud contributions are expected to be larger, unquenching effects are more notable.

To study the momentum dependence of the form factors separately we need knowledge of the axial current renormalization constant Z_A. For the case of the pion-nucleon and pion-nucleon-Δ form factors the renormalization constant of the pseudo-scalar current Z_P which appears in the operator cancels with that which appears from the extraction of the renormalized quark mass from two-point functions. The values for Z_A are known and

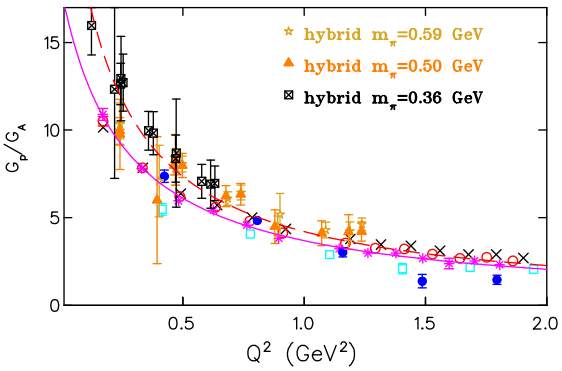

Figure 5.13: The ratio $G_p(Q^2)/G_A(Q^2)$ as a function of the momentum transfer squared. The notation is the same as in Fig. 5.9. We additionally include results from a hybrid calculation taken from Ref. [67] at the three pion masses we use here: m_π=0.59 GeV (stars), m_π=0.50 GeV (filled triangles) and m_π=0.36 GeV (inscribed squares). The dashed line shows the expected behavior according to Eq. (5.42) for the quenched case at $\kappa = 0.1562$, while the solid line shows the result of fitting the quenched data at $\kappa = 0.1562$ to the monopole form of Eq. 5.44.

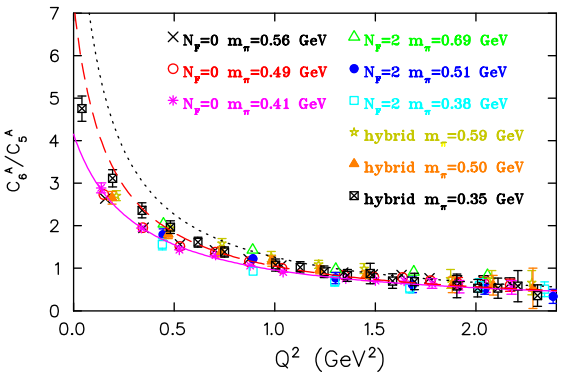

Figure 5.14: The ratio of $C_6^A(Q^2)/C_5^A(Q^2)$ as a function of Q^2. The notation is the same as in Fig. (5.13). The dotted line shows the expected behavior according to Eq. (5.43) for the hybrid case at the lowest pion mass.

are shown in Table 5.2. In Fig. 5.15 we show results obtained for the axial nucleon form factor $G_A(Q^2)$ and the induced pseudo-scalar form factor $G_p(Q^2)$ using Wilson quenched and Wilson dynamical quarks. We include results in the hybrid scheme from Ref. [67]. As can be seen, results obtained using the lightest pion mass in the hybrid scheme show deviations at low Q^2 as was the case with the ratios we have already seen. In particular, the nucleon axial coupling g_A becomes larger in the hybrid scheme approaching the experimental value. Recent state-of-the art lattice measurements of this quantity can be found in Refs [88, 89], therefore we shall not elaborate further on g_A but rather focus on the momentum dependence of the form factors. The deviations at low Q^2 when using the lightest pion mass in the hybrid scheme are also seen in $G_p(Q^2)$. In Fig. 5.16 we show the corresponding nucleon to Δ axial transition form factors. The same discrepancy between the Q^2 dependence of the hybrid scheme and using the quenched lattices is observed here as well.

The Q^2 dependence of $G_A(Q^2)$ and of $C_5^A(Q^2)$ is well described by a dipole Ansatz:

$$\frac{g_0}{(1+Q^2/m_A^2)^2}. \tag{5.45}$$

This form is used to describe experimental data yielding an axial mass of ∼1.1 GeV for $G_A(Q^2)$ and 1.28(10) GeV for $C_5^A(Q^2)$ [96]. We additionally fit to an exponential, $\tilde{g}_0 e^{-Q^2/\tilde{m}_A^2}$. We show fits to both forms in Figs. 5.15 and 5.16 for the quenched case where we see that both Ansätze describe the data well. The parameters obtained are presented in Table 5.3. The axial masses obtained are found larger than the experimental values.

Table 5.1: The table left (right) shows the result of fitting the ratio $G_p(Q^2)/G_A(Q^2)$ ($C_6^A(Q^2)/C_5^A(Q^2)$) to the monopole form given in Eq. (5.44).

Nucleon elastic		
m_π (GeV)	m (GeV)	c_0
Quenched Wilson fermions		
0.563(4)	0.671(14)	13.71(34)
0.490(4)	0.597(14)	15.23(43)
0.411(4)	0.511(16)	17.70(76)
$N_F = 2$ dynamical Wilson fermions		
0.691(8)	0.750(43)	14.13(1.01)
0.509(8)		
0.384(8)	0.642(77)	11.15(1.82)

Nucleon to Δ		
m_π (GeV)	m (GeV)	c_0
Quenched Wilson fermions		
0.563(4)	0.691(17)	3.43(9)
0.490(4)	0.628(16)	3.69(11)
0.411(4)	0.548(15)	4.15(14)
$N_F = 2$ dynamical Wilson fermions		
0.691(8)	0.711(53)	3.85(35)
0.509(8)	0.490(98)	5.27(1.59)
0.384(8)	0.520(63)	4.08(72)
Hybrid action		
0.594(1)	0.693(15)	3.90(8)
0.498(3)	0.627(11)	3.96(8)
0.353(3)	0.459(8)	5.62(12)

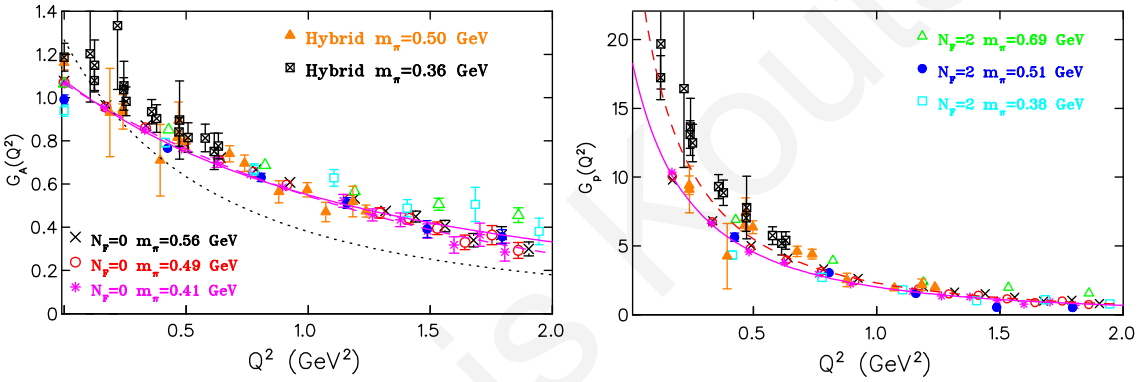

Figure 5.15: The nucleon axial form factor $G_A(Q^2)$ (left) and the induced pseudo-scalar nucleon form factor $G_p(Q^2)$ (right) as a function of Q^2. We compare our results using quenched Wilson and dynamical Wilson quarks to results obtained within the hybrid scheme taken from Ref. [67] at m_π=0.5 GeV (filled triangles) and m_π=0.36 GeV (inscribed squares). The notation for the quenched Wilson and dynamical Wilson results is the same as in Fig. 5.9. For the case of $G_A(Q^2)$, the solid curve shows a fit to a dipole form of the quenched results at the lowest pion mass. A fit to an exponential is shown with the dashed line which falls on top. The dotted line shows a dipole form with the dipole axial mass at m_A=1.1 GeV used to describe experimental data. For $G_p(Q^2)$, the solid line shows the form expected by pion pole dominance given by Eq. 5.42 using the fitted dipole form for $G_A(Q^2)$. The dashed line shows the form obtained when using the fitted monopole form for the ratio and the fitted dipole form for $G_A(Q^2)$ to extract the form of $G_p(Q^2)$ via Eq. 5.42 for the lightest pion mass in the quenched case.

This is expected from Fig. 5.15 where we include the experimentally defined curve with the dotted line. Having the form of $G_A(Q^2)$ and $C_5^A(Q^2)$ we can obtain the momentum dependence of $G_p(Q^2)$ and $C_6^A(Q^2)$ from Eqs. (5.42) and (5.43). The results are shown by the dashed curves in Figs. 5.15 and 5.16 for the lightest pion mass in the quenched case. The Q^2 dependence of the curves shows deviations at low Q^2. Similarly, we can use the fitted parameters for the ratios $G_p(Q^2)/G_A(Q^2)$ and $C_6^A(Q^2)/C_5^A(Q^2)$ given in Table 5.1

Table 5.2: The renormalized quark mass in lattice units, am_q, the unrenormalized pion decay constant, f_π/Z_A, and the axial current renormalization constant, Z_A, for each discretization scheme used, at every pion mass considered.

κ or m_l	am_q	af_π/Z_A	Z_A
Quenched Wilson fermions			
0.1554	0.0403(4)	0.0611(14)	0.808(7) [94]
0.1558	0.0307(4)	0.0587(16)	0.808(7)
0.1562	0.0213(4)	0.0563(17)	0.808(7)
$N_F = 2$ Wilson fermions			
0.1575	0.0441(4)	0.0649(8)	0.77(2) [95]
0.1580	0.0229(4)	0.0494(9)	0.78(4) [95]
0.15825	0.0122(3)	0.0467(13)	0.8[a]
Hybrid action			
0.03	0.0475(3)	0.0678(6)	1.1085(5) [88]
0.02	0.0324(4)	0.0648(8)	1.0994(4) [88]
0.01	0.0159(2)	0.0639(2)	1.0847(6) [88]

[a]Estimated from the values of Z_A at $\kappa = 0.1575$ and 0.1580

and obtain the Q^2 dependence of $G_p(Q^2)$ and $C_6^A(Q^2)$ by:

$$\frac{g_0}{(1+Q^2/m_A^2)^2}\frac{c_0}{1+Q^2/m^2}. \tag{5.46}$$

This form describes the data well, as can be seen by the solid curve shown in Figs. 5.15 and 5.16 where we show this for the lightest pion mass of the quenched case.

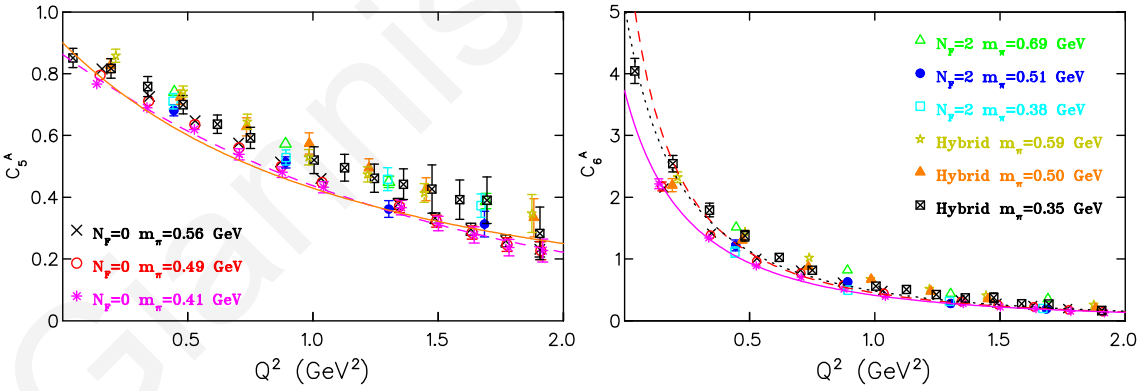

Figure 5.16: The nucleon to Δ axial transition form factors $C_5^A(Q^2)$ (left) and $C_6^A(Q^2)$ (right). For the case of $C_5^A(Q^2)$, the solid curve shows the result of fitting to a dipole form while the dashed curve the result of fitting to an exponential form. For $C_6^A(Q^2)$, the dashed curve shows Eq. (5.43) using the fitted dipole form for $C_5^A(Q^2)$ for the lightest pion mass in the quenched approximation. The solid curve shows the product of the fitted monopole form for $C_6^A(Q^2)/C_5^A(Q^2)$ with the fitted dipole form for $C_5^A(Q^2)$ for the lightest pion mass in the quenched approximation. The dotted curve shows the same for the hybrid scheme at the smallest pion mass. The rest of the notation is the same as in Fig. 5.14.

Before going on to results for $G_{\pi NN}$ and $G_{\pi N\Delta}$ we need to check for lattice effects on the renormalized quark mass m_q. As already mentioned, the AWI takes corrections to

Table 5.3: The parameters g_0 and m_A obtained by fitting $G_A(Q^2)$ and $C_5^A(Q^2)$ to the dipole form in Eq. (5.45). We include the parameters obtained when fitting to the exponential form $\tilde{g}_0 \exp(Q^2/\tilde{m}_A^2)$.

m_π (GeV)	m_A (GeV)	g_0	$\tilde{m}_A$ (GeV)	$\tilde{g}_0$
Nucleon elastic				
Quenched Wilson fermions				
0.563(4)	1.659(20)	1.088(8)	1.271(9)	1.074(5)
0.490(4)	1.632(19)	1.079(7)	1.249(9)	1.069(5)
0.411(4)	1.578(28)	1.080(12)	1.220(10)	1.066(6)
$N_F = 2$ dynamical Wilson fermions				
0.691(8)	1.831(22)	1.067(6)	1.393(16)	1.063(6)
0.509(8)	1.709(46)	0.999(17)	1.296(29)	0.995(17)
0.384(8)	2.019(78)	0.951(18)	1.528(44)	0.943(15)
Nucleon to Δ				
Quenched Wilson fermions				
0.563(4)	1.469(46)	0.972(26)	1.204(13)	0.923(9)
0.490(4)	1.467(51)	0.950(29)	1.201(16)	0.903(11)
0.411(4)	1.492(57)	0.901(28)	1.213(20)	0.863(13)
$N_F = 2$ dynamical Wilson fermions				
0.691(8)	1.649(36)	1.005(19)	1.384(29)	0.929(17)
0.509(8)	1.460(65)	1.003(47)	1.260(38)	0.898(29)
0.384(8)	1.593(69)	0.980(41)	1.337(38)	0.902(26)
Hybrid action				
0.594(1)	1.572(54)	1.040(29)	1.276(19)	0.990(13)
0.498(3)	1.789(46)	0.940(16)	1.402(19)	0.916(9)
0.357(2)	1.740(44)	0.914(15)	1.364(18)	0.895(8)

first order in the lattice spacing for Wilson fermions. As the quark mass goes to zero, this correction will dominate the right hand side of Eq. (5.7). For domain wall fermions, in the limit where the fifth dimension goes to infinity the renormalized quark mass is equal the domain wall quark mass listed in Table 4.1. Any deviations between these two masses are thus due to the residual quark mass which is due to the finite size of the fifth dimension. In Fig. 5.17 we show the renormalized quark mass as a function of the pion mass squared. As can be seen the quenched quark mass extrapolates to zero. For Wilson N_F=2, the quark mass has finite a corrections at $m_\pi^2 \to 0$ since it does not extrapolate to zero. For the case of domain wall fermions we include both the quark mass evaluated using the AWI and the domain wall quark mass, denoted by $m_q^{\rm DW}$, which is the hopping parameter of the domain wall operator and which was tuned in Ref. [67] so that it yields a pion mass equal to the lightest pseudo-scalar mass obtained when using the Asqtad improved Staggered action in both the valence and sea sector.

Knowing the values for f_π and m_q we carry on to show results for the pion-nucleon and pion-nucleon-Δ form factors. We first examine the simplified GTRs given in Eq. (5.16) by which the ratios $f_\pi G_{\pi NN}(Q^2)/(M_N G_A(Q^2))$ and $f_\pi G_{\pi N\Delta}(Q^2)/(2M_N C_5^A(Q^2))$ are expected to be equal to unity. We plot these ratios in Fig. 5.18. As can be seen these are

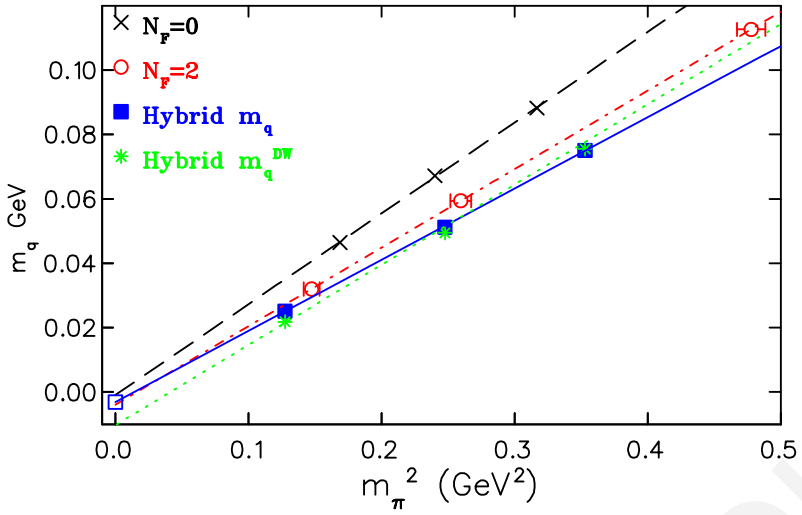

Figure 5.17: The renormalized quark mass as a function of the pion mass squared, crosses for the quenched case, circles for Wilson dynamical and filled squares for the hybrid scheme. We additionally include the domain wall quark mass, set by demanding that this yields a pion mass equal to the lightest pseudo-scalar mass using the MILC lattices [67].

consistent with unity for $Q^2 \geq 0.5$ GeV^2 when using dynamical Wilson and quenched Wilson fermions. Using the hybrid scheme the results show smaller deviations from unity at lower $Q^2 < 0.5$ GeV^2.

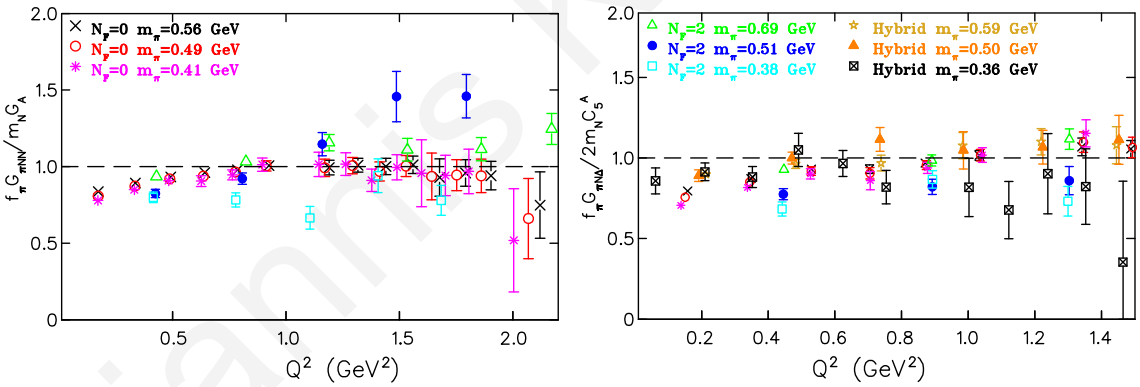

Figure 5.18: The ratios $f_\pi G_{\pi NN}(Q^2)/(M_N G_A(Q^2))$ (left) and $f_\pi G_{\pi N\Delta}(Q^2)/(2M_N C_5^A(Q^2))$ (right). The notation is the same as that of Fig. 5.14.

Assuming pion pole dominance of the form factors $G_p(Q^2)$ and $C_6^A(Q^2)$ as in Eq. (5.15), the ratios:

$$\frac{2G_{\pi NN}(Q^2)f_\pi}{m_\pi^2+Q^2}\frac{2M_N}{G_p(Q^2)} \quad \text{and} \quad \frac{1}{2}\frac{G_{\pi N\Delta}(Q^2)f_\pi}{m_\pi^2+Q^2}\frac{M_N}{C_6^A(Q^2)} \tag{5.47}$$

should also be consistent to unity. We show these ratios in Fig. 5.19 for the lightest pion mass for each discretization scheme considered, where we see that these are indeed consistent with unity.

Finally we shall present and discuss the pion-nucleon and pion-nucleon-Δ form factors

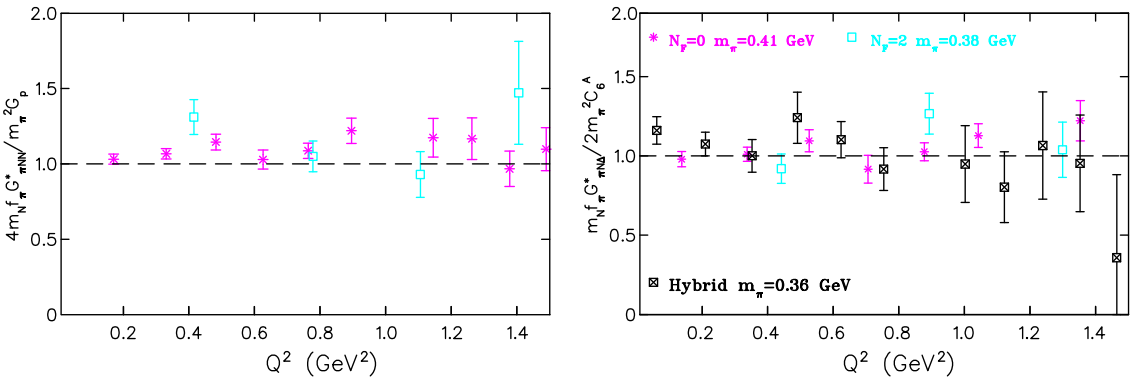

Figure 5.19: The ratios $4M_N f_\pi G^*_{\pi NN}(Q^2)/(m_\pi^2 G_p(Q^2))$ (left) and $M_N f_\pi G^*_{\pi N\Delta}(Q^2)/(2m_\pi^2 C_6^A(Q^2))$ (right) for the lightest quark mass of each discretization scheme used, where $G^*_{\pi NN}(Q^2) \equiv G_{\pi NN}(Q^2)/(1+Q^2/m_\pi^2)$ and equivalently for $G^*_{\pi N\Delta}(Q^2)$.

separately. In Fig. 5.20 we show these for the lightest pion mass for each discretization scheme considered. Our first observation is the consistency between results using Wilson fermions and in the hybrid scheme at low Q^2 indicating that unquenching effects for these quantities are smaller than for the axial form factors at pion masses as low as 0.35 GeV. The simplified GTRs relate $G_{\pi NN}$ and $G_{\pi N\Delta}$ to the axial form factors $G_A(Q^2)$ and $C_5^A(Q^2)$ respectively, which we have seen are described by a dipole form. Using the fitted parameters for $G_A(Q^2)$ and $C_5^A(Q^2)$ listed in Table 5.3 we plot the dashed curves in Fig. 5.20. The discrepancy noted in Fig. 5.19 at $Q^2 < 0.5$ GeV^2 are seen here as well. These deviations are confirmed by results in the hybrid scheme. The momentum dependence of these form factors can be described by the linear form:

$$G_{\pi NN}(Q^2) = a\left(1 - \Delta\frac{Q^2}{m_\pi^2}\right), \qquad (5.48)$$
$$G_{\pi N\Delta}(Q^2) = a'\left(1 - \Delta'\frac{Q^2}{m_\pi^2}\right).$$

We fit to the above expressions varying a and Δ for the case of $G_{\pi NN}$ and a' and Δ' for the case of $G_{\pi N\Delta}$. The results of the fits are shown by the solid lines in Fig. 5.20 and as can be seen describe the data well. We have omitted the point at the lowest momentum transfer in the fit, since we may be underestimating the statistical error on this point. The fitted parameters a, a', Δ and Δ' at each pion mass are shown in Table 5.4. Note that the parameters Δ and Δ' decrease with decreasing pion mass. Baryon chiral perturbation theory predicts a value of Δ=2.44% at the physical point [97]. This is reasonable given the quark mass dependence of the fitted values for Δ in Table 5.4. This is not the case for the parameter a which is found smaller than the value $M_N g_A/f_\pi$ which is expected by the GTRs.

In Fig. 5.21 we present the pion-nucleon and the pion-nucleon-Δ form factor at all pion masses using all three discretization schemes considered here. $G_{\pi NN}(Q^2)$ and $G_{\pi N\Delta}(Q^2)$ can be related via the GTRs to $G_p(Q^2)$ and $C_6^A(Q^2)$ respectively, of which we know the

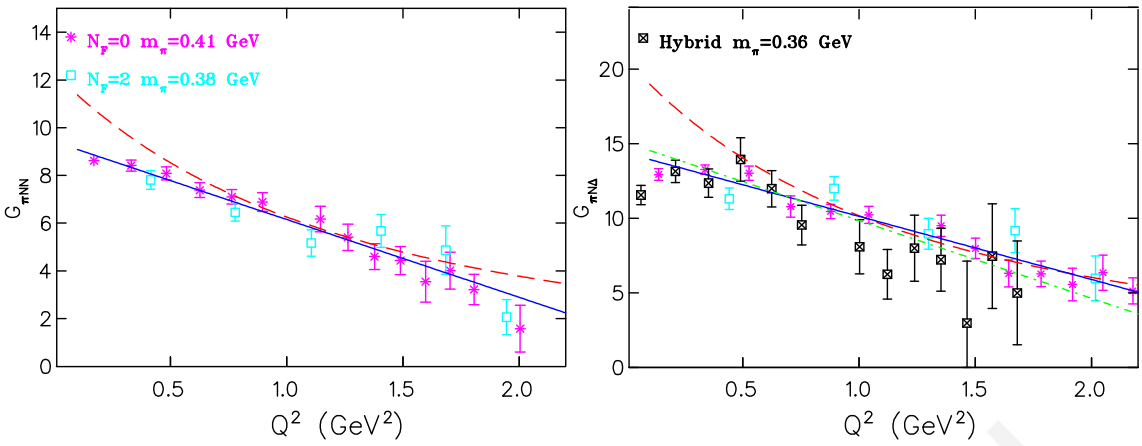

Figure 5.20: The pion-nucleon form factor (left) using Wilson dynamical (open squares) and Wilson quenched (asterisks) at the lightest pion mass available and the pion-nucleon-Δ form factor (right) additionally in the hybrid scheme at the lowest pion mass (inscribed squares). The dashed lines show the form expected by Eq. (5.16) using the fitted dipole forms for $G_A(Q^2)$ and $C_5^A(Q^2)$. The solid curves are the result of fitting to Eq. (5.48). We include the curve $G_{\pi N\Delta}(Q^2) = 1.6\, G_{\pi NN}(Q^2)$ denoted by the dash-dotted line, obtained by fitting a constant to the ratio $G_{\pi N\Delta}(Q^2)/G_{\pi NN}(Q^2)$.

Q^2 dependence from Eq. (5.46). Thus the pion-nucleon form factor is given by:

$$G_{\pi NN}(Q^2) = K_N \frac{Q^2/m_\pi^2 + 1}{(Q^2/m^2 + 1)(Q^2/m_A^2 + 1)^2} \tag{5.49}$$

where we can fit to obtain K_N and all other parameters are taken from Tables 5.1 and 5.3. An equivalent relation holds for the pion-nucleon-Δ form factor. From K_N and $K_{N\Delta}$ we extract the strong couplings $g_{\pi NN}$ and $g_{\pi N\Delta}$ respectively. These are shown in Table 5.4. We see that the value of the pion-nucleon strong coupling obtained is smaller than the experimental value of $13.21^{+0.11}_{-0.05}$ [98] and decreases with decreasing pion mass. This is due to the fact that the $G_{\pi NN}$ form factor has a weaker Q^2 dependence than what is expected by PCAC at low momentum transfer. If, on the other hand, we use $G_{\pi NN}(Q^2) = (M_N/f_\pi)\, G_A(Q^2)$ to extract $g_{\pi NN}$ we obtain the more reasonable value of $g_{\pi NN} = 11.8(3)$.

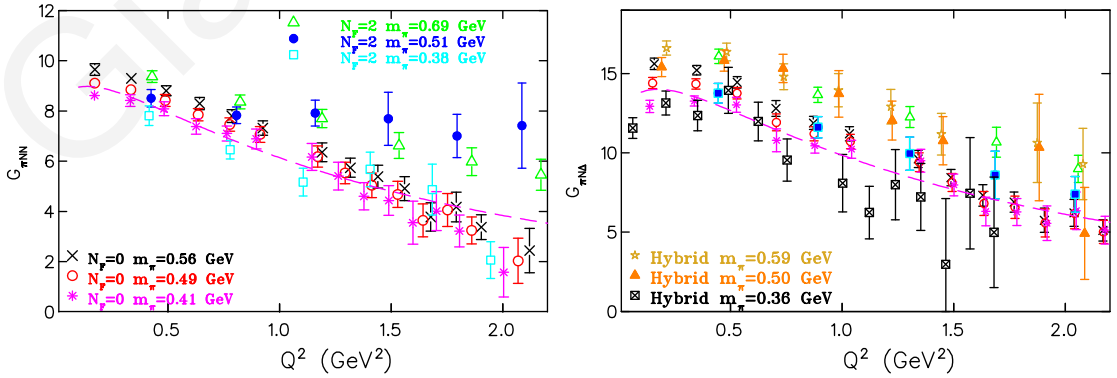

Figure 5.21: The pion-nucleon form factor (left) and the pion-nucleon-Δ form factor (right) with the notation of Fig. 5.14. The dashed curves show fits to Eq. (5.49) adjusting only K_N for the lightest pion mass of the quenched case.

Table 5.4: The parameters Δ and Δ′ obtained by fitting $G_{\pi NN}$ and $G_{\pi N\Delta}$ respectively to Eq. 5.48. The first column for $g_{\pi NN}$ and $g_{\pi N\Delta}$ is obtained by fitting to Eq. 5.48 while the second column is obtained by fitting to Eq. 5.49.

Nucleon elastic			
m_π (GeV)	Δ	$g_{\pi NN}$	
Quenched Wilson fermions			
0.563(4)	0.110(2)	9.943(99)	10.609(73)
0.490(4)	0.083(2)	9.126(93)	10.143(91)
0.411(4)	0.062(2)	8.410(100)	9.725(140)
$N_F = 2$ dynamical Wilson fermions			
0.691(8)	0.114(3)	11.48(245)	10.486(122)
0.509(8)	0.038(15)		9.071(294)
0.384(8)	0.044(10)		8.613(551)
Nucleon to Δ			
m_π (GeV)	Δ′	$g_{\pi N\Delta}$	
Quenched Wilson fermions			
0.563(4)	0.106(2)	16.560(194)	17.174(166)
0.490(4)	0.079(2)	14.692(188)	16.195(206)
0.411(4)	0.052(2)	12.609(180)	14.873(264)
$N_F = 2$ dynamical Wilson fermions			
0.691(8)	0.109(2)		17.536(190)
0.509(8)	0.063(2)		14.970(452)
0.384(8)	0.024(15)		12.685(1.416)
Hybrid action			
0.594(1)	0.076(5)		17.649(236)
0.498(3)	0.0648(7)		17.329(496)
0.353(3)	0.036(5)	12.282(289)	13.472(487)

5.4 Summary of Results

In this chapter we have presented a study of the axial nucleon form factors G_A and G_p and of the corresponding axial nucleon to Δ transition form factors C_5^A and C_6^A. We have also evaluated the pion-nucleon and the pion-nucleon-Δ form factors. We have shown results on ratios of these form factors that are expected to show weak quark mass dependence and thus can be compared to results extracted experimentally. Within this analysis we have reached a number of phenomenologically important conclusions. We have seen that $G_{\pi NN}$ and $G_{\pi N\Delta}$ have the same momentum dependence by showing that their ratio is constant and equal to 1.60(2) which is in agreement with what is expected phenomenologically. Similarly the ratio $2C_5^A(Q^2)/G_A(Q^2)$ is also Q^2 independent and equal to 1.61(1). Equality of these two ratios is expected if the Goldberger-Treiman relations hold, as is equality with the ratio $8C_6^A(Q^2)/G_p(Q^2)$ which, however, is found to be about 7% larger. We check pion pole dominance of the ratios $G_p(Q^2)/G_A(Q^2)$ and $C_6^A(Q^2)/C_5^A(Q^2)$ which is again expected phenomenologically. Both Wilson quenched and dynamical as well as results obtained in the hybrid scheme are described by a larger pole mass than m_π.

We have additionally presented results on the form factors separately. Comparison between hybrid and quenched results shows that unquenching effects are large, most notably at small momentum transfer, compared to what we observe when comparing ratios. This is another confirmation that pion cloud effects may be large at low momentum transfers as we go to smaller pion masses. The momentum dependence of the nucleon axial form factor G_A and the nucleon to Δ axial transition form factor C_5^A is well described by a dipole form. For the case of G_A we obtain an axial dipole mass m_A around 1.5 GeV compared to experiment which yields m_A=1.1 GeV. Our results also confirm the conclusions reached in a recent lattice study of the axial charge g_A [88]. Namely we find that this increases when using dynamical configurations, coming closer to experiment as compared to using quenched configurations.

Comparing the momentum dependence of the pion-nucleon form factor $G_{\pi NN}$ and of the pion-nucleon-Δ form factor $G_{\pi N\Delta}$ with what is expected phenomenologically we find discrepancies at low Q^2. As we have seen, these form factors increase less rapidly as $Q^2 \to 0$ than the expected dipole form. Because of this behavior the strong couplings $g_{\pi NN}$ and $g_{\pi N\Delta}$ extracted are smaller than what is obtained experimentally. To evaluate these form factors we need the renormalized quark mass which we have calculated on the lattice using the axial Ward-Takahashi identity. The axial Ward identity has $\mathcal{O}(a)$ corrections for the case of Wilson fermions which become more significant as the pion mass goes to zero. Domain wall fermions have corrections to the Ward identity due to the residual quark mass which is in turn due to the finite size of the fifth dimension. Even so, the renormalized quark mass can not account for discrepancies of the momentum dependence of the form factors since it is only a multiplicative constant at a given pion mass. Further investigation of the observed discrepancies requires the evaluation of these form factors at smaller pion masses where the question of the importance of pion cloud effects can be addressed. Such calculations will be possible in the near future since simulations at such pion masses are already underway.

Chapter 6

Δ Electromagnetic Form Factors

In Chapters 3 and 4 we have presented a lattice evaluation of the nucleon electromagnetic form factors as well as the nucleon to Δ electromagnetic transition form factors. In this chapter we present results on the electromagnetic form factors of the Δ [51, 99]. This study completes the investigation of the electromagnetic form factors of the nucleon/Δ system. As mentioned in the previous chapter, the Δ, being a spin-3/2 particle, has a spectroscopic quadrupole moment and thus a possible asymmetry in its charge distribution can be investigated by studying its electromagnetic form factors.

The very short lifetime ($\sim 6{\cdot}10^{-24}$ s) of the Δ baryon means that experimentally its form factors are notoriously difficult to measure experimentally. However the measurement of the Δ^+ magnetic moment has been carried out in Ref. [100] and of the Δ^{++} in Ref. [101]. A review of these experimental results can be found in Ref. [102]. The uncertainty accompanying these results is large, and the magnetic moment of the Δ^{++} is quoted to be between 3.7 μ_N and 7.5 μ_N [102]. Given this experimental situation, it is thus of interest to evaluate this quantity from first principles on the lattice. Furthermore, a non-zero value for the Δ quadrupole form factor would indicate that the Δ-baryon is deformed and would thus complement the calculation of the electric and Coulomb quadrupole form factors of the nucleon to Δ electromagnetic transition.

An early lattice calculation in quenched QCD of these form factors has been carried out in Ref. [103]. This calculation used sequential inversion through the insertion thus requiring a new inversion for each different lattice momentum. We apply the techniques developed in our previous studies to the evaluation of the Δ electromagnetic form factors. We obtain results using the large $32^3 \times 64$ quenched lattices and Wilson $N_F = 2$ lattices as well as using the hybrid action involving domain wall valence quarks and dynamical sea quarks. One of the main goals is to calculate the sub-dominant electric quadrupole form factor since a non-zero value signals deformation in the Δ. For this purpose we construct an optimized sequential source that isolates the quadrupole form factor from the dominant ones.

6.1 Lattice Formulation

The Δ electromagnetic matrix element is given by:

$$\langle \Delta(p',s')|j^{\mu}|\Delta(p,s)\rangle = \left(\frac{M_{\Delta}^2}{E_{\Delta}(p)E_{\Delta}(p')}\right)^{1/2} \bar{u}_{\sigma}(p',s')\mathcal{O}_{\sigma\mu\tau}u_{\tau}(p,s), \tag{6.1}$$

where $\bar{u}$ and u are spin-3/2 spinors in the Rarita-Schwinger formalism. The matrix element $\mathcal{O}_{\sigma\mu\tau}$ is given by:

$$\mathcal{O}_{\sigma\mu\tau} = -\delta_{\sigma\tau}\left[a_1(q^2)\gamma_{\mu} - i\frac{a_2(q^2)}{2M_{\Delta}}(p+p')\right] + \frac{q^{\sigma}q^{\tau}}{4M_{\Delta}^2}\left[c_1(q^2)\gamma_{\mu} - i\frac{c_2(q^2)}{2M_{\Delta}}(p+p')\right], \tag{6.2}$$

where c_1, c_2, a_1 and a_2 are the electromagnetic form factors of the Δ. These can be expressed in terms of the multipole form factors:

$$\begin{aligned}
G_{E0}(q^2) =& (1+\frac{2}{3}\frac{q^2}{4M_{\Delta}^2})\left[a_1(q^2) + (1+\frac{q^2}{4M_{\Delta}^2})a_2(q^2)\right] \\
&- \frac{1}{3}\frac{q^2}{4M_{\Delta}^2}(1+\frac{q^2}{4M_{\Delta}^2})\left[c_1(q^2) + (1+\frac{q^2}{4M_{\Delta}^2})c_2(q^2)\right], \\
G_{E2}(q^2) =& \left[a_1(q^2) + (1+\frac{q^2}{4M_{\Delta}^2})a_2(q^2)\right] - \frac{1}{2}(1+\frac{q^2}{4M_{\Delta}^2})\left[c_1(q^2) + (1+\frac{q^2}{4M_{\Delta}^2})c_2(q^2)\right], \\
G_{M1}(q^2) =& (1+\frac{4}{5}\frac{q^2}{4M_{\Delta}^2})a_1(q^2) - \frac{2}{5}\frac{q^2}{4M_{\Delta}^2}(1+\frac{q^2}{4M_{\Delta}^2})c_1(q^2), \\
G_{M3}(q^2) =& a_1(q^2) - \frac{1}{2}(1+\frac{q^2}{4M_{\Delta}^2})c_1(q^2).
\end{aligned} \tag{6.3}$$

The electric charge form factor G_{E0} and the magnetic dipole form factor G_{M1} are dominant while the electric quadrupole G_{E2} and the magnetic octapole G_{M3} form factors are sub-dominant. The matrix element is evaluated through the calculation of a three-point function:

$$\begin{aligned}
&G^{\Delta_{\sigma} j^{\mu} \Delta_{\tau}}(t_2,t_1;\vec{p}',\vec{p};\Gamma) = \\
&\qquad \sum_{\vec{x}_1,\vec{x}_2} e^{-i\vec{x}_2\cdot\vec{p}'}\langle\Omega|\Gamma^{\beta\alpha}\chi_{\alpha}^{\Delta_{\sigma}}(\vec{x}_2,t_2)j_{\mu}(\vec{x}_1,t_1)\bar{\chi}_{\beta}^{\Delta_{\tau}}|\Omega\rangle e^{-i\vec{x}_1\cdot(\vec{p}'-\vec{p})}.
\end{aligned} \tag{6.4}$$

The interpolating operator for the Δ is the same as that used in the evaluation of the nucleon to Δ form factors in the previous chapter (Eq. (4.9)). For the case of Wilson fermions we use the lattice conserved current in Eq. (3.8). For the hybrid calculation we use the local current. As in the case of the nucleon form factors, the three-point function has a contribution from a disconnected diagram. Assuming isospin symmetry between up and down quarks, we can avoid computing this disconnected quark loop by opting to calculate the isovector form factors of the Δ baryon, i.e. the form factors of the isovector current: $\bar{u}\gamma_{\mu}u - \bar{d}\gamma_{\mu}d$.

The three-point function is traced with a projection matrix Γ, given in Eq. (3.6). As in

the previous chapters, combinations of these matrices are used in order to isolate specific form factors. To cancel unknown overlaps with the initial and final states as well as cancel the exponentials appearing in the three-point function we construct a ratio with a combination of two-point functions similar to that presented in the previous chapters given by:

$$R_{\sigma\tau}(t_2,t_1,\vec{p}',\vec{p};\Gamma;\mu) = \frac{G^{\Delta j^\mu \Delta}_{\sigma\tau}(t_2,t_1;\vec{p}',\vec{p};\Gamma)}{G^{\Delta\Delta}_{ii}(t_2,\vec{p}';\Gamma_4)} \times \left[\frac{G^{\Delta\Delta}_{ii}(t_2-t_1,\vec{p};\Gamma_4)G^{\Delta\Delta}_{ii}(t_1,\vec{p}';\Gamma_4)G^{\Delta\Delta}_{ii}(t_2,\vec{p}';\Gamma_4)}{G^{\Delta\Delta}_{ii}(t_2-t_1,\vec{p}';\Gamma_4)G^{\Delta\Delta}_{ii}(t_1,\vec{p};\Gamma_4)G^{\Delta\Delta}_{ii}(t_2,\vec{p};\Gamma_4)}\right]^{1/2}. \tag{6.5}$$

In the large time limit where excited states are suppressed, this ratio becomes time independent:

$$R_{\sigma\tau}(t_2,t_1,\vec{p}',\vec{p};\Gamma;\mu) \xrightarrow[t_1\gg 1]{t_2-t_1\gg 1} \Pi_{\sigma\tau}(\vec{p}',\vec{p},\Gamma,\mu). \tag{6.6}$$

The Δ two-point function is given by

$$G^{\Delta\Delta}_{\sigma\sigma}(t,\vec{p},\Gamma) = \sum_{\vec{x}} e^{-i\vec{p}\cdot\vec{x}}\Gamma^{\beta\alpha}\langle\Omega|\chi^{\Delta}_{\alpha}{}^{\sigma}(\vec{x},t)\bar{\chi}^{\Delta}_{\beta}{}^{\sigma}(\vec{0},0)|\Omega\rangle, \tag{6.7}$$

where the Rarita-Schwinger spin sum rule for spin-3/2 spinors given in Eq. (4.6) has been used and the projection matrices, Γ, are given in Eq. (3.6). For the special case where the projection matrix is Γ_4 and the spinor index σ is summed over the spacial components, as in the case of the two-point functions that enter the ratio, this gives:

$$\sum_{i=1}^{3} G^{\Delta\Delta}_{ii}(t,\vec{p},\Gamma_4) \xrightarrow{t\gg 1} |Z_\Delta(\vec{p})|^2 \frac{2}{3}\frac{E_\Delta(\vec{p})}{2M_\Delta^2}\left[E_\Delta(\vec{p})+M_\Delta\right]e^{-E_\Delta(\vec{p})t}. \tag{6.8}$$

We use the fixed-sink sequential inversion method to sum over the sink coordinate of the three-point function. We thus need to fix the sink momentum prior to the sequential inversion. We work in the frame where the final state is at rest i.e. $\vec{p}' = 0$. By momentum conservation this means that the momentum of the initial state, $\vec{p}$, is related to the momentum transfer $\vec{q}$ by $\vec{q} = -\vec{p}$. The ratio of Eq. (6.5) in this reference frame is given by:

$$\Pi_{\sigma\tau}(\vec{0},-\vec{q},\Gamma,\mu) = \left(\frac{3}{2}\right)^{1/2}\left[\frac{2E_\Delta(\vec{q})}{M_\Delta}+\frac{2E^2_\Delta(\vec{q})}{M^2_\Delta}+\frac{E^3_\Delta(\vec{q})}{M^3_\Delta}+\frac{E^4_\Delta(\vec{q})}{M^4_\Delta}\right]^{-1/2}\times \mathrm{Tr}\left[\Gamma\Lambda_{\sigma\sigma'}(p)\mathcal{O}_{\sigma'\mu\tau}\Lambda_{\tau'\tau}(p')\right], \tag{6.9}$$

where

$$\Lambda_{\sigma\tau}(p) = \frac{-i\not{p}+M_\Delta}{2M_\Delta}[\delta_{\sigma\tau}+2p_\sigma p_\tau 2M^2_\Delta - i\frac{p_\sigma\gamma_\tau - p_\tau\gamma_\sigma}{3M_\Delta}-\frac{1}{3}\gamma_\sigma\gamma_\tau], \tag{6.10}$$

and the trace in Eq. (6.9) is meant over Dirac indices. Performing the sum over the sink coordinate with a sequential inversion through the sink means we can set the current

direction μ after the sequential inversion. We however need to choose the projection matrix Γ and spinor indices σ and τ prior to the inversion since these enter the sequential source. To gain as many measurements of a single form factor with only one inversion we thus construct optimal sources by linear combinations of the indices of the ratio in Eq. (6.9). We take three such linear combinations:

$$\begin{aligned}
S_1(\vec{q};\mu) =& \sum_{j=1}^{3} \varepsilon_{jkl}\Pi_{kl}(0,-\vec{q},\Gamma_4,\mu) \\
=& \mathcal{K}(q)\frac{5i(E_\Delta(\vec{q})+M_\Delta)}{18M_\Delta^2}[\delta_{1,\mu}(q_3-q_2)+\delta_{2,\mu}(q_1-q_3)+\delta_{3,\mu}(q_2-q_1)]G_{M1}(q), \\
S_2(\vec{q};\mu) =& \sum_{j=1}^{3} \Pi_{jj}(0,-\vec{q},\Gamma_4,\mu) \\
=& \mathcal{K}(q)\left[-G_{E0}(q)\frac{E_\Delta(\vec{q})+2M_\Delta}{2M_\Delta^2}iq^\mu - G_{E2}(q)\frac{(E_\Delta(\vec{q})-M_\Delta)^2}{9M_\Delta^3}\right]iq^\mu \\
S_3(\vec{q};\mu) =& \sum_{j=1}^{3} \varepsilon_{jkl}\Pi_{kl}(0,-\vec{q},\Gamma_k,\mu) = \mathcal{A}_k^\mu(q)G_{E2}(q)+\mathcal{B}_k^\mu(q)G_{M1}(q)+\mathcal{C}_k^\mu(q)G_{M3}(q),
\end{aligned} \tag{6.11}$$

where:

$$\mathcal{K}(q) = \left(\frac{3}{2}\right)^{1/2}\left[\frac{2E_\Delta(\vec{q})}{M_\Delta}+\frac{2E_\Delta^2(\vec{q})}{M_\Delta^2}+\frac{E_\Delta^3(\vec{q})}{M_\Delta^3}+\frac{E_\Delta^4(\vec{q})}{M_\Delta^4}\right]^{-1/2}. \tag{6.12}$$

$\mathcal{A}_k^\mu$, $\mathcal{B}_k^\mu$ and $\mathcal{C}_k^\mu$ are complicated kinematic factors which we shall omit writing out explicitly here. For completeness they are given in Appendix D. As can be seen, the combination S_1 isolates the G_{M1} form factor. The kinematic factors $\mathcal{B}_k^\mu$ and $\mathcal{C}_k^\mu$ vanish for $\mu = 4$ and thus $S_3(\vec{q},\mu=4)$ isolates the sub-dominant G_{E2} form factor. We can then extract the electric charge form factor G_{E0} using S_2 and hence the magnetic octapole G_{M3} from S_3. In practice, as explained in Chapter 3, this is all done by solving an over-complete set of equations, through the singular value decomposition of the matrix of kinematic factors $D(\vec{q},\mu)$ in:

$$P(\vec{q},\mu) = D(\vec{q},\mu)\cdot F(Q^2) \tag{6.13}$$

where P is a vector of lattice measurements and F is a vector of the form factors we want to compute.

6.2 Lattice Parameters

For the results that follow we have used the three ensembles of Wilson quenched and the three ensembles of Wilson N_F=2 configurations used in the calculation of the nucleon and nucleon to Δ transition form factors (Chapters 3 and 4). We additionally use the large $28^3 \times 64$ MILC lattice in the hybrid scheme at $m_\pi = 0.353(2)$ GeV used to calculate the nucleon to Δ transition form factors. We list the parameters of the calculation, as well as the mass of the Δ for the gauge configurations used in Table 6.1.

Table 6.1: Details of the gauge configuration ensembles used in this calculation. The Wilson dynamical configurations at $\kappa = 0.1575$ and $\kappa = 0.1580$ are taken from [8] while the ensemble at $\kappa = 0.15825$ was taken from [45].

number of confs	κ	m_π (GeV)	M_Δ (GeV)
	Quenched $32^3 \times 64$ $a^{-1} = 2.14(6)$ GeV		
200	0.1554	0.563(4)	1.470(15)
200	0.1558	0.490(4)	1.425(16)
200	0.1562	0.411(4)	1.382(15)
	κ_c =0.1571	0.	
	Unquenched $24^3 \times 40$ $a^{-1} = 2.56(10)$ GeV		
185	0.1575	0.691(8)	1.687(15)
157	0.1580	0.509(8)	1.559(19)
	Unquenched $24^3 \times 32$ $a^{-1} = 2.56(10)$ GeV		
200	0.15825	0.384(8)	1.395(18)
	$\kappa_c = 0.1585$	0.	

number of confs	$(am_{\mathrm{u,d/s}})^{\mathrm{Asqtad}}$	$(am_{\mathrm{u,d}})^{\mathrm{DWF}}$	m_π (GeV)	M_Δ (GeV)
	Volume: $28^3 \times 64$, b.c: antiperiodic			
300	0.01/0.05	0.0138	0.353(2)	1.533(27)

We use Wuppertal smearing with HYP smeared gauge links entering the Wuppertal smearing hopping matrix are used on the initial and final states to increase overlap with the Δ state. Setting the sink-source separation was based on our experience from the previous calculations. For the quenched calculation this is set to t_2/a=11 time-slices, for the Wilson N_F=2 to t_2/a=12 time-slices and for the hybrid we use t_2/a=8.

6.3 Lattice Results

In Fig. 6.1 we show the Δ electric charge form factor computed using quenched Wilson fermions as a function of the pion mass squared. As can be seen the dependence on m_π^2 is linear, hence we perform a linear extrapolation to the physical point in the same manner as in Chapter 3. In Fig. 6.3 we show the Δ electric charge form factor at the three pion masses of the quenched lattices. On the same graph we plot the form factor obtained by a linear extrapolation to the physical pion mass. In Fig. 6.4 we present G_{E0} at the lightest mass of the three discretization schemes considered. From this figure we can conclude that unquenching effects are small for this quantity since Wilson quenched and unquenched are consistent. The agreement between the Wilson data and the hybrid results is non-trivial since these two schemes carry different finite lattice spacing effects. The consistency means that lattice artifacts are under control. The data are well described by a dipole form:

$$G_{E0}(Q^2) = \frac{1}{(1 + Q^2/M_{E0})^2}, \tag{6.14}$$

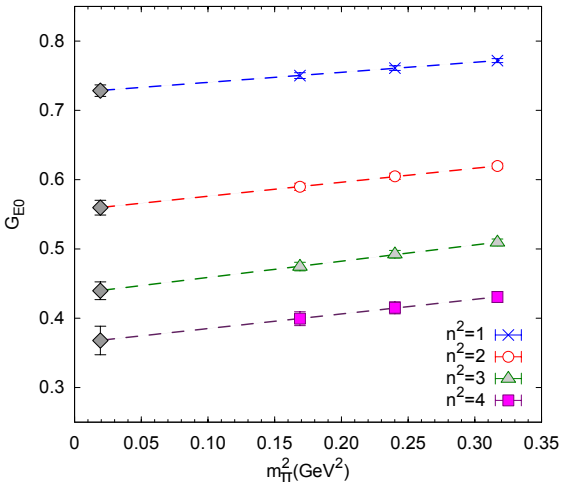

Figure 6.1: The electric charge form factor using quenched Wilson quarks as a function of the pion mass squared for the four smallest non-zero momentum transfers. The rhombuses show the linearly extrapolated value for the form factor at the physical pion mass.

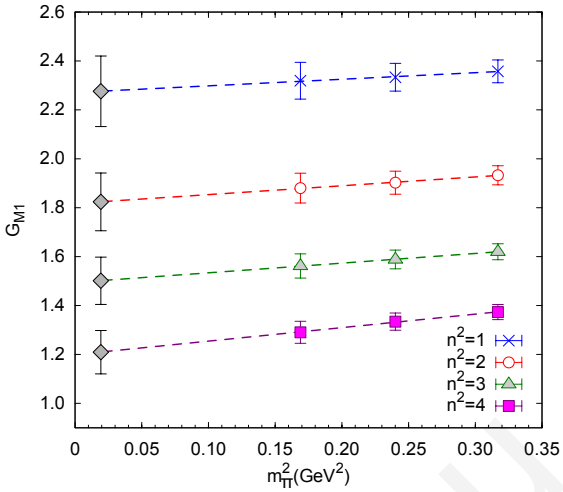

Figure 6.2: The magnetic dipole form factor using quenched Wilson quarks as a function of the pion mass squared for the four smallest non-zero momentum transfers. The notation is the same as that of Fig. 6.1.

as can be seen by the curves plotted along with the data in Figs. 6.3 and 6.4. Fitting to this form we can extract the Δ charge radius since, in the non-relativistic limit, it is associated with the slope of the form factor:

$$\langle r^2 \rangle = -6 \frac{\partial}{\partial Q^2} G_{E0}(Q^2)\Big|_{Q^2=0} = \frac{12}{M_{E0}}. \tag{6.15}$$

This is done for the form factor obtained by extrapolating to the physical point the quenched results, where we gain an estimate for the charge radius of $\langle r^2 \rangle^{1/2} = 0.691(6)$ fm. For the lightest pion mass in the Wilson N_F=2 calculation we obtain $\langle r^2 \rangle^{1/2} = 0.634(9)$ fm and for the hybrid calculation we obtain $\langle r^2 \rangle^{1/2} = 0.629(6)$ fm. These values are in agreement with the value of 0.63(7) fm computed in Ref. [103]. The results for the charge radius at each pion mass are listed in Table 6.2.

In Fig. 6.5 we show the magnetic dipole form factor for the three pion masses in the quenched case. The dependence on the pion mass of this form factor is similar to that of G_{E0}, namely that it decreases linearly with the pion mass squared as can be seen in Fig. 6.2, thus we linearly extrapolate to the physical pion mass. In Fig. 6.6 we show the G_{M1} form factor at the lightest pion mass of the three discretization schemes used. As in the case of the G_{E0}, the data are well described by the dipole form:

$$G_{M1}(Q^2) = \frac{G_{M1}(0)}{(1 + Q^2/M_{M1})^2}. \tag{6.16}$$

Since the kinematic factors multiplying G_{M1} vanish at $Q^2 = 0$, we extrapolate the data

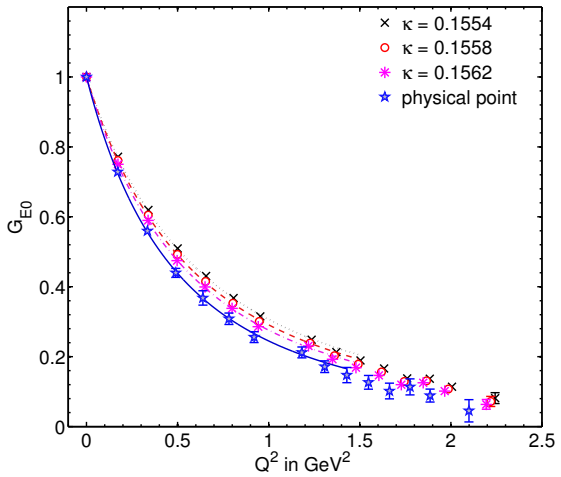

Figure 6.3: The electric form factor G_{E0} for the quenched case at three pion masses: $m_\pi = 0.563(4)$ GeV (crosses), $m_\pi = 0.490(4)$ GeV (open circles) and $m_\pi = 0.411(4)$ GeV (asterisks). The open stars show the result of the linear extrapolation to the physical pion mass. The curves are fits to a dipole form (Eq. (6.14)).

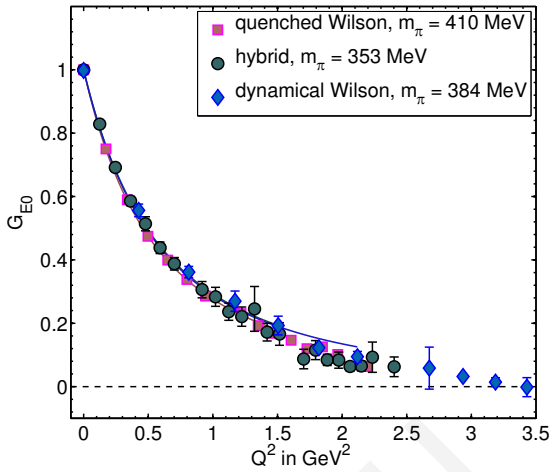

Figure 6.4: The electric form factor G_{E0} for the lightest pion mass in all three discretization schemes used: Filled squares for the quenched case at $m_\pi = 0.411(4)$ GeV, filled rhombus for the Wilson dynamical calculation at $m_\pi = 0.384(8)$ GeV and filled circles for the hybrid calculation at $m_\pi = 0.353(2)$ GeV.

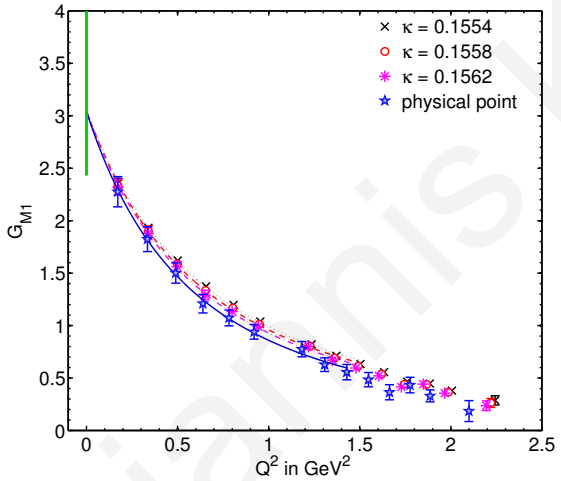

Figure 6.5: The magnetic dipole form factor G_{M1} of the Δ, in the quenched case. The notation is the same as in Fig. 6.3. The vertical band at $Q^2 = 0$ shows the range of experimental results cited in Ref. [102].

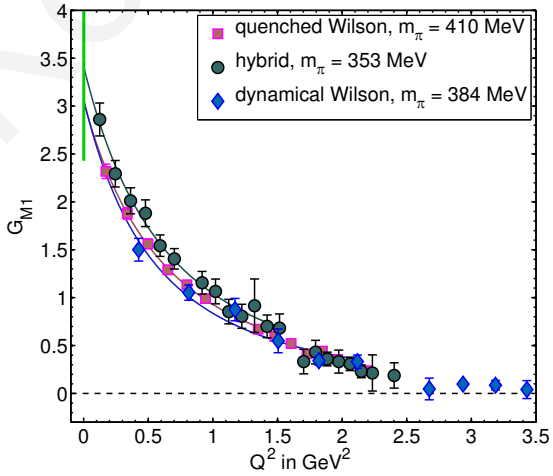

Figure 6.6: The magnetic dipole form factor G_{M1} of the Δ, for the lightest pion mass of the three discretization schemes considered. The notation is the same as in Fig. 6.4. The vertical band at $Q^2 = 0$ shows the range of experimental results cited in Ref. [102].

to zero momentum transfer by fitting to Eq. (6.16) in order to calculate the magnetic moment of the Δ: $\mu_{\Delta^+} = G_{M1}(0)(\frac{e}{2M_\Delta})$. The wide range of experimental results for this quantity is shown in Fig 6.5 by the vertical band at $Q^2 = 0$. The extracted values for $G_{M1}(0)$ obtained using the dipole form are listed in Table 6.2. Our value for the magnetic

Table 6.2: The charge radius and $G_{M1}(0)$ obtained by fitting the form factors at each pion mass as described in the text. For the quenched case we additionally show $G_{E2}(0)$, since the data are accurate enough to do so. We linearly extrapolate the quenched data to the physical pion mass, and fit to this form factor to obtain the parameters at $m_\pi = 0.135$ GeV.

m_π (GeV)	$\langle r^2\rangle^{\frac{1}{2}}$	$G_{M1}(0)$	$G_{E2}(0)$
	Wilson $N_F = 0$		
0.563(4)	0.614(2)	3.05(7)	−0.6(3)
0.490(4)	0.632(2)	3.05(8)	−0.7(4)
0.411(4)	0.650(3)	3.05(10)	−0.7(4)
0.135	0.691(6)	3.04(21)	

m_π (GeV)	$\langle r^2\rangle^{\frac{1}{2}}$	$G_{M1}(0)$
	Wilson $N_F = 2$	
0.691(8)	0.530(2)	3.04(22)
0.509(8)	0.595(1)	3.35(34)
0.385(8)	0.634(9)	3.07(51)
	Hybrid	
0.353(2)	0.629(6)	3.42(20)

moment is 2.32(16) μ_N at the physical pion mass for the quenched case. For the Wilson $N_F = 2$ calculation we obtain $\mu_{\Delta^+} = 2.33(39)\mu_N$ at the lightest pion mass and for the hybrid action $\mu_{\Delta^+} = 2.60(15)\mu_N$. The most recent experiment [101] which measured the Δ^{++} magnetic moment finds $\mu_{\Delta^{++}} = 2\mu_{\Delta^+} = 6.14(51)\mu_N$. The Δ^+ magnetic moment was measured in Ref. [100] and found at a value of $\mu_{\Delta^+} = (2.7 \pm 1 \pm 1.5 \pm 3)\mu_N$. The value quoted by the particle data group [102] for the Δ^{++} magnetic moment is 3.7–7.5 μ_N. Finally, a lattice measurement of the Δ^+ magnetic moment found in Ref. [104] finds this at $1.6(3)\mu_N$ at a pion mass of ∼0.3 GeV.

The electric quadrupole form factor is phenomenologically interesting since it probes the Δ deformation. Non-relativistically, the quadrupole moment $\mathcal{Q}$ of a particle is given by:

$$\mathcal{Q} = \frac{G_{E2}(0)}{M^2} = \int d^3r \bar{\psi}(\vec{r})(3z^2 - r^2)\psi(\vec{r}), \tag{6.17}$$

where $\psi(\vec{r})$ is the wave function of the particle in the maximum spin projection state, in this case $m_z = 3/2$. A positive quadrupole moment means the particle has a prolate shape while a negative quadrupole moment means an oblate distribution. In Fig. 6.7, we show the G_{E2} for all pion masses of the quenched case. The form factor is clearly negative, and increases in amplitude with decreasing pion mass. This means that the Δ is an oblate, with deformation that increases as we approach the chiral limit. The worse errors do not allow an accurate extrapolation to the chiral limit and therefor we present values of $G_{E2}(0)$ at the three pion masses obtained by fits to a dipole form. The extracted parameters of the fit are given in Table 6.2. The values we find for the quadrupole moment are compatible with $G_{E2}(0) = -0.4(14)$ obtained in Ref. [103]. In Fig. 6.8 we show the electric quadrupole moment using quenched and N_F=2 Wilson fermions and using the hybrid action. For dynamical Wilson fermions we can only obtain reliable results for two values of the momentum transfer. For the hybrid case we obtain results which are systematically negative albeit with large errors.

The results for the octapole magnetic form factor are very noisy, as can be seen in Fig. 6.9 where we show results for the quenched calculation at three pion masses. The

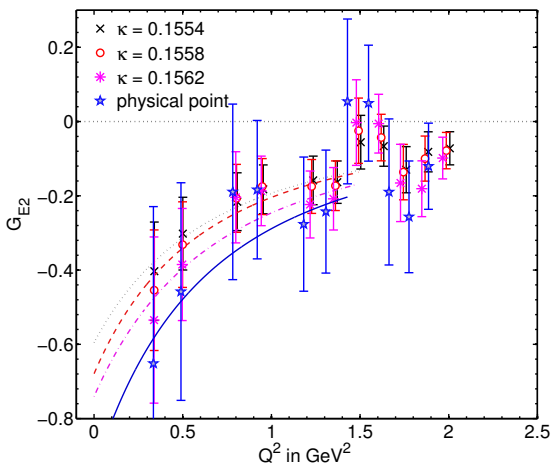

Figure 6.7: The electric quadrupole form factor G_{E2} of the Δ, in the quenched case. The notation is the same as in Fig. 6.3.

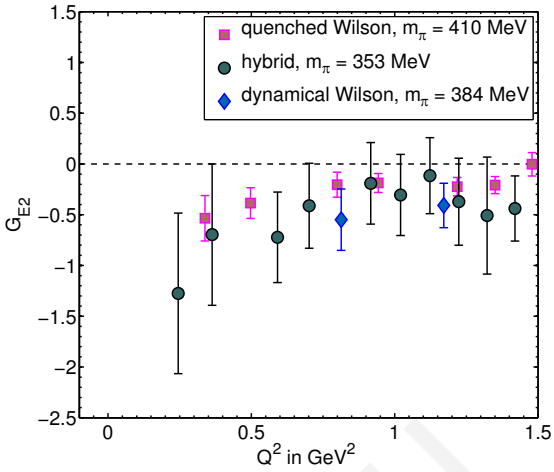

Figure 6.8: The electric quadrupole form factor G_{E2} of the Δ, for the lightest pion mass of the three discretization schemes considered. The notation is the same as in Fig. 6.4.

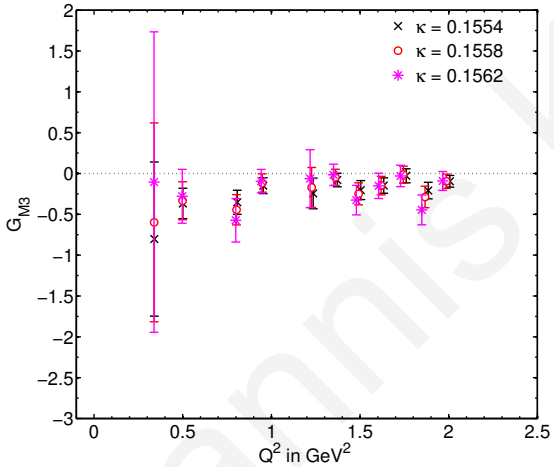

Figure 6.9: The magnetic octapole form factor G_{M3} of the Δ, in the quenched case. The notation is the same as in Fig. 6.3.

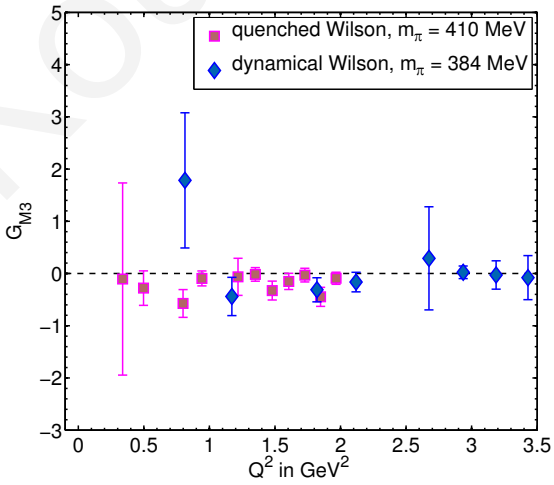

Figure 6.10: The magnetic octapole form factor G_{M3} of the Δ, for the lightest pion mass of the Wilson quenched (filled squares) and Wilson N_F=2 (filled rhombus) calculations. The hybrid calculation is omitted since statistical errors are too large for meaningful comparisons.

errors are even larger for the hybrid case. We include a figure where we show the lightest pion mass of the Wilson dynamical case for completeness in Fig. 6.10. Within these large errors, this form factor is consistent with zero. This is in fact expected from a chiral perturbation theory analysis carried out to leading order [105].

6.4 Summary of Results

In this chapter we have presented a calculation of the Δ electromagnetic form factors in lattice QCD. This calculation improved on several aspects of an early calculation carried out in quenched lattice QCD [103]. We use two dynamical flavors of Wilson fermions and a hybrid action where we use domain wall fermions for the valence sector and N_F=2+1 staggered sea quarks. The three-point function is evaluated by carrying out the sequential inversion through the sink, allowing evaluation of the form factors at any momentum transfer with no extra inversions. We use three carefully selected sequential sources so that for certain directions of the current insertion we isolate specific form factors. We show for the first time in lattice QCD that the electric quadrupole form factor is non-zero which means the Δ is deformed.

For the pion masses considered in the quenched case, the form factors decrease linearly with decreasing pion mass thus we extrapolate linearly to the physical point. The results are well described by a dipole form. We fit the electric charge form factor to a dipole form to obtain the r.m.s. radius of the Δ. We find an r.m.s. radius of 0.691(6) fm at the physical point using the quenched lattices. Using Wilson $N_F = 2$ we find $\langle r^2 \rangle^{1/2} = 0.634(9)$ fm at $m_\pi = 0.385(8)$ GeV and for the hybrid case $\langle r^2 \rangle^{1/2} = 0.629(6)$ fm at $m_\pi = 0.353(2)$ GeV. The magnetic dipole form factor is fitted to obtain the magnetic moment. The value that we find is $\mu_{\Delta^+} = 2.32(16)\mu_N$ by extrapolating the results obtained in the quenched case to the physical pion mass. This value is in agreement with the values computed with Wilson dynamical quarks at the lightest pion mass ($\mu_{\Delta^+} = 2.33(39)\mu_N$) and in the hybrid scheme ($\mu_{\Delta^+} = 2.60(15)\mu_N$) as well as with the range 3.7–7.5 μ_N quoted by the particle data group [102].

A very important conclusion of this study is the negative sub-dominant electric quadrupole form factor. The accuracy obtained for this quantity is due to the improvements applied. For the unquenched lattices this form factor is very noisy, giving a reliable estimate for only two momentum transfers for the Wilson dynamical case. A negative electric quadrupole means an oblate charge distribution, and from the quenched study we see that this deformation increases as we approach the chiral limit. The magnetic octapole form factor is very noisy and within error bars is consistent with zero at all pion masses. This is in agreement with a chiral perturbation analysis to leading order that shows that G_{M3} is zero in the chiral [105].

Chapter 7

Density-Density Correlators

In Chapters 3 and 4 we presented studies on the nucleon and nucleon to Δ transition form factors. The nucleon to Δ electromagnetic transition form factors, measured experimentally provide an indirect way to investigate the question of nucleon deformation. On the lattice this required the calculation of a three-point function, for which we employed several improvement techniques such as the sequential inversion which allowed the extraction of these quantities to very high accuracy. These calculations additionally allowed comparison with experiment as well as quantitative results on phenomenologically interesting quantities such as charge radii and magnetic moments.

In this chapter we shall address the question of hadron deformation in a more direct manner. Namely, we present a calculation where the quark distribution in the hadron is probed explicitly by means of using density operators. The equal-time density-density correlator [106, 107] for a given hadron state H, is defined by:

$$\tilde{C}_H(\vec{x}_2, t_1) = \int d^3x_1 \langle H | j_0^u(\vec{x}_2 + \vec{x}_1, t_1) j_0^d(\vec{x}_1, t_1) | H \rangle \tag{7.1}$$

where j_0^q is the normal ordered density operator : $\bar{q}\gamma_0 q$:. This quantity provides in the non-relativistic limit a gauge invariant definition of the hadron wave function. The combination of the two sums projects the state to zero momentum. By construction, the sum over the sink coordinate cannot be carried out through a sequential inversion as was done for the case of the three-point function. Thus the challenging aspect of investigating hadron deformation through this method is the fact that the all-to-all propagator must be computed. A study has been carried out in the quenched approximation [108]. In this work the density-density correlator was calculated approximately, since summation of the sink coordinate was neglected consequently eliminating the need for an all-to-all propagator. The large time separation between source and sink was thus relied upon to project out the zero momentum state. The calculation showed a deformation in the ρ-meson charge distribution as well as a slightly non-spherical Δ-baryon as the pion mass decreased. The study was carried out for relatively heavy pion masses ($\sim$ 600 MeV) and on lattices of about 1.5 fm spatial extent.

In what follows we shall present results for the pion, the ρ-meson, the nucleon and the Δ density-density correlator with several improvements compared to the quenched calculation [109]. The most significant of these improvements is the fact that here we compute

the all-to-all propagator and thus carry out the sum over the sink spatial coordinates to explicitly project the hadronic state to zero momentum. Additionally, we use the three ensembles of $N_F = 2$ Wilson dynamical configurations used in the previous calculations which give access to pion masses as low as ~ 0.38 GeV [8, 45]. The large number of inversions needed for the all-to-all propagator currently prohibits the extension of this calculation to the hybrid scheme. A third improvement we shall introduce in this calculation is the application of the Liverpool one-end trick to the meson density-density correlator. As explained in Chapter 2, the one-end trick provides a clever way of combining solution vectors in order to obtain meson two-point functions summed over both source and sink coordinates without having to carry out both sums explicitly [110]. As we shall see, this can be implemented for the case of the meson four-point function [111] thus suppressing stochastic noise considerably.

7.1 Lattice Formulation

We consider the equal-time density-density correlator:

$$G^{Hj^0j^0H}(\vec{x}_2, t_1) = \sum_{\vec{x}} \sum_{\vec{x}_1} d^3x_1 \langle \Omega | \chi_H(\vec{x}, t) j_0^u(\vec{x}_2 + \vec{x}_1, t_1) j_0^d(\vec{x}_1, t_1) \bar{\chi}_H(\vec{x}_0, t_0) | \Omega \rangle \tag{7.2}$$

where $\chi_H(x)$ is an interpolating operator with the quantum numbers of the lowest lying hadron. The two sums in Eq. (7.2) ensure the state is projected to zero momentum; one sum sets the momentum of the sink equal to that of the source while the other sets both to zero. This can be shown explicitly by inserting three complete sets of states in Eq. (7.2) giving:

$$\begin{aligned} \sum_{\vec{p},n,n_i,n_f} & \langle \Omega | \chi_H | n_f, \vec{0} \rangle \frac{e^{-E_{n_f}(\vec{0})(t-t_1)}}{2E_{n_f}(\vec{0})} \langle n_f, \vec{0} | j_0^u | n, \vec{p} \rangle \frac{e^{i\vec{p}\cdot\vec{x}_2}}{2E_n(\vec{p})} \times \\ & \langle n, \vec{p} | j_0^d | n_i, \vec{0} \rangle \frac{e^{-E_{n_i}(\vec{0})(t_1-t_0)}}{2E_{n_i}(\vec{0})} \langle n_i, \vec{0} | \bar{\chi}_H | \Omega \rangle. \end{aligned} \tag{7.3}$$

In the large $t_1 - t_0$ and $t - t_1$ limit we have:

$$\begin{aligned} G^{Hj^0j^0H}(\vec{x}_2) & \xrightarrow[t_1-t_0 \gg]{t-t_1 \gg} G^{Hj^0j^0H}(\vec{x}_2, t_1) \\ & = \sum_{\vec{p},n} |\langle \Omega | \chi_H | H \rangle|^2 \frac{e^{-m_H(t-t_0)}}{4m_H^2} \langle H | j_0^u | n, \vec{p} \rangle \frac{e^{i\vec{p}\cdot\vec{x}_2}}{2E_n(\vec{p})} \langle n, \vec{p} | j_0^d | H \rangle. \end{aligned} \tag{7.4}$$

If we divide by the hadron two-point function at zero momentum $G^{HH}(\vec{0}, t - t_0)$ then the exponential dependence on $t - t_0$ and overlaps cancel and we obtain the expectation value of the two density insertions, $\langle H | j_0^u(\vec{x}_2) j_0^d | H \rangle$. In the non-relativistic limit, this expectation value gives the charge distribution of the hadron. It can be written in terms

of the non-relativistic form factors [107]

$$\langle H|j_0^u(\vec{x}_2)j_0^d|H\rangle = \sum_{\vec{p},n} F_{Hn}^u(\vec{p})\frac{e^{i\vec{p}\cdot\vec{x}_2}}{2E_n(\vec{p})}F_{nH}^d(-\vec{p}) \tag{7.5}$$

where

$$F_{Hn}^u(\vec{p}) = \langle H|j_0^u|n,\vec{p}\rangle. \tag{7.6}$$

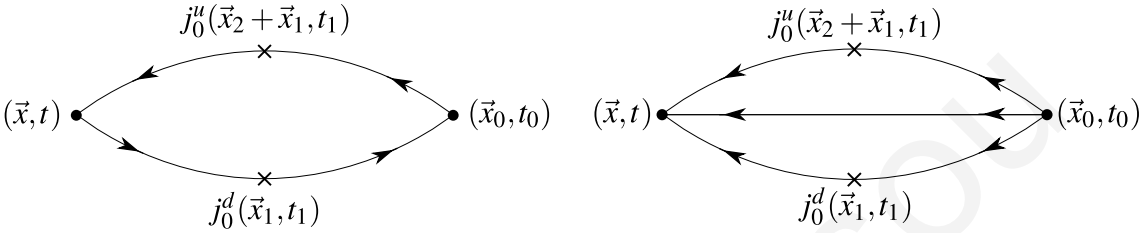

Figure 7.1: Equal-time density-density correlators for mesons (left diagram) and for baryons (right diagram).

In Fig. 7.1 we show the diagrams of the density-density correlators for mesons and baryons. In principle, if one wants the charge content of the baryons one would need a three-density correlator to probe for the distances of the two quarks relative to the third. The baryon diagram in Fig. 7.1 however, yields a correlator that depends only on one relative distance instead of two. Evaluation of the three-density correlator requires the evaluation of two types of five-point functions shown in Fig. 7.2. In Ref. [108] the three-density correlator – or five-point function – was evaluated neglecting the sum over the sink coordinate for the left of the two diagrams shown in Fig. 7.2 for which each quark line has only one density insertion. It was shown that integrating over one relative distance yields a correlator consistent with the corresponding two-density correlator. Therefore in this calculation we only consider two-density insertions for the case of baryons. This gives the distribution of one quark relative to the other irrespective of the position of the third. In other words, in the non-relativistic limit, it corresponds to the one-body charge distribution.

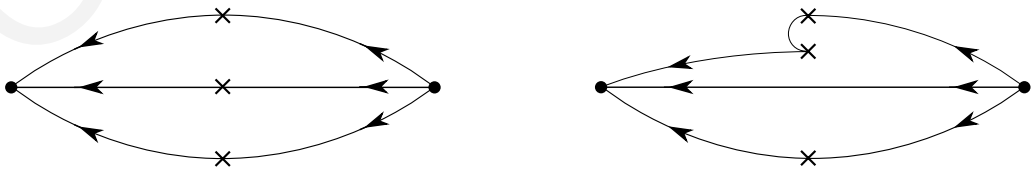

Figure 7.2: The three-density correlator for baryons.

As already mentioned the challenging aspect of this calculation is the explicit need of an all-to-all propagator. Carrying out the sum over the sink coordinate through a sequential inversion does not eliminate this need as was the case for three-point functions.

To be more specific, consider the arbitrary meson four-point function:

$$\sum_{\vec{x}_1,\vec{x}} G^{\chi_\Gamma j^0 j^0 \chi_\Gamma}(x,x_2,x_1,x_0) = \sum_{\vec{x}_1,\vec{x}} \langle\Omega|\chi_\Gamma(x) j_u^0(x_{2+1}) j_d^0(x_1)\bar{\chi}_\Gamma(x_0)|\Omega\rangle \tag{7.7}$$
$$= \sum_{\vec{x}_1,\vec{x}} \mathrm{Tr}\left[\Gamma G(x;x_1)\gamma_0 G(x_1;x_0)\bar{\Gamma} G(x_0;x_{2+1})\gamma_0 G(x_{2+1};x)\right]$$

where the interpolating operator is of the form $\chi(x) = \bar{d}(x)\Gamma u(x)$ as we have extensively used in Chapter 2, $\bar{\Gamma} = \gamma_0\Gamma^\dagger\gamma_0$ and $x = (\vec{x},t)$, $x_{2+1} = (\vec{x}_2+\vec{x}_1,t_1)$, $x_1 = (\vec{x}_1,t_1)$ and $x_0 = (\vec{x}_0,t_0)$. As can be seen, the summation over $\vec{x}_1$ involves the spatial coordinate of both insertions. Hence a sequential inversion over the sink would not eliminate the need for an all-to-all propagator.

For the computation of the four-point function we use stochastic techniques to estimate the all-to-all propagator. We have introduced these techniques in Chapter 2. We thus replace each propagator of which a sum is needed over both ends, by the cross product of a set of solution vectors with their corresponding noise vectors:

$$G(x;y) = \frac{1}{N_r}\sum_r \phi(x)_r \otimes \xi^\dagger(y)_r, \tag{7.8}$$
$$\Rightarrow \sum_{\vec{x}_1,\vec{x}} \mathrm{Tr}\left[G(x_1;x_0)\bar{\Gamma}G(x_0;x_{2+1})\gamma_0 G(x_{2+1};x)\Gamma G(x;x_1)\gamma_0\right] =$$
$$\sum_{rr'}\frac{1}{N_r N_{r'}}\sum_{\vec{x}_1,\vec{x}} \mathrm{Tr}\left[G(x_1;x_0)\bar{\Gamma}G(x_0;x_{2+1})\gamma_0\phi(x_{2+1})_r \otimes \xi^\dagger(x)_r\Gamma\phi(x)_{r'}\otimes\xi^\dagger(x_1)_{r'}\gamma_0\right].$$

This can be trivially generalized to baryons. The point-to-all propagator from x_0 can be computed as usual using point sources and the propagator ending at x_0 can be obtained by conjugating this point-to-all propagator. For this calculation we thus need two sets of stochastic inversions, one with the stochastic source localized on the insertion time-slice (t_1) and one stochastic inversion from the sink time-slice (t). We will refer to this method as the direct method, since this involves directly substituting the all-to-all propagators with the solution-source cross product.

As already mentioned, we can alternatively compute the meson four-point function using the one-end trick which has the additional advantage of summing over the source coordinate automatically. To see how this can be implemented, we first define a set of spin diluted noise vectors:

$$\xi^a_\mu(x)_{(r,\sigma)} = \xi^a(x)_r\delta_{\mu\sigma}. \tag{7.9}$$

This is the same dilution we used for the two-point function one-end trick in Chapter 2. Consider additionally that these noise vectors are localized on a given time-slice, i.e. $\xi^a_\mu(\vec{x},t)_r = \xi^a_\mu(\vec{x})_r\delta(t-t_0)$. We use the same notation for the solution vectors as we have in Chapter 2:

$$\phi^a_\mu(x;t_0)_{(r,\sigma)} = \sum_{x_0} G^{ab}_{\mu\nu}(x;x_0)\xi^b_\nu(x_0)_{(r,\sigma)} = \sum_{\vec{x}_0} G^{ab}_{\mu\nu}(\vec{x},t;\vec{x}_0,t_0)\xi^b(\vec{x}_0)_r\delta_{\sigma\nu}. \tag{7.10}$$

Now consider the propagator:

$$S^{ab}_{\mu\nu}(\Gamma; x; y; t_0) \equiv \sum_r \phi^a_\mu(x; t_0)_{(r,\sigma)} \Gamma_{\sigma\kappa} \phi^{*b}_\nu(y; t_0)_{(r,\kappa)}, \tag{7.11}$$

where $x = (\vec{x}, t_x)$ and $y = (\vec{y}, t_y)$. The sum over the stochastic ensemble gives rise to delta functions after we replace the solution vectors with Eq. (7.10) giving:

$$\begin{aligned} S^{ab}_{\mu\nu}(\Gamma; x; y; t_0) &= \sum_{\vec{x}_0, \vec{y}_0} G^{aa'}_{\mu\sigma}(\vec{x}, t_x; \vec{x}_0, t_0) \Gamma_{\sigma\kappa} G^{*bb'}_{\nu\kappa}(\vec{y}, t_y; \vec{y}_0, t_0) \delta_{a'b'} \delta(\vec{x}_0 - \vec{y}_0) \\ &= \sum_{\vec{x}_0} G(\vec{x}, t_x; \vec{x}_0, t_0) \Gamma \, G^\dagger(\vec{y}, t_y; \vec{x}_0, t_0) \Big|^{ab}_{\mu\nu}. \end{aligned} \tag{7.12}$$

The combination:

$$\sum_{\vec{x}_1} \mathrm{Tr} \left[\gamma_5 \gamma_0 S(\bar{\Gamma} \gamma_5; x_1; x_{2+1}; t_0) \gamma_5 \gamma_0 S(\gamma_5 \Gamma; x_{2+1}; x_1; t) \right], \tag{7.13}$$

gives the meson four-point function (Eq. (7.8)) summed over both source and sink coordinates. This is the generalization of the one-end trick to meson four-point functions. As in the case of two-point functions, the additional sum over the source coordinate is expected to outweigh stochastic noise. It is apparent that for this method we need two sets of stochastic inversions; one with the noise vectors localized on the source time-slice and one with the noise vectors localized on the sink time-slice.

The generalization to baryons is not as straight forward. Briefly, for the case of the density-density correlator, the odd number of quark lines means we cannot combine solution vectors in such a way so that pairs of source vectors appear to eventually give delta functions. On the other hand, the one-end trick could be applicable to the three-density baryon correlator for the case where each quark line carries a density insertion. In this case we have an even number of quark lines and thus pairs of noise vectors arise giving delta functions. In what follows, we do not consider five point functions, hence we only compute the one-body baryon wave function using the direct method.

7.2 Lattice Parameters and Optimization

In this study we computed the density-density correlator for the pion and ρ-meson using both the direct method and using the one-end trick. We additionally computed the nucleon and the Δ density-density correlators using the direct method. Since we are interested in detecting an intrinsic asymmetry in the hadrons, we must use interpolating operators that select a physical spin projection. For the mesons we use:

$$\chi_M(x) = \bar{d}(x) \Gamma u(x) \tag{7.14}$$

where $\Gamma = \gamma_5$ for the pion and $\Gamma = \{\frac{\gamma_1 - i\gamma_2}{2}, \gamma_3, \frac{\gamma_1 + i\gamma_2}{2}\}$ for the $m_z = +1, 0$ and -1 spin projections of the ρ-meson. For the nucleon we use the interpolating operator used so far:

$$\chi_N(x) = \varepsilon^{abc} u^{a\top}(x)(C\gamma_5)d^b(x)u^c(x), \tag{7.15}$$

and for the delta we use the $m_z = \pm 3/2$ spin projections:

$$\begin{aligned} \chi_{\Delta_{+\frac{3}{2}}} =& \frac{\epsilon^{abc}}{\sqrt{3}} \left[u_1^a (2u^{b\top} C\Gamma_+ d^c) + d_1^a (u^{b\top} C\Gamma_+ u^c) \right] \\ \chi_{\Delta_{-\frac{3}{2}}} =& \frac{\epsilon^{abc}}{\sqrt{3}} \left[u_2^a (2u^{b\top} C\Gamma_- d^c) + d_2^a (u^{b\top} C\Gamma_- u^c) \right] \end{aligned} \tag{7.16}$$

with $\Gamma_\pm = \frac{\gamma_1 \mp i\gamma_2}{2}$.

The calculation is carried out on the unquenched Wilson configurations quoted in Table 3.1. Once again we use Wuppertal smeared initial and final states with HYP smeared gauge links entering the source smearing to improve ground state dominance of the correlator. For the direct method we need a stochastic inversions from the insertion and sink time-slices hence we must fix both prior to the inversions. We take $t_1 - t_0 = 5a$ and $t - t_0 = 10a$ or 0.38 fm or 0.77 fm respectively. Based on the optimizations carried out in the previous chapters, these source-sink separations are large enough to ensure excited states have been suppressed at the insertion time-slice. For the case of the one-end trick we set the sink 14 time-slices or ~ 1 fm from the source. As we shall see, the improvement in statistics gained from the one-end trick allows for such a relatively large separation. Consistency between results using the trick and the direct method will additionally reassure us the time separations chosen are large enough for ground state dominance. By construction of the one-end trick four-point correlator, we can vary the insertion time-slices arbitrarily. For all results that follow that where computed with the one-end trick we have set this to the midpoint between source and sink i. e. $t_1 - t_0 = 7a$.

We first give the details of the computation in the case of the direct method. We require two sets of stochastic propagators per configuration, one with the noise vectors localized on the insertion time-slice and one with the noise vectors localized on the sink. We also compute a point-to-all propagator from the source time-slice to all lattice sites. The noise vectors are diluted in color, spin and even-odd spatial sites. Dilution in time is automatic here since we invert with the noise vectors localized on a single time-slice. Thus each noise vector is diluted to twenty-four independent noise vectors requiring twenty-four times more inversions. The number of noise vectors used is determined through a tuning process. For this tuning the Δ-baryon correlator at the lightest pion mass is considered. By comparing the decrease of the relative statistical error when increasing on one hand statistics and on the other hand the number of noise vectors used, we determine the optimum number of stochastic vectors. For this tuning we use 50 configurations and compute the Δ-baryon correlator for three, six and nine such 24-fold diluted noise vectors. For N_r=3, 6 and 9 we find a relative statistical error of 50%, 20% and 16% respectively. The fact that

by doubling the number of noise vectors from 3 to 6 the statistical error decreases by more than one half is an indication that N_r=3 is too small yielding large stochastic noise. On the other hand, increasing the number of noise vectors from 6 to 9 the relative error decreases by $\sqrt{6/9}$, which is what is expected from scaling. This indicates that at this point increasing N_r or the number of configurations is equivalent. We thus fix the number of noise vectors to six. Since we carry out two sets of stochastic inversions, one at the sink and one at the insertion time-slice, and since we use color, spin and even-odd dilution we need 288 stochastic inversions per configuration. This amounts to a total of 300 inversions per density-density correlator if we additionally consider the point-to-all propagating from the origin. To increase statistics for the two ensembles corresponding to the two lightest pion masses needed for the baryons, we calculate density-density correlators using the first and second half time interval of each configuration. Furthermore, for the lightest pion mass we improve statistics by using N_r=9 noise vectors for the correlators. Thus for $\kappa = 0.1580$ we carry out 600 inversions per configuration while for $\kappa = 0.15825$ 888 inversions per configuration. For the case of the one-end trick we use $N_r = 8$. The one-end trick requires these to be spin diluted as in Eq. (7.9). Hence we need 32 inversions from the source and 32 from the sink thus 64 inversions per configuration.

7.3 Results

In Fig. 7.3 we show the pion correlator computed using the one-end trick and the direct method as a function of the distance from the origin. Being a function of the spatial coordinate $\vec{x}_2$, to plot the correlator with no averaging would over-clutter the graph. On the other hand, binning the data over a range Δr over the x axis would produce an inaccurate graph, since this would average out the spikes seen after about 0.8 fm, which are due to finite volume effects and which we shall investigate thoroughly further on. Thus we replace the points lying in a cell of size 0.015 fm$\times$0.05 by their average. The wave function is normalized by dividing by its value at the origin. The errors in Fig. 7.3 are additionally suppressed for clarity. As can be seen, we find that the two methods yield consistent results for the correlators, meaning excited state contributions between source and insertion and between insertion and sink time-slices have been effectively suppressed. Even with the errors omitted we see that at a given distance r, the correlator computed using the direct method shows more spread than the one computed using the one-end trick. That this reflects larger statistical noise is shown in Fig. 7.4, where we compare the relative errors of the two binned correlators. As can be seen, at large distances the maximum relative error exhibited by the one-end trick method is around 4% while for the direct method exceeds 10%. This is a direct consequence of the double sum accomplished with the implementation of the one-end trick. In addition, when using the one-end trick the density-density correlator of a state of spin projection $m_z = 0$ is symmetric under reflections of the spatial coordinates i.e. $C(\vec{r}) = C(-\vec{r})$ by construction whereas in the direct method it is symmetric only statistically. For the $m_z = \pm 1$ projections of the

vector meson we instead have $C^{m_z=+1}(\vec{r}) = C^{m_z=-1}(-\vec{r})$. Because of this symmetry we average over the results for the $m_z = +1$ and $m_z = -1$ spin projections and hereby denote this correlator by $m_z = \pm 1$. The same is done for the spin projections $m_z = \pm 3/2$ of the Δ. The reduction of the error by more than a factor two when using the one-end trick comes at a reduced computational cost. As already mentioned, for the one-end trick the computation of the correlator is done using 64 inversions while for the direct method we carried out 300 inversions per configuration i.e. we need 4.7 times less inversions for twice the accuracy. This clearly shows the superiority of the one-end trick, even more if we consider that the source-sink separation is larger in this case, given that the relative statistical error grows exponentially with this separation.

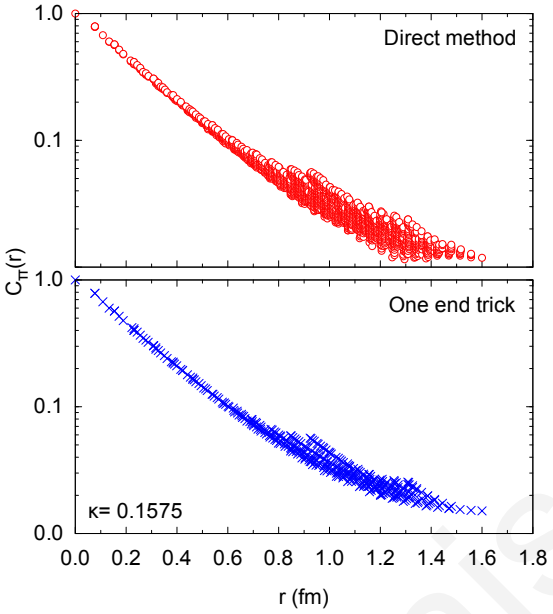

Figure 7.3: The pion density-density correlator using the one-end trick (upper graph) and using the direct method (lower graph). The data are averaged as described in the text and error bars are suppressed for clarity.

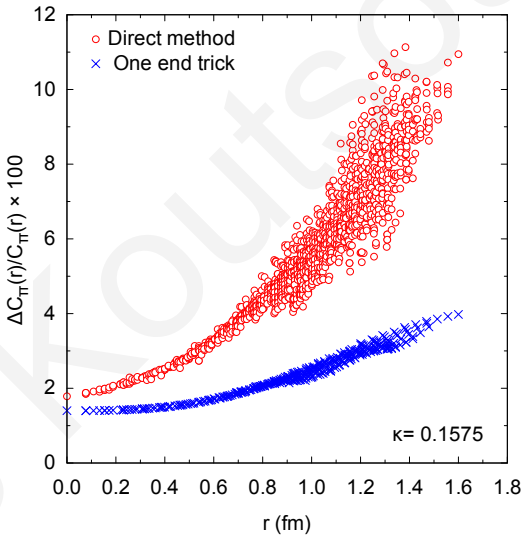

Figure 7.4: Comparison between the relative error of the correlator computed with the one-end trick (blue crosses) and the direct method (red circles).

One of the main goals of this calculation is to detect a possible asymmetry in the hadron charge distribution. In Fig. 7.5 we compare the two methods for the case of the $m_z = 0$ spin projection of the vector meson at the lowest pion mass available. Only the profile of the correlator along the three axes is plotted so that we can detect a possible asymmetry. As can be seen, an elongation along the z axis is observed in both cases. However, the error estimated in the direct method is not small enough to draw definite conclusions since the correlator along all three axes is consistent within error bars. On the other hand, by using the one-end trick the fluctuations due to stochastic noise are suppressed enough for one to come to the conclusion that the vector meson is indeed prolonged along the z axis. Having demonstrated the effectiveness of the one-end trick in suppressing stochastic noise, all meson observables that we present hereon are computed

with the one-end trick.

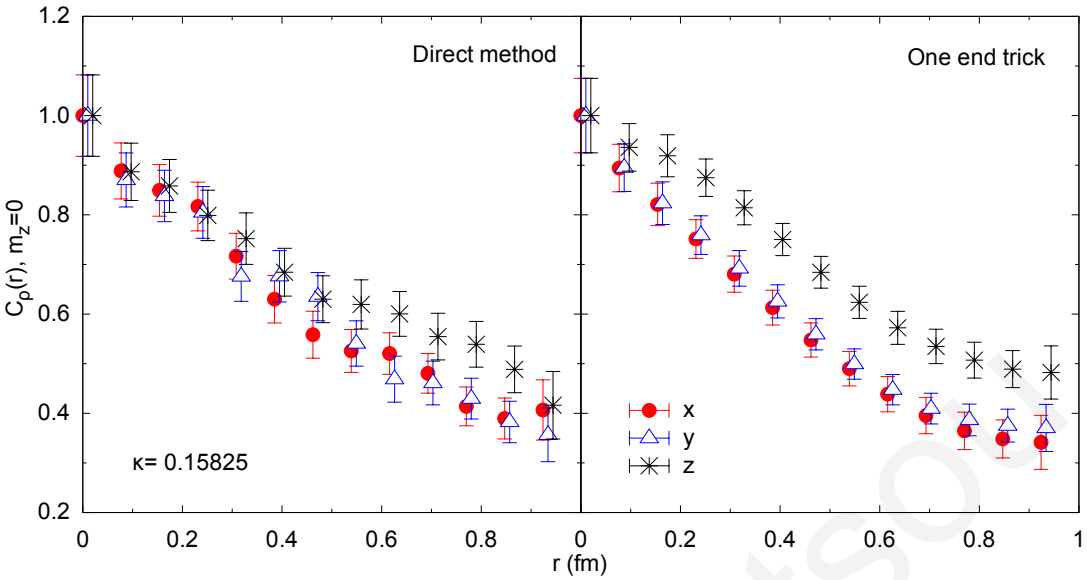

Figure 7.5: Comparison between the vector meson $m_z = 0$ correlator projected along the three axes computed with the direct method (left) and with the one-end trick (right).

In Fig. 7.6 we show the density-density correlators for the pion and the spin zero projection ($m_z = 0$) of the ρ-meson using the one-end trick and for the nucleon and spin $m_z = \pm\frac{3}{2}$ projection of the Δ using the direct method. All correlators are projected along the three axes to display a possible asymmetry. This is done for the largest pion mass available, namely $m_\pi = 0.691(8)$ GeV. As can be seen, a clear elongation of the vector meson along the z axis is observed even at this large pion mass confirming our previous results [108]. The asymmetry is clearly smaller than for the lightest pion mass shown in Fig. 7.5. On the other hand, the nucleon shows no asymmetry, at least within this method, while also for the case of the Δ no asymmetry is observed at this heavy pion mass.

To better visualize the asymmetry for the case of the vector meson, we show in Figs. 7.7 and 7.8 two-dimensional contour plots of the spin $m_z = 0$ and spin $m_z = \pm 1$ projections respectively. As can be seen, for the case of the $m_z = 0$ projection, the contours are elongated along the z axis as compare to a circle of radius equal to the smallest contour radius. The observation is consistent at all three pion masses showing a clear asymmetry. This leads to the conclusion that the vector meson in the spin projection zero state is prolate. On the other hand, the $m_z = \pm 1$ ρ-meson state, shown in Fig. 7.8, shows the opposite behavior. Namely the correlator is found to be larger along the x axis, as compared to a circle, evidence that in this spin state the ρ is in fact an oblate. This is in agreement with what is derived in Ref. [108] where it is shown that if the spin-0 state is a prolate the ± 1 channels will be oblate with about half the amount of deformation. The fact that the ρ-meson in its maximal spin projection state is an oblate is in agreement with a recent calculation of a negative electric quadrupole form factor evaluated in quenched lattice QCD [112].

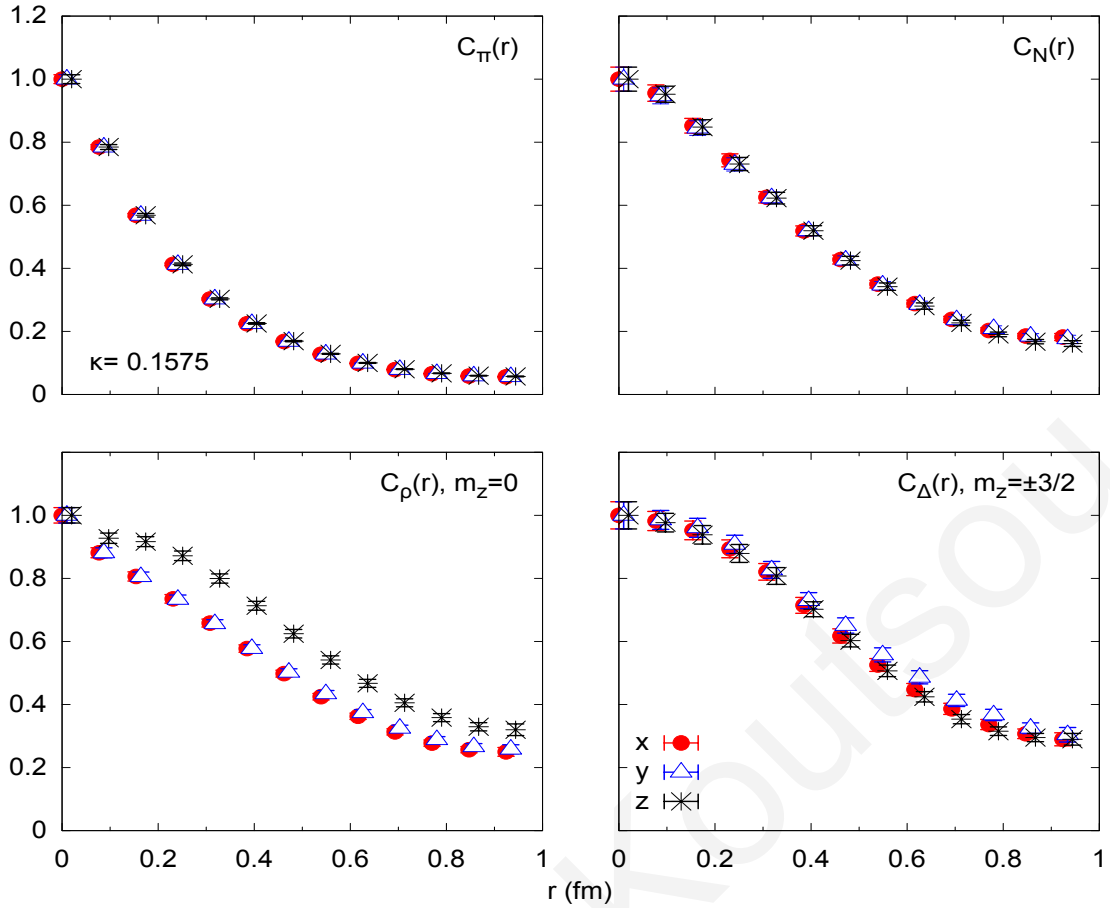

Figure 7.6: Projections of the pion (top left), the ρ-meson (bottom left), the nucleon (top right) and the Δ (bottom right) correlators projected on the three axes.

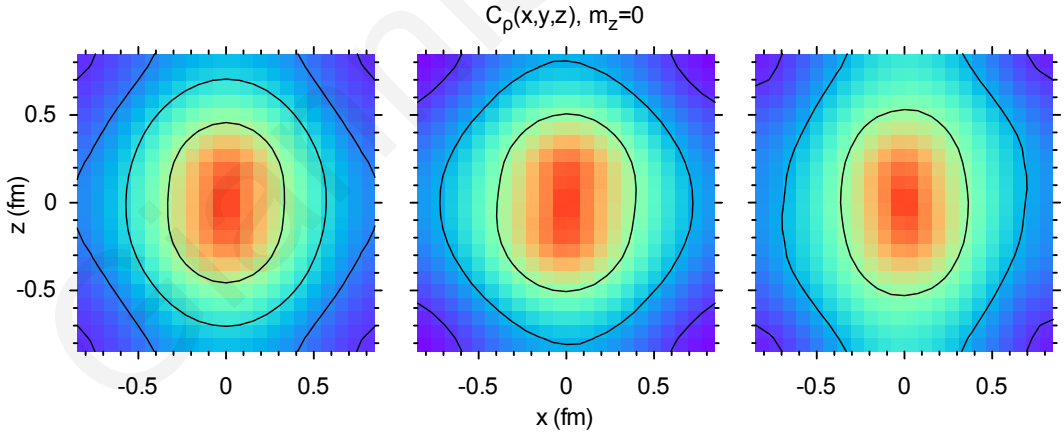

Figure 7.7: The correlator of the ρ-meson, $m_z = 0$ projected on the x - z plane for decreasing pion mass left to right. The dashed circles are to guide the eye.

7.3.1 Finite Volume Effects

Density-density correlators computed in a finite box with periodic boundary conditions are susceptible to finite volume effects. Finite volume effects mostly affect the tail of the

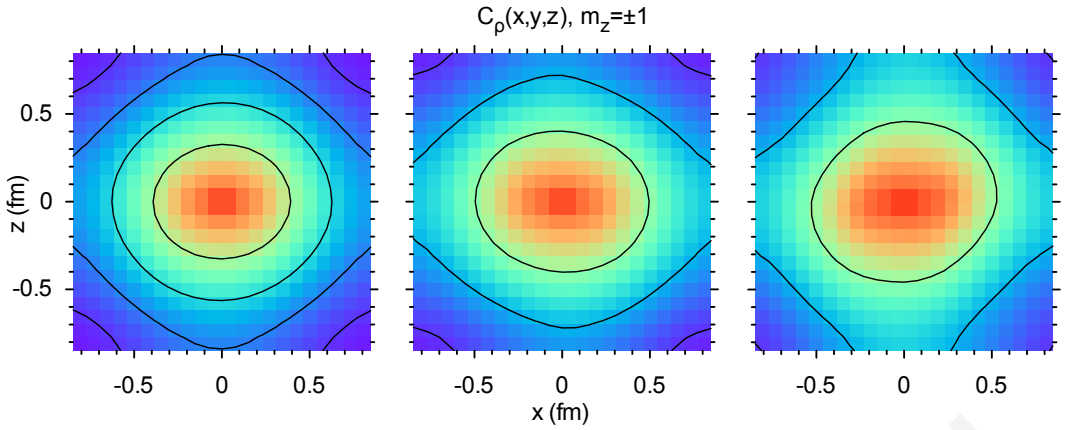

Figure 7.8: The correlator of the ρ-meson, $m_z = \pm 1$ projected on the x - z plane for decreasing pion mass left to right. The dashed circles are to guide the eye.

distributions and need to be corrected. To perform these corrections we follow the analysis developed in Ref. [107]. The density-density correlation function computed on a lattice of spatial dimension L can be written as an infinite sum over the Brillouin zones:

$$C(\vec{r}) = \sum_{\vec{n}=0}^{\infty} C_0(\vec{r} + \vec{n}L) \tag{7.17}$$

where $C(\vec{r})$ is the density-density correlator computed on the periodic lattice and $C_0(\vec{r})$ is the "correct" correlator that one would compute if the lattice were of infinite size. Thus the correlation function computed in a finite box with periodic boundary conditions is in fact a sum of all images arising from the surrounding boxes. Since $C_0(\vec{r})$ is a fast decaying function, approximated by an exponential or a Gaussian dependence on the distance from the origin, this means that the leading contributions to the sum come from the nearest neighboring Brillouin zones.

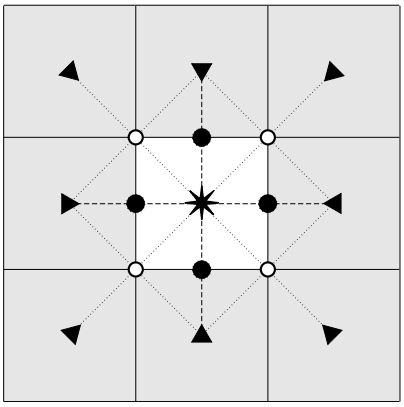

Figure 7.9: Two-dimensional example of image contributions. The correlator computed at the filled circles (open circles) is approximately two (four) times larger than the "correct" correlator.

A two-dimensional sketch is drawn in Fig. 7.3.1 that demonstrates the images that contribute to the correlator. In this figure, the asterisk shows the origin of the fundamental cell (white box) while the triangles show the origins of the neighboring cells (gray boxes). To first order, the correlator computed in the white box is a superposition of the correlator with origin the asterisk and the eight correlators with origins the filled triangles, in accord with the expression given in Eq. (7.17). Thus the correlator that we compute on a periodic lattice is overestimated. This is particularly severe close to the boundaries of the lattice where contributions from the images are largest. For example, the correlator at the distances indicated by the filled circles in Fig. 7.3.1 is approximately twice as large as the "correct" correlator since besides the contribution from the fundamental cell, a neighboring cell contributes equally as indicated by the dashed line. Similarly, the correlator computed at the distances indicated by the open circles at the corners of the fundamental cell is approximately four times larger since there are contributions from three neighboring cells, as shown by the dotted line.

This analysis can be extended to three dimensions. The correlator is twice as large at the six distances given by $\pm L/2\hat{n}_i, i = x, y, z$ where $\hat{n}_i$ is the unit vector in the i-direction. Similarly, the correlator is four times as large at the twelve distances $L/2(\hat{n}_i \pm \hat{n}_j), i \neq j$ and eight times as large at the eight corners $L/2(\pm\hat{n}_x \pm \hat{n}_y \pm \hat{n}_z)$. All results that have been discussed so far are for the correlators computed on the lattice with no corrections applied for the images. For the analysis of quantities, such as the root mean squared radius, that are sensitive to the long distance behavior of the distributions it is important to take in to account the image contributions and define a corrected correlator.

To correct for the images and extract $C_0(\vec{r})$ of Eq. (7.17) by knowing only $C(\vec{r})$ we need to have an Ansatz for the asymptotic behavior of $C_0(\vec{r})$. If the asymptotic behavior is known then we can subtract from the lattice data the contribution from the images, up to a given order, and extract $C_0(\vec{r})$. In this work, we consider only nearest neighbor contributions to the correlator. Thus Eq. (7.17) becomes:

$$C(\vec{r}) \simeq \sum_{|\vec{n}|\in[0,\sqrt{3}]} C_0(\vec{r} + \vec{n}L). \tag{7.18}$$

We make an Ansatz for the functional form of $C_0(\vec{r})$ that provides a good description of the data. For instance for the pion correlator that is found to be independent of the angles, a spherically symmetric Ansatz is used. We then perform a least squares fit to the lattice data of the sum given on the right hand side of Eq. (7.18) extracting the fit parameters of the function that describes $C_0(\vec{r})$. The corrected correlator is then constructed by subtracting from the lattice data the images determined from the fitted function to obtain:

$$C^{corr}(\vec{r}) = C(\vec{r}) - \sum_{|\vec{n}|\in(0,\sqrt{3}]} C_0(\vec{r} + \vec{n}L). \tag{7.19}$$

The Ansätze for $C_0(\vec{r})$ for each particle are summarized below:

$$\begin{aligned} C_0^{\pi} &= A_0 \exp\left(-m_0 r^{\sigma}\right), \\ C_0^{\rho} &= \left[A_0 \exp\left(-m_0 r^{\sigma}\right) + A_1 \exp\left(-m_1 r^{\sigma}\right) r^2 P_2(\cos\theta)\right]^2, \\ C_0^{N} &= \text{same as for } \pi, \\ C_0^{\Delta} &= \text{same as for } \rho. \end{aligned} \tag{7.20}$$

As can be seen, for the pion and the nucleon we take spherical functions. For the case of the ρ and the Δ we have parametrized the correlator in such a way so that an asymmetry is allowed. Since the spatial part of the correlators is even under reflection, only $L = 0$ and $L = 2$ angular momentum quantum numbers are allowed. Thus for the ρ-meson and the Δ we include an $L = 2$ component by including the Legendre polynomial $P_2(\cos\theta)$. The parameters reached to from the fits, at every pion mass are summarized in Table E.1 in Appendix E. For the case of the spin projection $m_z = 0$ ρ state, the asymmetric term with coefficient A_1 is found consistently non-zero and positive thus corroborating our findings so far that this spin state of the ρ is indeed elongated along the z-axis (prolate). On the other hand, the same parameter is consistently negative for the $m_z = \pm 1$ ρ channels pointing to a correlator larger at the equator (oblate).

In Figs. 7.10 and 7.11 we show a comparison between the raw lattice data and the lattice data after subtracting image contributions for the heaviest pion mass available. As can be seen, the correction procedure clearly compensates for the images, i.e. the spikes at $L/2$, $\sqrt{2}L/2$ and $\sqrt{3}L/2$ are corrected for, leading to a smoother correlator that decreases more rapidly at the tails.

Having corrected the data for the nearest images we can now proceed to a quantitative analysis of the particle charge distributions. In Table 7.1 we give $\langle x^2 + y^2 \rangle/2$, $\langle z^2 \rangle$ and their difference for each particle at each pion mass available. All errors are jack-knife errors. Here, the moments presented are computed using the corrected correlator:

$$\langle \mathcal{O} \rangle = \frac{\sum_{\vec{r}} \mathcal{O}(\vec{r}) C^{corr}(\vec{r})}{\sum_{\vec{r}} C^{corr}(\vec{r})}. \tag{7.21}$$

From the difference $\langle z^2 - \frac{x^2+y^2}{2} \rangle$ we see once again that the $m_z = 0$ projection of the ρ is larger along the z axis while the $m_z = \pm 1$ projections are larger along the equator. For the case of the baryons the results are inconclusive, even for this large number of stochastic inversions. Given the improvement obtained in the case of the mesons, implementing the one-end trick for the three-density baryon correlator is expected to suppress stochastic noise considerably, allowing concrete conclusions. This will additionally provide more detailed information, since the charge distribution will be available as a function of two coordinates, the relative distances of the two quarks from the third.

The asymmetry in the ρ can be reveal by a three-dimensional contour plot. In Figs. 7.12 and 7.13 we show contour surfaces for the ρ-meson in the $m_z = 0$ and $m_z = \pm 1$ channels

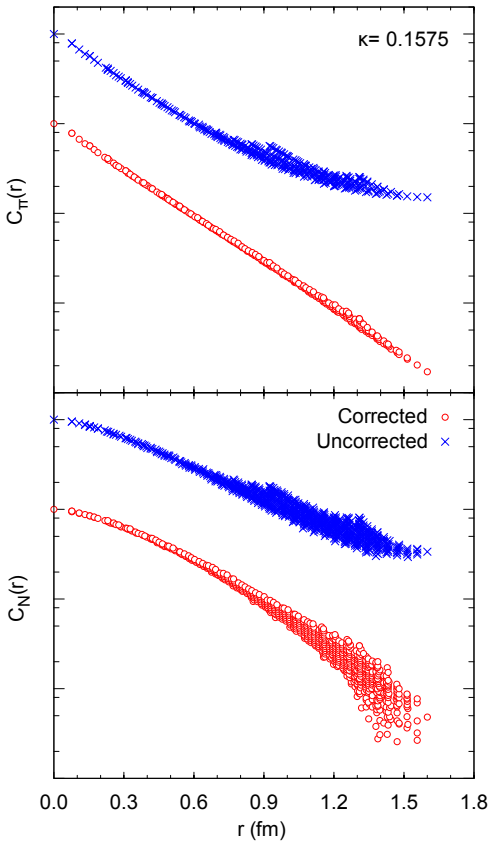

Figure 7.10: The pion correlator (top) and the nucleon correlator (bottom) as computed on the lattice (crosses) and corrected for the images of nearest neighboring lattices (open circles). The corrected correlator is divided by a factor of ten for clarity. Data are binned and error bars are omitted to avoid cluttering.

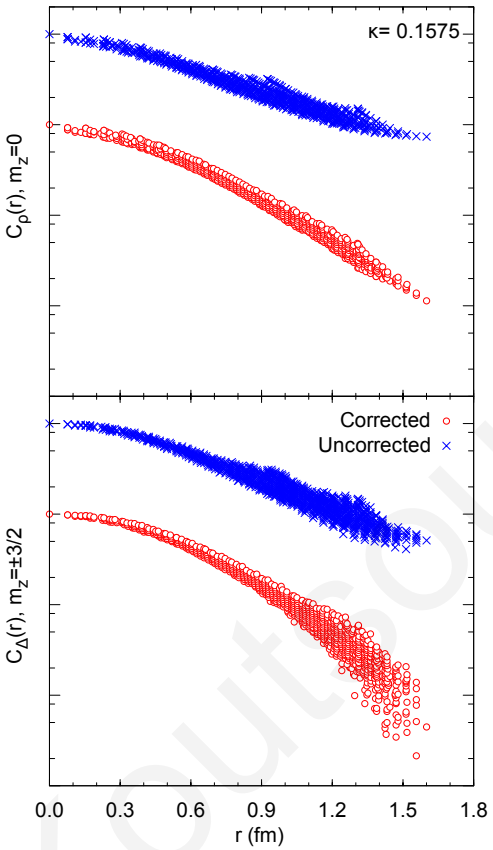

Figure 7.11: The ρ-meson, $m_z = 0$ correlator (top) and the Δ, $m_z = \pm 3/2$ correlator (bottom). The notation is the same as that of Fig. 7.10.

respectively, at the intermediate pion mass. The correlator is compared to a sphere centered at the origin. In both cases the contour is taken at approximately half the value of the correlator at the origin. Once again we see that the $m_z = 0$ state is elongated along the poles while the $m_z = \pm 1$ channels are flatter.

7.4 Summary of Results

In this chapter we have presented a direct method of investigating hadron deformation, namely through the calculation of density-density correlators. We have shown how one explicitly probes the charge distribution of a hadron to detect an intrinsic deformation, as opposed to the previous chapter where hadron deformation was derived from the spectroscopic quadrupole moment. The challenging aspect of this direct method is that an all-to-all propagator is needed which we use stochastic techniques to evaluate. Having the all-to-all propagator allowed summation over the sink coordinate of the correlator thus explicitly projecting the state to zero momentum. The pion, ρ-meson, nucleon and Δ

Table 7.1: $\langle x^2+y^2\rangle/2$, $\langle z^2\rangle$ and their difference for each particle at all three pion masses in fm^2, left for mesons and right for baryons. All errors are jack - knife errors.

m_π^2 (GeV^2)	$\langle\frac{x^2+y^2}{2}\rangle$	$\langle z^2\rangle$	$\langle z^2-\frac{x^2+y^2}{2}\rangle$
	π		
0.477	0.1449(6)	0.1460(7)	0.0011(8)
0.259	0.1542(7)	0.1531(9)	-0.0010(10)
0.147	0.1529(7)	0.1533(14)	0.0005(18)
	ρ, $m_z=0$		
0.477	0.174(2)	0.192(2)	0.018(3)
0.259	0.188(4)	0.196(6)	0.007(7)
0.147	0.190(5)	0.207(6)	0.016(7)
	ρ, $m_z=\pm1$		
0.477	0.183(1)	0.173(2)	-0.009(2)
0.259	0.199(2)	0.186(2)	-0.013(2)
0.147	0.200(4)	0.193(5)	-0.007(6)

$\langle\frac{x^2+y^2}{2}\rangle$	$\langle z^2\rangle$	$\langle z^2-\frac{x^2+y^2}{2}\rangle$
	N	
0.164(1)	0.159(1)	-0.006(2)
0.170(1)	0.168(2)	-0.002(3)
0.181(1)	0.182(2)	0.0008(31)
	Δ, $m_z=\pm\frac{3}{2}$	
0.177(1)	0.172(1)	-0.005(2)
0.182(1)	0.180(2)	-0.001(2)
0.195(2)	0.198(3)	0.003(4)

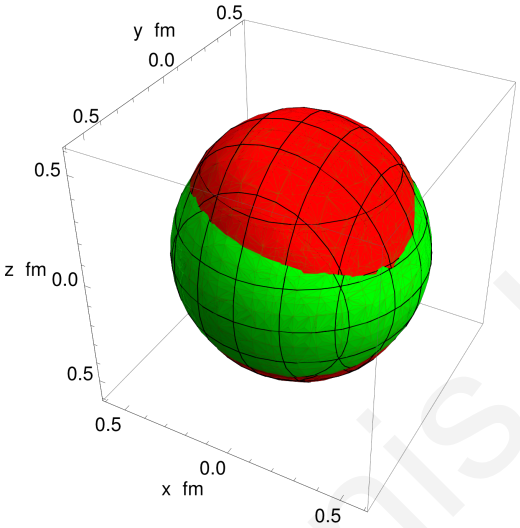

Figure 7.12: Three-dimensional contour plot of the ρ-meson, $m_z=0$ correlator (red or darker surface) compared to a sphere (green or lighter surface). The sphere radius is approximately 0.5 fm. The contour shows all $\vec{r}$ such that $C(\vec{r})=\frac{1}{2}C(0)$.

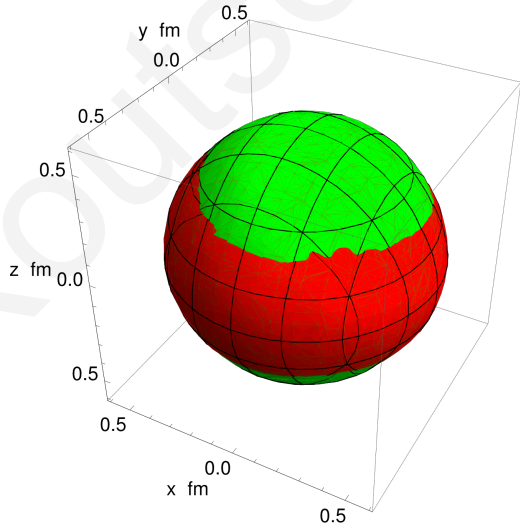

Figure 7.13: Three-dimensional contour plot of the ρ-meson, $m_z=\pm1$ correlator (red or darker surface) compared to a sphere (green or lighter surface). The sphere radius is approximately 0.5 fm. The contour shows all $\vec{r}$ such that $C(\vec{r})=\frac{1}{2}C(0)$.

density-density correlators where calculated. We have additionally shown how to implement the one-end trick for the case of mesons, which leads to a significant improvement in the accuracy with which the meson correlators are obtained. The significant conclusion of this study is that the ρ-meson is deformed. When its spin projection is zero it is elongated along the spin axis (prolate), whereas when its spin projection is ±1 it is elongated perpendicularly to the spin axis (oblate). This result corroborates previous studies where the density-density correlator of the ρ was calculated without explicit zero-momentum projection and with less accuracy [108]. It is also in agreement with a negative quadrupole form factor calculated recently on the lattice [112]. For the nucleon as well as for the Δ

the results are noisy and do not allow a definite conclusion to be drawn.

Finite spatial volume effects lead to a distortion of the long distance behavior of the correlators. By adopting an Ansatz for the asymptotic dependence of the correlators we can subtract the first image contributions and correct the lattice data. The functional form determined from fits to the corrected data confirm a prolate shape for the ρ meson.

Whether the baryons studied here carry an intrinsic deformation could not be concluded due primarily to stochastic noise, even when using such a large ensemble of noise vectors. An additional source of error is the fact that the density-density correlator for baryons includes a quark propagating from source to sink. Thus it is expected that implementing the one-end trick to the three-density correlators for baryons, given the improvement gained in the case of mesons, will allow concrete conclusions regarding their asymmetry. This would be an interesting cross-check of lattice results, given results on the Δ electromagnetic form factors [51] indicating a negative quadrupole moment, as we have seen in Chapter 6.

Chapter 8

The Pion Form Factor using Density-Density Correlators

Having presented the density-density correlator in the previous chapter, we carry on to investigate one potential use of four-point functions, namely the calculation of form factors. We shall present a calculation of the pion form factor using the density-density correlator we have already computed for the hadron charge distributions. The pion form factor has been extensively studied on the lattice using three-point functions [112–115] and is still being studied using various improvements [116–118].

Apart from being simple to calculate, there is active interest in this quantity since certain predictions of perturbative QCD concerning the pion form factor at high momentum transfer are yet to be verified, either by experiment or on the lattice. As we have seen in previous chapters, lattice calculations become noise dominated at high momentum transfers in the case of three-point functions, making very difficult the extraction of quantities at energies where perturbative QCD sets in. Being the simplest and lightest hadron, quantities associated with the pion are easier to extract, and are expected to reach the perturbative regime at momentum transfer higher than 2 GeV^2, i.e. at much lower momentum transfer than other quantities. The aim of this study is to investigate on the accuracy obtained using density-density correlators, given the fact that the all-to-all propagator allows summation over all lattice sites. Having at hand lattice measurements using three-point functions, we can compare and assess the advantages of each method.

8.1 Lattice Formulation

The pion, being a pseudo-scalar, has only one form factor given by the matrix element:

$$\langle \pi(p)|j^{\mu}|\pi(p')\rangle = \left(\frac{m_{\pi}^2}{E_{\pi}(p)E_{\pi}(p')}\right)^{1/2} \frac{p'^{\mu}+p^{\mu}}{2m_{\pi}} F_{\pi}(Q^2). \tag{8.1}$$

The form factor can be extracted by calculating three-point functions in analogy to the form factors described in the previous chapters. In this chapter we present a calculation of the pion form factor using four-point functions. In particular we are interested in comparing the accuracy obtained using this method as compared to results obtained using

three-point functions. The relevant pion four-point function is given by:

$$G^{\pi\mu\mu\pi}(t,t_2,t_1,t_0;\vec{x}_2) = \sum_{\vec{x}_1\vec{x}\vec{x}_0} \langle\chi_\pi(x)|j_u^\mu(x_{2+1})j_d^\mu(x_1)|\bar{\chi}_\pi(x_0)\rangle, \tag{8.2}$$

$$j_q^\mu(x) = \bar{q}(x)\gamma_\mu q(x), \quad q = u,d,$$

where $x_{2+1} = (t_2, \vec{x}_2 + \vec{x}_1)$, $x_1 = (t_1, \vec{x}_1)$, $x = (t, \vec{x})$ and $x_0 = (t_0, \vec{x}_0)$ and where we have already included the sum over source coordinate $\vec{x}_0$ which as we have seen in the previous chapter is made possible using the one-end trick. Note, that this is a generalization of the density-density correlator we used for the charge distributions since the insertions are not necessarily at equal times and are for arbitrary direction (Fig. 8.1). If we now insert three complete sets of states, then in the large time limits $t - t_2 \gg 1$, $t_1 - t_0 \gg 1$ and $t_2 - t_1 \gg 1$ when excited state contributions are suppressed we have:

$$G^{\pi\mu\mu\pi}(t,t_2,t_1,t_0;\vec{x}_2) \xrightarrow[t_2-t_1\gg1]{t-t_2\gg1,\quad t_1-t_0\gg1} \tag{8.3}$$

$$\sum_{\vec{p}} V_3 \langle\chi_\pi(0)|\pi(0)\rangle\langle\pi(0)|j_u^\mu|\pi(\vec{p})\rangle\langle\pi(\vec{p})|j_d^\mu|\pi(0)\rangle\langle\pi(0)|\bar{\chi}_\pi(0)\rangle\times$$

$$e^{-m_\pi(t-(t_2-t_1)-t_0)}e^{-E_\pi(\vec{p})(t_2-t_1)}e^{i\vec{p}\cdot\vec{x}_2}.$$

The sum over $\vec{x}_1$ sets the momentum of the sink equal to that of the source. The sum over the sink sets the momentum of the sink (and thus of the source) to zero. The sum over the source coordinate $\vec{x}_0$ accumulates the four-point function over the volume of the lattice thus increasing the statistics by V_3. It is the accuracy of the form factor obtained by carrying out this sum that we wish to investigate. Assuming SU(2) flavor symmetry, Eq. (8.3) becomes:

$$G^{\pi\mu\mu\pi}(t,t_2,t_1,t_0;\vec{x}_2) \xrightarrow[t_2-t_1\gg1]{t-t_2\gg1,\quad t_1-t_0\gg1} \tag{8.4}$$

$$\sum_{\vec{p}} V_3 |\langle\chi_\pi|\pi(0)\rangle|^2 |\langle\pi(0)|j^\mu|\pi(\vec{p})\rangle|^2 e^{-m_\pi(t-(t_2-t_1)-t_0)}e^{-E_\pi(\vec{p})(t_2-t_1)}e^{i\vec{p}\cdot\vec{x}_2}$$

$$= \sum_{\vec{p}} V_3 |Z_\pi(0)|^2 \frac{m_\pi^2}{m_\pi E_\pi(\vec{p})} \left|\frac{p^\mu + p_0^\mu}{2m_\pi} F_\pi(Q^2)\right|^2 e^{-m_\pi(t-(t_2-t_1)-t_0)}e^{-E_\pi(\vec{p})(t_2-t_1)}e^{i\vec{p}\cdot\vec{x}_2},$$

where we have used: $\langle\chi_\pi|\pi(\vec{p})\rangle = \sqrt{\frac{m_\pi}{E_\pi(\vec{p})}} Z_\pi(\vec{p})$ and p_0 is the initial and final four-momentum: $p_0 = (m_\pi, \vec{0})$. We now carry out a Fourier transform over $\vec{x}_2$ and take $\mu = 0$:

$$G^{\pi 00\pi}(t,t_2,t_1,t_0;\vec{q}) = \sum_{\vec{x}_2} G^{\pi 00\pi}(t,t_2,t_1,t_0;\vec{x}_2)e^{-i\vec{x}_2\cdot\vec{q}} \xrightarrow[t_2-t_1\gg1]{t-t_2\gg1,\quad t_1-t_0\gg1} \tag{8.5}$$

$$V_3 |Z_\pi(0)|^2 \frac{(E_\pi(\vec{q}) + m_\pi)^2}{4m_\pi E_\pi(\vec{q})} F_\pi^2(Q^2) e^{-m_\pi(t-(t_2-t_1)-t_0)}e^{-E_\pi(\vec{q})(t_2-t_1)},$$

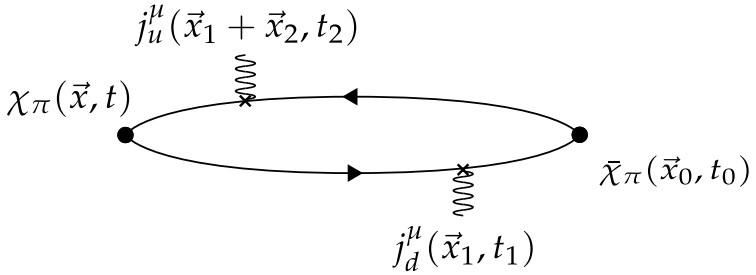

Figure 8.1: Diagram of the pion four-point function

from which we can extract the form factor squared. Once again we use a ratio of two-point functions to cancel unknown overlaps and the exponential dependence. The specific ratio used will be presented in the next section. What we would like to emphasize is that in this specific frame, a pion initially at rest is scattered by two photons of equal amplitude and opposite sign thus initial and final pion states are stationary, allowing the implementation of the one-end trick, without fixing the momentum transfer to a specific value. Indeed, in principle we have the four-point function at arbitrary momentum transfer, limited only by statistical noise.

8.2 Lattice Parameters

For this calculation we shall use the three ensembles of $N_F = 2$ Wilson lattices (Table 3.1) used in the calculation of the hadron charge distributions computed in the previous chapter, since we already have the stochastic propagators needed. The main disadvantage in using the four-point function is the large time intervals required in order to damp excited state contributions. Although initial and final states are smeared in order to achieve greater overlap with the ground state, the state propagating between the current insertions is not smeared and hence needs more time to saturate. As we have seen in Chapter 2, a local propagator needs around 0.6 fm for excited state contributions to be suppressed, while smeared propagators need approximately half the time. In terms of the Wilson $N_F = 2$ lattices we shall use here, this means three time-slices are needed for smeared propagators and six time-slices for local. We additionally need a window over time in order to vary the insertions in search for a plateau. Thus for the lattices with a temporal extent of 40 time-slices we have set the source sink separation at 16 time-slices. This allows three to five time-slices between source (sink) and first (second) insertion leaving six to ten time-slices between the insertions, which shall be varied in search for a plateau. For the shorter lattice, with a temporal extent of 32, we have set the source-sink separation to 14 in order to stay within half the extent of the lattice.

Given the large time intervals involved, careful selection of the combination of two-point functions is crucial in obtaining a good signal. The unknown overlap and the exponential $\exp(-m_\pi(t-(t_2-t_1)-t_0)$ can be easily canceled by a zero-momentum two-point function.

The zero-momentum two-point function can be computed using the one-end trick to a high enough accuracy. Having canceled this term we are left with:

$$\frac{\left(E_\pi(\vec{q})+m_\pi\right)^2}{4m_\pi E_\pi(\vec{q})}F_\pi^2(Q^2)e^{-E_\pi(\vec{q})(t_2-t_1)}. \tag{8.6}$$

In order to cancel the remaining exponential we need the two-point function at finite momentum. This can be computed using the one-end trick albeit with an inversion required for each momentum vector needed which would render this method impractical due to the extensive computational resources it would require. Thus we use the point-to-all propagator to compute the finite-momentum two-point function, which is the main source of statistical noise of this computation. A naive option would be to divide the expression in Eq. (8.6) by:

$$\frac{G^{\pi\pi}(\vec{q},t_2-t_0)}{G^{\pi\pi}(\vec{q},t_1-t_0)}. \tag{8.7}$$

Although this cancels the exponential, t_2-t_0 is the longest time interval and varies between eight to twelve time-slices becoming noise dominated for large momentum transfer. A combination involving shorter time intervals is:

$$\left[\frac{G^{\pi\pi}(\vec{q},(t_2+t_1)/2-t_0)}{G^{\pi\pi}(\vec{q},t_1-t_0)}\right]^2, \tag{8.8}$$

however this restricts the time-slices we can consider since t_2+t_1 must be even in order for $(t_2+t_1)/2$ to be integer. Hence, when dividing to extract the form factor, we use the optimal ratio of Eq. (8.8) when possible and for the intermediate time-slices where t_2+t_1 is odd we use the naive ratio of Eq. (8.7). To summarize:

$$R(t_2,t_1)=\begin{cases} t_2+t_1 \quad \text{odd}: & \frac{G^{\pi 00\pi}(t,t_2,t_1,t_0;\vec{q})}{G^{\pi\pi}(\vec{0},t-(t_2-t_1)-t_0)}\frac{G^{\pi\pi}(\vec{q},t_1-t_0)}{G^{\pi\pi}(\vec{q},t_2-t_0)} \\ t_2+t_1 \quad \text{even}: & \frac{G^{\pi 00\pi}(t,t_2,t_1,t_0;\vec{q})}{G^{\pi\pi}(\vec{0},t-(t_2-t_1)-t_0)}\left[\frac{G^{\pi\pi}(\vec{q},t_1-t_0)}{G^{\pi\pi}(\vec{q},(t_2+t_1)/2-t_0)}\right]^2 \end{cases} \tag{8.9}$$

In Fig. 8.2 we show for the lattice at $\kappa=0.1575$ the ratio obtained for the first four lattice momenta as a function of the difference t_2-t_1. For this plot we take several combinations of t_1 and t_2 and average over the same difference. The fluctuations between odd and even t_2-t_1 are due to the different combination of two-point functions used in the ratio. That the naive choice for the ratio is more noisy can be clearly seen for the largest momentum transfer displayed. We see a plateau in the ratio between $(t_2-t_1)/a=6$ and 9. The dashed lines in the figure show fits to the range they span. Note, however, that in practice we vary the fit range to determine a systematic error for the fit.

8.3 Lattice Results

In Fig. 8.3 we show the pion form factor computed using the density-density correlator. The form factor is normalized to one at $F_\pi(0)$ by demanding charge conservation. In the

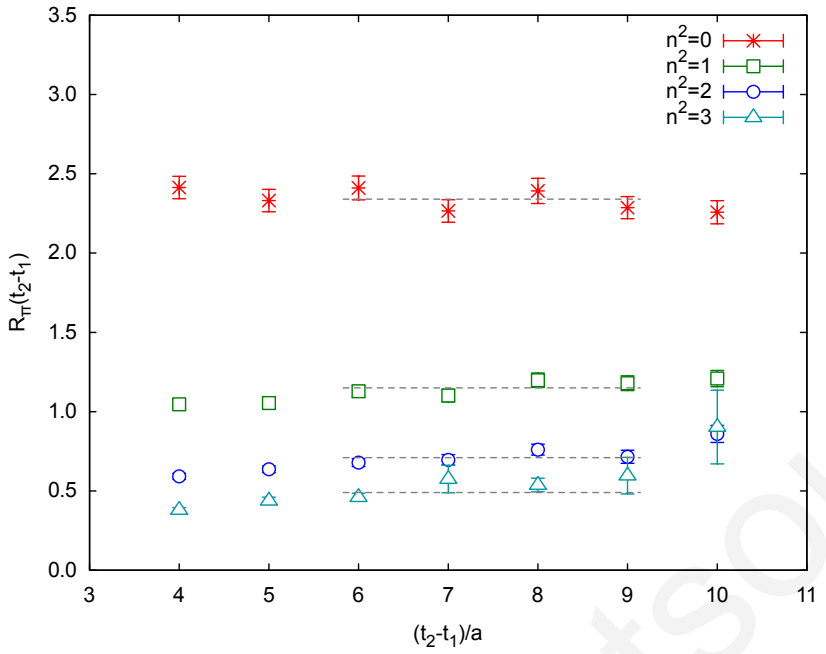

Figure 8.2: Ratio of the four-point function by the combination of two-point functions as in Eq. (8.9) for the first four lattice momenta for $\kappa = 0.1575$. The dashed lines are fits to the range they span.

same figure, we show the prediction assuming Vector Meson Dominance (VMD), i.e. the monopole form $1/(1+Q^2/M^2_{\rm VMD})$ with $M_{\rm VMD} = M_\rho = 0.77$ GeV. This form is consistent with experimental measurements up to the momentum transfer considered here [119–121]. We can generally say that the form factor decreases with decreasing pion mass bringing it closer with the experimentally determined curve. This is more clearly seen at the smallest momentum transfer which carry smaller errors.

Since we initially would like to compare the quality of the results obtained with this method with those obtained using three-point functions we show in the same figure results obtained by two other lattice groups. One is a calculation carried out in the hybrid described in Chapter 4. They used pions of mass $m_\pi = 0.32$ GeV which is the smallest value of all the results shown. The calculation was carried out using three-point functions and a sequential inversion through the sink [114]. The second lattice measurement we compare to is a calculation in twisted mass QCD at $m_\pi = 0.47$ GeV [116]. This calculation was carried out using the one-end trick for the evaluation of the three-point function. This requires an inversion for each momentum vector desired, since the sum over both sink and source requires their momentum to be fixed prior to the inversion as we have seen in previous chapters. Although this summation increases statistics considerably, at high Q^2 where several momentum vectors contribute, inverting to obtain each one becomes too computationally intensive and thus the form factor is computed for only a few vectors for the results presented in this figure. As can be seen this method yields the most accurate form factor.

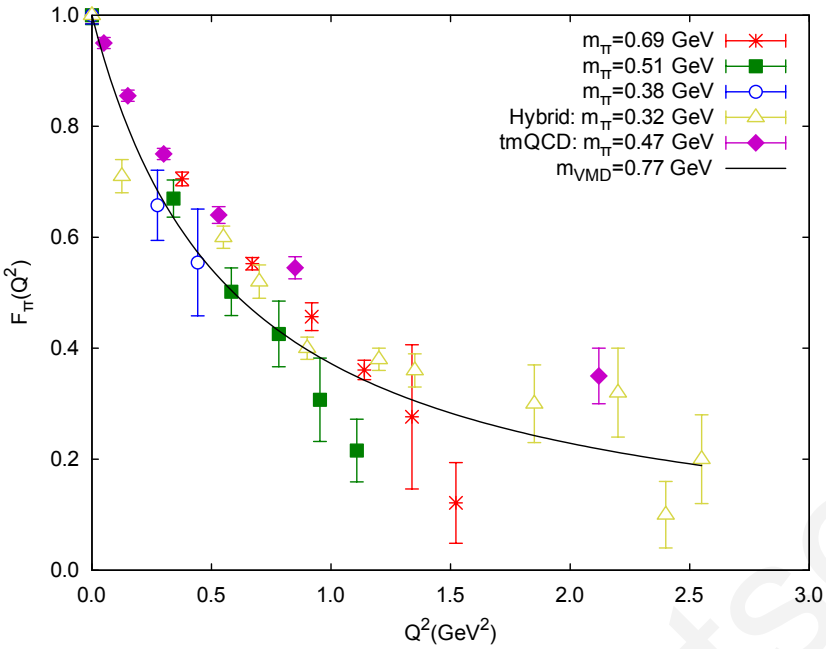

Figure 8.3: The pion form factor computed using the density-density correlator in $N_F = 2$ Wilson QCD, at three pion masses: 0.69 GeV (asterisks), 0.51 GeV (filled squares) and 0.38 GeV (open circles). We compare to two other lattice measurements: A hybrid calculation using Domain Wall valence and Staggered sea quarks at $m_\pi = 0.32$ GeV [114] (open triangles), and a calculation in twisted mass QCD at $m_\pi = 0.47$ GeV [116] (filled rhombus). The solid line shows Vector Meson Dominance using the physical mass of the ρ meson which describes experimental measurements well up to the momentum transfer considered here.

Compared to other lattice results, the form factor computed with the four-point function shows reasonable behavior at low Q^2. Namely we see our results, although carrying large errors for the lightest two pion masses, are consistent with the two other lattice measurements cited here. However, we observe deviations at high Q^2. Namely, we see our calculation of the form factor falls off more rapidly than when using three-point functions which follow the monopole determined by experiment. One major source of error is the short time interval available for the identification of the plateau (Fig. 8.2). This is even shorter for the case of the lightest pion mass, where the temporal extent is 32 compared with 40 for the other two. In this case, we set the source-sink separation at 14 time-slices, just one time-slice shorter than the largest possible separation. The limited interval available to fit, combined with the statistical noise carried by the two-point functions at larger momentum transfer make the determination of the form factor for momenta higher than 0.5 GeV^2 unreliable, since a huge systematic error is involved. We would like to note that for the case of the heavier two pion masses, what limits the calculation to the momentum transfer presented is the statistical uncertainty of the two-point functions rather than that of the four-point function.

We find that a monopole form does not describe our data well which is not surprising

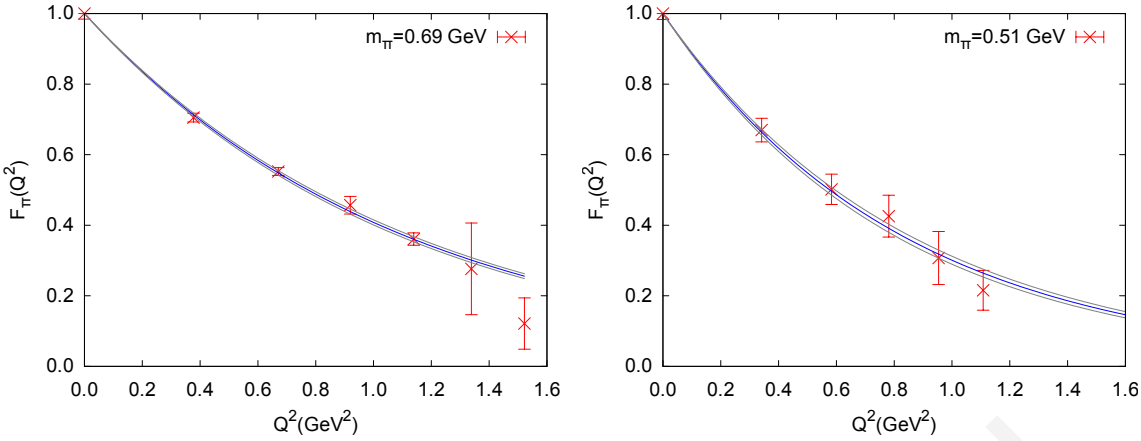

Figure 8.4: Fit of the pion form factor extracted using the density-density correlator to an exponential form. The dashed line shows the error band. Left for $m_\pi = 0.69$ GeV, right for $m_\pi = 0.51$ GeV.

Table 8.1: Parameter M obtained by fitting the pion form factor to the exponential form $\exp(-Q^2/M^2)$ compared to the vector meson mass at each pion mass.

m_π (GeV)	m_π/m_ρ	M (GeV)	m_ρ (GeV)
0.691(8)	0.70(1)	1.06(1)	1.009(10)
0.509(8)	0.57(1)	0.91(1)	0.901(23)
0.384(8)	0.45(3)	0.83(2)	0.850(2)

since our results fall off faster than the results of the two other groups. On the other hand, we find that an exponential form gives a good fit to our data. This is consistent with a monopole form at low Q^2, i.e.: $1/(1+Q^2/M^2) \simeq \exp(-Q^2/M^2) \simeq 1 - Q^2/M^2$ as $Q^2 \to 0$. In Fig. 8.4 we show fits of the heaviest two pion masses to the exponential form $\exp(-Q^2/M^2)$. The fitted values of M for each pion mass are summarized in Table 8.1 where we compare with the vector meson mass.

The parameter M obtained by fitting to exponentials is consistent with the vector meson mass at all pion masses. This shows that at low momentum transfer the form factor is consistent with the prediction from Vector Meson Dominance, with a pole at the value of the ρ mass for the specific pion mass. As in the case of the nucleon, non-relativistically the slope of the form factor at low momentum transfer is associated with the pion charge radius:

$$\langle r_\pi^2 \rangle = -6 \frac{\partial}{\partial Q^2} F_\pi(Q^2) \Big|_{Q^2=0} = \frac{6}{M^2}. \tag{8.10}$$

The primary goal of this study is to see the accuracy obtained for the pion form factor when using the four-point function. Hence we use only three pion masses at approximately the same lattice spacing in order to investigate the applicability of this method. Although one would need several pion masses and at least three lattice spacings for a reliable ex-

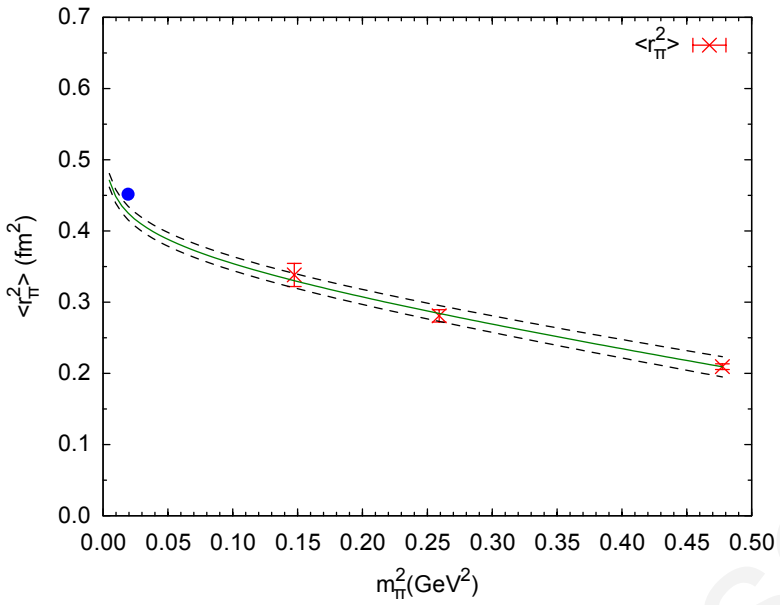

Figure 8.5: Chiral extrapolation of the pion charge radius. The filled circle is the experimentally measured value of the pion charge radius. The solid line is a fit to Eq. (8.11) fitting c_0 and c_1 while the empirical value of 0.0924 GeV is taken for f_π. The dashed line shows the error band.

traction of the pion charge radius, it is interesting to see whether the above results are consistent with the chiral limit. We use the chiral expansion obtained from one loop chiral perturbation theory [122]:

$$\langle r_\pi^2 \rangle = c_0 - \frac{1}{(4\pi f_\pi)^2} \log(m_\pi^2) + c_1 m_\pi^2 \tag{8.11}$$

The terms c_0 and c_1 are fitted while we use the empirical value for f_π (Table 3.3). The resulting fit is shown in Fig. 8.3. As can be seen the fit describes the data well leading to a pion charge radius slightly lower than 0.672(8) fm which is what is quoted experimentally [102].

8.4 Summary of Results

In this chapter we have presented an exploratory study of using four-point functions for the computation of form factors. Given the technology developed for the calculation of the hadron charge distributions in the previous chapter, this investigation came at a minimal computational cost since the stochastic propagators where already computed. We have shown that using four-point functions, one can calculate the form factor squared for any momentum transfer while simultaneously fixing initial and final states to zero momentum. This specific setup, which cannot be achieved with only one current insertion (three-point function), allows applying the one-end trick to sum over sink and source coordinates without having to fix the momentum transfer prior to the inversion.

Although the double summation provides an accurate four-point function, dividing with two-point functions in order to cancel exponentials and unknown overlaps with the interpolating operators introduces noise which translates to an uncertainty in the form factor comparable with that obtained using standard methods such as three-point functions. We find that at low momentum transfer the form factor obtained with this method is consistent with that obtained from other lattice measurements. Although the experimentally measured form factor is well described by a monopole form, our data are better described by an exponential. The fitted parameter of the exponential is consistent with the ρ-meson mass. Having the Q^2 dependence of the form factor, we test our results against a chiral expansion for the charge radius of the pion. We find that our data are consistent with this chiral expansion, and a naive fit leads to a pion charge radius slightly lower than experiment.

Chapter 9

Summary and Conclusions

In this thesis we describe the techniques developed to extract form factors in the nucleon/Δ system accurately. We also describe the methods developed to calculate all-to-all propagators and apply them for the evaluation of four-point functions. These quantities are of importance both experimentally and phenomenologically and the results presented here are of direct relevance to ongoing experiments. For example results on the nucleon electromagnetic form factors presented in Chapter 3 are particularly relevant to the extensive experimental program at Jefferson Laboratory which aims at accurate measurements of the electromagnetic form factors over a large range of momentum transfer. For the calculation of the nucleon form factors we used quenched Wilson fermions and two dynamical degenerate flavors of Wilson quarks. A number of improvement techniques are applied: Gaussian smearing of the source and sink with parameters optimized so that the nucleon state dominates as early as three time-slices or 0.3 fm from the source. This improvement allows a relatively short source-sink separation which in turn leads to less statistical noise in the three-point function. The three-point function is evaluated using a sequential inversion through the sink, which means we can insert the electromagnetic current operator at any time and at any momentum with no extra inversions. Selecting appropriately the quantum numbers of the sequential source allows the isolation of specific form factors thus leading to a more accurate estimate. In addition we can insert any operator without requiring any additional sequential inversions. This allows evaluation of the electromagnetic, axial and pseudo-scalar form factors with the same set of propagators. In the case of the electromagnetic form factors we evaluate the isovector part that does not have any disconnected contributions which have not been included in lattice calculations so far. In order to compare with experiment, we interpolate the experimentally measured electric and magnetic form factors of the proton and neutron to the same momentum transfer so that we can subtract and obtain the isovector form factors. The general observation is that the electric form factor disagrees more with experiment than the magnetic form factor. The most probable source of this discrepancy is the fact that we work with pion masses larger than 300 MeV. It is expected that at lower pion masses non-analytic contributions will become important in the chiral expansion yielding agreement with experiment. A calculation at pion masses less than 300 MeV is expected to become feasible in the next couple of years. The anomalous magnetic moment and Dirac and Pauli radii are chirally

extrapolated to the physical point. We obtain an anomalous magnetic moment at the physical point consistent with that observed experimentally. This is not the case for the r.m.s. radii for which we obtain values lower than experiment.

In Chapter 4 we present a lattice calculation of the nucleon to Δ electromagnetic transition form factors. The electromagnetic nucleon to Δ transition is used experimentally to investigate deformation in the nucleon. There are three nucleon to Δ electromagnetic transition form factors: the dominant magnetic dipole G_{M1} and the sub-dominant electric quadrupole and Coulomb quadrupole form factors G_{E2} and G_{C2}. Non-zero values for these sub-dominant form factors points to a deformation in either the nucleon or the Δ or both. This calculation is carried out in the quenched approximation, using two degenerate flavors of dynamical Wilson quarks and using a hybrid action with domain wall valence quarks and dynamical staggered sea quarks. Apart from the fact that this hybrid scheme preserves chiral symmetry on the lattice, it allows the evaluation of the form factors at a pion mass as low as 350 MeV. For the case of the dominant magnetic dipole form factor we observe weak unquenching effects and consistency between results obtained using the hybrid action and results obtained with the Wilson lattices. This consistency is non-trivial given that discretization errors appear to different order in the lattice spacing for the two discretization schemes and shows that lattice artifacts are under control. At low momentum transfer the results for G_{M1} are lower than experiment. Once more, a calculation at pion masses less than 300 MeV where pion cloud contributions are expected to become important is needed in order to investigate the approach to the physical point. To compare our results for the sub-dominant form factors with experiment we construct the ratios $-\frac{G_{E2}(q^2)}{G_{M1}(q^2)}$ and $-\frac{|\vec{q}|}{2M_\Delta}\frac{G_{C2}(q^2)}{G_{M1}(q^2)}$ in the rest frame of the Δ. Apart from allowing comparison with experimental results which are customarily presented in this way, ratios are less pruned to systematic errors. We find, for the first time in unquenched lattice QCD, that the sub-dominant form factors are clearly non-zero and negative pointing to a deformed nucleon and/or Δ. We also observe unquenching effects in the Coulomb quadrupole form factor, at the smallest pion mass, bringing lattice results closer to experiment.

In Chapter 5 we presented a calculation of the axial nucleon and nucleon to Δ axial transition form factors. We additionally evaluated the pion-nucleon and pion-nucleon-Δ form factors. Having the sequential propagators used to compute the electromagnetic form factors presented in Chapters 3 and 4, we need only replace the electromagnetic current with the axial or pseudo-scalar current in the three-point function thus requiring no extra inversions. Phenomenological arguments relate the two axial nucleon form factors G_A and G_p to the pion-nucleon form factor $G_{\pi NN}$. This relation is known as the diagonal Goldberger-Treiman relation. Furthermore, assuming pion pole dominance for the induced pseudo-scalar form factor G_p, we obtain a simplified Goldberger-Treiman relation. The same arguments hold for the dominant nucleon to Δ axial transition form factors C_5^A and C_6^A which are similarly related to the pion-nucleon-Δ form factor $G_{\pi N\Delta}$ through the off-diagonal Goldberger-Treiman relation. Given these relations we have constructed and presented ratios of these form factors which are expected to show no dependence on the

momentum transfer and have the additional advantage of exhibiting weaker quark mass dependence thus allowing comparison with experimental results. We have seen that the pion-nucleon and pion-nucleon-Δ form factors show the same Q^2 dependence and that their ratio $G_{\pi NN}(Q^2)/G_{\pi N\Delta}(Q^2)$ is equal to 1.60(2). The ratio $2C_5^A(Q^2)/G_A(Q^2)$ is also constant with respect to the momentum transfer and equal to 1.61(1). Equality of these two ratios is implied by the Goldberger-Treiman relations as is also implied for the ratio $8C_6^A(Q^2)/G_p(Q^2)$ which is found, however, about 7% larger. Another phenomenological expectation is that the momentum dependence of $G_p(Q^2)/G_A(Q^2)$ and $C_6^A(Q^2)/C_5^A(Q^2)$ is of a monopole form with the pion mass at the pole. We find that lattice results, at the pion masses considered here, are better described by a larger pole mass than m_π. This is confirmed when using results obtained in the hybrid scheme. We have additionally studied the momentum dependence of the form factors separately, where we find that unquenching effects are large when comparing quenched and hybrid results which is another indication of the importance of pion cloud effects in these quantities. The axial nucleon form factor G_A is fitted to a dipole form yielding a dipole mass decreasing with the pion mass. We find m_A =1.5 GeV at the smallest pion mass of the quenched case compared to m_A =1.1 GeV found experimentally. The momentum dependence of the pion-nucleon and pion-nucleon-Δ form factors are found different at low Q^2 than what phenomenology expects. This discrepancy leads to values of the strong couplings $g_{\pi NN}$ and $g_{\pi N\Delta}$ which are smaller than what is experimentally measured. A calculation at pion masses below 300 MeV is needed in order to investigate these discrepancy.

A calculation of the Δ form factors was presented in Chapter 6. Due to its short lifetime, experimental measurements for the Δ are difficult and thus measurements of its magnetic moment and charge radius carry large errors. The Δ has four form factors: the dominant charge form factor G_{E0} and magnetic dipole form factor G_{M1}, and the sub-dominant electric quadrupole G_{E2} and magnetic octapole form factors G_{M3}. A non-zero value for the electric quadrupole form factor at zero momentum transfer means a non-vanishing quadrupole moment and thus a deformed Δ. The calculation is carried out in quenched QCD, using two degenerate dynamical quarks at three pion masses as well as in the hybrid scheme at the smallest pion mass available. The magnetic moment is in agreement with experimental results, which however carry large errors. The electric quadrupole form factor is non-zero and negative showing that the Δ is oblate.

In Chapter 7 we discuss an approach for studying deformation in hadrons by directly probing their charge distribution. This is achieved by calculating the equal-time density-density correlator, which in the non-relativistic limit becomes the hadron charge distribution. This is technically challenging since it requires the evaluation of a four-point function, which in turn requires all-to-all propagators. We estimate the all-to-all propagator using stochastic techniques and dilution. We compute the density-density correlator for the pion, the ρ-meson, the nucleon and the Δ-baryon in N_F=2 Wilson QCD. In addition we extend the one-end trick to the four-point function and evaluate the density-density correlators for mesons. The implementation of the one-end trick greatly improves the signal

due to summation over both sink and source coordinates. By projecting the correlators on the three axes we find a clear elongation of the zero spin projection of the ρ-meson along the spin axis. This observation would not have been possible using the direct method due to stochastic noise. We correct for finite volume effects by modeling the asymptotic form of the correlator and subtracting contributions of nearest neighboring lattices from the correlator computed on the lattice. Using this corrected correlator we measure deformation by calculating the expectation value $\langle z^2 - \frac{x^2+y^2}{2} \rangle$. We find a non-zero value for this expectation value and therefore this analysis corroborates previous findings that the ρ-meson is deformed. For baryons the evaluation of the density-density correlator using stochastic techniques and dilution yields large statistical errors obscuring any definite conclusion within the current statistics. An immediate extension of the work presented here is the implementation of the one-end trick to compute the baryon charge distribution. This could be applied to the three-density correlator to obtain a more accurate evaluation of the baryon wave function in terms of two relative distances. It is important that the asymmetry in the Δ-baryon indicated by its negative electric quadrupole form factor is corroborated by a deformed charge distribution.

In the final chapter of this thesis we extract the pion form factor using the density-density correlator. Our results are in agreement with other lattice results. They are best described by an exponential decay to which we fit to obtain estimates of the charge radius of the pion at each pion mass. A chiral extrapolation to the physical point describes our data on the charge radius well and yields a value for the pion r.m.s. radius in agreement with experiment.

In summary, we have established the setup for the accurate extraction of hadron form factors including the sub-dominant form factors which up to now could not be obtained to the required accuracy to make comparison with experiment meaningful. Extending the calculation of these form factors to lower pion masses can be under taken within the setup developed. Such a calculation is important in view of the observed deviations from experiment at low momentum transfer where, as we go to pion masses below 300 MeV, pion cloud contributions are expected to become important.

Bibliography

[1] D. J. Gross and F. Wilczek *Phys. Rev. Lett.* **30** (1973) 1343–1346.

[2] H. D. Politzer *Phys. Rev. Lett.* **30** (1973) 1346–1349.

[3] K. G. Wilson *Phys. Rev.* **D10** (1974) 2445–2459.

[4] H. B. Nielsen and M. Ninomiya *Nucl. Phys.* **B185** (1981) 20.

[5] P. H. Ginsparg and K. G. Wilson *Phys. Rev.* **D25** (1982) 2649.

[6] D. B. Kaplan *Phys. Lett.* **B288** (1992) 342–347 [hep-lat/9206013].

[7] H. Neuberger *Phys. Lett.* **B417** (1998) 141–144 [hep-lat/9707022].

[8] B. Orth, T. Lippert and K. Schilling *Phys. Rev.* **D72** (2005) 014503 [hep-lat/0503016].

[9] R. Gupta hep-lat/9807028.

[10] C. Alexandrou, S. Gusken, F. Jegerlehner, K. Schilling and R. Sommer *Nucl. Phys.* **B414** (1994) 815–855 [hep-lat/9211042].

[11] S. Gusken *Nucl. Phys. Proc. Suppl.* **17** (1990) 361–364.

[12] C. Morningstar and M. J. Peardon *Phys. Rev.* **D69** (2004) 054501 [hep-lat/0311018].

[13] **APE** Collaboration, M. Albanese *et. al. Phys. Lett.* **B192** (1987) 163.

[14] A. Hasenfratz and F. Knechtli *Phys. Rev.* **D64** (2001) 034504 [hep-lat/0103029].

[15] C. Alexandrou, G. Koutsou, J. W. Negele and A. Tsapalis *Phys. Rev.* **D74** (2006) 034508 [hep-lat/0605017].

[16] **UKQCD** Collaboration, C. Michael and J. Peisa *Phys. Rev.* **D58** (1998) 034506 [hep-lat/9802015].

[17] J. Foley *et. al. Comput. Phys. Commun.* **172** (2005) 145–162 [hep-lat/0505023].

[18] **UKQCD** Collaboration, C. McNeile and C. Michael *Phys. Lett.* **B556** (2003) 177–184 [hep-lat/0212020].

[19] C. Alexandrou *et. al. Phys. Rev.* **D77** (2008) 085012 [0710.4621].

[20] C. W. Bernard *et. al. Phys. Rev.* **D64** (2001) 054506 [hep-lat/0104002].

[21] Y. Shamir *Nucl. Phys.* **B406** (1993) 90–106 [hep-lat/9303005].

[22] R. Narayanan and H. Neuberger *Phys. Lett.* **B302** (1993) 62–69 [hep-lat/9212019].

[23] R. Hofstadter and R. W. McAllister *Phys. Rev.* **98** (1955) 217–218.

[24] M. N. Rosenbluth *Phys. Rev.* **79** (1950) 615–619.

[25] **Jefferson Lab Hall A** Collaboration, M. K. Jones *et. al. Phys. Rev. Lett.* **84** (2000) 1398–1402 [nucl-ex/9910005].

[26] O. Gayou *et. al. Phys. Rev.* **C64** (2001) 038202.

[27] **Jefferson Lab Hall A** Collaboration, O. Gayou *et. al. Phys. Rev. Lett.* **88** (2002) 092301 [nucl-ex/0111010].

[28] **QCDSF** Collaboration, M. Gockeler *et. al. Phys. Rev.* **D71** (2005) 034508 [hep-lat/0303019].

[29] L. Andivahis *et. al. Phys. Rev.* **D50** (1994) 5491–5517.

[30] R. C. Walker *et. al. Phys. Rev.* **D49** (1994) 5671–5689.

[31] A. F. Sill *et. al. Phys. Rev.* **D48** (1993) 29–55.

[32] P. E. Bosted *et. al. Phys. Rev.* **C42** (1990) 38–64.

[33] F. Borkowski, P. Peuser, G. G. Simon, V. H. Walther and R. D. Wendling *Nucl. Phys.* **B93** (1975) 461.

[34] H. Anklin *et. al. Phys. Lett.* **B336** (1994) 313–318.

[35] H. Anklin *et. al. Phys. Lett.* **B428** (1998) 248–253.

[36] G. Kubon *et. al. Phys. Lett.* **B524** (2002) 26–32 [nucl-ex/0107016].

[37] W. Xu *et. al. Phys. Rev. Lett.* **85** (2000) 2900–2904 [nucl-ex/0008003].

[38] **Jefferson Lab E95-001** Collaboration, W. Xu *et. al. Phys. Rev.* **C67** (2003) 012201 [nucl-ex/0208007].

[39] A. Lung *et. al. Phys. Rev. Lett.* **70** (1993) 718–721.

[40] **E93-038** Collaboration, R. Madey *et. al. Phys. Rev. Lett.* **91** (2003) 122002 [nucl-ex/0308007].

[41] **Jefferson Lab E93-026** Collaboration, G. Warren *et. al. Phys. Rev. Lett.* **92** (2004) 042301 [nucl-ex/0308021].

[42] D. Rohe *et. al. Phys. Rev. Lett.* **83** (1999) 4257–4260.

[43] J. Bermuth *et. al. Phys. Lett.* **B564** (2003) 199–204 [nucl-ex/0303015].

[44] S. Galster *et. al. Nucl. Phys.* **B32** (1971) 221–237.

[45] C. Urbach, K. Jansen, A. Shindler and U. Wenger *Comput. Phys. Commun.* **174** (2006) 87–98 [hep-lat/0506011].

[46] M. Burkardt *Int. J. Mod. Phys.* **A18** (2003) 173–208 [hep-ph/0207047].

[47] S.-i. Ando, J.-W. Chen and C.-W. Kao *Phys. Rev.* **D74** (2006) 094013 [hep-ph/0602200].

[48] T. R. Hemmert and W. Weise *Eur. Phys. J.* **A15** (2002) 487–504 [hep-lat/0204005].

[49] N. Isgur, G. Karl and R. Koniuk *Phys. Rev.* **D25** (1982) 2394.

[50] S. Capstick and G. Karl *Phys. Rev.* **D41** (1990) 2767.

[51] C. Alexandrou, T. Korzec, T. Leontiou, J. W. Negele and A. Tsapalis *PoS* **LATTICE2007** (2007) 149 [0710.2744].

[52] **LEGS** Collaboration, G. Blanpied *et. al. Phys. Rev. Lett.* **76** (1996) 1023–1026.

[53] C. Mertz *et. al. Phys. Rev. Lett.* **86** (2001) 2963–2966 [nucl-ex/9902012].

[54] T. Pospischil *et. al. Phys. Rev. Lett.* **86** (2001) 2959–2962 [nucl-ex/0010020].

[55] **CLAS** Collaboration, K. Joo *et. al. Phys. Rev. Lett.* **88** (2002) 122001 [hep-ex/0110007].

[56] **OOPS** Collaboration, N. F. Sparveris *et. al. Phys. Rev. Lett.* **94** (2005) 022003 [nucl-ex/0408003].

[57] S. Stave *et. al. Eur. Phys. J.* **A30** (2006) 471–476 [nucl-ex/0604013].

[58] N. F. Sparveris *et. al. Phys. Lett.* **B651** (2007) 102–107 [nucl-ex/0611033].

[59] D. B. Leinweber, T. Draper and R. M. Woloshyn *Phys. Rev.* **D48** (1993) 2230–2249 [hep-lat/9212016].

[60] C. Alexandrou *et. al. Phys. Rev. Lett.* **94** (2005) 021601 [hep-lat/0409122].

[61] **MILC** Collaboration, K. Orginos, D. Toussaint and R. L. Sugar *Phys. Rev.* **D60** (1999) 054503 [hep-lat/9903032].

[62] J. B. Kogut and L. Susskind *Phys. Rev.* **D11** (1975) 395.

[63] J.-W. Chen, D. O'Connell and A. Walker-Loud *Phys. Rev.* **D75** (2007) 054501 [hep-lat/0611003].

[64] H. F. Jones and M. D. Scadron *Ann. Phys.* **81** (1973) 1–14.

[65] C. Aubin *et. al. Phys. Rev.* **D70** (2004) 094505 [hep-lat/0402030].

[66] T. Blum *et. al. Phys. Rev.* **D69** (2004) 074502 [hep-lat/0007038].

[67] **LHPC** Collaboration, P. Hagler *et. al. Phys. Rev.* **D77** (2008) 094502 [0705.4295].

[68] W. Bartel *et. al. Phys. Lett.* **B28** (1968) 148–151.

[69] J. C. Alder *et. al. Nucl. Phys.* **B46** (1972) 573–592.

[70] K. Baetzner *et. al. Phys. Lett.* **B39** (1972) 575–578.

[71] S. Stein *et. al. Phys. Rev.* **D12** (1975) 1884.

[72] L. Tiator, D. Drechsel, O. Hanstein, S. S. Kamalov and S. N. Yang *Nucl. Phys.* **A689** (2001) 205–214 [nucl-th/0012046].

[73] L. Tiator, D. Drechsel, S. S. Kamalov and S. N. Yang *Eur. Phys. J.* **A17** (2003) 357–363.

[74] **OOPS** Collaboration, S. Stave *et. al. Eur. Phys. J.* **A30** (2006) 471 [nucl-ex/0604013].

[75] R. Beck *et. al. Phys. Rev.* **C61** (2000) 035204 [nucl-ex/9908017].

[76] D. Drechsel, O. Hanstein, S. S. Kamalov and L. Tiator *Nucl. Phys.* **A645** (1999) 145–174 [nucl-th/9807001].

[77] T. Sato and T. S. H. Lee *Phys. Rev.* **C63** (2001) 055201 [nucl-th/0010025].

[78] V. Pascalutsa and M. Vanderhaeghen *Phys. Rev. Lett.* **95** (2005) 232001 [hep-ph/0508060].

[79] **OOPS** Collaboration, C. Mertz *et. al. Phys. Rev. Lett.* **86** (2001) 2963–2966 [nucl-ex/9902012].

[80] **Particle Data Group** Collaboration, K. Hagiwara *et. al. Phys. Rev.* **D66** (2002) 010001.

[81] C. Alexandrou, G. Koutsou, T. Leontiou, J. W. Negele and A. Tsapalis *Phys. Rev.* **D76** (2007) 094511.

[82] L. A. Ahrens *et. al. Phys. Lett.* **B202** (1988) 284–288.

[83] V. Bernard, N. Kaiser and U. G. Meissner *Phys. Rev. Lett.* **69** (1992) 1877–1879.

[84] S. Choi *et. al. Phys. Rev. Lett.* **71** (1993) 3927–3930.

[85] T. Gorringe and H. W. Fearing *Rev. Mod. Phys.* **76** (2004) 31–91 [nucl-th/0206039].

[86] S. L. Adler *Ann. Phys.* **50** (1968) 189–311.

[87] S. J. Barish *et. al. Phys. Rev.* **D19** (1979) 2521.

[88] **LHPC** Collaboration, R. G. Edwards *et. al. Phys. Rev. Lett.* **96** (2006) 052001 [hep-lat/0510062].

[89] A. A. Khan *et. al. Phys. Rev.* **D74** (2006) 094508 [hep-lat/0603028].

[90] **the RIKEN-BNL-Columbia-KEK** Collaboration, S. Sasaki, K. Orginos, S. Ohta and T. Blum *Phys. Rev.* **D68** (2003) 054509 [hep-lat/0306007].

[91] K. F. Liu, S. J. Dong, T. Draper and W. Wilcox *Phys. Rev. Lett.* **74** (1995) 2172–2175 [hep-lat/9406007].

[92] C. Alexandrou, T. Leontiou, J. W. Negele and A. Tsapalis *Phys. Rev. Lett.* **98** (2007) 052003 [hep-lat/0607030].

[93] V. Furman and Y. Shamir *Nucl. Phys.* **B439** (1995) 54–78 [hep-lat/9405004].

[94] V. Gimenez, L. Giusti, F. Rapuano and M. Talevi *Nucl. Phys.* **B531** (1998) 429–445 [hep-lat/9806006].

[95] D. Becirevic *et. al. Nucl. Phys.* **B734** (2006) 138–155 [hep-lat/0510014].

[96] T. Kitagaki *et. al. Phys. Rev.* **D42** (1990) 1331–1338.

[97] M. R. Schindler, T. Fuchs, J. Gegelia and S. Scherer *Phys. Rev.* **C75** (2007) 025202 [nucl-th/0611083].

[98] H. C. Schroder *et. al. Eur. Phys. J.* **C21** (2001) 473–488.

[99] C. Alexandrou, T. Korzec, T. Leontiou, J. W. Negele and A. Tsapalis *in preparation* (2008).

[100] M. Kotulla *et. al. Phys. Rev. Lett.* **89** (2002) 272001 [nucl-ex/0210040].

[101] G. Lopez Castro and A. Mariano *Phys. Lett.* **B517** (2001) 339–344 [nucl-th/0006031].

[102] **Particle Data Group** Collaboration, W. M. Yao *et. al. J. Phys.* **G33** (2006) 1–1232.

[103] D. B. Leinweber, T. Draper and R. M. Woloshyn *Phys. Rev.* **D46** (1992) 3067–3085 [hep-lat/9208025].

[104] S. Boinepalli *et. al. PoS* **LAT2006** (2006) 124 [hep-lat/0611028].

[105] D. Arndt and B. C. Tiburzi *Phys. Rev.* **D68** (2003) 114503 [hep-lat/0308001].

[106] W. Wilcox *Phys. Rev.* **D43** (1991) 2443–2446.

[107] M. Burkardt, J. M. Grandy and J. W. Negele *Ann. Phys.* **238** (1995) 441–472 [hep-lat/9406009].

[108] C. Alexandrou, P. de Forcrand and A. Tsapalis *Phys. Rev.* **D66** (2002) 094503 [hep-lat/0206026].

[109] C. Alexandrou and G. Koutsou 0809.2056.

[110] **UKQCD** Collaboration, C. McNeile and C. Michael *Phys. Rev.* **D73** (2006) 074506 [hep-lat/0603007].

[111] C. Alexandrou and G. Koutsou *PoS* **LAT2007** (2007) 150 [arXiv:0710.2441].

[112] J. N. Hedditch *et. al. Phys. Rev.* **D75** (2007) 094504 [hep-lat/0703014].

[113] J. van der Heide, J. H. Koch and E. Laermann *Phys. Rev.* **D69** (2004) 094511 [hep-lat/0312023].

[114] **Lattice Hadron Physics** Collaboration, F. D. R. Bonnet, R. G. Edwards, G. T. Fleming, R. Lewis and D. G. Richards *Phys. Rev.* **D72** (2005) 054506 [hep-lat/0411028].

[115] **Bern-Graz-Regensburg (BGR)** Collaboration, S. Capitani, C. Gattringer and C. B. Lang *Phys. Rev.* **D73** (2006) 034505 [hep-lat/0511040].

[116] **ETMC** Collaboration, S. Simula *PoS* **LATTICE2007** (2007) 371 [0710.0097].

[117] **JLQCD** Collaboration, T. Kaneko *et. al. PoS* **LAT2007** (2007) 148 [0710.2390].

[118] P.-h. J. Hsu and G. T. Fleming *PoS* **LATTICE** (2007) 145 [0710.4538].

[119] W. R. Frazer and J. R. Fulco *Phys. Rev. Lett.* **2** (1959) 365.

[120] C. J. Bebek *et. al. Phys. Rev.* **D17** (1978) 1693.

[121] **NA7** Collaboration, S. R. Amendolia *et. al. Nucl. Phys.* **B277** (1986) 168.

[122] J. Gasser and H. Leutwyler *Ann. Phys.* **158** (1984) 142.

Appendix A

Gamma Matrix Representation

We use a Euclidean, non - relativistic γ - matrix representation obeying:

$$\{\gamma_\mu, \gamma_\nu\} = 2\delta_{\mu\nu} \quad \mu = 1, ..., 4. \tag{A.1}$$

These are given by:

$$\gamma_k = \begin{pmatrix} 0 & i\sigma_k \\ -i\sigma_k & 0 \end{pmatrix}, \quad \gamma_4 = \begin{pmatrix} \mathbb{1} & 0 \\ 0 & \mathbb{1} \end{pmatrix} \tag{A.2}$$

where σ_k are the Pauli matrices and $\mathbb{1}$ is the 2×2 unit matrix. The fifth γ - matrix is defined as:

$$\gamma_5 = \gamma_1\gamma_2\gamma_3\gamma_4 = \begin{pmatrix} 0 & \mathbb{1} \\ \mathbb{1} & 0 \end{pmatrix}, \tag{A.3}$$

while the charge conjugation matrix is given by:

$$C = \gamma_4\gamma_2. \tag{A.4}$$

We will also often use the abbreviations:

$$\gamma_\mp = \frac{\gamma_1 \pm i\gamma_2}{\sqrt{2}}. \tag{A.5}$$

Appendix B

Nucleon Three-Point Function

We will perform the contractions for the nucleon three-point function and show how one constructs the sequential source, needed in order to compute the nucleon electromagnetic form factors as in Chapter 3.

We consider the local isovector current:

$$j^{\rho}(x) = \bar{u}(x)\gamma_{\rho}u(x) - \bar{d}(x)\gamma_{\rho}d(x). \tag{B.1}$$

We give the three-point function:

$$G_{\alpha\beta}^{Nj^{\rho}N}(x_2; x_1; 0) = \langle\Omega|\chi_{\alpha}^{N}(x_2)j^{\rho}(x_1)\bar{\chi}_{\beta}^{N}(0)|\Omega\rangle \tag{B.2}$$

and the interpolating operator for the nucleon:

$$\chi_{\alpha}^{N}(x) = \varepsilon^{abc}u_{\mu}^{a}(C\gamma_5)_{\mu\nu}d_{\nu}^{b}(x)u_{\alpha}^{c}(x). \tag{B.3}$$

Expanding the tree point function we have:

$$\begin{aligned} G_{\alpha\beta}^{Nj^{\rho}N}(x_2; x_1; 0) = \langle\Omega|\varepsilon^{abc}u_{\mu}^{a}(x_2)(C\gamma_5)_{\mu\nu}d_{\nu}^{b}(x_2)u_{\alpha}^{c}(x_2)\times \\ [\bar{u}_{\kappa}^{f}(x_1)(\gamma_{\rho})_{\kappa\lambda}u_{\lambda}^{f}(x_1) - \bar{d}_{\lambda'}^{f'}(x_1)(\gamma_{\rho})_{\kappa'\lambda'}d_{\lambda'}^{f'}(x_1)]\times \\ \varepsilon^{a'b'c'}\bar{u}_{\beta}^{c'}(0)\bar{d}_{\nu'}^{b'}(0)(C\gamma_5)_{\nu'\mu'}\bar{u}_{\mu'}^{a'}(0)|\Omega\rangle. \end{aligned} \tag{B.4}$$

We split the three-point function into the term in which the current couples with the up quarks and that which the current couples with the down quark:

$$G_{\alpha\beta}^{Nj^{\rho}N}(x_2, x_1, 0) = U_{\alpha\beta}^{Nj^{\rho}N}(x_2, x_1, 0) - D_{\alpha\beta}^{Nj^{\rho}N}(x_2, x_1, 0). \tag{B.5}$$

$$U_{\alpha\beta}^{Nj^{\rho}N}(x_2, x_1, 0) = \tag{B.6}$$

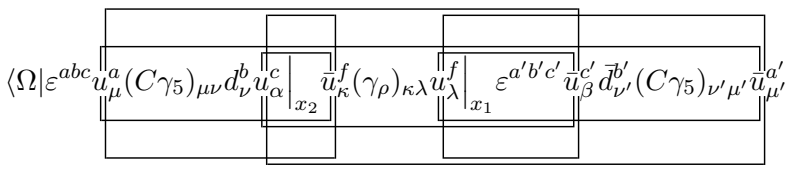

The four possible ways to contract the up quark fields are indicated by the heights of the lines. We have neglected the contractions that give the disconnected contribution since these cancel with those from $D^{Nj^\mu N}_{\alpha\beta}(x_2, x_1, 0)$. We have also suppressed the single possible contraction between down quarks. Rearranging appropriately the color indices while changing the sign of the antisymmetric tensor ε^{abc} we have:

$$\begin{aligned} U^{Nj^\rho N}_{\alpha\beta}(x_2, x_1, 0) =& \varepsilon^{abc}\varepsilon^{a'b'c'} \left[C\gamma_5 G(x_2;0)\overline{C\gamma_5}\right]^{aa'}_{\mu\nu} \\ &\times\Big\{ G(x_2;x_1)\gamma_\rho G(x_1;0)\Big|^{bb'}_{\alpha\beta} G^{cc'}_{\mu\nu}(x_2;0) \\ &+G(x_2;x_1)\gamma_\rho G(x_1;0)\Big|^{bb'}_{\alpha\nu} G^{cc'}_{\mu\beta}(x_2;0) \\ &+G(x_2;x_1)\gamma_\rho G(x_1;0)\Big|^{bb'}_{\mu\nu} G^{cc'}_{\alpha\beta}(x_2;0) \\ &+G(x_2;x_1)\gamma_\rho G(x_1;0)\Big|^{bb'}_{\mu\beta} G^{cc'}_{\alpha\nu}(x_2;0)\Big\}. \end{aligned} \tag{B.7}$$

For the contribution where the current is coupled with the down quark we have:

$$\begin{aligned} &D^{Nj^\rho N}_{\alpha\beta}(x_2, x_1, 0) = \\ &\langle\Omega|\varepsilon^{abc} u^a_\mu (C\gamma_5)_{\mu\nu} d^b_\nu u^c_\alpha\Big|_{x_2} \bar{d}^f_\kappa (\gamma_\rho)_{\kappa\lambda} d^f_\lambda\Big|_{x_1} \varepsilon^{a'b'c'} \bar{u}^{c'}_\beta \bar{d}^{b'}_{\nu'} (C\gamma_5)_{\nu'\mu'} \bar{u}^{a'}_{\mu'}\Big|_0 |\Omega\rangle \end{aligned} \tag{B.8}$$

where once again we have suppressed the down quark contractions since there is only one way to do so. The contractions give:

$$\begin{aligned} D^{Nj^\rho N}_{\alpha\beta}(x_2, x_1, 0) = \varepsilon^{abc}\varepsilon^{a'b'c'} &\left[C\gamma_5 G(x_2;x_1)\gamma_\rho G(x_1;0)\overline{C\gamma_5}\right]^{aa'}_{\mu\nu} \\ &\times\Big\{ G^{bb'}_{\alpha\beta}(x_2;0) G^{cc'}_{\mu\nu}(x_2;0) \\ &+G^{bb'}_{\mu\beta}(x_2;0) G^{cc'}_{\alpha\nu}(x_2;0)\Big\}. \end{aligned} \tag{B.9}$$

In Chapter 3 we use the fixed sink sequential inversion method in order to compute the three-point function and extract the nucleon form factors. With the fixed sink method, the sum over $\vec{x}_2$ is carried out in the sequential inversion. To identify the correct sequential source we must rearrange the above expressions. We will demonstrate this for $D^{Nj^\mu N}_{\alpha\beta}$. We now include the projection matrix Γ:

$$\begin{aligned} \sum_{\vec{x}_2} \mathrm{Tr}[D^{Nj^\mu N}(x_2;x_1;0)\Gamma] =& \sum_{\vec{x}_2} \gamma_\rho G(x_1;0)\Big|^{ra'}_{\mu\nu} G^{ar}_{\kappa\mu}(x_2;x_1)\Gamma_{\beta\alpha} \\ \times\varepsilon^{abc}\varepsilon^{a'b'c'} &\Big[C\gamma_5{}^\top \overline{G(x_2;0)C\gamma_5}^\top\Big|^{bb'}_{\kappa\nu} G^{cc'}_{\alpha\beta}(x_2;0) + C\gamma_5^\top G(x_2;0)\Big|^{bb'}_{\kappa\beta} G(x_2;0)\overline{C\gamma_5}^\top\Big|^{cc'}_{\alpha\nu}\Big]. \end{aligned} \tag{B.10}$$

The above is just a rearrangement of Eq. B.10 with a more convenient labeling of the indices. It is obvious that the bracketed expression is associated to the sequential source.

We rewrite the above expression more compactly:

$$\begin{aligned}\sum_{\vec{x}_2}\mathrm{Tr}[D^{Nj^\mu N}(x_2;x_1;0)\Gamma] &= \sum_{\vec{x}_2}\gamma_\rho G(x_1;0)\Big|_{\mu\nu}^{ra'} G^{ar}_{\kappa\mu}(x_2;x_1)P^{aa'}_{\kappa\nu}(x_2;0) \\ &= \sum_{\vec{x}_2}\gamma_\rho G(x_1;0)\Big|_{\mu\nu}^{ra'}\left[\gamma_5 G^\dagger(x_1;x_2)\gamma_5\right]^{ar}_{\kappa\mu} P^{aa'}_{\kappa\nu}(x_2;0) \\ &= \sum_{\vec{x}_2}\gamma_\rho G(x_1;0)\Big|_{\mu\nu}^{ra'}\left[\gamma_5 G^*(x_1;x_2)\right]^{ra}_{\mu\kappa}\left[\gamma_5 P(x_2;0)\right]^{aa'}_{\kappa\nu}.\end{aligned} \tag{B.11}$$

We can now show that the sequential source needed is given by:

$$K^{ab}_{\mu\nu}(x) = \left[\gamma_5 P(x;0)\right]^{*ab}_{\mu\nu}, \tag{B.12}$$

where:

$$\begin{aligned}P^{ab}_{\mu\nu}(x;0) = \varepsilon^{abc}\varepsilon^{a'b'c'}\Gamma_{\beta\alpha}\times \\ \Big[C\gamma_5{}^\top G(x_2;0)\overline{C\gamma_5}^\top\Big|_{\kappa\nu}^{bb'} G^{cc'}_{\alpha\beta}(x_2;0) + C\gamma_5^\top G(x_2;0)\Big|_{\kappa\beta}^{bb'} G(x_2;0)\overline{C\gamma_5}^\top\Big|_{\alpha\nu}^{cc'}\Big].\end{aligned} \tag{B.13}$$

Solving the Dirac equation for each of the indices b,ν of the source of Eq. B.12 we have:

$$\begin{aligned}S^{ab}_{\mu\nu}(y;0) &= \sum_{\vec{x}} G^{ac}_{\mu\kappa}(y;x)K^{cb}_{\kappa\nu}(x) = \sum_{\vec{x}} G^{ac}_{\mu\kappa}(y;x)\left[\gamma_5 P(x;0)\right]^{*cb}_{\kappa\nu} \Rightarrow \\ \left[\gamma_5 S(y;0)\right]^* &= \sum_{\vec{x}}\left[\gamma_5 G(y;x)\right]^*\gamma_5 P(x;0).\end{aligned} \tag{B.14}$$

In this form, we can return and insert the sequential propagator directly into Eq. B.11:

$$\sum_{\vec{x}_2}\mathrm{Tr}[D^{Nj^\mu N}(x_2;x_1;0)\Gamma] = \mathrm{Tr}\left\{\gamma_\rho G(x_1;0)[\gamma_5 S(x_1;0]]^*\right\}. \tag{B.15}$$

We can similarly construct the sequential source for the $U^{Nj^\mu N}(x_2;x_1;0)$ term and add this to the source found in Eq. B.12 to compute the complete isovector matrix element. Note that $\Gamma_{\alpha\beta}$ is traced within the sequential source thus we need a new inversion for each projection matrix needed. On the other hand we now have the three-point function as a function of $\vec{x}_1$ which means we can Fourier transform to obtain all lattice momenta. Finally we would like to note that the projection matrices Γ are usually of the form:

$$\Gamma = \begin{pmatrix}\alpha & 0\\ 0 & 0\end{pmatrix}, \tag{B.16}$$

where α is some 2×2 matrix. This means that two of the spinor components of the sequential source are zero meaning that we need not invert for these components thus reducing the computational cost of the sequential inversion by two compared to a regular inversion of all twelve spin and color indices.

Appendix C

Nucleon to Δ Transition Form Factors: Tables of Results

Numerical results for the electromagnetic N to Δ transition form factors, presented in Chapter 4.

Table C.1: Results in the hybrid approach for $\mathcal{G}_{M1}$, EMR and CMR. For the smallest quark mass we include the errors in the determination of Q^2 since these are substantial for the small values of Q^2 allowed on this lattice.

Hybrid action			
Q^2 (GeV^2)	$\mathcal{G}_{M1}$	EMR %	CMR %
Hybrid action, $a^{-1} = 1.58$ GeV			
$m_\pi = 594(1)$			
0.213	1.850(44)	-0.16(52)	
0.482	1.434(36)	-0.45(67)	-3.52(1.16)
0.738	1.143(41)	-0.52(1.42)	-3.88(1.73)
0.983	0.954(42)		
1.218	0.789(38)		-6.25(2.78)
1.445	0.665(45)		
1.874	0.471(68)		
2.079	0.413(64)		
2.278	0.363(72)		
2.472	0.322(89)		
2.660	0.262(145)		
2.844	0.172(158)		
$m_\pi = 498(3)$			
0.191	1.557(46)	-0.243(91)	
0.471	1.177(38)	-1.14(1.21)	-1.96(1.45)
0.735	0.924(40)	-0.56(2.53)	-0.20(2.42)
0.985	0.783(46)		
1.224	0.641(40)		
1.452	0.565(47)		
1.883	0.371(70)		
2.087	0.381(96)		
2.284	0.294(172)		
2.476	0.260(240)		
2.662	0.104(226)		
2.843	0.146(120)		

Hybrid action			
Q^2 (GeV^2)	$\mathcal{G}_{M1}$	EMR %	CMR %
Hybrid action, $a^{-1} = 1.58$ GeV			
$m_\pi = 353(2)$			
0.042(16)	1.681(59)	-0.72(88)	-1.523(89)
0.194(14)	1.404(49)	-1.56(79)	-2.98(92)
0.341(8)	1.199(51)	-1.09(1.13)	-2.41(1.61)
0.482(9)	1.070(48)	0.22(1.82)	-2.55(2.27)
0.619(8)	0.930(47)	-1.70(1.57)	-2.79(1.77)
0.751(9)	0.813(48)	-2.94(2.18)	-1.54(2.22)
1.005(11)	0.723(53)		-3.98(3.65)
1.127(16)	0.660(53)		-2.145(3.14)
1.246(16)	0.623(60)		-6.08(3.84)
1.362(23)	0.581(62)		-7.80(4.08)
1.475(51)	0.518(89)		
1.586(18)	0.525(84)		
1.695(35)	0.518(94)		
1.906(65)	0.392(116)		
2.009(26)	0.328(87)		
2.111(13)	0.298(94)		
2.209(20)	0.275(128)		
2.306(23)	0.230(94)		
2.402(34)	0.222(124)		
2.497(34)	0.073(108)		
2.682(20)	0.087(170)		

Table C.2: Quenched results for $\mathcal{G}_{M1}$, EMR and CMR

Wilson fermions			
Q^2 (GeV^2)	$\mathcal{G}_{M1}$	EMR %	CMR %
Quenched, $\beta = 6.0$, $a^{-1} = 2.14(6)$ GeV			
$m_\pi = 563(4)$ MeV			
0.158	1.646(30)	-0.72(26)	-0.82(26)
0.348	1.332(23)	-0.86(29)	-2.09(39)
0.530	1.102(29)	-0.60(57)	-2.62(52)
0.704	0.933(22)	-0.51(47)	-1.80(60)
0.871	0.804(22)	-0.82(45)	-3.11(77)
1.033	0.698(23)	-0.62(63)	-2.92(84)
1.341	0.545(25)	-1.33(93)	-4.31(1.21)
1.488	0.474(24)		
1.631	0.424(26)		
1.770	0.373(25)		
1.906	0.309(28)		
2.039	0.306(34)		
2.169	0.254(28)		
2.420	0.202(52)		
$m_\pi = 490(4)$ MeV			
0.151	1.572(33)	-0.93(36)	-0.92(33)
0.344	1.259(31)	-1.18(38)	-2.33(48)
0.529	1.033(30)	-1.03(76)	-2.99(66)
0.705	0.873(26)	-0.47(64)	-1.97(74)
0.874	0.749(24)	-1.05(62)	-3.87(93)
1.037	0.649(25)	-0.79(83)	-3.46(1.04)
1.346	0.510(28)	-1.65(1.28)	-5.44(1.54)
1.493	0.441(25)		
1.636	0.393(28)		
1.775	0.346(28)		
1.910	0.283(31)		
2.042	0.290(38)		
2.171	0.238(30)		
2.420	0.185(52)		

Wilson fermions			
Q^2 (GeV^2)	$\mathcal{G}_{M1}$	EMR %	CMR %
Quenched, $\beta = 6.0$, $a^{-1} = 2.14(6)$ GeV			
$m_\pi = 411(4)$ MeV			
0.138	1.479(44)	-1.36(59)	-0.99(50)
0.338	1.171(37)	-1.73(62)	-2.49(69)
0.527	0.951(35)	-1.82(1.10)	-3.59(93)
0.706	0.804(32)	-0.26(99)	-2.22(1.05)
0.878	0.687(26)	-1.30(94)	-5.44(1.30)
1.042	0.595(29)	-0.95(1.24)	-4.74(1.42)
1.353	0.475(34)	-2.14(2.04)	-7.01(1.22)
1.501	0.406(28)		
1.644	0.359(30)		
1.783	0.317(31)		
1.918	0.252(35)		
2.050	0.276(45)		
2.178	0.223(34)		
2.426	0.172(57)		

Table C.3: Wilson $N_F = 2$ results for $\mathcal{G}_{M1}$, EMR and CMR

Wilson fermions			
Q^2 (GeV^2)	$\mathcal{G}_{M1}$	EMR %	CMR %
$N_F = 2$ Wilson, $\beta = 5.6$, $a^{-1} = 2.56(10)$ GeV			
$m_\pi = 691(8)$			
0.447	1.437(36)	-0.76(43)	-1.76(69)
0.891	0.989(31)	-0.86(71)	-3.03(1.04)
1.304	0.717(30)	-1.44(1.33)	-0.88(1.34)
1.691	0.509(40)	-2.28(1.42)	-5.75(1.95)
2.058	0.443(38)	-2.08(1.48)	-10.06(2.41)
2.407	0.341(37)		
3.060	0.208(55)		
$m_\pi = 509(8)$			
0.445	1.210(42)	-1.00(1.28)	-0.93(1.42)
0.892	0.794(32)	-5.26(1.87)	-6.17(2.10)
1.303	0.521(32)	-5.95(4.43)	-3.49(3.44)
1.685	0.474(52)	-5.65(3.47)	-4.02(3.33)
2.044	0.296(32)		
2.384	0.211(48)		

Wilson fermions			
Q^2 (GeV^2)	$\mathcal{G}_{M1}$	EMR %	CMR %
$N_F = 2$ Wilson, $\beta = 5.6$, $a^{-1} = 2.56(10)$ GeV			
$m_\pi = 384(8)$			
0.442	1.066(43)	-1.49(1.59)	-1.27(1.57)
0.893	0.798(44)	-1.83(2.10)	-6.47(2.37)
1.299	0.589(37)		
1.671	0.396(48)		
2.017	0.244(47)		
2.342	0.181(41)		

Appendix D

Δ Electromagnetic Form Factors: Kinematic Coefficients

In Chapter 6 we give three linear combinations of the three-point function used to construct three optimal sequential sources. The third combination used is given by:

$$S_3(\vec{q};\mu) = \sum_{j=1}^{3} \varepsilon_{jkl}\Pi_{kl}(0,-\vec{q},\Gamma_k,\mu) = \mathcal{A}_k^{\mu}(q)G_{E2}(q) + \mathcal{B}_k^{\mu}(q)G_{M1}(q) + \mathcal{C}_k^{\mu}(q)G_{M3}(q). \quad \text{(D.1)}$$

The kinematic coefficients are given by:

$$\mathcal{A}_k^{\mu}(q) = \frac{i}{3M_\Delta^2(E_\Delta(q)+M_\Delta)}(q_1q_2+q_2q_3+q_3q_1)iq_\mu \quad \text{(D.2)}$$

$$\begin{aligned}\mathcal{B}_k^{\mu}(q) = -\frac{1}{6M_\Delta^2(E_\Delta(q)+M_\Delta)}\big[&\delta_{1,\mu}(q_3q_2^2+q_2q_3^2-2q_1q_2q_3) \\ &+\delta_{2,\mu}(q_1q_3^2+q_3q_1^2-2q_1q_2q_3) \\ &+\delta_{3,\mu}(q_1q_2^2+q_2q_1^2-2q_1q_2q_3)\big]\end{aligned} \quad \text{(D.3)}$$

$$\begin{aligned}\mathcal{C}_k^{\mu}(q) = -\frac{1}{30M_\Delta^3(E_\Delta(q)+M_\Delta)}\big\{&\\ \delta_{1,\mu}[&(8E_\Delta(q)+7M_\Delta)(q_3q_2^2+q_2q_3^2)-(16E_\Delta(q)+14M_\Delta)q_1q_2q_3 \\ &-5M_\Delta(E_\Delta(q)^2-M_\Delta^2)(q_2+q_3)+10M_\Delta(q_1q_2+q_2q_3+q_3q_1)q_1] \\ +\delta_{2,\mu}[&(8E_\Delta(q)+7M_\Delta)(q_1q_3^2+q_3q_1^2)-(16E_\Delta(q)+14M_\Delta)q_1q_2q_3 \\ &-5M_\Delta(E_\Delta(q)^2-M_\Delta^2)(q_1+q_3)+10M_\Delta(q_1q_2+q_2q_3+q_3q_1)q_2] \\ +\delta_{3,\mu}[&(8E_\Delta(q)+7M_\Delta)(q_1q_2^2+q_2q_1^2)-(16E_\Delta(q)+14M_\Delta)q_1q_2q_3 \\ &-5M_\Delta(E_\Delta(q)^2-M_\Delta^2)(q_1+q_2)+10M_\Delta(q_1q_2+q_2q_3+q_3q_1)q_3]\big\}.\end{aligned} \quad \text{(D.4)}$$

Appendix E

Density-Density Correlators: Image Correction Fit Parameters

In the following table we quote the parameters obtained when fitting the density-density correlators presented in Chapter 7 to the following forms:

$$\begin{aligned} C_0^{\pi} &= A_0 \exp\left(-m_0 r^{\sigma}\right), \\ C_0^{\rho} &= \left[A_0 \exp\left(-m_0 r^{\sigma}\right) + A_1 \exp\left(-m_1 r^{\sigma}\right) r^2 P_2(\cos\theta)\right]^2, \\ C_0^{N} &= \text{same as for } \pi, \\ C_0^{\Delta} &= \text{same as for } \rho. \end{aligned} \tag{E.1}$$

Table E.1: The parameters obtained from fitting the sum of images to the lattice data.

		Mesons			Baryons	
κ	0.1575	0.1580	0.15825	0.1575	0.1580	0.15825
		π			N	
A_0	0.986(21)	1.129(33)	1.437(78)	1.014(39)	1.039(34)	1.057(34)
m_0	0.307(7)	0.405(11)	0.579(25)	0.0673(40)	0.0698(44)	0.0548(38)
σ	0.993(7)	0.884(9)	0.779(12)	1.451(20)	1.413(22)	1.450(24)
		ρ, $m_z = 0$			Δ, $m_z = \pm\frac{3}{2}$	
A_0	0.969(13)	0.964(21)	0.919(31)	1.024(22)	1.033(19)	1.023(16)
m_0	0.0173(19)	0.0140(26)	0.0093(26)	0.0125(11)	0.0130(12)	0.0087(8)
A_1	0.00170(31)	0.0031(16)	0.00183(46)	0.00029(25)	-0.0007(14)	-0.00121(49)
m_1	0.0466(87)	0.077(33)	0.0033(12)	0.024(13)	0.022(25)	0.077(30)
σ	1.615(41)	1.646(69)	1.76(11)	1.750(32)	1.708(34)	1.787(33)
		ρ, $m_z = \pm 1$				
A_0	0.976(10)	0.961(16)	0.977(28)			
m_0	0.0194(16)	0.0128(16)	0.0141(34)			
A_1	-0.00113(18)	-0.00054(34)	-0.0012(17)			
m_1	0.0560(91)	0.025(12)	0.066(69)			
σ	1.577(30)	1.659(47)	1.613(87)			